UNIVERSITÀ DEGLI STUDI DI PISA
Facoltà di Scienze Matematiche, Fisiche e Naturali

Tesi per il Conseguimento del
Dottorato di Ricerca in Fisica

XIV Ciclo - AA.AA. 1998-2001

Scalar Top Quark Search at LHC with the CMS Detector

Candidato:
Dott. Gabriele Segneri

Supervisore:
Prof. Guido Tonelli

Contents

Introduction

The Standard Model[1] provides a remarkably successful description of the electroweak interactions up to the explored energy scales. It was extensively tested by the recent experiments and no deviation from theoretical predictions has been observed yet[2].

However, the theory is still far from being definitive and many aspects still need to be understood. There is not yet an experimental evidence of the Higgs boson, which is responsible of the electroweak symmetry breaking and the fermion mass hierarchy. Moreover, the theory is still a low energy effective theory: the radiative corrections to the Higgs mass show a quadratic dependence on the cut-off parameter, which is of the order of the Planck mass. This dependence of the electroweak scale on the Planck scale is *unnatural*. A more general framework is thus needed to provide a solution to the unsatisfactory aspects of the Standard Model. Supersymmetry (SUSY), and the minimal supersymmetric extension of the Standard Model (MSSM) in particular, are the most interesting options at the moment[3]. They offer elegant solutions to the main Standard Model inconsistencies and provide the gauge coupling unification at an energy scale ($\sim 2 \times 10^{16}$ GeV) which is intermediate between the Electroweak scale and the Planck mass scale ($\sim 2 \times 10^{18}$ GeV).

From the phenomenological point of view, one of the most striking features of Supersymmetry is the prediction of the existence of a large number of new particles, each one associated to a Standard Model partner. These particles can be directly produced at high energy Colliders, or alternatively, indirect evidence of their existence can be found through the effect of radiative corrections to a large number of observables, such as the muon anomalous magnetic moment or the branching ratio of $b \to s\gamma$. Several searches and precision measurements were performed in the past but no direct signal or indirect evidence have been found so far[4][5].

The Large Hadron Collider will be a very important test bench for this physics. By providing proton collisions at a centre-of-mass energy of 14 TeV, it will allow searches of the SUSY particles in the most favored mass range.

CMS is one of the two multipurpose experiments of LHC. Its main goals are Higgs boson discovery, electroweak precision measurements and searches for new phenomena beyond the Standard Model.

This work is dedicated to the search of the scalar top quark (*stop* or $\tilde{t}$), which is the supersymmetric partner of the top quark, in the MSSM-mSUGRA scenario. In a large portion of the mSUGRA parameter space, $\tilde{t}$ is the lightest scalar quark. For this reason it affects, through loop corrections, a large number of observables; in a very large mixing scenario it also plays an important role in Cosmology.

The production process examined in this work is $pp \to \tilde{t}\bar{\tilde{t}}$. The considered decay modes are $\tilde{t} \to t\tilde{\chi}_1^0$ and $\tilde{t} \to b\tilde{\chi}_1^{\pm}$, $\tilde{\chi}_1^{\pm} \to W^{\pm}\tilde{\chi}_1^0$. The main difficulty of the search is the

separation of the $\tilde{t}\bar{\tilde{t}}$ signal from the $t\bar{t}$ and $W^{\pm}$ plus jets backgrounds, which are copiously produced at LHC and produce very similar decays. The search is performed for several SUSY parameters values corresponding to different $\tilde{t}$ and $\tilde{\chi}_1^0$ masses and different $\tilde{t}\bar{\tilde{t}}$ cross sections. A Model Independent search is also performed for different values of the $\tilde{t}$ mass ($m_{\tilde{t}}$) and the $\tilde{\chi}_1^0$ mass ($m_{\tilde{\chi}_1^0}$) for each decay mode separately. The possibility to separate the $\tilde{t}\bar{\tilde{t}}$ signal from the overall supersymmetric particles production is also investigated.

The reconstruction of these events requires the reconstruction of hadron jets and leptons produced from $W^{\pm}$ decays ($W^{\pm}$ can be produced from t and $\tilde{\chi}_1^{\pm}$), $b-$jets produced from t and $\tilde{t}$ decays and a large missing transverse momentum due to neutrinos and neutralinos. All sub-detectors of the experiment play a role in producing the informations relevant for this analysis: leptons are reconstructed with Tracker, electromagnetic calorimeter and muon system, jets are reconstructed with hadron calorimeter and identified as $b-$jets with the Tracker; the reconstruction of missing transverse momentum requires informations from all sub-detectors.

The identification of $b-$jets ($b-$tagging), which is one of the main requirements for the search, is analysed in detail. The $b-$tagging capability at LHC is a very demanding request both for the detector and for the reconstruction software and a large number of tools, *ad hoc* developed for this purpose, are described in detail.

For what concerns the instrumental part, a powerful tracking and microvertex detector are required to reconstruct long lived particles whose decays occur very close to the primary interaction vertex. The basic requirements on such kind of devices is a high granularity, to separate very close charged tracks, a good position resolution, to measure tracks parameters, a fast DAQ system, to cope with the high Collision rate and a radiation hard technology to operate for 10 years in the LHC high radiation environment. A very large area Tracker, based on Silicon detectors, was designed by the CMS Collaboration to fulfill these requirements. Sensors were designed in collaboration with the main producers and studies were performed on their electrical properties and the performance after irradiation. Complete detector modules, made of sensors, readout chips and mechanical supports, were also assembled and carefully tested to investigate their performance under different running conditions.

The offline reconstruction required for $b-$tagging is also very complex. The $b-$tagging methods rely on the presence of secondary vertices, with the topologies of a B-decay, or on tracks with a large impact parameter. Complex algorithms are needed to reconstruct charged tracks and secondary vertices in a very dense particles environment. An algorithm for secondary vertices reconstruction and two algorithms based on track impact parameter and secondary vertices were adapted to the CMS Tracker. The performance of these algorithms are carefully studied for jets with different E_T in various pseudorapidity intervals.

The thesis is divided in two parts: the first part contains a general description of the theoretical and experimental framework of this study, while the second part is dedicated to the scalar top quark search with the CMS detector and to the tools developed for this purpose.

The first chapter provides the current status of the knowledge about fundamental interactions and the supersymmetric extensions of the Standard Model. The aspects of the Standard Model, which require an extension of the theory, are then described together with the solutions provided by Supersymmetry. All elements needed to derive the scalar

top quark phenomenology are provided. The current status of Supersymmetry searches is also illustrated in this chapter and the exclusion contours for the SUSY parameters are presented.

The second chapter provides a general overview of the experimental facility: the accelerator complex as well as the CMS detector and its subunits are described in some detail. The chapter also provides the informations about the reconstructed objects used in the analysis.

The second part describes the scalar top quark search and the tools which were developed for this work.

The third chapter illustrates the main strategies for Supersymmetry searches at LHC. The scalar top quark search is introduced and the complementarity with the other searches is shown. The chapter also provides an outline of the main experimental requirements needed for event reconstruction, in particular those related with the tracking detector, which will be developed in the next three chapters.

The fourth chapter is dedicated to the instrumental aspects of the Tracker. The performance of the silicon microstrip detectors are shown together with the status of the Tracker construction.

The fifth chapter is concentrated on the track reconstruction. The goal of this chapter is to provide a description of all objects which are required to optimise the $b-$tagging performance.

The $b-$tagging methods are fully described in the sixth chapter. The performance of the various algorithms are compared and the $b-$tagging efficiency and mistagging rate of u and c jets are provided for different E_T and η ranges. An application of $b-$tagging to High Level Trigger Reconstruction is also discussed.

In the last chapter the search strategy of the scalar top quark is finally described. The results are discussed in terms of $S/\sqrt{B}$, being S the expected signal and B the expected background events, for the low luminosity period of data taking (corresponding to an integrated luminosity of 30 fb^{-1}). Different points in the mSUGRA parameter space and $m_{\tilde{t}}-m_{\tilde{\chi}_1^0}$ plane are considered. The analysis is also extended to incorporate the background due to the other SUSY processes. The effect of $b-$tagging and a reduced ECAL coverage are also investigated.

Conclusions are finally drawn from the results illustrated in the last four chapters.

The thesis contains my personal contribution to the CMS Collaboration activities in the last three years.

For what concerns the Tracker related studies, I participated personally to the activities related to sensors and modules described in the fourth chapter: electrical characterisation, irradiation, analysis of measurements and data collected in test beams.

I consider the work done on the Tracker software, as described in the fifth and sixth chapters my most important contributions to the experiment: study of the track reconstruction performance, development of the secondary vertex finder and of the package containing tools and algorithms for $b-$tagging. I used the same package to evaluate the $b-$tagging performance with High Level Trigger Reconstruction. All these studies provided a quick feedback to evaluate the impact on performance of changes in the base Tracker design and the inclusion of experimental effects on simulation.

Finally, to evaluate the physics potential of CMS in several theoretical and experimental

scenarios, I performed the study on the scalar top quark search described in chapter 7, drawing inspiration from older studies [6] and searches performed in recent experiments.

Part I

Theoretical and Experimental Framework

Chapter 1

Supersymmetry

This chapter provides an overview of the current understanding of the physics of fundamental interactions. Supersymmetry, and the supersymmetric extension of the Standard Model, are introduced together with the elements which are necessary to describe the scalar top quark phenomenology.

The Standard Model theory is discussed first: the Supersymmetry framework as well as the Minimal Supersymmetric Standard Model are then introduced; special subsections are dedicated to the problem of Supersymmetry breaking, the electroweak symmetry breaking in the SUSY framework and the mixing of supersymmetric particles. The mSUGRA model, a constrained version of the Standard Model, is also discussed. Finally, a discussion of the most important constraints on the model are provided to identify the regions in the SUSY parameter space and the mass intervals which will be explored with LHC.

1.1 The Standard Model of Electroweak Interactions

The Standard Model of Electroweak Interactions[1] is a Quantum Field Theory based on a local $SU(3)_C \otimes SU(2)_L \otimes U(1)_Y$ gauge symmetry. The $SU(3)_C$ symmetry is associated to colour interactions, the $SU(2)_L$ and $U(1)_Y$ symmetries to the so called weak isospin and hypercharge interaction.

Matter fields are described by spin$-\frac{1}{2}$ particles ($fermions$). Interactions between fermions are mediated by spin-1 particles (bosons).

Fermions are divided in two classes: *leptons* and *quarks*, both interacting electroweakly. The latter feel strong interactions as well. Three families of leptons and three families of quarks have been discovered. Each lepton family consists of a massive charged lepton (e, μ and τ) of charge $-e$ ($-e$ being the electron charge) and a massless neutral neutrino (ν_e, ν_μ, ν_τ). Each quark family contains a charge $\frac{2}{3}e$ (u, c, t) and a charge $-\frac{1}{3}e$ (d, s, b) massive quark.

Four vector bosons mediate the electroweak interactions:

- two massive charged bosons $W^\pm$ ($M_W \sim 80$ GeV) responsible of the charged current interactions
- a massive neutral vector boson Z^0 ($M_Z \sim 91$ GeV) responsible of the neutral currents
- a neutral massless boson, the photon (γ), responsible of the electromagnetic interactions.

Strong interactions are mediated by massless gluons. A scalar field, the Higgs boson, is also included to achieve the $SU(2)_L \otimes U(1)_Y$ symmetry breaking.

1.1.1 The Electroweak Sector

In the Standard Model, left-handed leptons and neutrinos are arranged in $SU(2)$ isospin doublets:

$$L_L = \begin{pmatrix} \nu_l \\ l_L \end{pmatrix} \tag{1.1}$$

being $l = e,\ \mu,\ \tau$. The right handed components are arranged in $SU(2)$ singlets l_R.

In absence of gauge interactions the Electroweak Lagrangian (L_{EW}) contains only the kinetic terms:

$$\mathcal{L}_{EW}^{leptons} = i \sum_{i=1}^{3} (L_L^{\dagger i} \bar{\sigma}^\mu \partial_\mu L_L^i + l_R^{\dagger i} \sigma^\mu \partial_\mu l_R^i) \tag{1.2}$$

being $\sigma^\mu = (1, \sigma^i)$, $\bar{\sigma}_i = (1, -\sigma^i)$ and σ^i the Pauli matrices. All leptons are massless at this stage. The local $SU(2)_L \otimes U(1)_Y$ gauge invariance is obtained by replacing the partial derivative with the covariant derivative:

$$\mathcal{D}_\mu = \partial_\mu + \frac{i}{2} g W_\mu^a \sigma_a - \frac{i}{2} g' Y B_\mu. \tag{1.3}$$

W_μ^a and B_μ are the vector bosons associated to the $SU(2)_L$ and $U(1)_Y$ gauge symmetries and g and g' their couplings. Y is the hypercharge, the quantum number related to $U(1)$ symmetry, ($Y = -\frac{1}{2}$ for left handed leptons and 1 for the right handed ones) which acts as a multiplicative factor. The kinetic terms for the vector bosons are given by:

$$\mathcal{L}_{EW}^{bosons} = -\frac{1}{4} W_a^{\mu\nu} W_{\mu\nu}^a - \frac{1}{2} B^{\mu\nu} B_{\mu\nu}. \tag{1.4}$$

1.1.2 The Quark Sector

The left handed components of the quarks are also arranged in $Y = 1/6$ $SU(2)_L$ weak isospin doublets:

$$Q_L = \begin{pmatrix} U_L \\ D_L \end{pmatrix}, \tag{1.5}$$

while the right handed components are arranged in $Y = -2/3$ and $1/3$ $SU(2)_L$ singlets U_R and D_R respectively. U and D are combinations of the mass eigenstates u and d:

$$U_{L,R}^i = \sum_j X(U)_{L,R}^{ij} u_{L,R}^j, \quad D_{L,R}^i = \sum_j X(D)_{L,R}^{ij} d_{L,R}^j \tag{1.6}$$

($u^i = u, c, t$ and $d^i = d, s, b$) to reproduce the observed behaviour of flavour changing charged currents. $X(U, D)_{L,R}$ are 3×3 unitary matrices. As in the leptonic case, the Lagrangian is:

$$\mathcal{L}_{EW}^{quarks} = i \sum_i (Q_L^{\dagger i} \bar{\sigma}^\mu \mathcal{D}_\mu Q_L^i + U_R^{\dagger i} \sigma^\mu \mathcal{D}_\mu U_R^i + D_R^{\dagger i} \sigma^\mu \mathcal{D}_\mu D_R^i) \tag{1.7}$$

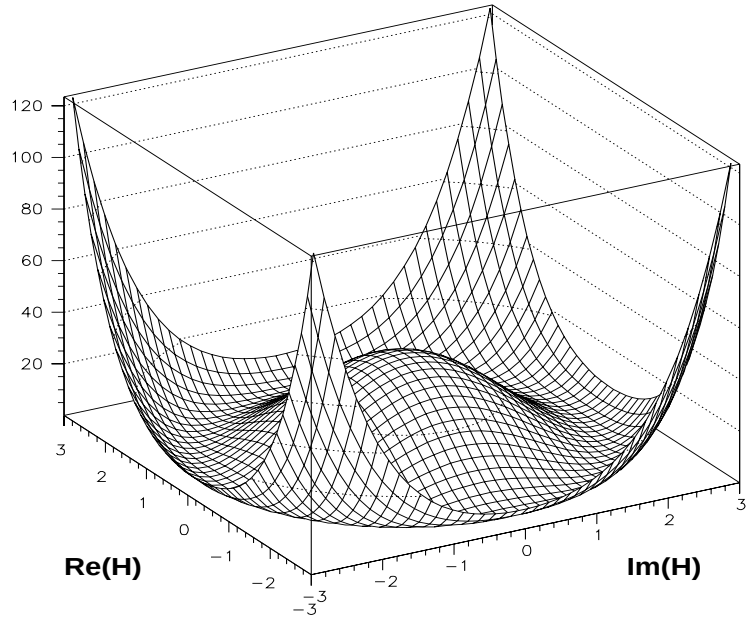

Figure 1.1: The potential of the Higgs field (arbitrary units).

($\mathcal{D}_\mu$ is provided by 1.3). The colour interactions are included in the terms:

$$\mathcal{L}_{strong} = -g_s \sum_{ijk} (\bar{q}_i^k \gamma^\mu T_a^{ij} q_j^k) G_\mu^a - \frac{1}{4} G_{\mu\nu}^a G_a^{\mu\nu} \tag{1.8}$$

which represent the interaction with the gluon field G_μ^a and the gluon kinetic term.

1.1.3 The Higgs Mechanism and Electroweak Symmetry Breaking

The last ingredient of the Standard Model is the Higgs boson[7]: it is a $Y = \frac{1}{2}$ doublet of scalar fields (ϕ^+, ϕ^0). Its associated Lagrangian is:

$$\mathcal{L}_{Higgs} = \partial_\mu H^\dagger \partial^\mu H - \mathcal{V}(H^\dagger H). \tag{1.9}$$

The first term is the Higgs kinetic term and the second one is the Higgs potential. Such potential is invariant under $SU(2)_L \otimes U(1)_Y$ gauge symmetry . The gauge invariance of the Higgs Lagrangian is accomplished by replacing the partial derivative with the covariant one of Eq. 1.3. The breaking of the Electroweak symmetry relies on the Higgs potential: it occurs if the potential is gauge invariant and has degenerate minima. The ensemble of minima, but not each minimum, should be gauge invariant. If the Higgs field takes a vacuum expectation value (VEV) in one of these minima, the symmetry breaks. The Higgs potential is:

$$\mathcal{V}(H^\dagger H) = k(H^\dagger H - v^2)^2 \tag{1.10}$$

being k and v positive constants. The shape of this potential is shown in Fig. 1.1.

Minima are defined by $H^\dagger H = v^2$. The vacuum expectation value of the Higgs field is:

$$|\langle 0|H|0\rangle|^2 = v^2. \tag{1.11}$$

The vector bosons mix and become massive through this mechanism: the Higgs degrees of freedom are expressed in the real coordinates χ and θ^a related to the complex components ϕ^+ and ϕ^0 through the transformation:

$$\begin{pmatrix}\phi^+\\ \phi^0\end{pmatrix} \rightarrow e^{-\frac{i}{2}\theta_a\sigma^a}\begin{pmatrix}0\\ v+\chi/\sqrt{2}\end{pmatrix}. \tag{1.12}$$

χ represents the displacement from the minimum in the direction passing through the origin. Due to gauge invariance, the minimum can always be rotated around the point $(0, v)$. In this basis, the term $\mathcal{D}_\mu H^\dagger \mathcal{D}^\mu H$ contains the contributions:

$$\frac{1}{4}v^2(gW_3^\mu - g'B_\mu)^2 + \frac{1}{2}g^2 W_\mu^- W^{+\mu}, \tag{1.13}$$

which are the mass terms for the charged vector bosons $W^\pm$ and a neutral field which is the superposition of W_3 and B. The effect of the local symmetry breaking is the redistribution of the degrees of freedom: the θ^a bosons become the transverse degrees of freedom of the gauge bosons which mix and get masses and χ is the physical Higgs state.

The Weinberg angle, defined by $\tan\theta_W = g'/g$, is introduced and the neutral components of W and B are rotated yielding the following superpositions:

$$Z_\mu = -W_\mu^3 \sin\theta_W + B_\mu \cos\theta_W, \quad A_\mu = W_\mu^3 \cos\theta_W + B_\mu \sin\theta_W. \tag{1.14}$$

The first field, the Z^0 boson, is the one associated to the mass term in Eq. 1.13 while the second one is the photon, which remains massless because it does not interact with the Higgs field.

In this framework the masses and the couplings can be related to g, g' and v. As an example, the vector bosons masses are:

$$m_W = \frac{gv}{\sqrt{2}}, \quad m_Z = \frac{v}{2}\sqrt{g^2 + g'^2} \tag{1.15}$$

and the electron charge is:

$$e = g\sin\theta_W = g'\cos\theta_W. \tag{1.16}$$

The Higgs field provides also masses to the fermions through the interaction:

$$\begin{aligned}\mathcal{L}_{Higgs-fermions} = &-\sum_i y^i (L_L^{\dagger i} H l_R^i + l_i H^\dagger L_L^i)\\ &-\sum_{ij}(Y^{ij} Q_L^{\dagger i} H D_R^j + Y'^{ij} Q_L^{\dagger i} \hat{H} U_R^j + h.c.),\end{aligned} \tag{1.17}$$

y^i and Y^{ij} being the Yukawa couplings to leptons and quarks and $\hat{H} = i\sigma^2 H^*$. After electroweak symmetry breaking, these terms become mass terms for leptons and quarks. The Yukawa couplings are related to the fermion masses through the relations:

$$m^i = v y^i \tag{1.18}$$

$$Y^{ij} = \frac{1}{v}\sum_k X(U)_L^{ik}(X(U)_R^{-1})^{kj}m_u^k, \quad Y'^{ij} = \frac{1}{v}\sum_k X(D)_L^{ik}(X(D)_R^{-1})^{kj}m_d^k. \tag{1.19}$$

The Higgs sector is the only sector of the Standard Model which is not yet tested: the only informations about it can be derived from indirect constraints and direct searches. However, the theory provides some constraints on the mass range. The upper limit $m_h < 1.2$ TeV comes from the unitarity requirements for the scattering amplitude of longitudinally polarised W bosons[8]. The lower limit is:

$$m_h^2 > \frac{3(2m_W^4 + m_Z^4) - 4\sum_\ell m_\ell^4 - 12\sum_q m_q^4}{16\pi^2 v^4}. \tag{1.20}$$

The sums run over the lepton and quarks families and $v = (\sqrt{2}G_F)^{-1/2} \sim 246$ GeV comes from the vacuum state stability requirement[8]. The lower limit on m_h coming from this relationship is 7 GeV/c^2.

Tighter theoretical constraints come from the one-loop matching conditions relating the particles coupling with the masses: the allowed upper and lower bands are shown in Fig. 1.1.3 [9] as a function of the cutoff parameter Λ for $m_t = 175$ GeV. If the validity of the Standard Model is assumed up to the Planck scale ($\sim 10^{19}$ GeV), the allowed mass gap ranges between 130 and 190 GeV. However, this gap can be restricted if a new physics is assumed above the electroweak scale: as an example, if $\Lambda \sim 1$ TeV, the allowed mass gap restricts to the $55 \div 750$ GeV interval.

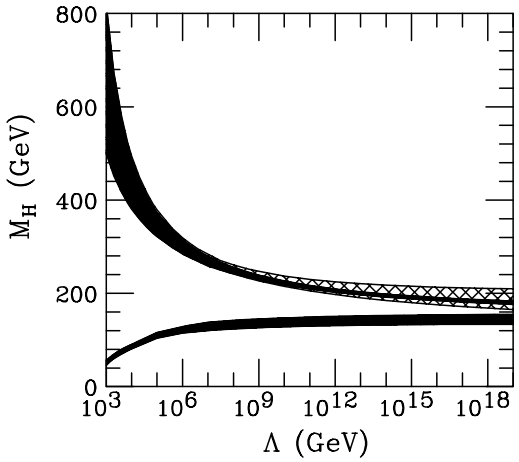

Figure 1.2: Upper and lower bound on the Higgs mass as a function of the cutoff parameter Λ for $m_t = 175$ GeV and $\alpha_s = 0.118$. The hatched area shows the additional uncertainty varying m_t between 150 and 200 GeV[9].

1.1.4 The Standard Model Validation

The results of the electroweak precision tests and the indirect results on the Higgs sector are described in this section to provide a general overview of the status of the Standard Model validation.

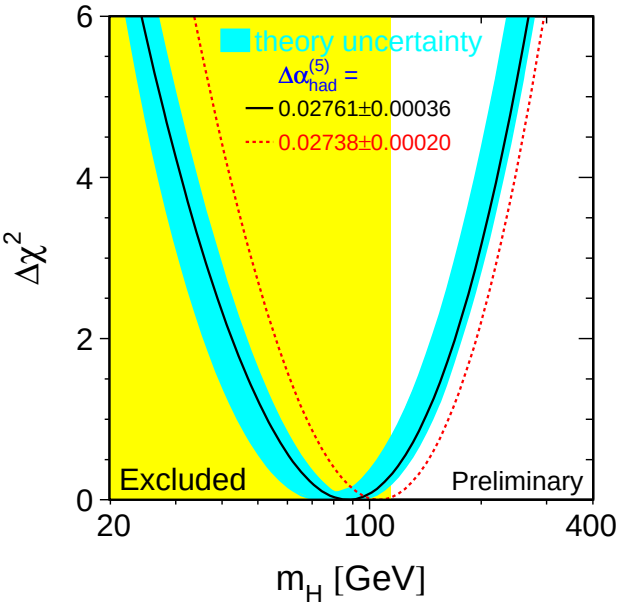

Figure 1.3: $\Delta\chi^2 = \chi^2 - \chi^2_{min}$ as a function of m_H. The solid line corresponds to the result of the fit using all data, the band represents an estimate of the theoretical error due to missing higher order corrections. The vertical band shows the 95% C.L. exclusion limit on m_H due to the direct searches[2]. The dashed curve is the result obtained using the evaluation of $\Delta\alpha^{(5)}_{had}(m^2_Z)$ from [10].

Electroweak Precision Tests

A global fit was performed from a large number of measurements obtained from many experiments to extract the parameters of the Standard Model [2]. A first set of measurements used in this fit is related to the lepton asymmetries, Z^0 line-shape, τ polarisation, $q\bar{q}$ charge asymmetries and heavy-flavours performed at LEP and LSD. The W and top masses measurements performed at Tevatron are also taken into account. Finally some measurements not exclusively related with accelerator physics, like the $\sin^2\theta_{eff}$ measurement from neutrino interactions, the atomic parity violation in Cesium and G_F constant from muon lifetime are included. In this fit the Higgs mass is left as a free parameter since no direct observation has been performed so far. The fundamental parameters of the Standard Model are extracted from the fit.

A large number of self-consistency tests are performed to assess the robustness of the method. As an example, the fit is repeated leaving m_W and/or m_t as free parameters to test the consistency of the model and in all cases the predictions are in agreement with experimental measurements.

Once the robustness of the method is assessed, the fitted parameters are used to probe indirectly the Higgs sector which is still unexplored. The best accuracy on the prediction is achieved including all data in the fit. Fig. 1.3 shows the $\Delta\chi^2 = \chi^2 - \chi^2_{min}$ of the fit as a function of m_h.

The result of the fit is $\log(m_h/\mathrm{GeV}) = 2.03 \pm 0.19$, corresponding to $m_h = 106^{+57}_{-38}$ and the upper limit is 222 GeV at 95% C.L. As it will be shown this prediction is compatible with the experimental limit from direct searches.

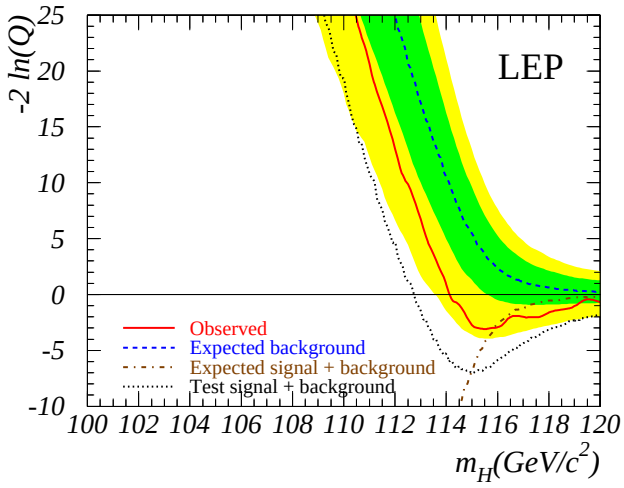

Figure 1.4: Observed and expected behaviour of the likelihood ratio $-2\log Q$ as a function of the test-mass m_H obtained with the combination of the four LEP experiments. The solid line represents data, the dashed and dashed/dash-dotted lines show the median background/ signal+background expectations. The dark/light shading bands represent the $\pm 1/\pm 2$ standard deviation spread of the background expectation and the dotted line the expectation with a test signal of $m_h = 115$ GeV[12].

Higgs Boson Direct Searches

The tightest constraint on the Higgs boson mass comes from the combined results of the four LEP experiments [11][12].

The Higgs boson is expected to be produced in association with the Z^0 boson through the Higgstrahlung process $e^+e^- \to HZ$. In the mass range accessible to LEP, the dominant decay mode is $H \to b\bar{b}$ with a branching ratio of $\sim$ 74%. The topology is therefore determined by the Z^0 decay. All final states with $Z^0 \to q\bar{q}$, $\ell^+\ell^-$, $\nu\bar{\nu}$ and $\tau\bar{\tau}$ and $H \to \tau\bar{\tau}$, $Z^0 \to q\bar{q}$ are considered.

The data obtained by the four LEP experiments at a centre-of-mass energy ranging between 189 and 209 GeV are combined together for a total integrated luminosity of 2465 fb^{-1}. A likelihood analysis is performed to test two hypothetical scenarios where data would receive contributions only from an Higgs boson signal of known mass plus Standard Model backgrounds processes and only backgrounds. The test-statistics variable is shown in Fig. 1.4 as a function of m_h (Higgs-like events have large Q value).

The lower bound on m_h at 95% C.L. (intersection of the solid line with the horizontal line) is $m_h > 114.1$ GeV, while the preferred mass value corresponding to the maximum of the Likelihood $-2\log Q = -2.88$ is $m_h = 115.6$ GeV (minimum of the solid line). The minimum indicates a deviation from the background hypothesis and coincides with the signal+background expectation for the same test mass. The signal-like behaviour mainly originates from ALEPH data and is concentrated in the four jets final state. None of the experiments considered separately has the power to distinguish the background and signal+background hypotheses at the level of two standard deviations.

1.1.5 Quadratic Divergencies and Hierarchy Problem

One of the inconsistencies of the Standard Model arises when the radiative corrections to the scalar masses, due to the fermion loop contributions (shown in Fig. 1.5) are included.

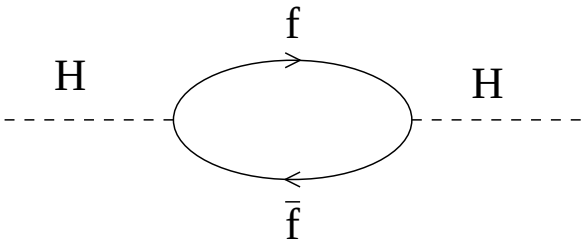

Figure 1.5: Fermion-antifermion contribution to the Higgs boson self-energy in the Standard Model.

The coupling to fermions is a Yukawa coupling of the form $-\lambda_f H \bar{f} f$, which provides the mass correction:

$$\Delta m_H^2 = -2\lambda_f^2 \int \frac{d^4k}{(2\pi)^4} \left[\frac{1}{k^2 - m_f^2} + \frac{2m_f^2}{(k^2 - m_f^2)^2} \right]. \tag{1.21}$$

This contribution is multiplied by 3 for quarks, due to summation over colour indices. Both contributions of the integral diverge at high momentum. If a cutoff Λ is introduced to regulate the integrals, the correction becomes:

$$\Delta m_h^2 = \frac{\lambda_f^2}{16\pi^2} \left[-2\Lambda^2 + 6m_f^2 \log \frac{\Lambda}{m_f} \right]. \tag{1.22}$$

The first contribution diverges quadratically. If the cutoff scale corresponds to the Planck energy scale, a fine tuning of 30 orders of magnitude would be required to bring m_h below the TeV scale. In addition, this contribution is independent from m_h and cannot be ruled out when $m_h \to 0$ as in the fermion case. There is nothing in the Standard Model that protects the Higgs mass in the same way the chiral symmetry protects fermion masses and the gauge invariance protects vector bosons.

This huge energy gap between the electroweak energy scale and the Planck scale is considered unnatural and the dependence of the electroweak scale on the Planck scale constitutes an inconsistency of the Standard Model. This problem of the Standard Model is called *hierarchy problem* and requires an extension of the theory to be overcome.

1.2 Supersymmetry

Supersymmetry (SUSY) [3] offers an elegant solution to the hierarchy problem because it introduces new physics between the Planck scale and the electroweak scale and predicts new particles which protect the Higgs mass from large radiative corrections.

The solution to cancel the quadratic divergencies on the Higgs mass is here explained to provide a motivation for the introduction of this new theoretical framework. The theoretical structure of the theory is then outlined and mechanisms for Supersymmetry breaking are introduced.

1.2.1 Radiative Corrections to the Higgs Mass

A solution which removes the quadratic divergencies in the Higgs mass is the introduction of new scalar fields called sfermions, $\tilde{f}_{L,R}$, which couple to the Higgs fields through:

$$\mathcal{L}_{Hf} = \frac{1}{2}\tilde{\lambda_f}H^2(|\tilde{f}_L|^2 + |\tilde{f}_R|^2) + v\tilde{\lambda_f}H(|\tilde{f}_L|^2 + |\tilde{f}_R|^2) + (\frac{\lambda_f}{\sqrt{2}}A_f H\tilde{f}_L\tilde{f}_R^* + h.c.), \qquad (1.23)$$

v being the vacuum expectation value of the Higgs field. The second term is related to $SU(2)_L \otimes U(1)_Y$ symmetry breaking and A_f is an arbitrary parameter. The radiative correction to m_h^2 is:

$$\begin{aligned}\Delta m_H^2 = &-\tilde{\lambda_f}\int \frac{d^4k}{(2\pi)^4}\left[\frac{1}{k^2 - m^2_{\tilde{f}_L^2}} + \frac{1}{k^2 - m^2_{\tilde{f}_R^2}}\right] \\ &+(\tilde{\lambda_f}v)^2\int \frac{d^4k}{(2\pi)^4}\left[\frac{1}{(k^2 - m^2_{\tilde{f}_L^2})^2} + \frac{1}{(k^2 - m^2_{\tilde{f}_R^2})^2}\right. \\ &\left.+|\tilde{\lambda}_f A_f|^2\int \frac{d^4k}{(2\pi)^4}\frac{1}{(k^2 - m^2_{\tilde{f}_L^2})(k^2 - m^2_{\tilde{f}_R^2})}\right.\end{aligned} \qquad (1.24)$$

The first contribution, (left hand side of Fig. 1.6) is quadratically divergent and cancels out with the first one in Eq. 1.21 if, for each fermion, two sfermion scalar fields, $\tilde{f}_L$ and $\tilde{f}_R$ with $\tilde{\lambda}_f = -\lambda_f^2$, are introduced.

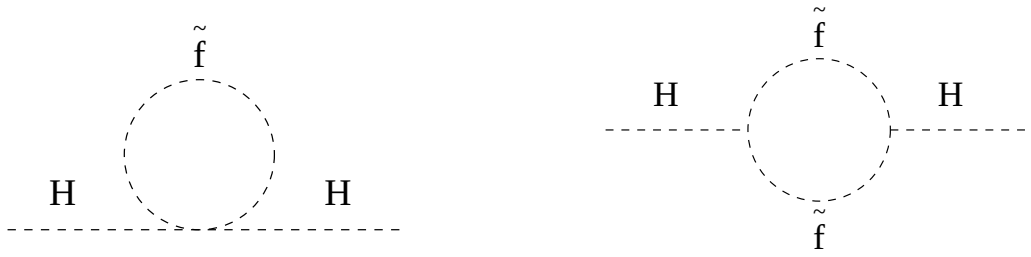

Figure 1.6: Sfermion contributions to the Higgs self-energy. $\tilde{f}$ stands either for $\tilde{f}_R$ or $\tilde{f}_L$.

The right hand side of Fig. 1.6 is associated to the second and third terms. Under this condition, and assuming $m_{\tilde{f}_L} = m_{\tilde{f}_R} = m_{\tilde{f}}$, the overall contribution to Δm_h^2 due to the remaining terms is:

$$\begin{aligned}\Delta m_H^2 = i\frac{\lambda_f^2}{16\pi^2}\left[-2m_f^2\left(1 - \log\frac{m_f^2}{\Lambda^2}\right) + 4m_f^2\log\frac{m_f^2}{\Lambda^2} + \right. \\ \left. 2m_{\tilde{f}}^2\left(1 - \log\frac{m_{\tilde{f}}^2}{\Lambda^2}\right) - 4m_f^2\log\frac{m_{\tilde{f}}^2}{\Lambda^2} - |A_f|^2\log\frac{m_{\tilde{f}}^2}{\Lambda^2}\right],\end{aligned} \qquad (1.25)$$

which cancels out if $m_{\tilde{f}} \sim m_f$ and $A_f \to 0$.

The introduction of the $\tilde{f}_L$ and $\tilde{f}_R$ fields not only allows the cancellation of quadratic divergencies, but also shields the weak scale from loop corrections involving heavy particles.

1.2.2 The Supersymmetry Algebra

The new scalar fields, which have been introduced to reduce the radiative corrections to the Higgs mass, are strongly correlated to the standard fermion fields. This correspondence can be interpreted as a new symmetry between fermion and bosons. This symmetry should also be broken at some energy scale because the supersymmetric particles, degenerate in mass with known particles, have never been discovered so far. From the mathematical point of view, the Coleman-Mandula theorem [13] states that this new symmetry is consistent with Quantum Field Theory. It was also demonstrated by Haag, Lopuzanski and Sohnius [14] that supersymmetry is the only possible additional symmetry of the S-matrix. Since it intercharges fermions with bosons, Supersymmetry is an extension of Poincaré space-time symmetry algebra rather than an internal symmetry. Its generators have to be spinors and their algebra is defined by anti-commutation rules:

$$\{Q^A_\alpha, \bar{Q}^B_{\dot{\beta}}\} = 2\delta^{A,B}\sigma^\mu_{\alpha,\dot{\beta}}P_\mu \tag{1.26}$$

$$\{Q^A_\alpha, Q^B_\beta\} = \{\bar{Q}^A_{\dot{\alpha}}, \bar{Q}^B_{\dot{\beta}}\} = 0 \tag{1.27}$$

$$[Q^A_\alpha, P_\mu] = 0. \tag{1.28}$$

being α, β ($\dot{\alpha}$, $\dot{\beta}$) the spinorial indices of the generators (their conjugate), A and B the internal indices of the supersymmetry algebra and N the number of generators. $N > 1$ are called extended supersymmetry algebras but will be ignored in this discussion because they cannot allow, in four-dimensional field theories, chiral fermions and parity violation as observed in the Standard Model. To describe the additional degrees of freedom due to supersymmetry Grassmann variables θ and $\bar{\theta}$, i.e. such that $\{\theta, \theta\} = \{\bar{\theta}, \bar{\theta}\} = \{\theta, \bar{\theta}\} = 0$, can be used. The physical objects undergoing supersymmetry transformations are called *superfields* $\Phi(x, \theta, \bar{\theta})$, which are complex scalar function of x, θ and $\bar{\theta}$. Superfields are the linear representations of the Supersymmetry algebra. In this notation, a Supersymmetry transformation can be written as $\exp[i(\theta Q + \bar{Q}\bar{\theta} - x_\mu P^\mu)]$.

Among all irreducible representations of the Supersymmetry algebra, only two of them are required to extend the Standard Model: the *chiral superfields*, which describe spin-0 and spin-$\frac{1}{2}$ particles and their superpartners, and *vector superfields*, which describe the gauge bosons and their superpartners.

Chiral Superfields

Chiral superfields are defined by the relations:

$$\bar{D}_\alpha \Phi_L = 0, \quad D_\alpha \Phi_R = 0. \tag{1.29}$$

Here $\bar{D}$ and D are the covariant derivatives, i.e. operators anticommuting with the supersymmetry generators. It can be demonstrated that:

$$\Phi(x, \theta) = \phi(x) + \sqrt{2}\theta^\alpha \bar{\psi}_\alpha(x) + \theta^\alpha \theta^\beta \epsilon_{\alpha\beta} F(x) \tag{1.30}$$

being ϕ and F complex scalar fields, $\bar{\psi}$ a spinorial field and $\epsilon_{\alpha\beta}$ an asymmetric tensor. F is also called *auxiliarity field*, transforms under Supersymmetry with a total derivative and it is not a physical degree of freedom of Φ since, according to the Lagrangian which will be shown below, it does not propagate.

Vector Superfields

Vector superfields are defined by the relationship:

$$V(x,\theta,\bar{\theta}) = V(x,\bar{\theta},\theta). \tag{1.31}$$

Using the Wess-Zumino gauge, V can also be expressed in a component form:

$$V(x,\theta,\bar{\theta}) = -\theta\sigma^{\mu}\bar{\theta}A_{\mu}(x) + i\theta\theta\bar{\theta}\bar{\lambda}(x) - i\bar{\theta}\bar{\theta}\theta\lambda(x) + \frac{1}{2}\theta\theta\bar{\theta}\bar{\theta}D(x). \tag{1.32}$$

A_{μ} is the ordinary gauge boson, λ is a chiral superfield (*gaugino*) associated to the boson and D is a scalar field which transforms, like F, with a total derivative.

The Supersymmetric Lagrangian

The most general Supersymmetry Lagrangian contains renormalisable terms and is invariant under Supersymmetry transformations. This Lagrangian contains a kinetic term providing the correct propagation of the field and a potential term providing masses and interactions. The kinetic term is: [1]

$$\int d^2\theta d^2\bar{\theta}\Phi_L\Phi_L^{\dagger} = FF^* - \phi\partial_{\mu}\partial^{\mu}\phi^* - i\bar{\psi}\sigma_{\mu}\partial^{\mu}\psi. \tag{1.33}$$

The potential term is (from now on L is omitted):

$$\int d^2\theta\ \mathcal{W}(\Phi_i), \quad \mathcal{W}(\Phi_i) = \sum_i k_i\Phi_i + \frac{1}{2}\sum_{i,j} m_{ij}\Phi_i\Phi_j + \frac{1}{3}\sum_{i,j,k} y_{ijk}\Phi_i\Phi_j\Phi_k. \tag{1.34}$$

where $\mathcal{W}$ is the so called *superpotential*, i runs on chiral superfields, k and m have respectively dimension of squared mass and mass and y is adimensional. The second term of the potential contains a mass term for fermions ($\psi_i\psi_j$) and the third one provides couplings. With some substitutions, the Lagrangian can be written:

$$\mathcal{L}_{chiral} = -\partial_{\mu}\phi_i^*\partial^{\mu}\phi - i\psi_i^{\dagger}\bar{\sigma}^{\mu}\partial_{\mu}\psi_i - \frac{1}{2}\left(\frac{\delta^2\mathcal{W}}{\delta\phi_i\delta\phi_j}\psi_i\psi_j + h.c.\right) + \left|\frac{\delta\mathcal{W}}{\delta\phi_i}\right|^2. \tag{1.35}$$

One of the consequences of these hypotheses is that the simple requirements of renormalisability and invariance under supersymmetry transformations fix all couplings between fields and their relative strength.

In analogy with the non supersymmetric field theory, interaction with gauge superfield may be accomplished by replacing $\Phi \rightarrow \exp(gV)\Phi$ and replacing the partial derivative with the covariant one. The kinetic term thus transforms into:

$$\int d^2\theta d^2\bar{\theta}\Phi^{\dagger}e^{2gV}\Phi = |D_{\mu}\phi|^2 - i\bar{\psi}\sigma_{\mu}D^{\mu}\psi + g\phi^*D\phi + ig\sqrt{2}(\phi^*\lambda\psi - \bar{\lambda}\bar{\psi}\phi) + |F|^2. \tag{1.36}$$

This term provides the interaction of fermions and scalars with gauge fields and the interactions gaugino-fermion-scalar. The kinetic term due to gauge fields is provided by:

$$-\frac{1}{4}F_a^{\mu\nu}F_{\mu\nu}^a + \frac{1}{2}D_aD^a + \left(\frac{i}{2}\lambda^a\sigma_{\mu}\partial^{\mu}\bar{\lambda}_a + \frac{1}{2}gf^{abc}\lambda_a\sigma_{\mu}A_b^{\mu}\bar{\lambda}_c + h.c.\right) \tag{1.37}$$

[1] integration over Grassman variables is defined by $\int d\theta_{\alpha} = 0$, $\int \theta_{\alpha}d\theta_{\alpha} = 1$

being f^{abc} the group structure functions and the term contains the gaugino kinetic term and the gaugino-gauge boson interaction. In analogy with F, D has no propagation and its equation of motion is:

$$D_a = -g \sum_{i,j} \phi_i^* T_{ij}^a \phi_j. \tag{1.38}$$

The terms involving D (the third one in 1.36 and the second one in 1.37) provide a contribution to the scalar interaction given by:

$$-\mathcal{V}_D = -\frac{1}{2} \sum_a \left| \sum_{ij} \phi_i^* T_{ij}^a \phi_j \right|^2. \tag{1.39}$$

1.2.3 Supersymmetry Breaking

The Supersymmetry breaking is motivated by the non observation of the supersymmetric partners of the known particles degenerate in mass with them. The Supersymmetry breaking is introduced externally and there are many hypotheses about this mechanisms.

The methods which have been proposed so far share some analogies with the internal symmetry breaking: a symmetry can be spontaneously broken if the vacuum state is not symmetric, i.e. if at least one symmetry generator Q does not annihilate the vacuum state $Q|0\rangle \neq 0$. In global Supersymmetry, the Hamiltonian can be expressed by:

$$\mathcal{H} = P^0 = \frac{1}{4}(\bar{Q}_1 Q_1 + Q_1 \bar{Q}_1 + \bar{Q}_2 Q_2 + Q_2 \bar{Q}_2), \tag{1.40}$$

and if supersymmetry is broken, the vacuum would have a positive energy $\langle 0|\mathcal{H}|0\rangle > 0$. This can be accomplished by non vanishing F terms (Fayet-Iliopoulos [15] mechanism) or D terms (O'Raifertaigh [16] mechanism) on the ground state.

In the latter case, Supersymmetry can be broken by some chiral superfields Φ_i with a superpotential such that $F_i = \partial \mathcal{W}^* / \partial \phi^* = 0$ have no simultaneous solution for each i and $\mathcal{V} = \sum_i |F_i|^2$ is positive at its minimum. The simplest example is:

$$\mathcal{W} = -k\Phi_1 + m\Phi_2\Phi_3 + \frac{y}{3}\Phi_1\Phi_3^2. \tag{1.41}$$

Φ_1 has to be a gauge singlet and $k \neq 0$ to break supersymmetry. If $m^2 > yk$ there is a minimum at $\phi_2 = \phi_3 = 0$ with $F_1 = k$ and $\mathcal{V} = k^2$. ϕ_1 is undetermined. In analogy with the Nambu-Goldstone mechanism, if $\mathcal{V}$ is expanded around $\phi_1 = 0$, some of the 6 scalar and 3 fermion fields are mixed and acquire mass. The fermion component of Φ_1, ψ_1 is the field associated to the broken Supersymmetry generator because it is the fermionic partner of the auxiliarity field F_1. It is thus massless and neutral and it is called *Goldstino*. A similar mechanism occurs in the gravity mediated (SUGRA) [17] and gauge mediated [18] (GMSB) supersymmetry breaking.

In both SUGRA and GMSB models, the supersymmetry breaking terms arise radiatively rather than from tree-level renormalisable couplings. Supersymmetry breaking occurs through a *hidden sector* which does not couple directly with the chiral supermultiplets. The two sectors share some interactions and the hidden one communicates with the visible one only through radiative corrections which provide the Supersymmetry breaking

terms. The interactions responsible of the Supersymmetry breaking is gravitation in the gravity-mediated case and the ordinary gauge interactions in the gauge mediated case.

From a practical point of view, the Supersymmetry breaking can be accomplished by adding *Soft Breaking terms* to the Lagrangian. Since supersymmetric particles were never observed, they are supposed to be heavier than the corresponding Standard Model ones. Therefore, the soft breaking terms are mass terms for gauginos and scalars and bilinear and three-linear term for scalars. The most general Lagrangian containing these terms is:

$$\mathcal{L}_{soft} = -m_{ij}^2 \phi_i^2 \phi_j^2 - \frac{1}{2} M_l \bar{\lambda}_a \lambda^a - \left(\frac{1}{2} b^{ij} \phi_i \phi_j + \frac{1}{6} a^{ijk} \phi_i \phi_j \phi_k + h.c. \right). \tag{1.42}$$

In particular b_{ij} and a_{ijk} are similar to the M_{ij} and y_{ijk} which appear in the superpotential. It was demonstrated that with such Lagrangian, the cancellation of quadratic divergencies holds at every perturbative order [19]. At this stage the m, M, a and b are free parameters. Additional constraints on these parameters are related to the experimental limits on the flavour changing neutral current process $\mu \to e\gamma$, and the observed $K^0 - \bar{K}^0$ mixing.

1.3 The MSSM Model

This section describes a possible supersymmetric extension of the Standard Model theory, the Minimal Supersymmetric Standard Model (MSSM): this model is minimal in the sense that it has the minimal content of particles which allow a viable theory from the phenomenological point of view.

For each Standard Model family, five chiral superfields are defined: Q which contains the $SU(2)_L$ doublet quarks and their scalar partners called *squarks*, U^c and D^c containing the $SU(2)_L$ singlets, L which contains the lepton doublets and their scalar partners, the *sleptons* and E^c with lepton singlets. Scalar fields associated with leptons and quarks $q_{L,R}$, $l_{L,R}$ are denoted with $\tilde{q}_{L,R}$ and $\tilde{l}_{L,R}$ (e.g. $\tilde{e}_{L,R}$, $\tilde{\mu}_{L,R}$, $\tilde{\tau}_{L,R}$, $\tilde{t}_{L,R}$, $\tilde{b}_{L,R}$, ...) and have the same name of Standard Model particles plus an s at the beginning (e.g. *selectron, smuon, stau, sneutrino, stop, sbottom, ...*). To describe the gauge sector, vector superfields are introduced; in particular, the $\tilde{B}$ (*bino*), $\tilde{W}$ (*wino*) and $\tilde{g}$ (*gluino*) are the fermion fields associated to gauge bosons. Two $SU(2)_L \otimes U(1)$ chiral superfield Higgs doublets H_u and H_d, with $Y = 1/2$ and $Y = -1/2$ respectively, are also introduced. Two Higgs doublets are required in the theory, since only one doublet would introduce triangle gauge anomalies. The superfield H_u couples with $u-$type quarks and provides them masses while H_d couples with $d-$type quarks and charged leptons. The particle content of the MSSM is reported in Tables 1.1 and 1.2 together with the $SU(3)_c \otimes SU(2)_L \otimes U(1)_Y$ symmetry quantum numbers.

The superpotential for MSSM is given by:

$$W_{MSSM} = y_u U^c Q H_u + y_d D^c Q H_d + y_e E^c L H_d + \mu H_u H_d, \tag{1.43}$$

where:

$$y_u U^c Q H_u = y_u^{\alpha\beta} \epsilon_{\gamma\delta} U_\alpha^c Q_\beta^\gamma H_u^\delta, \quad H_u H_d = \epsilon^{\alpha\beta} H_{u\alpha} H_d^\beta. \tag{1.44}$$

The first term in Eq.1.43 is the Yukawa coupling with $u-$like quarks, the second one with $d-$like quarks, the third one with leptons and the last one is a Higgs mass term. The

Table 1.1: Chiral supermultiplets in the MSSM.

Names		spin 0	spin 1/2	$SU(3)_c \otimes SU(2)_L \otimes U(1)_Y$
squarks, quarks	Q	$(\tilde{u}_L \quad \tilde{d}_L)$	$(u_L \quad d_L)$	$(3,\ 2,\ \frac{1}{6})$
($\times$3 families)	U^c	$\tilde{u}^*_R$	$u^\dagger_R$	$(\bar{3},\ 1,\ -\frac{2}{3})$
	D^c	$\tilde{d}^*_R$	$d^\dagger_R$	$(3,\ 1,\ \frac{1}{3})$
sleptons, leptons	L	$(\tilde{\nu} \quad \tilde{e}_L)$	$(\nu \quad e_L)$	$(1,\ 2,\ -\frac{1}{2})$
($\times$3 families)	E^c	$\tilde{e}^*_R$	$e^\dagger_R$	$(1,\ 1,\ 1)$
Higgs, higgsinos	H_u	$(H^+_u \quad H^0_u)$	$(\tilde{H}^+_u \quad \tilde{H}^0_u)$	$(1,\ 2,\ \frac{1}{2})$
	H_d	$(H^0_d \quad H^-_d)$	$(\tilde{H}^0_d \quad \tilde{H}^-_d)$	$(1,\ 2,\ -\frac{1}{2})$

Table 1.2: Gauge supermultiplets in the MSSM.

Names	spin 1/2	spin 1	$SU(3)_c \otimes SU(2)_L \otimes U(1)_Y$
gluino, gluon	$\tilde{g}$	g	$(8,\ 1,\ 0)$
wino, W	$\tilde{W}^\pm$, $\tilde{W}^0$	$W^\pm$, W^0	$(1,\ 3,\ 0)$
bino, B	$\tilde{B}^0$	B^0	$(1,\ 1,\ 0)$

Yukawa matrices $\mathbf{y_u}$, $\mathbf{y_d}$ and $\mathbf{y_e}$ provide masses and mixing to (s)quarks and (s)leptons and the interactions with the Higgs fields. $\mathbf{y_e}$ is diagonal because neutrinos are massless and the first two Yukawa matrices can be approximated to:

$$\mathbf{y_{u,d,e}} \sim y_{t,b,\tau} \begin{pmatrix} 0 & 0 & 0 \\ 0 & 0 & 0 \\ 0 & 0 & 1 \end{pmatrix} \tag{1.45}$$

because quarks and leptons of the third family (t, b, τ) are more massive than those of the first two. Extra terms violating lepton and baryon numbers and preserving renormalisability and gauge invariance can be introduced but are neglected due to the tight constraints from experimental observations.

Barion and lepton number conservation can be guaranteed by the *R-parity* conservation hypothesis: R-parity is a multiplicative quantum number which is 1 for Standard Model particles, and -1 for their supersymmetric partners. It is defined by:

$$R = (-1)^{3(B-L)+s} \tag{1.46}$$

being B and L barion and lepton number and s the spin. R-parity conservation has remarkable effects on phenomenology. In particular it implies that:

- in processes involving Standard Model particles in the initial states, supersymmetric particles must be produced in an even number
- each supersymmetric particle must decay into an odd number of supersymmetric particles and any number of Standard Model Particles

- the lightest supersymmetric particles (LSP) is not allowed to decay.

Since LSP is stable, some of them can have survived from the Big Bang Era. A neutral LSP is thus a good candidate for *hot dark matter*. Another consequence of R-Parity conservation is that supersymmetric particles should be produced at least in pair in collider experiments. Each SUSY particle would decay into lighter particles, producing cascades of Standard Model particles until the LSP is produced. The LSP would not interact within the detector and would lead to events with huge amount of missing energy.

According to all assumptions above, the most general soft supersymmetry breaking terms of the Lagrangian are:

$$\begin{aligned} -\mathcal{L}_{soft} = &\frac{1}{2}(M_1\tilde{B}\tilde{B} + M_2\tilde{W}\tilde{W} + M_3\tilde{g}\tilde{g} + h.c.) \\ &+(\tilde{u}^c a_u \tilde{Q} H_u + \tilde{d}^c a_d \tilde{Q} H_d + \tilde{E}^c a_e \tilde{L} H_d + h.c.) \\ &+\tilde{Q}^\dagger m_{\tilde{Q}} \tilde{Q} + \tilde{u}^\dagger m_{\tilde{u}} \tilde{u} + \tilde{d}^\dagger m_{\tilde{d}} \tilde{d} + \tilde{L}^\dagger m_{\tilde{L}} \tilde{L} + \tilde{e}^\dagger m_{\tilde{e}} \tilde{e} \\ &+m^2_{H_u} H_u^\dagger H_u + m^2_{H_d} H_d^\dagger H_d + (b H_u H_d + h.c.). \end{aligned} \tag{1.47}$$

These terms increase the SUSY particles masses with respect to those of the Standard Model. All these couplings are of the order of m_{soft} or m^2_{soft} according to their dimension. The overall number of free parameters is 105 at this stage: the reduction of it can be accomplished by experimental constraints and additional hypotheses which depend on the specific model of Supersymmetry breaking.

1.3.1 Electroweak Symmetry Breaking in MSSM

One of the requirements on the MSSM model is that it should be able to reproduce the observed electroweak symmetry breaking of the Standard Model.

This task is complicated by the presence of two Higgs doublets instead of one. However, in the MSSM case the Lagrangian terms which allow the symmetry breaking is provided by the potential and the soft breaking terms are not added by hand as in the Standard Model case. The requirement of the correct reproduction of the electroweak symmetry breaking introduces correlations between the parameters of the model.

The MSSM Higgs potential is:

$$\begin{aligned} \mathcal{V} = &(|\mu|^2 + m^2_{H_u})(|H_u^0|^2 + |H_u^+|^2) + (|\mu|^2 + m^2_{H_d})(|H_d^0|^2 + |H_d^-|^2) \\ &+[b(H_u^+ H_d^- - H_u^0 H_d^0) + h.c.] \\ &+\frac{1}{8}(g^2 + g'^2)(|H_u^0|^2 + |H_u^+|^2 - |H_d^0|^2 - |H_d^-|^2)^2 - \frac{1}{2}|H_u^+ H_d^{0*} + H_u^0 H_d^{-*}|^2. \end{aligned} \tag{1.48}$$

The first two lines are quadratic in H and correspond to the F-term contribution of the Lagrangian while the last term, which is quartic in H, corresponds to the D-term contribution. It also depends on gauge couplings. Without loss of generality, phases can be tuned in order to achieve $H_u^+ = 0$ and make b, H_u^0 and H_d^0 real. Under these assumptions, the scalar potential becomes:

$$\begin{aligned} \mathcal{V} = &(|\mu|^2 + m^2_{H_u})|H_u^0|^2 + (|\mu|^2 + m^2_{H_d})|H_d^0|^2 - (b H_u^0 H_d^0 + h.c.) \\ &+\frac{1}{8}(g^2 + g'^2)(|H_u^0|^2 - |H_d^0|^2)^2. \end{aligned} \tag{1.49}$$

In order to achieve a stable vacuum the potential should be bound from below and the origin should not be in a minimum, otherwise the symmetry breaking would not be possible. In the directions $|H_u^0| = |H_d^0|$ (the $D-$ flat direction) the quartic interaction vanishes and, in order to bind the potential from below, the following relationship should hold:

$$m_{H_u}^2 + m_{H_d}^2 + 2|\mu|^2 > 2b. \tag{1.50}$$

In this condition, the origin is required to be a saddle point in order to break the electroweak symmetry, and this implies that:

$$b^2 > (m_{H_u}^2 + |\mu|^2)(m_{H_u}^2 + |\mu|^2). \tag{1.51}$$

Conditions 1.50 and 1.51 also imply that $m_{H_u} \neq m_{H_d}$. The v and $\bar{v}$ variables are introduced and correspond to the VEVs of H_u and H_d. In order to reproduce the correct electroweak symmetry breaking an additional condition is required:

$$M_Z^2 = \frac{g^2 + g'^2}{2}(v^2 + \bar{v}^2) = (91.8 \text{ GeV})^2. \tag{1.52}$$

The $\tan\beta$ variable, defined as $\tan\beta = \bar{v}/v$ is also introduced and is a free parameter of the theory.

The minimisation of the potential with respect H_u and H_d, together with the conditions 1.50 and 1.51 provides the following relationships relating the μ and b parameters to $\tan\beta$, m_{H_u}, m_{H_d} and m_Z:

$$|\mu|^2 + m_{H_d}^2 = b\tan\beta - (m_Z^2)\cos 2\beta, \tag{1.53}$$

$$|\mu|^2 + m_{H_u}^2 = b\tan\beta + (m_Z^2)\cos 2\beta. \tag{1.54}$$

The eight degrees of freedom of the Higgs multiplets are rearranged after Supersymmetry breaking: three of them become the Nambu-Goldstone bosons (G^0 and $G^\pm$), corresponding to the longitudinal components of $W^\pm$ and Z^0 and the remaining five eigenstates are a CP-odd neutral scalar A^0, two charged scalar Higgs $H^\pm$ and two CP-even neutral scalars h^0 and H^0. The h^0 is equivalent to the Standard Model Higgs boson: the discovery of this particle only cannot allow the distinction between the two.

Masses and mixing matrices of the MSSM Higgs bosons at tree level are:

$$\begin{pmatrix} G^0 \\ A^0 \end{pmatrix} = \sqrt{2}\begin{pmatrix} \sin\beta & -\cos\beta \\ \cos\beta & \sin\beta \end{pmatrix}\begin{pmatrix} Im[H_u^0] \\ Im[H_d^0] \end{pmatrix}, \quad \begin{pmatrix} G^+ \\ H^+ \end{pmatrix} = \begin{pmatrix} \sin\beta & -\cos\beta \\ \cos\beta & \sin\beta \end{pmatrix}\begin{pmatrix} H_u^+ \\ H_d^{-*} \end{pmatrix}, \tag{1.55}$$

$$\begin{pmatrix} h^0 \\ H^0 \end{pmatrix} = \sqrt{2}\begin{pmatrix} \sin\alpha & -\cos\alpha \\ \cos\alpha & \sin\alpha \end{pmatrix}\begin{pmatrix} Re[H_u^0] - v \\ Re[H_d^0] - \bar{v} \end{pmatrix}, \tag{1.56}$$

$$m_{A_0}^2 = \frac{2b}{\sin 2\beta}, \quad m_{H^\pm}^2 = m_{A_0}^2 + m_W^2, \tag{1.57}$$

$$m_{H^0,h^0}^2 = \frac{1}{2}(m_{A_0}^2 + m_Z^2 \pm \sqrt{(m_{A_0}^2 + m_Z^2)^2 - 4m_Z^2 m_{A_0}^2\cos^2 2\beta}), \tag{1.58}$$

being

$$\tan 2\alpha = \frac{m_{A_0}^2 + m_Z^2}{m_{A_0}^2 - m_Z^2}. \tag{1.59}$$

Masses of A_0, $H^\pm$ and H^0 have no upper bound, whereas the mass of h_0 has an upper bound coming from Eq.1.58:

$$m_{h^0} < min(m_a, m_Z) \cdot |\cos 2\beta|. \tag{1.60}$$

Including the 1-loop radiative correction the latter equation becomes:

$$m_h^2 < M_Z^2 \cos^2(2\beta) + \frac{3m_t^4}{32\pi^2 \sin^2 \beta M_W^2} \log \frac{m_{\tilde{t}_1} m_{\tilde{t}_2}}{m_t^2} \sim (130 \text{ GeV}/c^2)^2. \tag{1.61}$$

This result is valid as long as $m_{\tilde{t}_{1,2}}$ does not exceed significantly the TeV scale and $m_t < 185$ GeV. This constraint is compatible with the current constraints on the Standard Model Higgs boson already discussed.

1.3.2 Sparticle Mixing

The mixing of supersymmetric particles is a consequence of Electroweak Symmetry breaking: mixing occurs between particles with different $SU(2)_L \times U(1)_Y$ quantum numbers and the same $SU(3)_c \times U(1)_{em}$ quantum numbers. Mixing is very important from the phenomenological point of view since a large mixing can provide a relatively light mass to the lightest eigenstate.

Gaugino and Higgsino Mixing

Mixing can occur between electroweak gauginos and higgsinos: after Higgs field gets a VEV, the Higgs-higgsino-gaugino coupling provides an off-diagonal element of the gaugino-higgsino mass matrix. The eigenvalues of the mass matrix are called *chargino* ($\tilde{\chi}_i^\pm$) and *neutralino* ($\tilde{\chi}_i^0$) for charged and neutral gauginos-higgsinos mixtures respectively. The mass matrix for the charged gaugino-higgsino system in the basis ($\tilde{W}^\pm$, $\tilde{H}^\pm$) is:

$$M_{\tilde{\chi}^\pm} = \begin{pmatrix} M_2 & \sqrt{2} M_W s_\beta \\ \sqrt{2} M_W c_\beta & \mu \end{pmatrix} \tag{1.62}$$

The neutralinos are mixtures of $\tilde{B}$, $\tilde{W}^0$ and of the two neutral higgsinos. In this basis, the mixing matrix becomes the following:

$$M_{\tilde{\chi}^0} = \begin{pmatrix} M_1 & 0 & -M_Z c_\beta s_W & M_Z s_\beta s_W \\ 0 & M_2 & M_Z c_\beta c_W & -M_Z s_\beta c_W \\ -M_Z c_\beta s_W & M_Z c_\beta c_W & 0 & -\mu \\ M_Z s_\beta s_W & -M_Z s_\beta c_W & -\mu & 0 \end{pmatrix} \tag{1.63}$$

In both matrices, the elements depend on the mass parameters M_1, M_2, μ and on $\tan\beta$. If one assumes, as it will be discussed in the next section, that the gaugino masses unify at

GUT scale and extrapolates them through the RGE to the electroweak scale, the following relationship holds:

$$M_1(M_Z) = \frac{5}{3}\tan^2\theta_W M_2(M_Z) \sim \frac{1}{2}M_2(M_Z). \tag{1.64}$$

If $|\mu| > |M_2| > M_Z$, the two lightest neutralino and the lightest chargino are mostly gaugino-like, being the lightest, $\tilde{\chi}_1^0$ dominated by $\tilde{B}$, $\tilde{\chi}_2^0$, the next to lightest neutralino dominated by $\tilde{W}^0$ and the lightest chargino $\tilde{\chi}_1^\pm$ dominated by $\tilde{W}^\pm$. On the other hand, the heaviest chargino $\tilde{\chi}_2^\pm$ is mostly $\tilde{H}^\pm$ and the two heaviest neutralinos are higgsino-like. Under these hypotheses, the following relationship is also valid:

$$m_{\tilde{\chi}_1^\pm} \sim m_{\tilde{\chi}_2^0} \sim 2m_{\tilde{\chi}_1^0}. \tag{1.65}$$

Stop, Sbottom and Stau Mixing

Sfermion mixing is remarkable in the third family, i.e. for $\tilde{t}$, $\tilde{b}$ and $\tilde{\tau}$. In the case of scalar top quark, the $F-$term contributions from $|\partial\mathcal{W}/\partial f_{L,R}|^2$ (the last term in Eq. 1.35) give diagonal mass terms proportional to m_f^2, while the contribution from $|\partial\mathcal{W}/\partial H_d|^2$ leads to off-diagonal terms proportional to $y_t v\mu \sim m_t\mu cot\beta$. $D-$terms from Eq. 1.39 also rise diagonal contributions which are different from $\tilde{t}_L$ and $\tilde{t}_R$ because they behave differently under $SU(2)_L\otimes U(1)_Y$ gauge symmetry. Finally, the soft-breaking terms of Eq. 1.47 provide the diagonal contributions equal to $m_{\tilde{t}_{L,R}}$ and the off-diagonal contribution $-A_t m_t$. In the basis ($m_{\tilde{t}_L}$,$m_{\tilde{t}_R}$) the mixing matrix is [20]:

$$M_{\tilde{t}}^2 = \begin{pmatrix} m_t^2 + m_{\tilde{t}_L}^2 + (\frac{1}{2} - \frac{2}{3}s_W^2)c_{2\beta}M_Z^2 & -m_t(A_t + \mu\cot\beta) \\ -m_t(A_t + \mu\cot\beta) & m_t^2 + m_{\tilde{t}_R}^2 + \frac{2}{3}s_W^2 c_{2\beta}M_Z^2 \end{pmatrix}. \tag{1.66}$$

The $\tilde{u}$ and $\tilde{c}$ mixing matrix is similar to the $\tilde{t}$ one but the mixing is less remarkable since $m_{u,c} << m_t$. In the $\tilde{t}$ mixing matrix the mixing is huge because the off-diagonal terms are proportional to m_t and $m_{\tilde{t}}$ is expected to be of the order of magnitude of m_t. The calculation of the $\tilde{b}$ is very similar to that of the $\tilde{t}$ one and the matrix is:

$$M_{\tilde{b}}^2 = \begin{pmatrix} m_b^2 + m_{\tilde{b}_L}^2 - (\frac{1}{2} - \frac{2}{3}s_W^2)c_{2\beta}M_Z^2 & -m_b(A_b + \mu\tan\beta) \\ -m_b(A_b + \mu\tan\beta) & m_b^2 + m_{\tilde{b}_R}^2 - \frac{1}{3}s_W^2 c_{2\beta}M_Z^2 \end{pmatrix}. \tag{1.67}$$

For the same reason the $\tilde{b}$ mixing is smaller than the $\tilde{t}$ one. It can be increased at large $\tan\beta$. The same considerations are valid for $\tilde{\tau}$ mixing. Mixing for the other leptons is more complicated and model-dependent due to experimental constraints on FCNC.

1.4 Minimal Supergravity Models

In this model, the interaction which provides the Supersymmetry breaking is gravitation. The Supergravity Lagrangian terms arising from the interaction with the hidden sector,

which also contain the MSSM multiplets, are of the type:

$$\begin{aligned}\mathcal{L}_{NR} = -\left(\frac{1}{M_P}\sum_a \frac{1}{2} f_a \lambda_a \lambda^a + c.c.\right) - \frac{1}{M_P^2} F_X F_X^* k_j^i \phi_i \phi^{*j} \\ -\frac{1}{M_P} F_X \left(\frac{1}{6} y'^{ijk} \phi_i \phi_j \phi_k + \frac{1}{2} \mu'^{ij} \phi_i \phi_j\right) + c.c.\end{aligned} \tag{1.68}$$

being F_X the auxiliarity fields of the multiplets of the hidden sector and f_a, k_j^i, y'^{ijk} and μ'^{ij} dimensionless parameters depending on the theory. This Lagrangian is very similar to the soft breaking lagrangian already shown. If the VEVs $\langle F_X \rangle$ are of the order of 10^{10-11} GeV, soft terms of the order of 100 GeV can be obtained.

An important assumption, which allows to reduce the parameters of the model, is that gravitation is *flavour blind*; in this case, there would be a common $f_a = f$ for all gauginos, $k_j^i = k\delta_j^i$ for all scalars, $y'^{ijk} = \alpha y^{ijk}$ and $\mu'^{ij} = \beta \mu^{ij}$ being y^{ijk} and μ^{ij} the superpotential parameters already introduced.

Under this hypothesis, the soft breaking terms depend only on four parameters:

$$M_1 = M_2 = M_3 = m_{1/2}, \tag{1.69}$$

$$\mathbf{m_{\tilde{Q}}}^2 = \mathbf{m_{\tilde{L}}}^2 = \mathbf{m_{\tilde{u}}}^2 = \mathbf{m_{\tilde{d}}}^2 = \mathbf{m_{\tilde{e}}}^2 = m_0 \mathbf{1}, \tag{1.70}$$

$$m_{H_u}^2 = m_{H_d}^2 = m_0^2, \tag{1.71}$$

$$\mathbf{a_u} = A_0 \mathbf{y_u}, \quad \mathbf{a_d} = A_0 \mathbf{y_d}, \quad \mathbf{a_e} = A_0 \mathbf{y_e}, \tag{1.72}$$

$$b = B_0 \mu \tag{1.73}$$

where:

$$m_{1/2} = f\frac{\langle F \rangle}{M_P}, \quad m_0^2 = k\frac{|\langle F \rangle|^2}{M_P^2}, \quad A_0 = \alpha\frac{\langle F \rangle}{M_P}, \quad B_0 = \beta\frac{\langle F \rangle}{M_P}. \tag{1.74}$$

These constraints are compatible and more restrictive than those from the $\mu \to e\gamma$ process and $K^0 - \bar{K}^0$ mixing.

The conditions above hold at a given input energy scale ($\sim M_P$). The Renormalisation Group Equation (RGE), applied to the soft parameters and extrapolated down to the electroweak scale, predict the entire MSSM mass spectrum in terms of only five parameters:

$$m_0,\ m_{1/2},\ A_0,\ B_0,\ \mu. \tag{1.75}$$

However, corrections are very small except for the third family of sleptons and squarks (stop, sbottom and stau) due to the large Yukawa couplings. The electroweak symmetry breaking, which is hidden at high scales, is induced by the large top Yukawa coupling, which drives the Higgs fields masses to a negative value[22][23].

The requirement of the correct electroweak symmetry breaking allows to reduce the number of free parameters: the minimisation of the Higgs potential provides equations 1.53 and 1.54, which, together with Eq. 1.74, allow to express μ and B_0 as a function of $\tan\beta$, m_Z and m_0. The sign of μ is not provided by the theory and it is thus a free parameter. Therefore, in these hypotheses the free parameters of the theory become:

$$m_0,\ m_{1/2},\ A_0,\ \tan\beta,\ \text{sign of } \mu. \tag{1.76}$$

1.4.1 Unification of Gauge Couplings

A striking feature of Supersymmetry is that it provides the right particle content to achieve the couplings unification at a scale lower than the Planck scale. This scale is obtained extrapolating to high energy scale the gauge coupling values at the electroweak scale through the RGE equations:

$$\frac{d}{d\log(Q/Q_0)}g_a = \frac{1}{16\pi^2}b_a g_a^3, \tag{1.77}$$

$g_1 = g(U(1)_Y)$, $g_2 = g(SU(2)_L)$, $g_3 = g(SU(3)_C)$ being the gauge couplings of the Standard Model ($\alpha_a = g_a^2/4\pi$) associated with the $U(1)_Y$, $SU(2)_L$ and $SU(3)_C$ gauge symmetries respectively and $b_a = (33/5, 1, -3)$ constants provided by the theory. The 2-loop evolutions of the gauge couplings converge to a common value at a mass scale of $M_U = 2 \times 10^{16}$ GeV. In Fig. 1.7 the running couplings for MSSM are compared with those of the Standard Model.

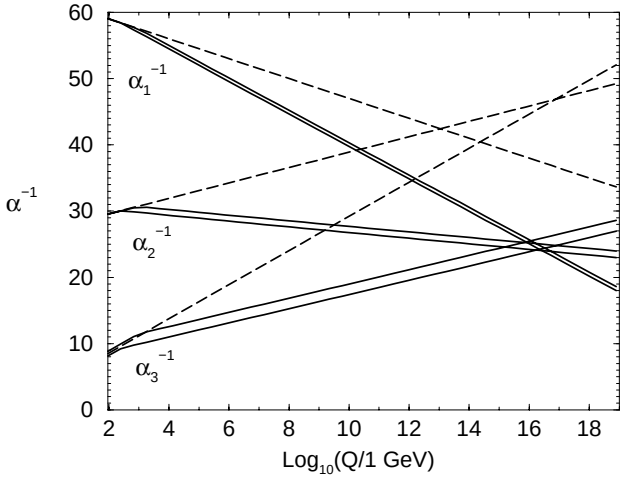

Figure 1.7: RG evolution of the inverse gauge coupling $\alpha_a^{-1}(A)$ in the Standard Model (dashed lines) and in the MSSM (solid lines). In the MSSM case, $\alpha_3(m_Z)$ is varied between 0.113 and 0.123 and the sparticle masses between 250 GeV and 1 TeV. Two loop effects are included as well.

In the SUSY case, a good convergence is achieved while in the Standard Model case no convergence is observed. This is another result which suggests a supersymmetric extension of the Standard Model.

1.5 Experimental Constraints on Supersymmetry

The constraints on the SUSY parameters are provided by a large number of direct searches and precision measurements. In this section the most relevant results are examined: lower bounds on SUSY particles masses coming from direct searches and constraints on SUSY parameters coming from precision measurements are described.

The discussion is concentrated on the Constrained version of MSSM model, the CMSSM or mSUGRA model as the rest of this work. Contours are displayed in the m_0-$m_{1/2}$ plane for different $\tan\beta$ and A_0 values and different signs on μ.

The main results are summarised in the plots of Fig. 1.8 [5]: different colours or shadings correspond to independent experimental constraints. Explanations are provided in the following subsections.

The future SUSY searches at LHC are discussed in the third chapter, which will also introduce the $\tilde{t}$ search. This section provides only the current limit on $\tilde{t}$ mass and the last chapter shows how the Large Hadron Collider can improve the current limits on it.

1.5.1 Constraints from Direct Searches

The clearest evidence of Supersymmetry would come from the discovery of the particles foreseen by the theory: for this reason, in the most recent experiments, a great effort has been dedicated to the direct SUSY particles searches. Both e^+e^- and hadron machines can be used for this purpose.

At e^+e^- machines, SUSY particles can be produced in electroweak processes with a SUSY particle and its anti-particle in the final state. Searches are thus limited to weakly interacting SUSY particles. Lepton colliders are optimal for these searches: the knowledge of the centre-of-mass energy and the clean environment allow to explore a very large range of kinematical conditions.

At hadron Colliders, the production of strongly interacting supersymmetric particles like squarks and gluino is enhanced, since QCD processes have larger cross sections and the sensitivity to these SUSY signals would therefore be higher. In particular, the highest sensitivity to Supersymmetry, is provided by the inclusive squarks and gluino searches, i.e. based on general features of the events: large E_T^{miss}, high E_T jets, leptons, b-jets and τ leptons from squarks and gluino cascade decays $\tilde{q} \rightarrow q\tilde{\chi}$ $\tilde{g} \rightarrow \tilde{q}q$. The efficiency on the signal is high in these searches since the identification of the specific processes is not required.

Hadron and e^+e^- machines are thus complementary in SUSY particle searches. The tightest constraints come from the experiments at LEP[4] and Tevatron[24]. The main results on the direct searches are summarised below for the main SUSY particles.

Chargino

Chargino search was performed at LEP: the production mechanism taken into account is pair production followed by the decay $\tilde{\chi}^{\pm} \rightarrow W^{\pm}\tilde{\chi}_1^0$ (being $W^{\pm}$ either real or virtual) assuming this process to have 100% branching ratio. A scan of all accessible chargino masses was performed as a function of neutralino masses. The best sensitivity was achieved with the combined results of the four LEP experiments[4]: for $m_{\tilde{\chi}^{\pm}} \sim 2m_{\tilde{\chi}_1^0}$, the upper limit for the production cross section at $\sqrt{s} > 207.5$ GeV is around 0.5 pb (at 90% C.L.). For some specific values of the parameters, this limit can be interpreted as a limit on the chargino mass: for $\tan\beta = 2$, $\mu = -200$ GeV and sneutrino mass above 300 GeV, $m_{\tilde{\chi}^{\pm}} > 103.5$ GeV.

Sleptons

Slepton searches were performed at LEP as well for $\sqrt{s}$ from 183 to 208 GeV. Sleptons would have been produced in pair and decay through the processes $\tilde{l} \rightarrow l\tilde{\chi}_1^0$. Slepton events would thus be made of two acoplanar opposite-sign leptons and a large missing momentum.

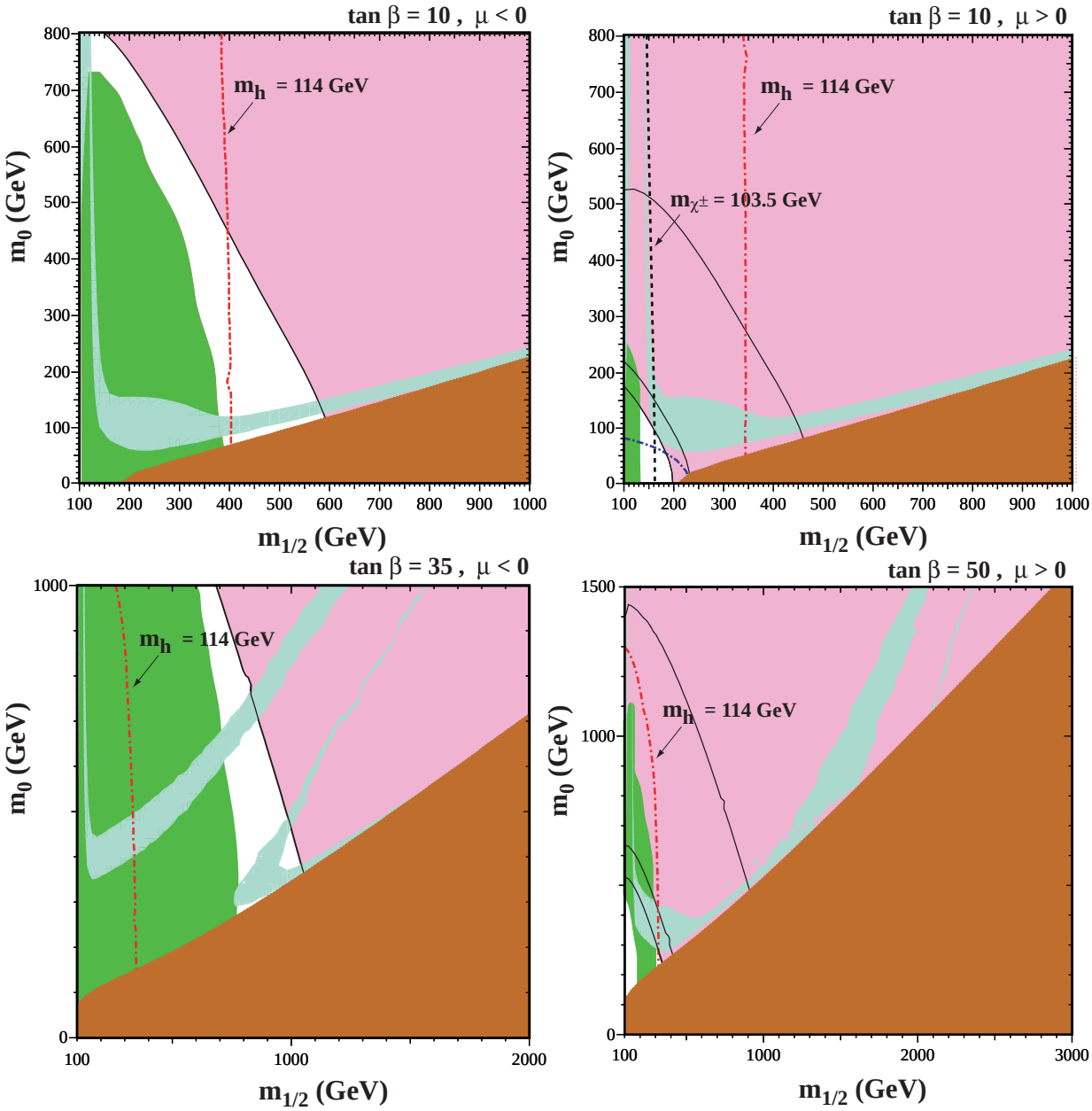

Figure 1.8: Contours associated with the theoretically excluded regions (dark shading or brick red), the regions excluded by the $b \to s\gamma$ constraint (intermediate shading or green), the regions compatible with the muon $g-2$ constraint (light shading or pink) and the regions compatible with neutralino dark matter hypothesis (very light shading or turquoise) in the $m_0 - m_{1/2}$ plane for $\tan\beta = 10$ and 35 and $\mu > 0$ and $\mu < 0$. The lines corresponding to $m_h = 114$ GeV and $m_{\chi^\pm} = 103.5$ GeV are also displayed[5].

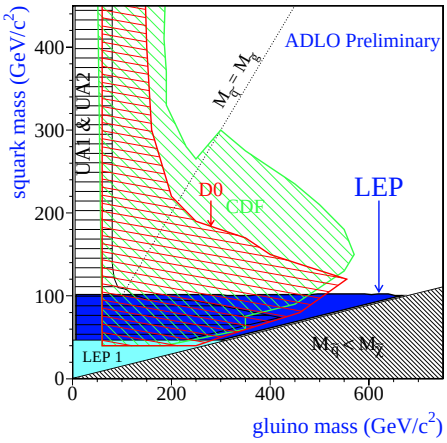

Figure 1.9: Gluino exclusion contours for three different signatures at CDF[25][27] and D0[26].

The best sensitivity was achieved by the combined results of the four LEP experiments [4]. For $\tan\beta = 1.5$, $\mu = -200$ GeV and a neutralino mass around 40 GeV the lower limit on right handed slepton masses are 99.4 GeV, 96.4 GeV and 87.1 GeV for $\tilde{e}$, $\tilde{\mu}$ and $\tilde{\tau}$ respectively.

Gluino

Gluino searches were performed at the Tevatron: this searches were based on hadron jets, leptons and E_T^{miss}. A multijet-multilepton search was performed by the CDF[25] and D0[26] Collaborations and the exclusion contours are shown in Fig. 1.9 in the $m_{\tilde{q}} - m_{\tilde{g}}$ plane. A lower bound independent on the $m_{\tilde{q}}$ mass was set at $m_{\tilde{g}} > 195$ GeV while the bound $m_{\tilde{g}} > 300$ GeV was set for $m_{\tilde{q}} = m_{\tilde{g}}$.

An inclusive search based on same flavour and same sign lepton pairs in multijet and large E_T^{miss} events was performed by the CDF Collaboration [27]: at $\tan\beta = 2$ and $\mu = -800$ GeV limits $m_{\tilde{g}} > 221$ GeV at $m_{\tilde{q}} = m_{\tilde{g}}$ and $m_{\tilde{g}} > 168$ GeV for $m_{\tilde{q}} \gg m_{\tilde{g}}$ were set.

Sbottom

Sbottom searches were focused on sbottom pair production and sbottom decay through $\tilde{b} \to b\tilde{\chi}_1^0$ occurring at large mixing scenarios [28], where the $\tilde{b}$ would be the lightest squark. In these analyses, two b-tagged hadron jets and missing momentum were required. Sbottom search was performed at LEP and Tevatron experiments and the exclusion contours are shown in the left side of Fig. 1.10 in the plane $m_{\tilde{b}} - m_{\tilde{\chi}_1^0}$ for the combined results of the four LEP experiments[4] and the Tevatron experiments[29][30].

The lower bound on $m_{\tilde{b}}$ is $m_{\tilde{b}} < 100$ GeV at $m_{\tilde{\chi}_1^0} > 75$ GeV and $m_{\tilde{b}} < 140$ GeV at $m_{\tilde{\chi}_1^0} < 75$ GeV.

Experiments at e^+e^- colliders are more sensitive to small mass differences $m_{\tilde{f}} - m_{\tilde{\chi}_1^0}$ ($\tilde{f} = \tilde{l}, \tilde{q}$) because the kinematics is closed and the total missing energy measurement (E^{miss}) is possible. In this case, the exclusion contours are closer to the line $m_{\tilde{f}} = m_f + m_{\tilde{\chi}_1^0}$.

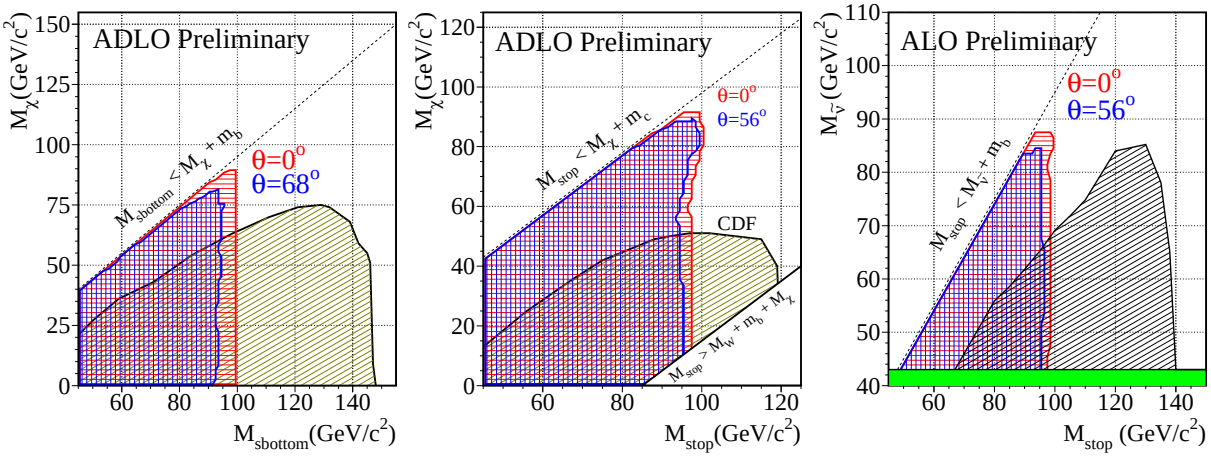

Figure 1.10: Left: sbottom exclusion contours in the $m_{\tilde{b}} - m_{\tilde{\chi}_1^0}$ plane for $\tilde{b} \to \tilde{\chi}_1^0 b$ achieved with the combined LEP results[4] and by the Tevatron experiments[29][30]. Center: stop exclusion contours in the $m_{\tilde{t}} - m_{\tilde{\chi}_1^0}$ plane for $\tilde{t} \to \tilde{\chi}_1^0 c$ achieved with the combined LEP results[4] and by CDF[29]. Right: stop exclusion contours in the $m_{\tilde{t}} - m_{\tilde{\nu}}$ plane for $\tilde{t} \to \tilde{\nu} bl$ achieved with the combined LEP results[4] and by the Tevatron experiments[31][33].

On the other hand, hadron collider experiments can explore higher mass ranges.

The $\tilde{b}$ search will be repeated at Run II and it will be possible to explore a mass range up to 250 GeV with 20 fb^{-1}[32].

Stop

Three different $\tilde{t}$ searches were performed so far: $\tilde{t} \to \tilde{\chi}_1^0 c$, $\tilde{t} \to \tilde{\nu} bl$ and $\tilde{t} \to \tilde{\chi}_1^{\pm} b$. In all cases the $\tilde{t}$ pair production process was considered. Searches were limited to a $\tilde{t}$ lighter than the t due to the limited center of mass energy.

The $\tilde{t} \to \tilde{\chi}_1^0 c$ was performed at both LEP and Tevatron experiments: two $c-$jets and a large E^{miss} or E_T^{miss} were required in these events and the exclusion contours achieved from the combined LEP results[4] and CDF[29] are shown in the central plot of Fig. 1.10. The lower limit on the $\tilde{t}$ mass are $m_{\tilde{t}} < 100$ GeV at $m_{\tilde{\chi}_1^0} > 50$ and $m_{\tilde{t}} < 120$ GeV at $m_{\tilde{\chi}_1^0} < 50$ GeV. The bound on $m_{\tilde{t}}$ at 100 GeV will be extended at $\sim 200 - 225$ GeV with Run II at Tevatron[32].

The $\tilde{t} \to \tilde{\nu} bl$ search was also performed at LEP and Tevatron: in this case, the search was based on the requirements of $b-$jets, leptons and E^{miss} or E_T^{miss}. The exclusion contour is shown in the right side of Fig. 1.10 for the combined LEP results[4] and the Tevatron experiments [31][33]. A lower bound at $m_{\tilde{t}} < 140$ GeV was set and it will be extended to $\sim 200 - 250$ GeV with Run II at Tevatron with 20 fb^{-1}[32].

The $\tilde{t} \to \tilde{\chi}_1^{\pm} b$ search was performed by the CDF [31] and D0[34] Collaborations. The sensitivity on this process was not sufficient to reach the predictions expected from the NLO calculations. It will be possible to exploit this decay mode at Run II and explore mass values up to ~ 200 GeV with 20 fb^{-1}.

Lightest Neutralino

The lower bound on the lightest neutralino mass is calculated from the combination of the ALEPH results on the search for the lightest chargino and the LEP combined results of slepton searches and Higgs boson searches in the hZ channel[4].

The calculation is performed in the framework of the constrained MSSM Model with the lowest order Gaugino and Sfermion mass Unification at GUT scale according to the method described in [35]. Fig. 1.11 shows the lowest limit on $\tilde{\chi}_1^0$ mass obtained from these studies as a function of $\tan\beta$.

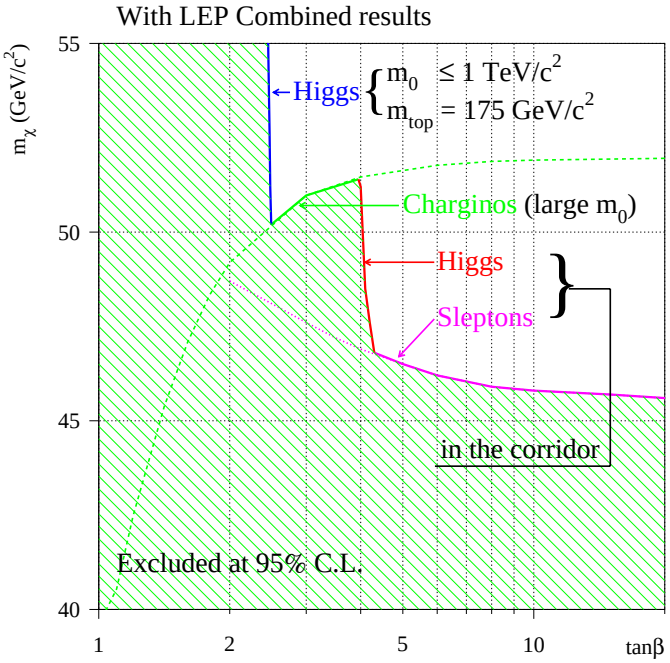

Figure 1.11: Lower limit on the mass of the lightest Neutralino as a function of $\tan\beta$ in the constrained MSSM Model from the combination of the LEP results[4]

For $\tan\beta < 4$, the lower limit is set at large m_0 by the Higgs boson search for $\tan\beta < 2.5$ and chargino search for $2.5 < \tan\beta < 4$, while for $\tan\beta > 4$, the limit is set at small m_0 by the Higgs boson search for $\tan\beta < 4.2$ and slepton searches for $\tan\beta > 4.2$. Under these hypotheses, the lower limit on the LSP mass is found at about 45 GeV/c^2 at large $\tan\beta$.

Among all particle searches discussed here, the tightest limits on the mSUGRA parameters come from selectron and chargino searches: in the upper right plot of Fig. 1.8, the exclusion contours at 95% C.L. are displayed with a dashed-dotted line very close to the origin for selectron and a dashed line for chargino. The latter line is approximately parallel to the m_0 axis since chargino mass is independent from m_0 (apart radiative correction contributions). These contours are nearly independent on $\tan\beta$ and the sign of μ and are thus neglected in the other plots.

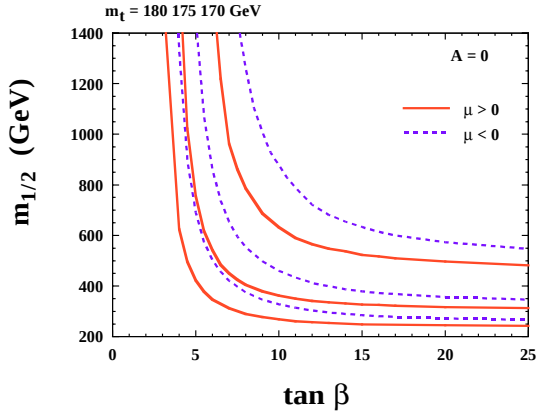

Figure 1.12: Lower limit on $m_{1/2}$ required to achieve $m_h > 113$ GeV for both signs of μ, $m_t = 170, 175, 180$ at different $\tan\beta$ [37].

1.5.2 Constraints from the Higgs Boson Search

The tightest constraint on SUSY parameters come from the Higgs boson direct search: m_h is sensitive to SUSY particles masses, in particular the *stop* through loop corrections involving SUSY particles with a dependence of the type:

$$\delta m_h^2 \propto \frac{m_t^4}{m_W^2} \log\left(\frac{m_{\tilde{t}}^2}{m_t^2}\right) + ... \tag{1.78}$$

The implications of the LEP limit were carefully investigated through the calculation of the higher order contributions of the SUSY particles to the Higgs mass [36].

The Higgs boson mass is approximately independent on m_0 while it is very sensitive to the $m_{1/2}$ parameter [37]. The line corresponding to $m_h = 114.1$ GeV is displayed in red in the plots of Fig. 1.8: $m_{1/2}$ values lower than 350 GeV are ruled out by the Higgs mass constraint at $\tan\beta = 10$. This prediction is strongly dependent on the top mass which enters in the loop correction.

The lowest $m_{1/2}$ allowed at $m_h > 113$ GeV is shown in Fig. 1.12 as a function of $\tan\beta$ for both signs of the μ parameter and $m_t = 170$, 175 and 180 GeV. The lowest bound on $m_{1/2}$ decreases with $\tan\beta$ and it is approximately constant for $\tan\beta > 10$. The dependence on μ is more remarkable at low $\tan\beta$ and does not hold at large $\tan\beta$.

This constraint has important effects for SUSY searches in the future experiments: a lower bound on $m_{1/2}$ corresponds to a lower bound on the masses of SUSY particles. Assuming as a constraint $m_{1/2} > 350$ GeV, the squarks and gluino would have masses above 600-700 GeV which would be far above the Tevatron domain[24] and the stop would be accessible only in a very large mixing scenario. In this case, chargino-neutralino pair production would offer brighter prospects at Tevatron [38]. These considerations are valid in the mSUGRA scenario; other models imply less tight bounds on masses.

1.5.3 Constraints from $b \to s\gamma$

The width of the inclusive decay $B \to X_s\gamma$ is determined by flavour violating loop diagrams and is thus sensitive to new physics beyond the Standard Model. In particular, it receives significant contributions from charged Higgs boson exchange and chargino-stop

contributions[41]. The MSSM with $\mu > 0$ predicts a branching ratio lower than the one predicted by the Standard Model. On the other hand, if $\mu < 0$ the branching ratio predicted by the MSSM is higher than the one of the Standard Model. The experimental value [42] for the inclusive branching ratio is

$$BR(b \to s\gamma) = (3.21 \pm 0.44 \pm 0.24) \times 10^{-4}. \tag{1.79}$$

The implementation of NLO calculations [43] yields

$$2.33 \times 10^{-4} < BR(b \to s\gamma) < 4.15 \times 10^{-4} \tag{1.80}$$

which is compatible with experimental results. The regions excluded by this constraint are shown in green (intermediate shading) in Fig. 1.8. This effect is more remarkable at higher $\tan\beta$ and negative μ.

1.5.4 The Muon Anomalous Magnetic Moment

The muon anomalous magnetic moment is also an observable very sensitive to new physics beyond the Standard Model. The BNL E821 recently reported [44] a new measurement of the muon magnetic anomaly:

$$a_\mu = \frac{1}{2}(g_\mu - 2) = 11\ 659\ 202(14)(6) \times 10^{-10}\ (1.3\ \text{ppm}). \tag{1.81}$$

This measurement is in agreement with the predicted theoretical value (e.g. [45]) and the deviation from it is:

$$-6 < \delta a_\mu \times 10^{10} < 58. \tag{1.82}$$

The regions preferred by this measurement are shown in Fig. 1.8 in pink (light shading): in the $\mu > 0$ case, no additional constraint to the Higgs mass is added, while in the $\mu < 0$ case, additional regions with relatively low m_0 and $m_{1/2}$ are excluded.

1.5.5 Cosmological Relic Density

One of the most attractive features of Supersymmetry is that the LSP can be a dark matter candidate. The hypothesis that the lightest neutralino constitute a dark matter candidate provides preferred regions in the parameter space. However, these indications do not constrain the parameters since other non-MSSM particles (e.g. gravitino and axino) could be dark matter candidates; in this latter case, the considerations reported below would not be valid anymore.

An exclusion contour can be derived by theoretical considerations: if the LSP would interact electromagnetically and strongly, it would bind to nuclei and form anomalous isotopes which were never observed so far. Therefore, the only allowed LSP interactions are the weak and gravitational ones[46]. Regions in parameter space at low m_0 where the $\tilde{\tau}$, which is charged, would be the LSP are excluded for this reason. These regions are shown in brick red (dark shading) in Fig. 1.8 (the theoretically excluded region).

According to the most recent measurements[47], the total density is $\Omega_m h^2 \sim 0.14$ being $h^2 \sim 0.5$ and only a small fraction of the dark matter is barionic ($\Omega_b h^2 \sim 0.02$). In

the hypothesis that the remaining amount of matter is due to relic neutralinos, the most conservative limits on its density are:

$$0.1 < \Omega_{\tilde{\chi}_1^0} h^2 < 0.3. \tag{1.83}$$

The upper bound comes from the lower limit on the age of the universe of 12 Gyr. The lower limit can be in principle even smaller since there may be other dark matter constituents. However, the extra area of parameters space gained by lowering this limit would be negligible. The associated region of the $m_0 - m_{1/2}$ plane is shown in turquoise (very light shading) in Fig. 1.8. At $\tan\beta = 10$, there is a bulk region at $m_0 \sim 100$ GeV and $m_{1/2} \sim 250$ GeV which extends to very high values of m_0 at $m_{1/2}$ between 100 and 150 GeV. Another thin strip extends up to very high $m_{1/2}$ values close to the theoretically excluded region. In this region, the $\tilde{\tau}$ is nearly degenerate with the lightest neutralino and the coannihilation processes $\tilde{\chi}\tilde{l}$ and the $\tilde{l}\tilde{l}$ annihilation have a cross-section comparable with the $\tilde{\chi}\tilde{\chi}$ one at freeze-out. The strips due to $\tilde{\chi}\tilde{l}$ coannihilation and $\tilde{l}\tilde{l}$ annihilation extend towards high values of $m_{1/2}$ as long as they do not enter into the theoretically excluded region. These coannihilation effects provide a neutralino relic density compatible with Eq.1.83 even at very high neutralino masses[48]. At $\tan\beta = 35$ and 50 the region splits in two and an asynthotum appears due to the resonant direct-channel neutralino annihilation through H and A. [49].

The presence of all these strips extending to high values of $m_{1/2}$ allows the neutralino dark matter candidate hypothesis to be still viable even after the Higgs mass constraint which discards the bulk region. The largest $m_{1/2}$ allowed at $\tan\beta < 20$ is $m_{1/2} \sim 1400$ GeV and increases up to $m_{1/2} \sim 2200$ GeV at $\tan\beta \sim 50$. In the latter case, the Supersymmetry discovery at LHC is not guaranteed.

In a very large mixing scenario, the *stop* can be the next to the lightest SUSY particle and, if the mass difference with the lightest neutralino is small enough, the $\tilde{t}\tilde{\chi}$ coannihilation and $\tilde{t}\tilde{t}$ annihilation processes can be remarkable[39][40] and provide additional regions in the parameter space compatible with Eq. 1.83. These regions are sketched in Fig. 1.13 in the $m_0 - m_{1/2}$ plane for $\tan\beta = 10$, $\mu > 0$, $A_0 = 0$, 1000, 2000 and 3000 GeV. The same color conventions of Fig. 1.8 are used. The theoretically excluded region on the left side is larger than in Fig. 1.8 to prevent the lightest *stop* to be the LSP. The additional region is the thin strip extending to very high m_0 values.

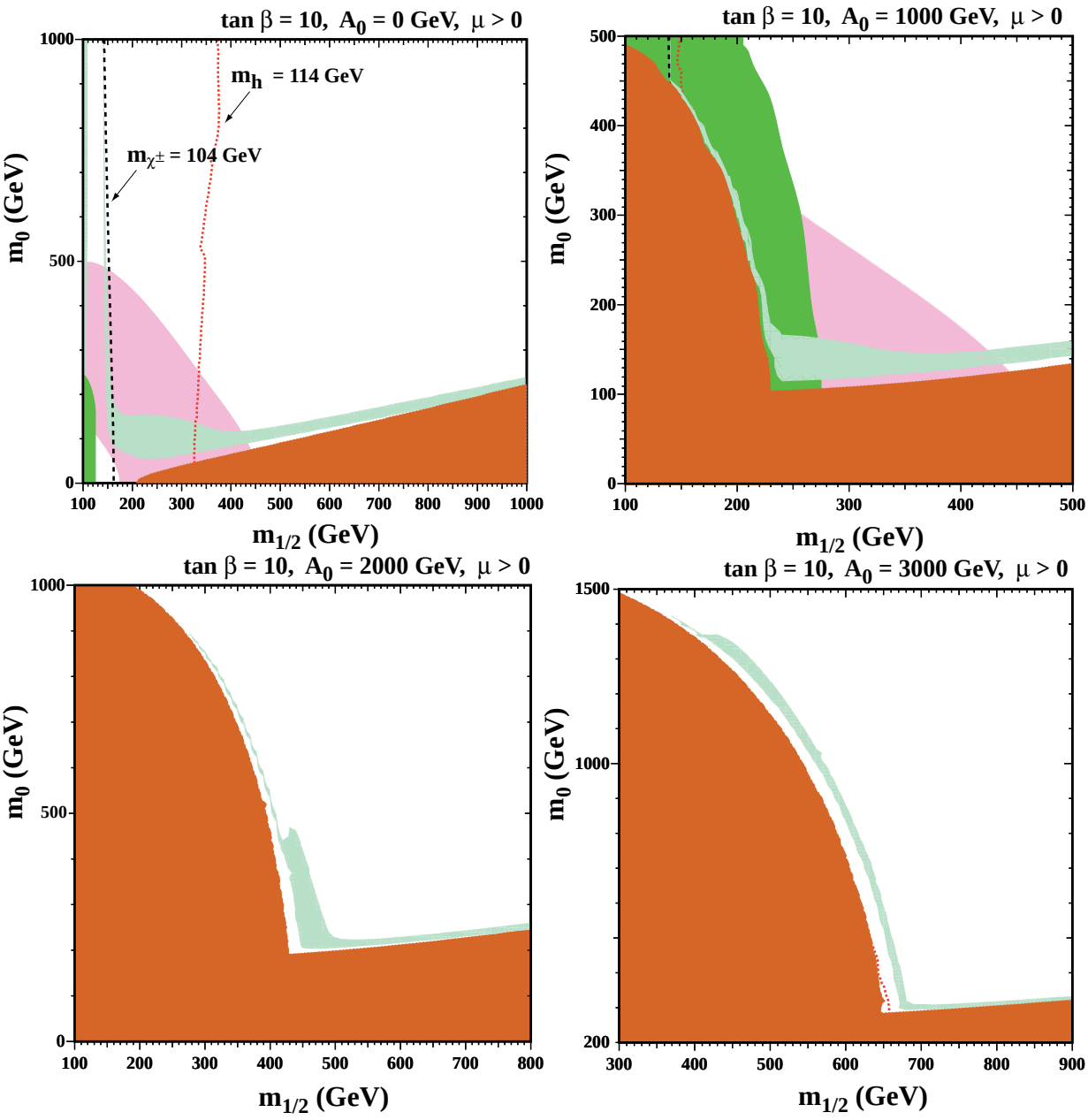

Figure 1.13: Theoretically excluded regions, regions excluded by the $b \to s\gamma$ constraint and regions compatible with the neutralino dark matter hypothesis in the $m_0 - m_{1/2}$ plane for $\tan\beta = 10$, $\mu > 0$, A_0=0 (upper left), A_0=1000 (upper right), A_0=2000 (lower left), A_0=3000 (lower right)[40]. The color conventions are the same of Fig. 1.8.

Chapter 2

The Large Hadron Collider and the CMS Experiment

This chapter provides an overview of the experimental facility. In the first paragraph the basic features of the accelerator are described, with a special emphasis on the aspects related with physics. Then the CMS experiment and the main subdetectors and the trigger system are reviewed.

2.1 The Large Hadron Collider

2.1.1 The Accelerator

The Large Hadron Collider (LHC) [50] will be the largest hadron collider in the world at its planned beginning in 2007. It will provide proton-proton collisions at a centre-of-mass energy $\sqrt{s} = 14$ TeV and it will be placed in the already existing LEP tunnel at CERN.

To supply the LHC with pre-accelerated protons, the existing CERN facilities will be upgraded. Protons will be accelerated through many steps by the already existing machines: a Linac will bring them up to 50 MeV, a Booster up to 1.4 GeV, the PS up to 25 GeV and the SPS up to 450 GeV. Finally, they will be introduced in the Large Hadron Collider where they will be accelerated up to 7 TeV. A scheme of the CERN acceleration complex is shown in Fig. 2.1.

Since collisions will occur between particles of the same type, two separate beam channels with opposite directions are required. The two channels, together with their superconducting dipole magnets and the corresponding coils, will be inserted in a single cryostatic structure. Dipoles will operate at 1.9 K and will provide a ~ 8 Tesla magnetic field. The boost will be provided by 400 MHz superconducting radiofrequency cavities with a voltage ranging from 8 to 16 MV/m.

The nominal number of protons per bunch will be 10^{11}: bunches will have a very small transverse spread, $\sigma_x \sim \sigma_y \sim 15\mu$m, while they will be 7.5 cm long in the z direction at the collision points. The main features of the accelerator are summarized in Table 2.1.

The accelerator parameter related to the rate of interactions is the *Luminosity* ($\mathcal{L}$): it depends on the number of protons per bunch (n_1 and n_2 for the two colliding beams respectively), the revolution frequency (f) and the widths which characterise the Gaussian transverse beam profiles in the horizontal (bending) and vertical directions (σ_x and σ_y

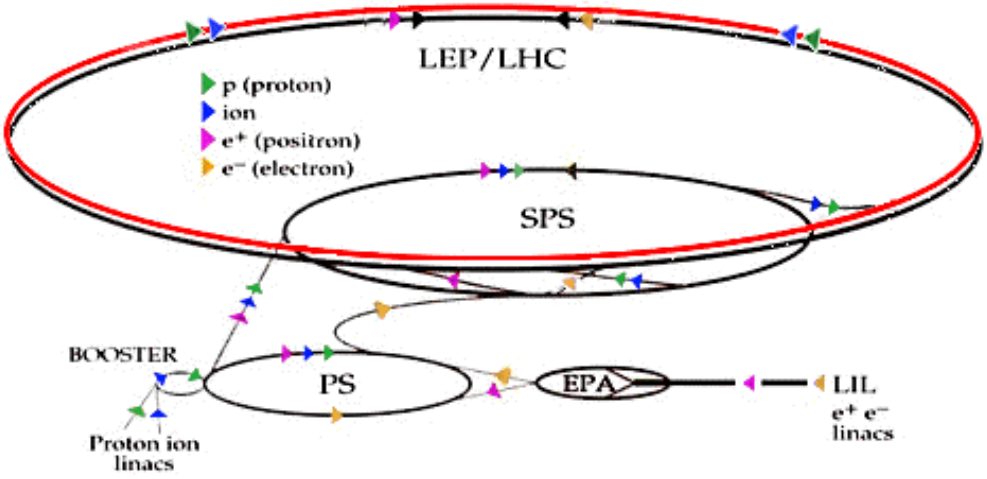

Figure 2.1: Overview of the accelerator complex at CERN. The sketch also shown the LEP electron and positrons trajectories as well as those of the LHC protons and heavy ions.

Table 2.1: Main technical parameters of LHC.

Parameter	Value
Circumference (km)	27
Number of magnet dipoles	1232
Dipolar magnetic field (Tesla)	8.386
Magnet Temperature (Kelvin)	1.9
Beam Energy (TeV)	7
Maximum Luminosity ($cm^{-2}s^{-1}$)	10^{34}
Protons per bunch	$1.05 \cdot 10^{11}$
Bunch spacing (ns)	24.95
R.M.S. bunch length	7.5 cm
Transverse beam size @ I.P.	16μm
Crossing angle	200μrad
Beam Lifetime	22 h
Luminosity Lifetime	10 h

respectively) through the formula:

$$\mathcal{L} = f\frac{n_1 n_2}{4\pi\sigma_x\sigma_y}. \tag{2.1}$$

The number of interactions N_i, corresponding to the process i with a cross section σ_i, is related to $\mathcal{L}$ through the relationship

$$N_i = \sigma_i \int \mathcal{L}dt. \tag{2.2}$$

$\int \mathcal{L}dt$ is also called *Integrated Luminosity*.

For the first three years the luminosity value will be $\mathcal{L} = 10^{33} cm^{-2}s^{-1}$ (low luminosity run). An integrated luminosity of 10 fb^{-1} per year for a total of 30 fb^{-1} will be collected. After this period, which will be mainly dedicated to tune the detector performance and to search for new particles, the luminosity will be increased to the design value $\mathcal{L} = 10^{34} cm^{-2}s^{-1}$.

The second phase of data taking, the high luminosity period, will be dedicated to extend the searches. It will last 5 years and 100 fb^{-1} of integrated luminosity will be collected each year for a total of 500 fb^{-1}.

Four detectors will be installed in the caverns around the collision points. Two of them will be multipurpose experiments: ATLAS[51] and CMS[52]. In the two remaining points, the ALICE[53] and LHCb[54] experiments will be dedicated respectively to heavy ions and $b-$physics.

2.1.2 Physics and Experimental Requirements

The main physics goal for the LHC experiments is the search for the Higgs boson. The new accelerator will make possible to explore a mass range from $\sim$ 100 GeV, which is the current lower bound, up to the TeV scale. Searches for Supersymmetry signals or tests of alternative models are the second physics goal of LHC, while the very large statistics of events will make possible also electroweak precision measurements, heavy flavours and QCD physics. To cope with this ambitious program, the LHC experiments were designed to achieve optimal sensitivity in the harsh experimental environment of the new machine.

The first challenge for LHC experiments comes from the very high event rate. The cross-sections for different processes at LHC span several orders of magnitude (see Fig. 2.2). A very high luminosity is required to allow reasonable statistics for rare processes. On the other hand, the rate of events at LHC, which is dominated by background events, is several order of magnitude larger than the maximum allowed for the data storage devices. The total inelastic cross-section is indeed estimated to be $\sigma_{inel} \sim 100$ mb, which corresponds to an average 10^9 interactions per second in the LHC conditions. Therefore, a strong online selection is required to reduce by $\sim$7 orders of magnitude the interaction rate before the storage on disks. A very high time resolution is also needed to distinguish events belonging to different bunch crossings separated only 25 ns in time.

The second challenge comes from the very dense particle environment. At high luminosity running, approximately 20 interactions are expected for each bunch crossing. A typical minimum bias collision at LHC will produce in average 5.5 charged particles with $\langle p_T \rangle \sim 0.5$ GeV and 8 primary photons per unit of pseudorapidity. The interesting signals,

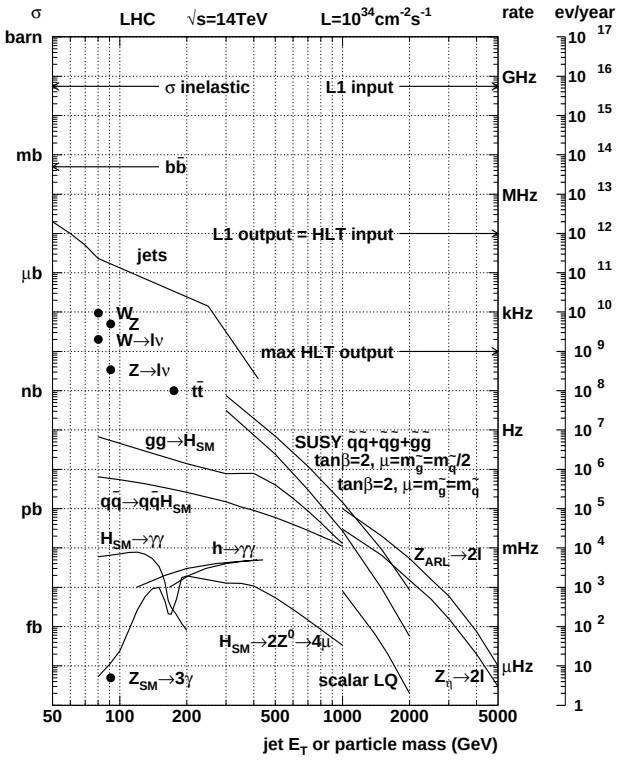

Figure 2.2: Inclusive proton cross section for basic physics processes. Interaction rates for the nominal luminosity are given on the right hand scale.

containing high p_T leptons, high E_T hadron jets, $b-$jets or large missing transverse momentum will always be superimposed to such background. Therefore, detector units must be finely segmented to separate particles very close in space. Sophisticated algorithms are also required to reconstruct particles in such a high density environment. Lastly, several technological restrictions apply to detectors which are supposed to withstand the high radiation dose expected at LHC.

Most of the processes under investigation would provide final states with leptons, hadron jets from quark fragmentation and missing energy. Therefore, the basic detector requirements for ATLAS and CMS are:

- capability to reconstruct muons in a large range of p_T and rapidity (to reconstruct Z^0, $W^{\pm}$ and tag bs)
- possibility to reconstruct electrons and photons (electrons from Z^0, $W^{\pm}$ and photons mainly for $H \rightarrow \gamma\gamma$ search)
- possibility to reconstruct charged tracks with a good precision on p_T and impact parameter for Bs and τs reconstruction and tagging
- possibility to reconstruct hadron jets from QCD processes and heavy particles decays (t, Z^0, $W^{\pm}$, H, SUSY particles)
- almost full hermeticity to allow missing transverse momentum reconstruction (and thus reconstruct neutrinos and neutralinos)

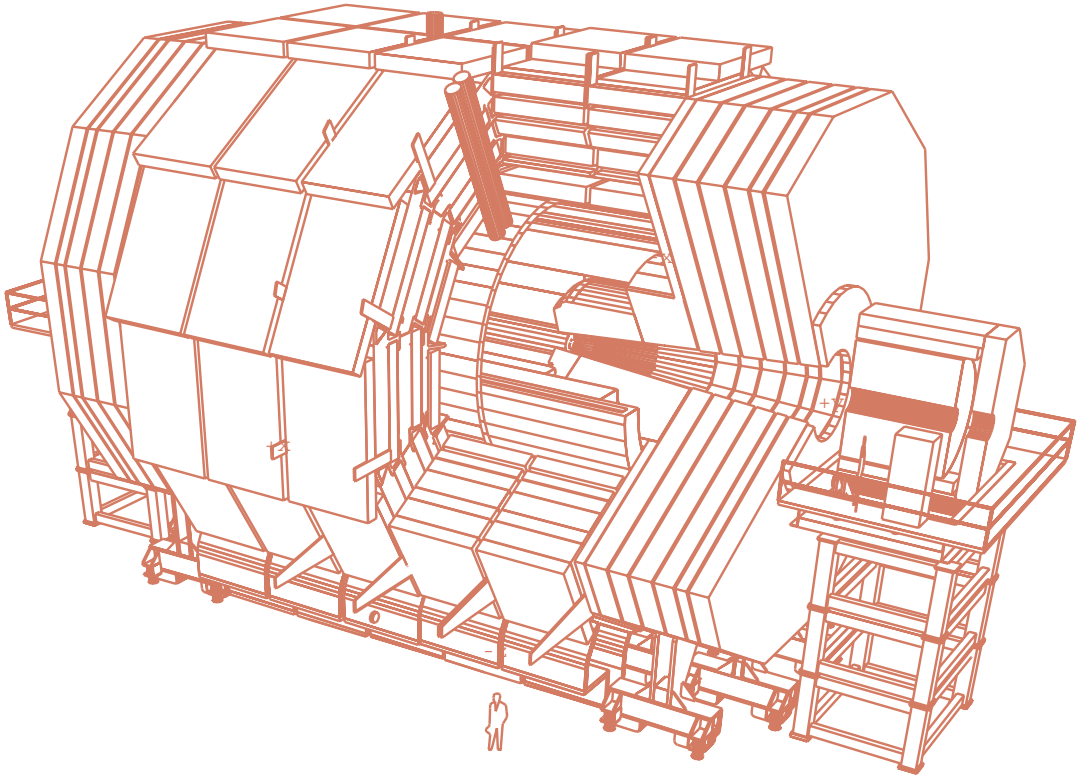

Figure 2.3: Overview of the CMS detector

Part of the reconstruction should be performed at the trigger level to reject the large fraction of background present in LHC events.

2.2 The CMS Experiment

The Compact Muon Solenoid (CMS) is designed to fulfill all requirements listed above. Its layout is sketched in Fig. 2.3. The apparatus has a cylindrical symmetry around the beam direction. It is made out of several layers of detectors around the beam direction in the central region (*barrel*) and several disks (*end-caps*) in the forward regions to allow a nearly hermetic coverage. The inner part of the apparatus is contained in a superconducting solenoid (7 m diameter, 12 m long) which provides a uniform 4 Tesla magnetic field for charged particles bending. The Tracking system and most of the Calorimetry are fully contained inside the magnet. Two very forward calorimeters extend the coverage up to $|\eta| < 5$. A complex system for muon detection is placed outside the magnet. The iron slabs used to filter the muons and to house the muon detectors act as a return yoke for the CMS magnetic field.

2.2.1 The Magnet

The goal of the CMS magnet[55] is to provide a 4 Tesla magnetic field to bend charged particles and thus provide the transverse momentum measurement.

The Magnet system includes a cryogenic system, power supply, quench protection,

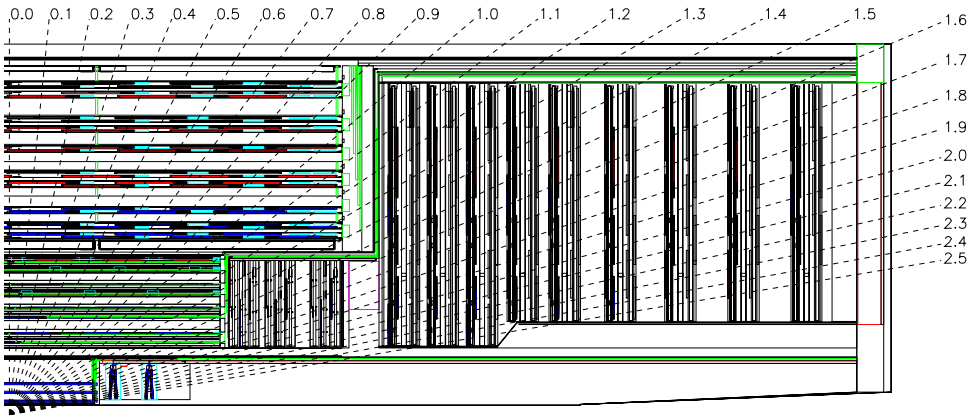

Figure 2.4: Layout of the Tracker.

vacuum pumping and control system. The coil is inserted inside the cryostat and consists of the windings with its structural support, the thermal radiation shield and vacuum tank. The conductor consists of three concentric parts: the central flat superconducting cable, with high purity aluminium stabiliser, and an external aluminium-alloy reinforcing sheath. The superconducting cable is of Rutherford type and contains 40 NiTb strands.

2.2.2 The Tracker

The Tracker [56][57] is the subdetector system which is closest to the interaction point. Its goal is the reconstruction of charged tracks and vertices. The main physics goal of the Tracker are the reconstruction of the primary vertex, the matching of charged tracks with Calorimetry and Muon system for lepton identification and secondary vertices reconstruction for B and τ decays detection. It is thus a key device for searches for new particles (e.g. $H \rightarrow b\bar{b}$, $H \rightarrow Z^0 Z^0 \rightarrow 4l$, SUSY searches, primary vertex reconstruction for $H \rightarrow \gamma\gamma$) and Standard Model physics (e.g. top quark and CP violation in B decays). A Tracker completely based on semiconductor detectors was designed for these purposes and its layout is shown in Fig. 2.4.

The innermost part of the Tracker is made of silicon pixel detectors to provide a good precision in the extrapolation to the primary vertex. According to the base design, the barrel part is made of three layers of pixel detectors while the end-caps are made of two pixel disks. The pseudorapidity range covered by the pixel detector, where $b-$tagging is possible, is $|\eta| < 2.4$.

The intermediate and outer parts of the Tracker are made of Silicon microstrip detectors of different design. The total numbers of barrel layers and forward disks are 4 and 3 in the intermediate Tracker and 6 and 9 in the outer Tracker. These parts of the Tracker allow an efficient pattern recognition, a precise measurement of the track momentum and a good matching with the outer detectors. Details on the silicon detectors, the readout system, optimisation of the layout and performance of the tracker are provided in the fourth chapter which is entirely dedicated to this device.

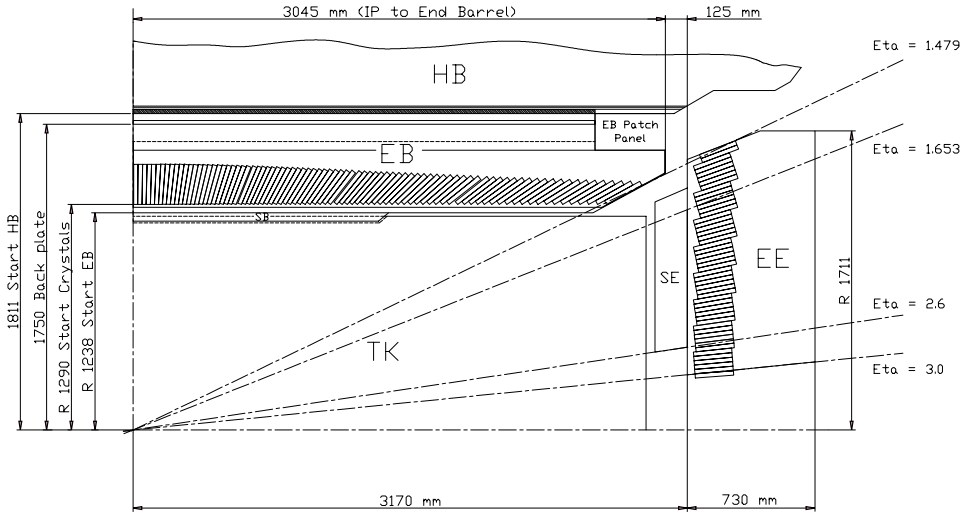

Figure 2.5: Layout of the Electromagnetic Calorimeter

2.2.3 The Electromagnetic Calorimeter

A complex Electromagnetic Calorimeter (ECAL) [58] is used for electron and photon reconstruction. The main goal of ECAL is to reconstruct the process $H \rightarrow \gamma\gamma$, where the reconstruction of the Higgs boson, almost completely, relies on the photon reconstruction. The subsystem was designed in order to achieve the best sensitivity for this process.

ECAL is made out of several arrays of $PbWO_4$ crystals. This material is suitable to work in the LHC conditions since it is radiation resistant and chemically inhert. Moreover, it has a very short decay time ($\sim$ 10 ns) for scintillation radiation emission and allows 85% light collection in 25 ns.

The layout of ECAL is shown in Fig. 2.5. A cylindrical barrel covers the region defined by $|\eta| < 1.48$, while two end-caps cover the forward region up to $|\eta| < 3$. The crystals have a very short radiation length of 0.89 cm which allows a very compact device. Barrel crystals are 23 cm long: this length corresponds to 26 radiation lengths and allows an almost complete shower containment. The cross section of the crystals is 22×22 mm^2 throughout all calorimeter. In the barrel region this corresponds to a granularity $\Delta\eta \times \Delta\phi \sim 0.0175 \times 0.0175$ which is high enough to separate photons from π^0 decay. The granularity decreases with η and reaches a maximum of $\Delta\eta \times \Delta\phi \sim 0.05 \times 0.05$ in the very forward crystals. To increase the π^0 rejection power in the forward regions, a silicon detectors preshower will be placed in front of the end-caps. Since the preshower will be 3 radiation lengths deep, the end-cap crystals length will be reduced to 22 cm. The cross section of these crystals is 24.7×24.7 mm^2.

Barrel crystals light is collected by avalanche photodiodes (APD). These devices are able to work in the presence of a high transverse magnetic field. In the end-cap regions the radiation dose will be much higher, hence vacuum phototriodes (VPT) were chosen to read out the signals.

The energy resolution that can be achieved by ECAL can be parametrised according

to the formula:

$$\frac{\sigma_E}{E} = \frac{a}{\sqrt{E}} \oplus b \oplus \frac{\sigma_N}{E}, \tag{2.3}$$

where the first term is the contribution due to the statistical fluctuations of the shower, the second one is due to calibration and the third one to electronics and pile-up. Test-beam measurements provide the following estimates for the parameters: $a = 2.7\%$, $b = 0.55\%$ and $\sigma_N = 155$ MeV for the barrel crystals while $a = 5.7\%$, $b = 0.55\%$ and $\sigma_N = 200$ MeV for the end-cap crystals.

It was recently envisaged the possibility of a staged ECAL scenario at the beginning of data taking due to a longer time scale required for construction and calibration. In the backup ECAL detector layout the end-caps are removed keeping only the preshower in the forward regions. The impact on dijet mass resolution and E_T is negligible[59]. In the analysis described in this document, the impact of a reduced ECAL coverage is also investigated.

2.2.4 The Hadron Calorimeter

The purpose of the Hadron Calorimeter (HCAL) [60] is to achieve a good jet energy resolution, a precise measurement of the jet direction and missing transverse momentum measurement. Therefore, the detector must be thick enough to fully contain the hadronic shower, have a good transverse granularity and be completely hermetic.

The CMS Hadron Calorimeter is a sampling calorimeter with active layers alternated with absorbers. Active layers are made out of plastic scintillators, while absorbers are made out of Copper. The overall thickness varies from 8.9 interaction lengths in the barrel region up to 10 in the end-caps.

A scheme of HCAL is shown in Fig. 2.6. A *tail catcher* is placed outside the magnet to improve the shower containment at $\eta = 0$. Scintillators are arranged in projective towers with a granularity $\Delta\phi \times \Delta\eta = 0.087 \times 0.087$ to guarantee an efficient two-jet separation. The coverage extends up to $|\eta| < 1.4$ for the barrel and $1.4 < |\eta| < 3$ for the end-cap.

According to test-beam data, the expected energy resolution for HCAL combined with ECAL is:

$$\frac{\sigma_E}{E} = \frac{100\%}{\sqrt{E}} \oplus 4.5\%. \tag{2.4}$$

A degradation of the response is expected at $|\eta| \sim 1.4$: in this region, the amount of inactive material is higher due to the presence of services and cables.

A very forward calorimeter (VFCAL) is placed outside the magnet to extend the hermetic coverage to the region between $3 < |\eta| < 5$. It is also a modular sampling calorimeter made of quartz crystals alternated with Copper. The granularity of VFCAL is $\Delta\eta \times \Delta\phi = 0.17 \times 0.1745$. The forward calorimetry is expected to provide an energy resolution of

$$\frac{\sigma_E}{E} = \frac{1.82}{\sqrt{E}} \oplus 0.09\%, \qquad \frac{\sigma_E}{E} = \frac{1.38}{\sqrt{E}} \oplus 0.05\% \tag{2.5}$$

for hadrons and electrons respectively.

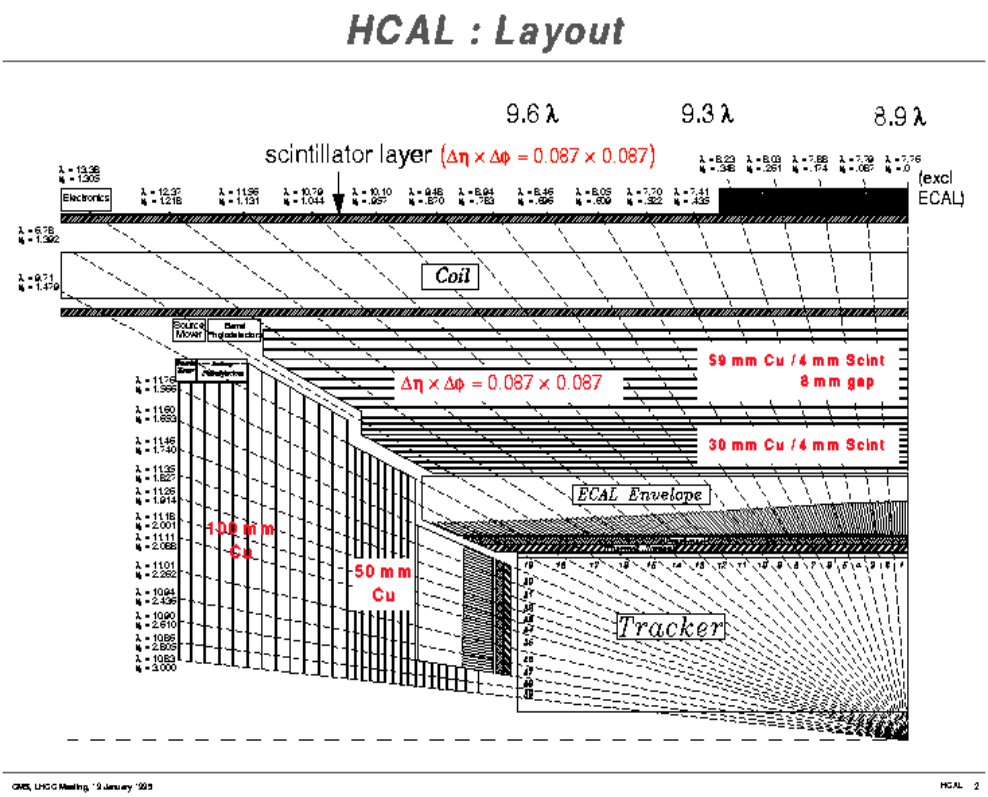

Figure 2.6: Layout of the Hadron Calorimeter

2.2.5 The Muon System

A huge muon detection system [61] is placed outside the magnet coil. Its purpose is multiple: it allows muon identification and measurement of their momentum, it provides the trigger signal for events with muons as well as a precise time measurement of the bunch crossings. The layout of the muon detection system is sketched in Fig. 2.7.

The muon detectors are integrated in the iron return yoke of the magnet. Both barrel and end-caps are made out of four active layers and three planes of absorber.

The barrel region extends up to $|\eta| < 1.3$. It is divided in five segments. Each detection unit houses 12 layers of Drift Tube (DT) with approximately 400 ns drift time and a time resolution of 5 ns.

Tubes are arranged in 3 modules of four layers each one. The first and third modules provide a ϕ measurement while the central one provides the z measurement. Layers of the same module are staggered by half cell to optimise the coverage. A certain redundancy guarantees full coverage even in the presence of dead regions. The DT spatial resolution is 250 μm per tube and an overall resolution of 100 μm in $R-\phi$ and 150 μm in z is expected. The system is fast enough to allow the measurement of muon position and to compute its direction for Level 1 Trigger signal.

End-caps extend the coverage up to $|\eta| < 2.4$. The active layers are equipped with trapezoidal shaped Cathode Strip Chamber (CSC) detectors. With the exception of the first layer, which has three detector rings, the other layers are made out of an inner disk of 18 detectors covering 20^0 in ϕ and an outer disk of 36 detectors covering 10^0 in ϕ. The last detector layer is followed by an iron layer, 1 cm thick, to protect detectors from radiation

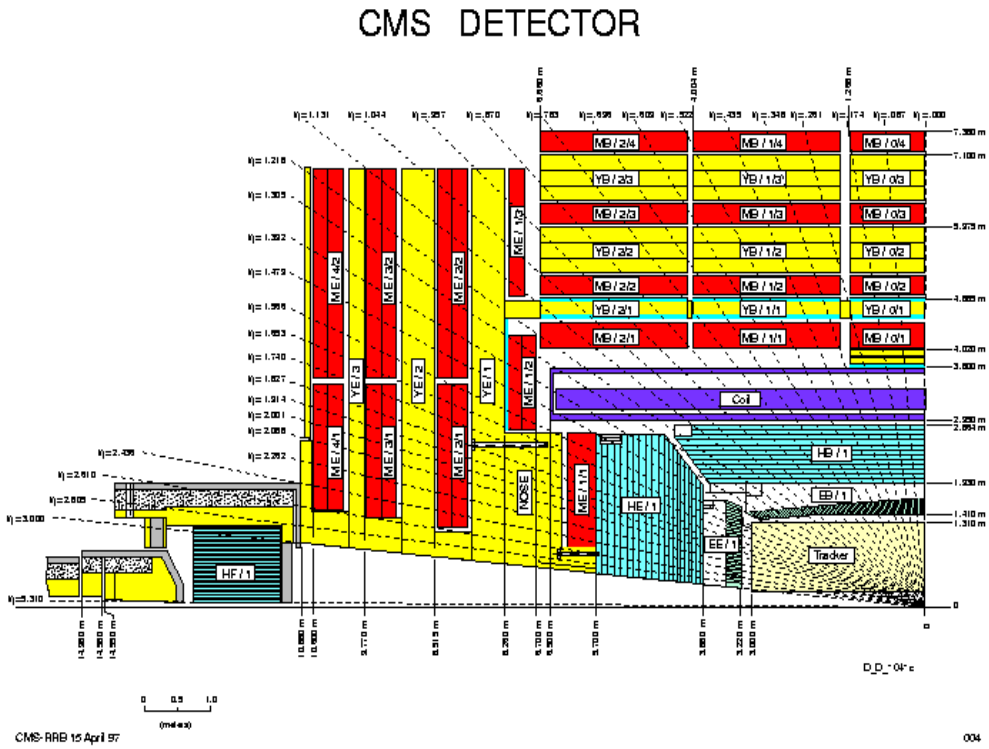

Figure 2.7: Layout of the muon detection system

coming from the accelerator.

Each chamber is made of 6 sandwiches of cathode strips and wires which provide three-dimensional reconstruction. CSC are designed to operate in non uniform magnetic field ranging from 1 to 3 Tesla. The spatial resolution varies from 75 μm, for the first two inner layers, to 150 μm for the outer ones. CSC informations is available at Level 1 Trigger. The time resolution of CSC is 6 ns. Bunch crossing identification is also available by CSC.

An additional muon Trigger is provided by the Resistive Plate Chambers (RPC). RPC detectors have excellent time resolution ($\sigma \sim 1-2$ ns). There is a plane of RPC detectors for each layer of CSC detectors in the end-caps and the first, second and fourth layers of DT detectors in the barrel.

Each RPC chamber in the barrel is made of two phenolic resin planes separated by a gap of a few mm filled by gas. Planes are coated by a conductive graphite paint in the shape of electrodes. Readout is made by plastic insulated aluminium strips outside the resin plates. The spatial resolution of RPC is of the order of the strip size (10$\div$40 mm in $R-\phi$) and 100 $\div$ 1300 mm in z. These devices operate in avalanche mode to cope with the LHC high rate.

The intrinsic p_t resolution of the overall muon system is $\Delta p_T/p_T = 8-15\%$ for $p_T = 10$ GeV/c muons and $\Delta p_T/p_T = 20-40\%$ for p_T up to 1 TeV/c. The matching with track segments in the Tracker allows to improve the resolution up to 1% and $7-16\%$ respectively.

2.2.6 The Trigger

A very complex Trigger System is being designed to reduce the 40 MHz event rate down to a value around 100 Hz which is considered the maximum that could be archived by a

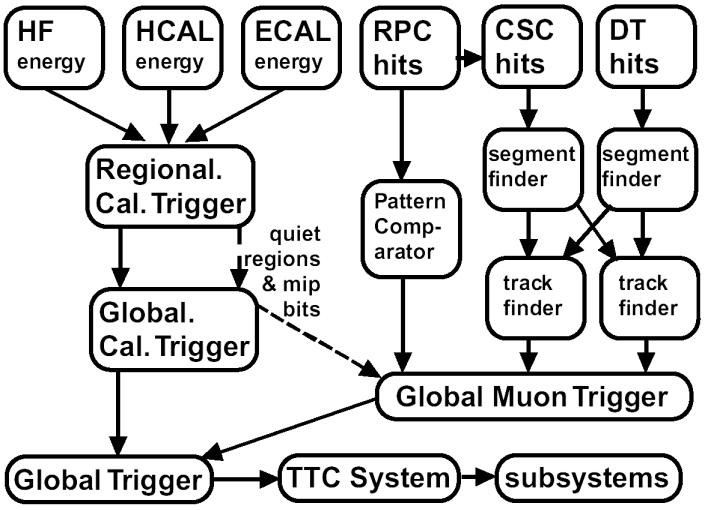

Figure 2.8: Overview of the Level 1 trigger flow.

computer farm. This system is the start of the physics analysis selection. Due to the 7 orders of magnitude which separate the LHC collision rate from the acquisition rate, the Trigger System has a very complicated structure. It must be very performant in terms of signal efficiency and background rejection rate and very fast. It operates in several steps applied in cascade. A very coarse and fast decision is taken at low levels to remove the bulk of the background, while more precise reconstruction is performed at higher levels.

The lowest level Trigger, called *Level 1* (L1) Trigger, is entirely based on hardware. It allows to reduce the event rate from 40 MHz to 100 kHz .

It is based exclusively on Calorimetry and Muon System informations. It has first a *regional* phase, where Calorimeter and Muon data are analysed locally to achieve a coarse reconstruction of jets and leptons, then the informations are combined together to extract the missing transverse momentum. An overview of the process is displayed in Fig. 2.8.

The Calorimeter L1 Trigger works as follows: individual ECAL, HCAL and HF Trigger Primitive Generator (TPG) circuits provide coarse calorimetric towers and send them to the Regional Calorimeter Trigger (RCT) which reconstructs jets, leptons and photons to be sent to the Global Trigger (GT). It also provides the map of inactive calorimetry regions to improve the muon isolation.

In the meantime, the muon tracks are reconstructed independently by the RPCs and the Drift Tubes or the CSCs. Informations are then combined together by the Global Muon Trigger (GMT) to resolve ambiguities and with the inactive calorimetry regions to remove fakes. GMT and GCT are again combined to calculate the missing transverse momentum and they determine the regions where higher level Triggers should focus on.

The L1 accept signal is distributed to the subsystems: front-end electronics was designed to store data in 3.2 μs pipelines (corresponding to 128 bunch crossings) which is the L1 decision time and send them to the PC farms only in case of L1 accept signal.

High Level Triggers (HLT) are being designed to reduce the Trigger rate from 100 kHz to 100 Hz. This reduction is entirely accomplished via software through some dedicated PC-farms in many steps.

Level 2 (L2) and *Level 3* Trigger (L3) are being designed to reduce the rate from 100 kHz to 100 Hz[63]. L2 refines leptons and jets reconstruction. Pixel hits are already available

at L2 and a coarse track and primary vertex and tracks reconstruction [64] from pixel hits is already be available to clean the L1 sample. Pixel hits tracking are also be used in exclusive channels dedicated triggers and thus it allows to improve the statistics for rare processes.

Part II

Scalar Top Quark Search

Chapter 3

Supersymmetry Searches at LHC

This chapter describes the prospects for Supersymmetry searches at LHC. The scalar top quark search is introduced within the main strategies to look for new physics at hadron colliders. The experimental requirements for the LHC experiments are discussed in general, while the tracking related tools developed for this work are illustrated in more detail in the following chapters.

3.1 Searches at the LHC

3.1.1 General Remarks

The Large Hadron Collider is an optimal environment to perform the search of SUSY particles and allows to cover the regions not yet ruled out by the current experimental constraints up to masses in the TeV scale.

Supersymmetry signals have very large cross sections at LHC: the contours corresponding to a constant overall cross section obtained with ISAJET 7.32[65] are shown in Fig. 3.1 in the $m_0 - m_{1/2}$ plane for $\tan\beta = 2$ and 35, $A_0 = 0$ and $\mu > 0$ [66]. The $\mu < 0$ case is very similar and is thus neglected.

The overall cross section is dominated by strongly interacting SUSY particles production (in particular $p\bar{p} \to \tilde{q}\tilde{g}$, $\tilde{g}\tilde{g}$, $\tilde{q}\tilde{q}$). The contours corresponding to inclusive cross section for processes with at least one strong interacting SUSY particle are displayed in the same figure with a dashed line. The two types of contours are very close at low m_0 and $m_{1/2}$, where squarks and gluino are relatively light, while they separate at higher values, where squarks and gluino are heavier and the production is dominated by chargino and neutralino. The expected production cross-section is large enough at LHC to allow a complete survey of the parameter space.

The supersymmetry phenomenology is very rich due to the large number of new particles foreseen by the theory and a huge number of final states.

In particular:

- Chargino and neutralino produce a large number of leptons, jets and large E_T^{miss} through the decay modes $\tilde{\chi}_2^0 \to \ell^+\ell^-\tilde{\chi}_1^0$, $\tilde{\chi}_2^0 \to \tilde{\ell}\ell \to \ell^+\ell^-\tilde{\chi}_1^0$, $\tilde{\chi}_2^0 \to Z^0\tilde{\chi}_1^0$, $\tilde{\chi}_2^0 \to h\tilde{\chi}_1^0$, $\tilde{\chi}_1^\pm \to W^\pm\tilde{\chi}_1^0$ with $Z^0 \to \ell^+\ell^-, jj$, $W^\pm \to \ell\nu, jj$, $h \to b\bar{b}$.

- Squarks and gluino produce a large number of jets and large E_T^{miss} through the decays

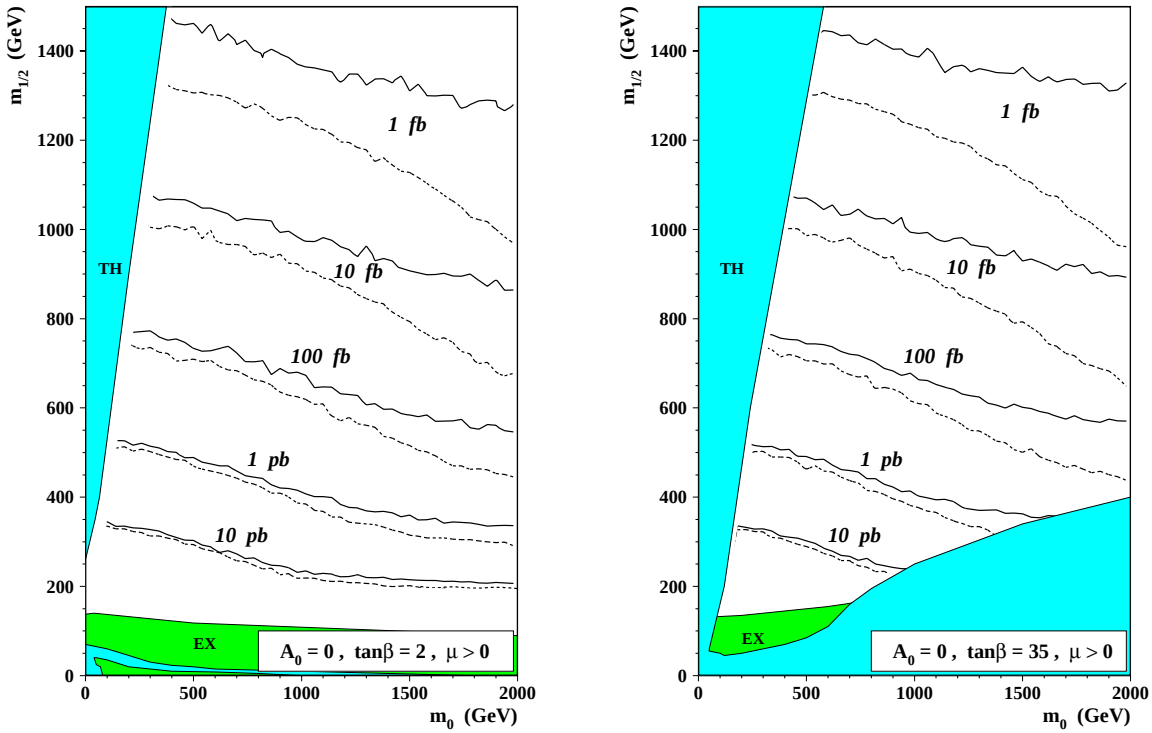

Figure 3.1: Total mSUGRA cross-section contours as function of m_0 and $m_{1/2}$ for $A_0 = 0$, $\mu > 0$ and $\tan\beta = 2$ (left) and $\tan\beta = 35$ (right) [66].

$\tilde{q} \to q\tilde{\chi}$, $\tilde{g} \to q\tilde{q}$, $\tilde{\chi}$ being either the LSP or heavier charginos and neutralinos. The latter produce additional leptons and jets with a softer p_T spectrum.

Therefore, in order to reconstruct the final state of SUSY events, the basic requirements for the LHC detectors are:

- an almost complete hermeticity to measure the missing transverse momentum due to the LSP escaping the detector
- a hadron calorimeter to reconstruct the jets produced by squarks, gluino, chargino and neutralino
- a muon system and an electromagnetic calorimeter to identify leptons produced in slepton, chargino and neutralino decays
- a good tracking system to identify $b-$hadrons from squarks, gluino and higgs decays and reconstruct τs which are produced in $\tilde{\tau}$ decays and chargino and neutralino decays at large $\tan\beta$.

All these requirements are fulfilled by the CMS detector and were in fact part of the guidelines when the detector was designed.

The program of SUSY searches is very wide due to the large number of predicted SUSY signals. The main search can be divided into two main streams: inclusive and exclusive searches. Both type of searches are described in this section and the complementarity of their results is discussed.

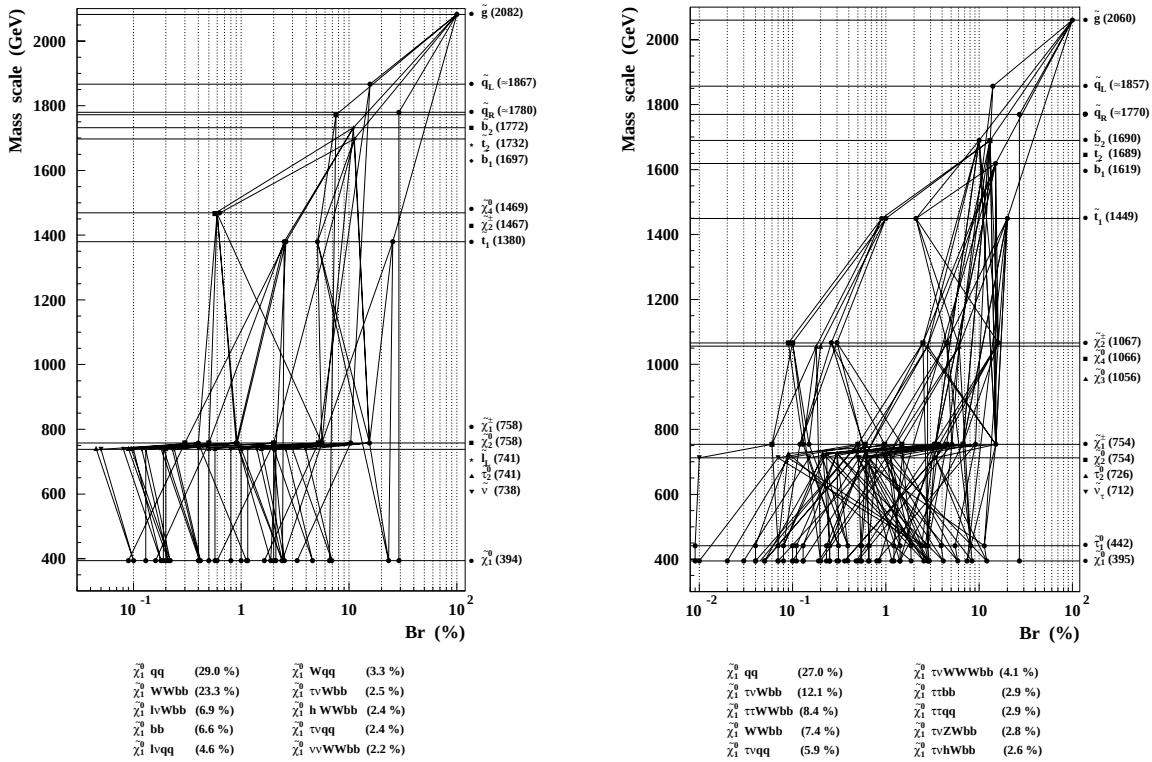

Figure 3.2: Typical decay modes for a massive gluino (2060) GeV for $m_0 = 400$ GeV, $m_{1/2} = 900$ GeV, $A_0 = 0$, $\mu > 0$, $\tan\beta = 2$ (left) and $\tan\beta = 35$ (right) [66].

3.1.2 Inclusive Searches

Despite the large production cross section, the complete reconstruction of the SUSY particles would be very difficult due to the huge number of decay topologies which can take place. An example of all possible decay chains of gluino and the corresponding branching ratios are shown in Fig. 3.2[66]. Each line connects a supersymmetric particle with its decay products for fixed $m_0 = 400$ GeV, $m_{1/2} = 900$ GeV, $A_0 = 0$, $\mu > 0$ and $\tan\beta = 2$ and 35. After each decay step, the spectrum of momenta becomes softer and therefore the reconstruction becomes less efficient.

The inclusive searches aim at tagging the event as a SUSY candidate from its general features and do not require the complete reconstruction of the SUSY particles. In this way, a very efficient tagging of SUSY signal can be achieved. The inclusive searches are therefore the first step in Supersymmetry search and can provide a signal even with a limited statistics.

Typical inclusive searches [66][67] are based on the requirement of a large E_T^{miss} and the presence of high E_T jets and leptons. Fig. 3.3 shows the five sigma discovery contours of some of these searches in the $m_0 - m_{1/2}$ plane for $A_0 = 0$, $\mu > 0$, $\tan\beta = 2$ and 35 for an integrated luminosity of 100 fb^{-1}. The analyses are indicated with E_T^{miss}, 0L, 1L, 2LSS, 2LOS, 3L and are based on large E_T^{miss}, and large E_T^{miss} and lepton veto, 2 leptons with the same charge sign, opposite charge sign and 3 leptons respectively.

The region below the contour can be explored by these searches. The iso-mass contours for some SUSY particles are also shown in the figure: these searches allow to discover Supersymmetry up to squark and gluino masses of 2.5 TeV for an integrated luminosity of 100 fb^{-1} (one year of running at high luminosity).

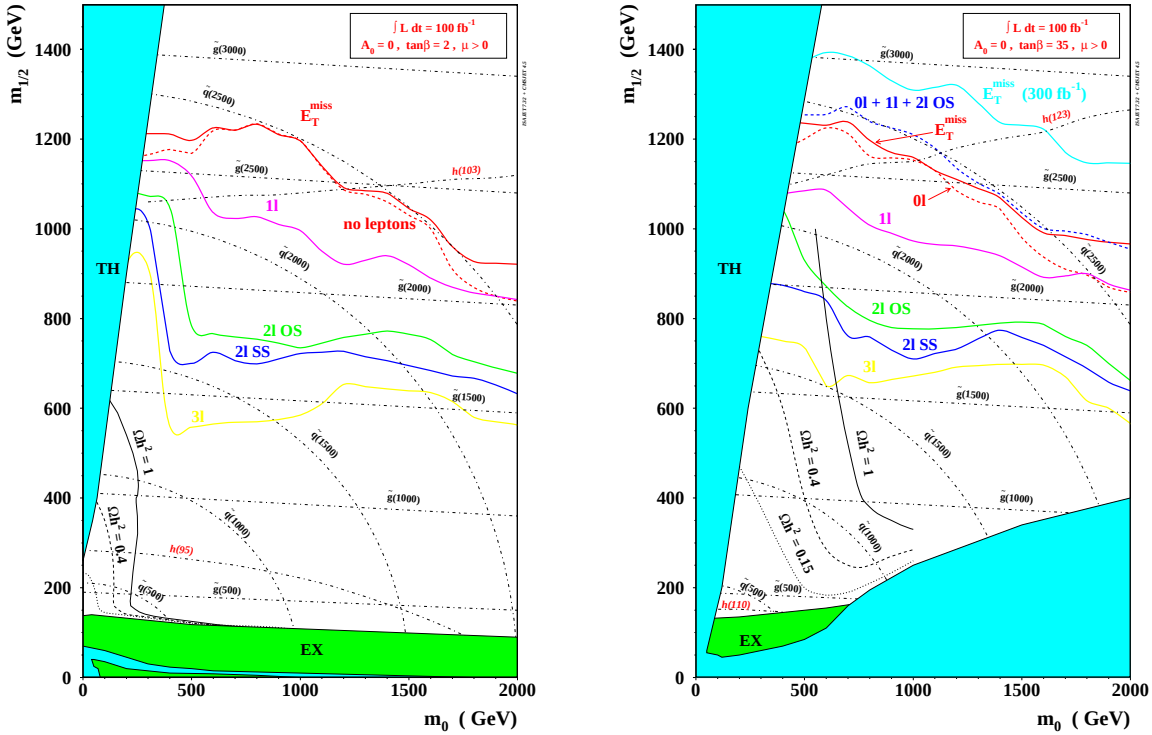

Figure 3.3: Five sigma discovery contours for various final states in $\int Ldt = 100\text{fb}^{-1}$ for $A_0 = 0$, $\mu > 0$ and $\tan\beta = 2$ (left figure) and $\tan\beta = 35$ (right figure)[66].

3.1.3 Identification of Exclusive Processes

One of the main challenges of LHC will be to disentangle the specific processes from the overall inclusive production. The identification of the exclusive processes would be a direct confirmation that an excess of events, observed with the inclusive searches, is due to Supersymmetry and would allow to measure the main Supersymmetry parameters. This task will be very difficult at an hadron machine but, if successful, would provide important informations on the model.

Lepton signatures would provide the clearest evidence of supersymmetry at least at the beginning of data taking: leptons from decays $\tilde{\chi}_2^0 \to \ell^+\ell^-\tilde{\chi}_1^0$ and $\tilde{\chi}_2^0 \to \tilde{\ell}\ell \to \ell^+\ell^-\tilde{\chi}_1^0$ have a sharp upper edge on the invariant mass distributions[68]. If $m_{\tilde{\chi}_2^0} < m_{\tilde{\ell}} + m_\ell$, the $\tilde{\chi}_2^0$ decay would be a three body decay mediated by a virtual slepton and the edge would be placed at $m_{\tilde{\chi}_2^0} - m_{\tilde{\chi}_1^0}$. In the case $m_{\tilde{\chi}_2^0} > m_{\tilde{\ell}} + m_\ell$, the neutralino decay is a two body decay and the edge would be placed at:

$$m_{\ell^+\ell^-} = \frac{\sqrt{(m^2_{\tilde{\chi}_2^0} - m^2_{\tilde{l}})(m^2_{\tilde{l}} - m^2_{\tilde{\chi}_1^0})}}{m_{\tilde{l}}}. \tag{3.1}$$

Informations about slepton and neutralino masses and thus on the SUSY parameters can be derived from the position of these edges.

An example of edge, corresponding to the $m_{\tilde{\chi}_2^0} < m_{\tilde{\ell}} + m_\ell$ case is shown in Fig. 3.4 for lepton pairs of an inclusive SUSY sample. The mass difference $m_{\tilde{\chi}_2^0} - m_{\tilde{\chi}_1^0}$ is around 40-50 GeV in this case. The region of parameter space which can be explored with this signature is shown in Fig. 3.5 in the $\tan\beta = 2$, $\mu < 0$, $A_0 = 0$ case for an integrated luminosity $\int Ldt = 10^5$ pb^{-1}[70].

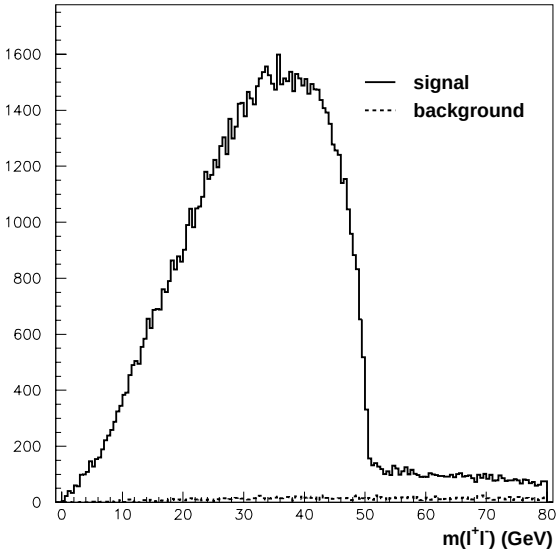

Figure 3.4: An example of $m_{\ell^+\ell^-}$ distribution for leptons coming from $\tilde{\chi}_2^0$ decay at $m_0 = 200$ GeV, $m_{1/2} = 100$ GeV, $A_0 = 0$, $\tan\beta = 2$, $\mu < 0$ [69].

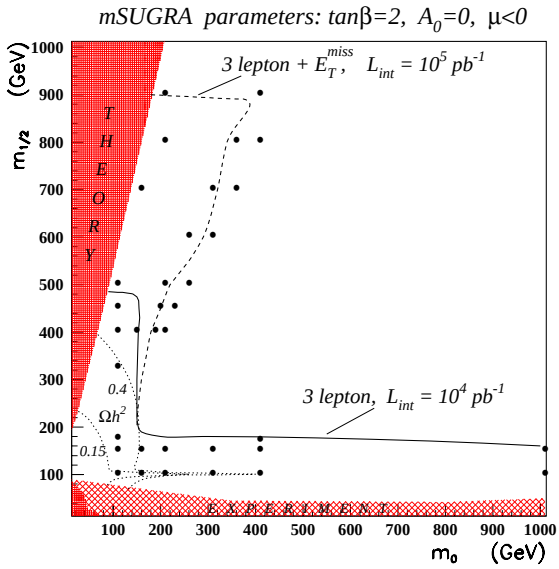

Figure 3.5: The discovery contours for the process $\tilde{\chi}_2^0 \to l^+l^-\tilde{\chi}_1^0$ in the three leptons and three leptons $+E_T^{miss}$ signatures for $\tan\beta = 2$, $\mu < 0$, $A_0 = 0$ and $\int Ldt = 10^5$ pb^{-1} [70].

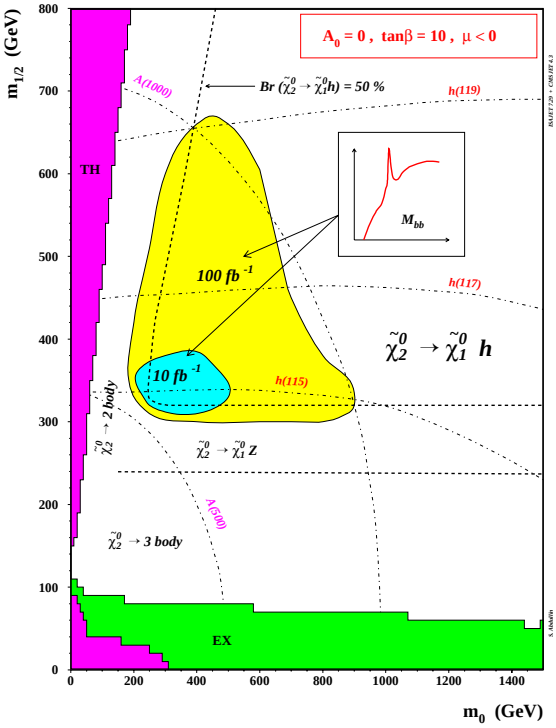

Figure 3.6: 5σ discovery contours for the process $\tilde{\chi}_2^0 \to h\tilde{\chi}_1^0$, $h \to \gamma\gamma$ in multijet $+E_T^{miss}$ events for $\tan\beta = 10$, $\mathrm{sgn}\mu < 0$, $A_0 = 0$ and $\int Ldt = 10$ and 100 fb^{-1} [71].

A complementary region can be explored through the process of Higgs boson production through $\tilde{\chi}_2^0 \to h\tilde{\chi}_1^0$, which allows to explore a region of parameter space complementary to the $\tilde{\chi}_2^0 \to \ell^+\ell^-\tilde{\chi}_1^0$ one [71]. Fig. 3.6 shows the five sigma discovery contours for $\tan\beta = 10$, $\mu < 0$, $A_0 = 0$ and $\int Ldt = 10$ and 100 fb^{-1}.

Other informations which can be extracted are sbottom and gluino reconstruction, through $\tilde{g} \to b\tilde{b}$, $\tilde{b} \to b\chi_2^0 \to b\ell^+\ell^-\chi_1^0$, which would provide the $\tilde{b}$ and $\tilde{g}$ masses, and $\tilde{q} \to q\chi_2^0$ reconstruction, which would allow to measure squarks masses [72][73]. The combination of all these measurements can provide an estimate of the mSUGRA parameters.

The scalar top quark search, which is the subject of this work, enters in this class of searches. The *stop* can be produced in pairs or from gluino decay $\tilde{g} \to t\tilde{t}$ and mainly decays through $\tilde{t} \to t\tilde{\chi}_1^0$ and $\tilde{t} \to b\tilde{\chi}_1^\pm \to W^\pm\tilde{\chi}_1^0$ producing a large number of leptons, jets, $b-$jets and missing transverse momentum. The first process is studied in this work.

The main goal of this work is to develop strategies to detect an excess of these events with respect to the expected Standard Model background. The discovery potential is studied as a function of the $\tilde{t}$ and $\tilde{\chi}_1^0$ masses and as a function of the SUSY parameters. In the latter case, the visibility of the $\tilde{t}$ signal over the entire Supersymmetric production is investigated as well.

Chapter 4

The CMS Tracker

To identify the $b-$flavoured jets, a powerful tracking system is a fundamental tool: the CMS Tracker is being designed to satisfy this requirement. In this chapter the instrumental aspects of the problem are explained; the track reconstruction and the application to the scalar top quark signal are described in the following chapters.

An introductory part is provided to motivate the necessity of this system. The main technical details are then discussed focusing on the most innovative ones. The R&D activity on silicon microstrip sensors is also illustrated together with a short description of the status of the construction.

4.1 Physics and Experimental Requirements

A robust tracking system played a crucial role in all accelerator experiments in the last decade and still will be a key element at LHC.

A measurement of track parameters is required by many physics studies. In particular, a precise measurement of the transverse momentum allows to reconstruct resonances and to measure invariant masses. In addition, the extrapolation of the track parameters to calorimeters and muon system helps in electron, hadron and muon identification. The precise extrapolation towards the interaction point is crucial for primary vertices reconstruction. Tracks with a large impact parameter with respect to the primary vertex can also be used to reconstruct secondary vertices and to tag jets from a $b-$quark.

The complexity of the final states at LHC and the harsh conditions where the CMS detector will operate translate in very challenging requirements for the tracking system.

First of all, the very high particle density of the LHC events requires highly segmented detectors. Particles in jets can produce hits very close in space and the pattern recognition algorithms can fail in associating them to the corresponding track. A sizeable effect on resolution of track parameters would be thus expected. Since the particle density is higher in the innermost detector layers, the granularity must increase when decreasing the radius.

Since many hits per track are needed to achieve good pattern recognition and transverse momentum resolution, a very large number of readout channels is required. On the other hand, the amount of material crossed by particles (*material budget*) should be kept as low as possible to keep secondary interactions and conversions at acceptable level in order not to spoil the tracking performance. A compromise between a large number of hits and a reasonable material budget is thus required.

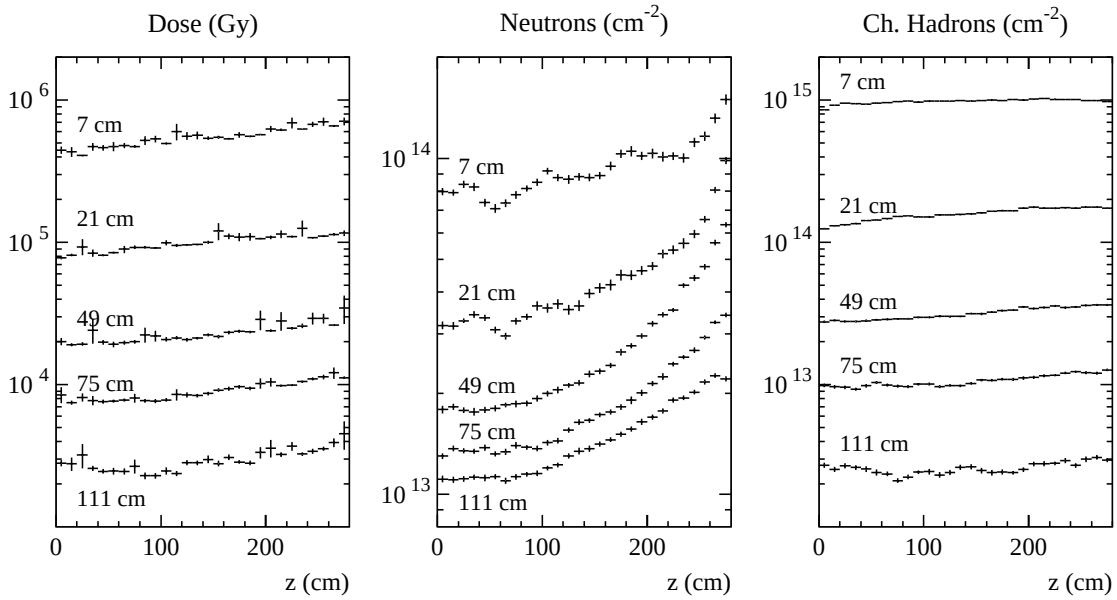

Figure 4.1: Radiation levels at selected radii in the CMS Tracker region. All values correspond to an integrated luminosity of 500 fb^{-1}.

As a consequence of the total cross section and high luminosity, the radiation levels foreseen for the tracking system will also be higher than in previous experiments. Fig. 4.1 shows radiation dose and fluence of neutrons and charged hadrons foreseen at 500 fb^{-1} integrated luminosity in different radial and longitudinal regions of the Tracker. For example, a layer of Si-strip detectors, placed at 22 cm from the interaction point, will experience a fluence of $1.6 \cdot 10^{14}$ 1-MeV-equivalent neutrons cm^{-2}. To survive in this environment, both the sensitive part of the detector and the readout electronics should be radiation resistant.

Finally, the tracker detectors must have a time resolution good enough to distinguish events belonging to different bunch crossings and the Tracker read-out electronics must fit the overall Trigger and DAQ system.

4.2 The Tracker Layout

In order to fulfill the above requirements, a Tracker completely based on silicon detectors was designed [56] [57]. Silicon detectors are very compact devices that provide an excellent position resolution ($\sim 10\mu$m) with a reasonably good time resolution ($\sim$ 10 ns). For these reasons, they have been successfully used so far as microvertex detectors. In CMS, for the first time in high energy physics, they will be used to instrument a complete Tracker. The extensive *R&D* work performed by the CMS Collaboration has made it realistic. Low cost and simpler production processes have been developed to produce a very large number of detectors (> 25000) in a reasonably short timescale (2.5 years) [75][76][77][79][78]. Automatic assembly and testing systems have been implemented to fabricate $\sim 16,000$ detector modules needed to instrument the tracking volume ($\sim 206\ m^2$ of active area) [80][81]. A careful tuning of the detector design has been performed to optimise the performance in different regions of the system.

A detailed description of the principles of operation of silicon detectors and their be-

havior under heavy irradiation is not in the scope of this work. A comprehensive review can be found in [82].

Silicon detectors are large area planar diodes based on a $n-$type substrate with p^+ implants on the surface. The entire thickness of the sensors can be fully depleted by operating the diodes in reverse bias.

A particle interacting with the silicon bulk creates electron-hole pairs. Due to the electric field perpendicular to the surface, electrons and holes drift towards the electrodes and produce signals that can be amplified. For a minimum ionising particle crossing a 300 μm thick device, $\sim$ 24000 electron-hole pairs are generated. According to the shape of the electrodes, different informations about the particle impact point position can be extracted.

In the CMS experiment, two different silicon devices are foreseen: pixel and microstrip detectors. In pixel detectors, the electrodes are shaped as small rectangles and provide a three-dimensional reconstruction of the track impact point: two informations are provided by the fired cells and the third one comes from the position of the detector itself.

In microstrip detectors, the implants are shaped as arrays of strips. A coordinate is provided by the fired strips and the other one comes again from the position of the detector. However, the three-dimensional information can be recovered by placing two detectors back-to-back with tilted strip directions. The *stereo coordinates* provide a worse resolution but the number of readout channels is much lower with respect to pixel devices.

As the other subsystems of CMS, the Tracker has a cylindrical symmetry around the beamline. The tracking volume is a cylinder of 1.1 m radius and 5.6 m in total length. Detector units are arranged in cylindrical layers around the beamline and disks in the end-cap regions. The granularity of the detectors depends on the distance from the primary interaction: in the innermost layers, the hit density is very high and a finer granularity is needed to improve the two track resolution and to allow the extrapolation to the interaction point. In the outer layers, the hit density becomes lower, while the sensitive surface increases with the distance from the beamline. A lower granularity is therefore sufficient to cope with the expected performance and compulsory to limit the number of readout channels.

Pixel detectors instrument the innermost layers, while the intermediate and outermost regions are thus instrumented with microstrip detectors with read-out pitch increasing with the distance from the beamline.

Barrel microstrip detectors are rectangular with strips parallel to the beam direction, while end-caps detectors are trapezoidal with radial strips. So barrel detectors provide the ϕ and r coordinates of the impact points, while the end-cap detectors provide the informations on ϕ and z.

In the low luminosity run, up to three cylindrical pixel layers can be placed at 4, 7 and 11 cm from the beamline and two disks in each end-cap region. The pixel detectors are moved to 7, 11 and 13 cm radial distance in the high luminosity run to cope with the higher radiation dose. The pixel rapidity coverage in this configuration extends up to $|\eta| < 2.4$. A sketch of the pixel detector is shown in Fig. 4.2. To reduce costs, it was recently envisaged the possibility of starting the data taking at low luminosity with 2 barrel layers keeping the innermost one at 4 cm radial distance, and 1 disk array for each end-cap region. The impact of this backup layout on the physics performance connected to this work is also investigated.

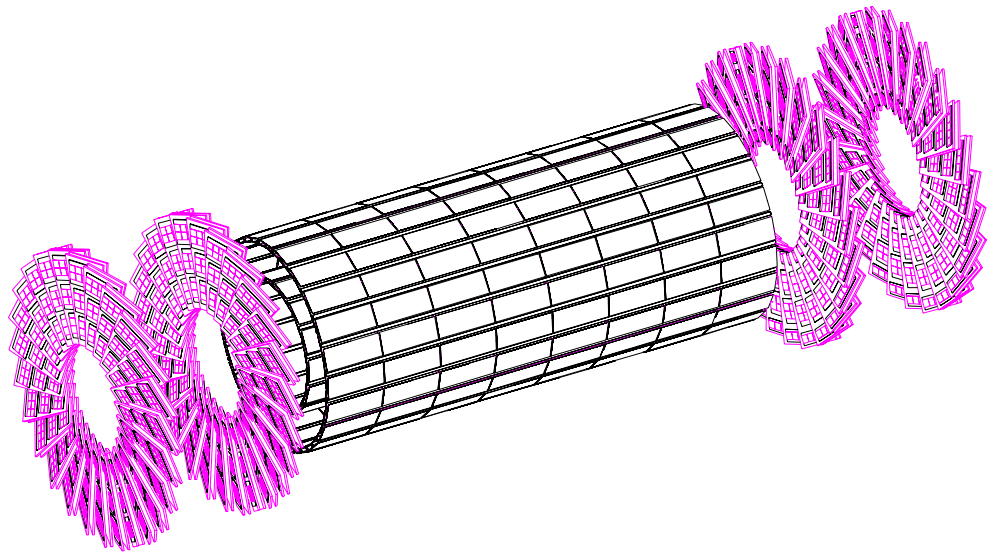

Figure 4.2: Scheme of the Pixel Detector

The Silicon-strip Tracker is divided into two parts: an inner and outer part with different types of microstrip sensors. The inner Tracker is made of 4 detector layers and 3 disks for each end-cap region. The outer Tracker has 6 layers in the barrel region and 9 disks in each end-cap. The first two layers and the first two rings of the end-cap disks in both inner and outer Trackers are double-sided to allow three-dimensional hit reconstruction. A sketch of the Si-strip Tracker is shown in Fig. 4.3. Single-sided layers are represented in blue while the double-sided ones are in red. Fig. 4.4 shows a cross sectional view of the Tracker comprehensive of the supporting structures and services.

In comparison with conventional tracking systems, the CMS Tracker provides a lower number of hits per track with a better position resolution. Sophisticated track reconstruction algorithms are being developed to perform pattern recognition with a low number of precise hits in a very dense particles environment.

Another peculiarity of such a complex device comes from the large amount of material needed to read out and service a high granularity detector. The material budget is calculated through a very detailed GEANT simulation which includes all known elements. The distribution of material budget, expressed in radiation and nuclear interaction lengths, is shown in Fig. 4.5 as a function of η for the main Tracker components (left side) and the different functions of the material (right side). The distribution of material in units of interaction lengths as a function of η is shown in Fig. 4.6 for the pixel detector (left) and the entire Tracker (right). The material budget is higher in the transition region between barrel and end-caps $|\eta| \sim 1$ due to cables and services which connect the Tracker modules to the outside systems.

4.2.1 Radiation Damage

A comprehensive review of radiation effects in semiconducting devices is outside of the scope of this work. A complete review can be found in [83]. Only the main parameters which affect the detector performance and played important role in the definition of the layout and the detector details of the silicon Tracker are here discussed.

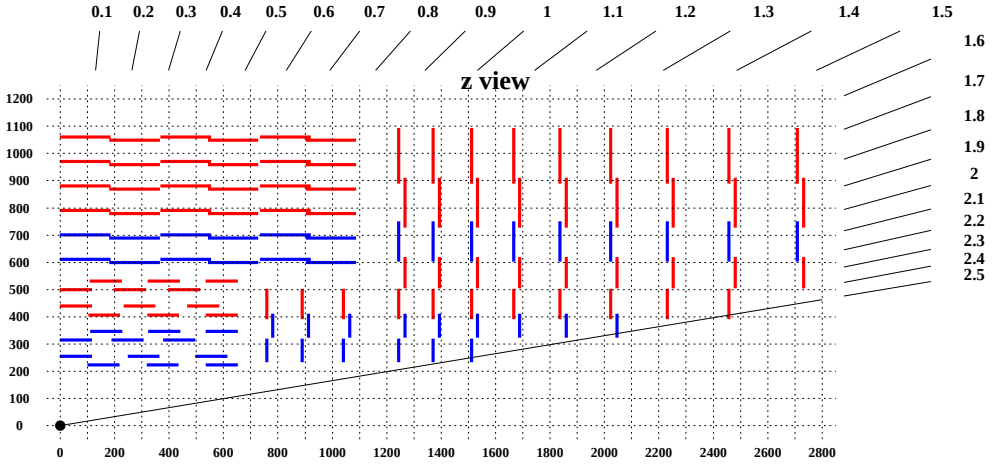

Figure 4.3: Layout of the Si-Strip Tracker in the $r - z$ view. Blue segments are associated to double side stereo layers while red segments are associated to single sided ones.

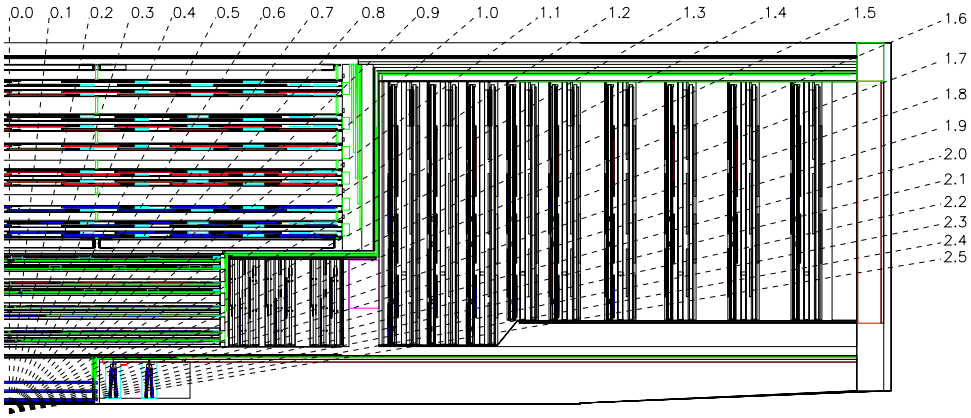

Figure 4.4: Schematic view of the Si-strip Tracker comprehensive of the supporting structures, cables and services.

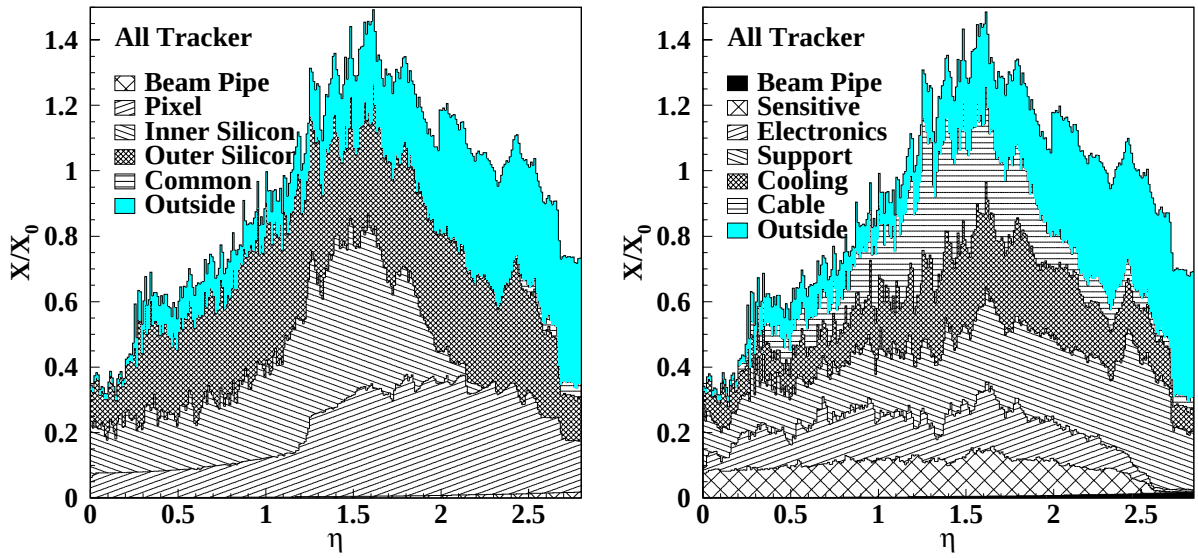

Figure 4.5: Tracker material budget in units of radiation length for the different components (left) and the different functions of the Tracker (right).

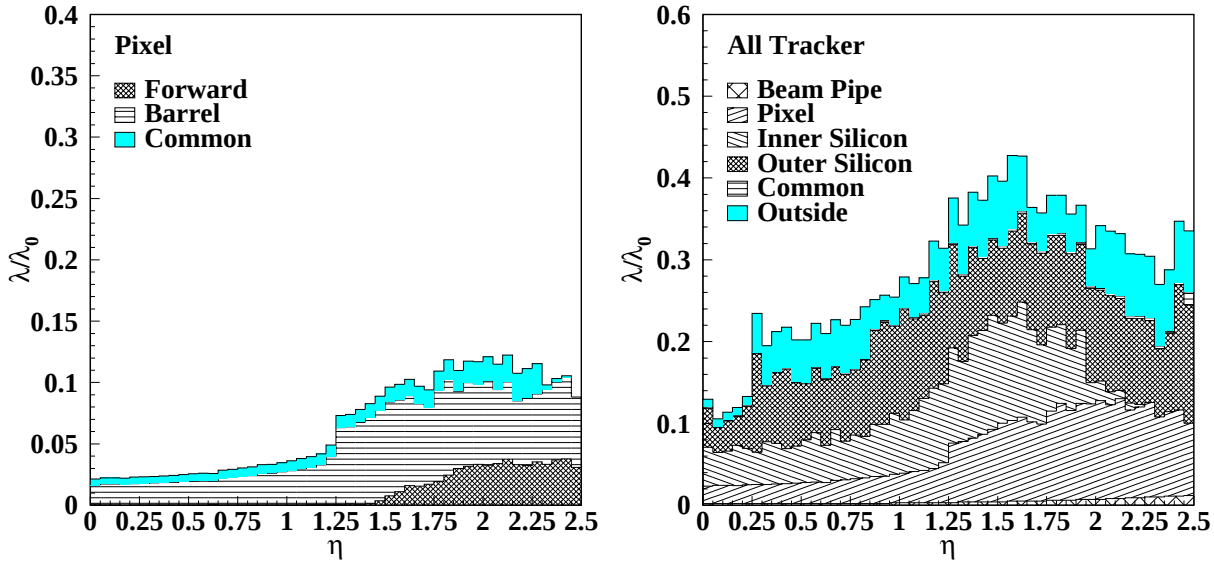

Figure 4.6: Tracker material budget in units of interaction length for the pixel detector (left side) and the overall tracker (right side).

The radiation damage effects can be classified in two main contributions: bulk and surface damage.

The bulk damage is due to defects introduced in the crystal structure: as a consequence of knock-on collisions, atoms can be displaced from their original position in the lattice. A displaced atom can move to an interstitial position and create a vacancy. If the collision is hard enough, a nuclear reaction can occur and nuclear fragments can move in the lattice and start further displacements. Defects can combine and generate very complex structures.

The experimental results show that defects act as generation centers. One of the consequences of the bulk radiation damage is the increase of current through the junction (*dark current*). The increase in dark current density ΔI_v $(A \cdot cm^{-3})$ depends on the fluence ϕ according to the relationship:

$$\Delta I_v = \alpha \cdot \Phi, \tag{4.1}$$

α being a constant. After the annealing effects, α value at 21^0C was estimated to be $\sim (2.9 \pm 0.2) \cdot 10^{-17}$ A cm^{-1} [84]. The main effect of an increase in dark current is a higher sensor noise. This effect can be reduced exploiting the strong dependence of α on temperature. For this reason, the whole Tracker will be kept at a temperature of -10^0C during operation.

The presence of defects also degrades the Charge Collection Efficiency since they can trap the charge released by the interaction and reduce the charge collected by the electrodes.

Since defects can act as acceptor centers, they also modify the effective dopant concentration N_{eff} linearly with the fluence. In particular, when the fluence reaches the value:

$$\Phi_{inv} \sim (1.8 \pm 0.6) N_{eff0}, \tag{4.2}$$

an inversion of the material type from n to p type occurs[87].

The depletion voltage is related to the dopant concentration through the relation:

$$V_{depletion} = \frac{ed^2}{2\epsilon_{Si}} N_{eff}, \tag{4.3}$$

being d the detector thickness. A variation in the effective dopant concentration also requires a change of the operating voltage during the different periods of data taking.

In the period after irradiation, the annealing behaviour of N_{eff} displays two distinct phases[85][86]: an initial reduction in negative space charge (*beneficial annealing*), which is later dominated by a slower, but much larger, increase in acceptor concentration (*reverse annealing*). The rate of increase of reverse annealing has a strong dependence on temperature and imposes strict limits on the operation temperature and the warm-up maintenance periods.

Stable defects are also responsible for the so called surface damage: charge is trapped in the junction between the Si-SiO_2 layers. The trapped charge modifies the electric field and introduce new levels in the forbidden energy band. Charge released in the interaction is shared between too many strips spoiling the signal reconstruction. Moreover, an increase of the interstrip capacitance enhances the overall electronic noise.

4.2.2 The Pixel Vertex Detector

For the first time in hadron collider experiments, CMS (and ATLAS) will use a microvertex system based on pixel detectors.

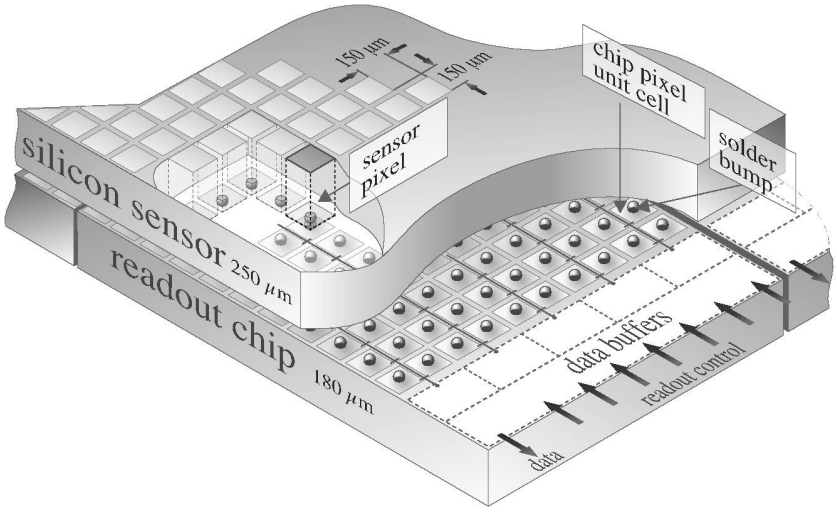

Figure 4.7: Schematic view of a pixel detector.

The scheme of a pixel detector is shown in Fig. 4.7. A pixel detector is made of a sensitive layer and a readout chip (ROC). The sensitive layer is a n-type Silicon crystal 200-300 μm thick with a continuous p^+ implant on the back and rectangular-shaped (100×150 μ m^2) n^+ implants (*pixel*) on the front surface. Each pixel is covered by a special metalisation followed by a passivation layer with a bump pad window of $\approx 13\mu$m diameter. Two p-implants with small opening at opposite side surround each pixel in order to reduce the nearest-neighbour capacitance. Each pixel is connected, through bump-bonding, to the Pixel Unit Cell (PUC) in the readout chip. Only one readout chip implementation is foreseen for all geometries of the pixel modules: each chip has 52 columns and 80 rows of PUC and can read-out 4160 pixels.

In the barrel region, the magnetic field is perpendicular to the electric field, so electrons produced in silicon by charged particles drift with a Lorentz angle of $\sim 32^0$ and the charge is collected by more than one pixel. In this way, charge sharing among different pixels can be exploited to improve the position resolution. In the end-caps, the electric field is parallel to the magnetic field. To mimic the effect of a Lorentz angle, the detector surface is tilted by 20^0 around the radial direction to distribute the charge over several pixel units.

Two different geometries are foreseen for barrel and forward detectors[88]. Barrel detectors are arranged in ladders of 8 modules of size $1.62(r-\phi)\times 6.63$(z) cm^2. Each module is read out by 16 ROC circuits. The main geometrical parameters of pixel barrel modules and half modules [1] are summarised in Table 4.1.

As shown in Fig. 4.2, the pixel forward disks have a turbine geometry to reproduce the Lorentz angle effect. The mechanical structure allows to house up to three pairs of disks. The z positions of the disks are 34.5 cm, 46.5 cm and 58.5 cm. Each disk is made of 24 blades. 7 different detector designs are foreseen to equip the blade. Each of these sensors has a rectangular surface whose dimensions are multiple of the ROC dimension in order to use the same readout circuit of the barrel modules. Each pair of disks has 48 blades, which require 48×45 readout chips, 192 readout links and 8.99×10^6 pixels.

[1] At the border of each half cylinder there are 4 half-width ladders.

Table 4.1: Main geometrical features of the barrel pixel modules[88].

	barrel 1	barrel 2	barrel 3
radius (mm)	41.05-46.46	70.16-75.55	98.88-104.26
faces in ϕ	18	30	42
detector modules/ half module	182/32	224/32	320/32
readout chips	2304	3840	5376
pixels ($\times 10^6$)	9.6	16	22.4
readout links	228	480	352

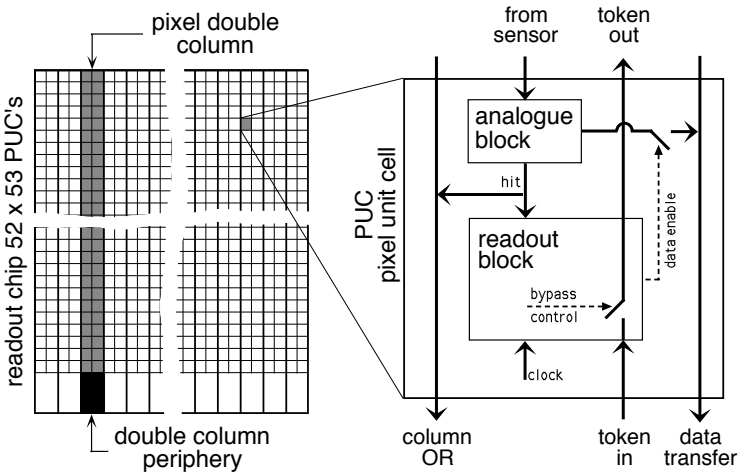

Figure 4.8: Schematic view of the pixel readout system.

The readout system [89] is sketched in Fig. 4.8. The main difficulty of the pixel readout system is to cope with the very large number of channels ($\sim 7.5 \times 10^7$); zero suppression is therefore required to reduce the huge data volume to a reasonable size. To this purpose, two nearby PUC columns are read out by one circuit placed in the periphery. Each PUC has an analog circuit which provides a logical positive output if the collected signal exceeds a given tunable threshold. Local bus lines connect the PUCs belonging to the same double column with a control circuit in the periphery. One of these lines is an OR line which provides a global OR of the combined PUC responses. The bunch crossing number is thus registered by the peripheral circuit and the pixel address and the corresponding analog signal are stored in dedicated pipelines and transmitted via optical fibers to the front end driver in the counting room in case of L1 accept. This readout mechanism needs more than 25 ns to react and introduces a dead time of two clocks. The total inefficiency due to the overall readout system is 3.6% and 0.59% for the layers at 4 and 7 cm respectively at low luminosity and L1 trigger rate of 100 MHz. These inefficiencies arise up to 12% and 3.6% at high luminosity at the same trigger rate while they go to 9% and 2.7% at a trigger rate of 30 MHz [88].

The expected resolution of pixel detectors was calculated for an older pixel layout with squared pixels 150×150 μm^2 and is 15 μm in both coordinates. Similar or better results

are expected for the final $100 \times 150\mu$ m^2 configuration.

An R&D activity has been performed in order to design pixel detector component capable to operate in high radiation environment. Most of the solutions are common with the microstrip detectors, so the discussion is reported in the next subsection.

4.2.3 The Si-Strip Tracker

Si-strip Modules and Sensors Layout

The strip sensors are organised in detector units called modules. A silicon strip module is made of one or two sensors glued on a carbon fiber mechanical support with the strips micro-bonded to an array of readout chips (APV25[74]) housed on a thin hybrid circuit. In the outer tracker modules, two sensors are glued together and daisy chained while only one sensor is used in the inner tracker modules. Typical dimensions of the outer barrel modules are 96×190 mm^2, while smaller size modules (64×120 mm^2) are used in the inner part of the detector. A sketch of the assembly of an inner barrel module is shown in Fig. 4.9.

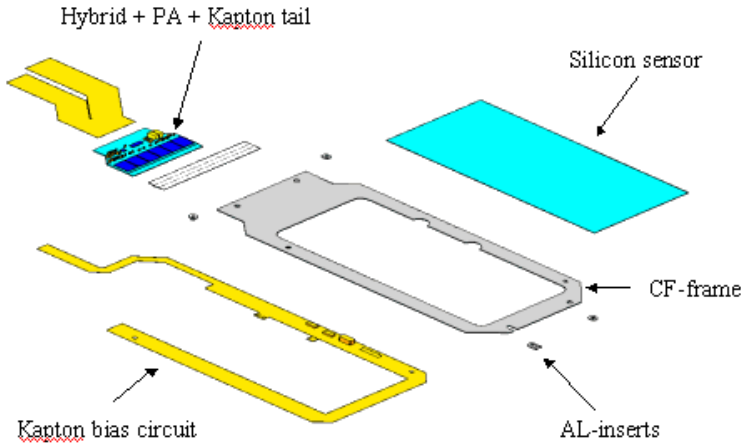

Figure 4.9: Layout of an inner barrel module.

The sensor geometry and manufacturing techniques were optimised with an R&D activity in collaboration with the main producers[76][77][79][78]. The inner barrel sensors (also called *thin sensors*) are 320 ± 20 μm thick while outer barrel sensors (also called *thick sensors*) are 500 ± 20 μm thick. The larger thickness in the latter case allows to collect a larger signal which compensates the higher noise due to longer strips. In addition, 500 μm thick sensors are produced in the 6″ commercial production lines with lower costs and shorter processing time.

A corner of a Si-strip barrel sensor is sketched in Fig. 4.10. The active area is surrounded by two p^+ implants, an inner one, the *bias ring* and an outer one, the *guard ring*. The inner ring is introduced to bias uniformly all strips through 1.5 MΩ polysilicon resistors. The outer one is introduced to limit the dark current from the sensor edges and thus improve the breakdown performance. A n^+ implant is also placed near the edge to limit the charge injection from the region damaged by the cut. On the opposite detector side (*ohmic side*), a n^+ implant connected to a thin aluminium layer covers the entire surface. A uniform

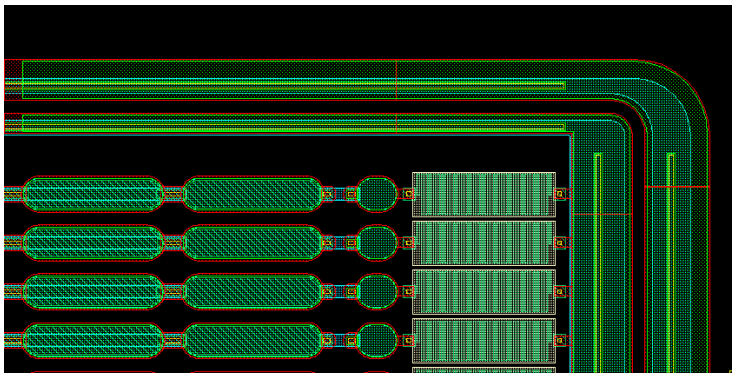

Figure 4.10: Corner of a microstrip detector sensor.

depletion of the sensor is achieved by an inverse polarisation applied to the back plane while the junction side is connected to ground.

The strip signals are decoupled from the leakage current through capacitors integrated in the substrate (see Fig. 4.11). Capacitors are made by growing thin insulating dielectric layers between the p^+ implants and the aluminium electrodes. In all sensors the aluminium strips are larger than the p^+ implants in order to improve the breakdown performance[78][90][77].

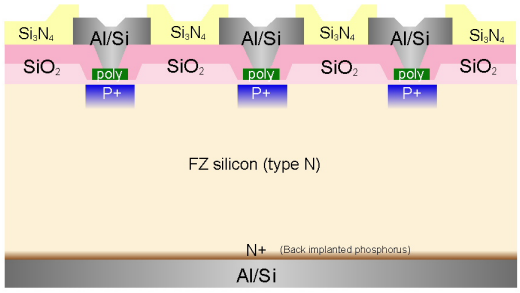

Figure 4.11: Cross section of a microstrip sensor[76].

The main geometrical features as well as the number of expected sensors are summarised in Table 4.2 for different types of sensors: IB and OB are rectangular sensors for inner and outer barrel respectively, while the W sensors are wedge-shaped sensors for the end-cap regions. Read-out pitches vary between 80 μm in the IB1 sensors and 205 μm for W6b devices. Outer barrel modules are made of two OB1 or OB2 sensors, while end-cap modules are made of W5a-W5b, W6a-W6b and W7a-W7b pairs of sensors .

Table 4.3 summarises the main geometrical features of the layers and the corresponding detector and APV multiplicities (TIB, TOB, TID and TEC correspond to inner barrel, outer barrel, inner disks and end-caps).

The total number of microstrip modules is $15,232$ ($6,136$ thin and 9096 thick ones). The total number of electronic channels is $9,648,128$, corresponding to $75,376$ APV chips. The surface covered by sensors is 206 m^2.

Table 4.2: Main geometrical features of the strip sensors[91].

type	width × length (mm×mm)	thickness (μm)	pitch (μm)	total n. of strips	total n. of sensors
IB1	63.4×119.2	300	80	768	1584
IB2	63.4×119.2	300	120	512	1224
OB1	96.4×94.5	500	122	768	5520
OB2	96.4×94.5	500	183	512	4896
W1	$64.1 - 88.1 \times 89.5$	300	81-112	768	576
W2	$88.2 - 112.4 \times 90.3$	300	113-143	768	864
W3	$65 - 83.2 \times 112.8$	300	124-158	512	880
W4	$59.9 - 82.4 \times 117.4$	300	113-139	512	1008
W5a	$99 - 112.4 \times 84$	500	126-143	768	1440
W5b	$112.4 - 123 \times 66.1$	500	143-156	768	1440
W6a	$86.1 - 97.5 \times 99$	500	163-185	512	1008
W6b	$97.5 - 107.6 \times 87.8$	500	186-205	512	1008
W7a	$74.1 - 82.9 \times 109.8$	500	140-156	512	1440
W7b	$82.9 - 90.9 \times 98.8$	500	152-172	512	1440

Readout System

A scheme of the readout electronics[93] is shown in Fig. 4.12. The capacitor pads, which collect the strip signals, are connected to one of the 128 input channels of the APV circuit placed in the front-end hybrid. To adapt the different pitches of the sensors to the fixed pitch of the read-out chip, a small circuit, the *pitch adapter*, is used. Each strip is read out by a charge sensitive amplifier with a time constant of 50 ns, whose output voltage is sampled at the beam crossing rate of 40 MHz. Analog data are then buffered in 3.2μs deep pipelines. In case of L1 accept, the pulse height signals are processed by an analogue circuit, the APSP filter. The APSP is capable to perform the deconvolution of the signal. If chips are operated in *peak* mode, the output is determined by the peak amplitude of the shaper output corresponding to the trigger. If chips are operated in *deconvolution* mode, the output is determined by the peak amplitude of the data as reshaped by the APSP, thus recovering the single crossing at the expense of an increased noise[94]. Fig.4.13 show the average amplifier pulse shape for a range of externally added capacitance values in peak and deconvolution mode. The peak mode pulse shape shows a good approximation to ideal 50 ns CR-RC pulse-shaping, while the deconvolution mode illustrates the effectiveness of this technique in achieving a pulse short enough to allow single bunch crossing resolution. Amplifiers, shapers, pipelines and APSP circuits are all integrated in the APV chip.

Pulse height data are multiplexed from pairs of APV circuits onto a differential line over a short distance to a laser driver transmitting at a wavelength of 1300 nm. Light signals are then transmitted through a 100 m single mode optical fiber to the counting room adjacent to the cavern.

The Tracker DAQ is based on a VME bus system. Pulse height data from the front-end chips, with no zero-suppression, are converted back to electrical levels matching the range

Table 4.3: Main geometrical features of the Si-strip Tracker. Layers with * have double-sided modules[92].

Layer	Avg. Radius (cm)	Modules in ϕ	Rings in z	Total Modules	APV/ det	sensor type	Total APV
TIB1*	255	56	-	336	12	IB1	4032
TIB2*	340	72	-	432	12	IB1	5184
TIB3	340	90	-	540	4	IB2	2160
TIB4	520	108	-	648	4	IB2	2592
TOB1*	608	42	-	504	8	OB2	4032
TOB2*	692	48	-	576	8	OB2	4608
TOB3	780	54	-	648	4	OB2	2592
TOB4	868	60	-	720	4	OB2	2880
TOB5	965	66	-	792	6	OB1	4752
TOB6	1080	74	-	888	6	OB1	5328
TID1*	-	24	6	144	12	W1	1782
TID2*	-	24	6	144	12	W2	1728
TID3	-	40	6	240	4	W3	960
TEC1*	-	24	6	144	12	W1	1728
TEC2*	-	24	12	288	12	W2	3456
TEC3	-	40	16	640	4	W3	2560
TEC4	-	56	18	1008	4	W4	4032
TEC5*	-	40	18	720	12	W5	8640
TEC6	-	56	18	1008	4	W6	4032
TEC7	-	80	18	1440	4	W7	5760

of a 10 bit ADC, which allows an adequate resolution over the signal range expected. The Front End Driver (FED) digitises the data, performs signal processing including reordering and pedestal subtraction and stores data in a local memory until required by higher level data acquisition. In high luminosity conditions and maximum trigger rate, cluster finding reduces the data volume to be transmitted.

The system is monitored by a VMEbus module, the Front End Controller (FEC). The FEC acts also as interface with the global Timing Trigger and Command (TTC), which distributes the LHC machine master clock and Trigger. The clocks and triggers are transmitted from the FEC to the front-end hybrids through optical cables and distributed to a series of detector modules by Communication and Control Unit (CCU). The clock signals are locally recovered by Phase Locked Loop (PLL) chips on each module to ensure high reliability and minimum phase jitter.

In the design of the CMS readout system, data are kept analog as long as possible to reduce the complexity of the front-end chip, reduce the power dissipation within the Tracker volume and achieve a better position resolution through charge sharing between detector strips, having data available as unaltered as possible all the way to the counting room. In this way, the algorithms can be easily and inexpensively modified through programmable circuits in FED.

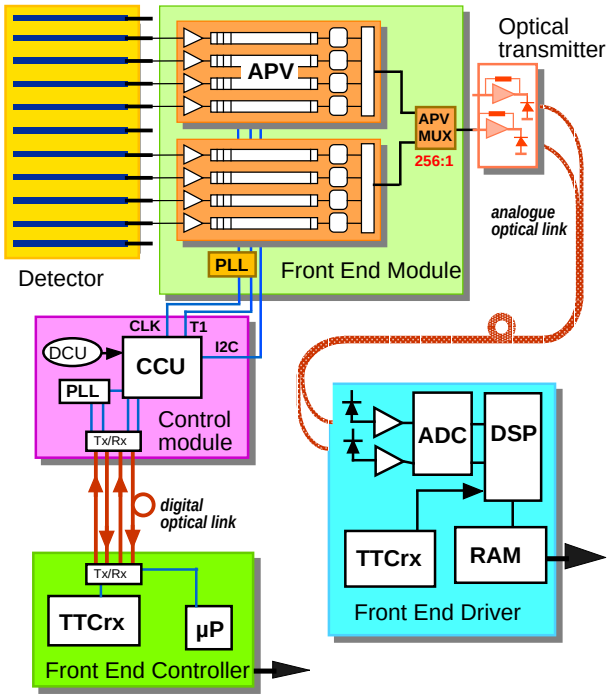

Figure 4.12: Scheme of the readout system for the Si-strip Tracker.

Expected Performance

The performance of front-end electronics coupled to silicon detectors is related to the characteristic impedances of the sensors and the main geometrical parameters.

The channel noise is one of the main performance parameters. The main sources of noise are the thermal noise due to strip and metal resistance (R_s), the amplifier noise, the shot noise due to the reverse bias current (I_b) and the thermal noise of the bias resistance (R_s). The noise sources are independent and therefore the total noise is obtained by summing in quadrature all contributions. Table 4.4 shows the analytical formulas for the main noise contributions and the multiplicative factors needed to account for the deconvolution process. The noise due to front-end electronics, which is added in series and it is independent on the temperature, is shown in Table 4.5 for different types of chips used in these

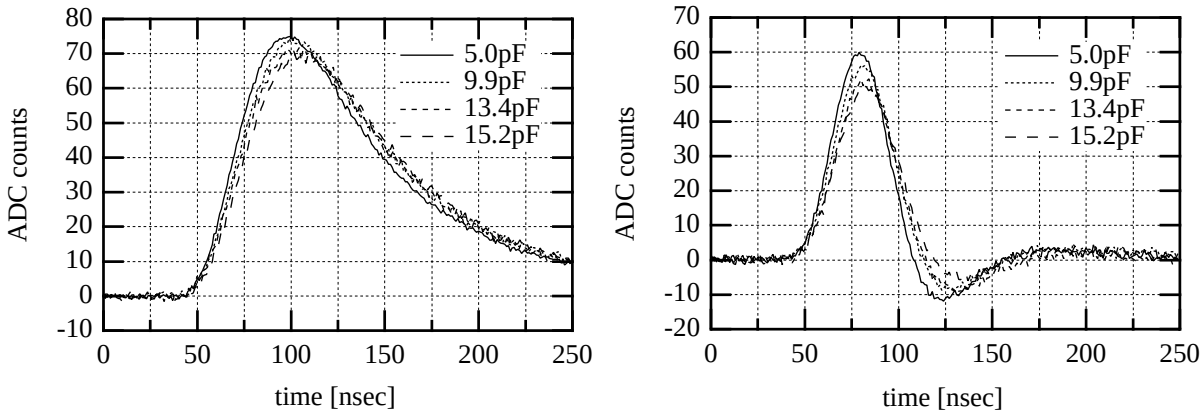

Figure 4.13: Analog pulse shape in peak (left) and deconvolution (right) mode[56].

studies.

Table 4.4: Noise sources, types and ENC evaluation formulas. e is the Neper constant, q_e the electron charge, τ the shaping time and C_{tot} the total capacitive load[56].

Noise Source	type	ENC (e^-)	ENC (e^-) @$T = -10^0 C$	deconvolution
Reverse bias current (I_b)	parallel	$\frac{e}{q_e}\sqrt{\frac{q_e \tau I_b}{4}}$	$\approx 108\sqrt{I_b(\mu A)\tau(ns)}$	$\times 0.45$
Polarisation Resistor (R_p)	parallel	$\frac{e}{q_e}\sqrt{\frac{kT\tau}{2R_p}}$	$\approx 22.5\sqrt{\frac{\tau(ns)}{R_p(M\Omega)}}$	$\times 0.45$
Metal Strip Resistance (R_s)	series	$\frac{e}{q_e}C_{tot}\sqrt{\frac{kTR_s}{6\tau}}$	$\approx 13 C_{tot}(pF)\cdot \sqrt{R_s(\Omega)}\tau(ns)$	$\times 1.45$

Table 4.5: ENC evaluation formulas for electronics noise in different chips in peak and deconvolution mode.

Chip	ENC (e^-) in peak	ENC (e^-) in dec.
PREMUX-128	$558 + 41.5 C_{tot}$	-
APV6	$510 + 36 C_{tot}$	$10^3 + 46 C_{tot}$
APV25	$250 + 36 C_{tot}$	$400 + 60 C_{tot}$

The total noise is dominated by the front-end electronics contribution which is proportional to the total capacitance seen by the amplifier. The total capacitance depends on the sensor geometry. Several studies were performed to optimise the sensor geometry in order to keep the total capacitance as low as possible [57][79][78]. The total strip capacitance, C_{tot}, is evaluated by adding the backplane capacitance, C_{back} and the interstrip-capacitance (C_{int}):

$$C_{tot} = C_{back} + C_{int}. \tag{4.4}$$

According to [95], both backplane and interstrip capacitances depend on strip pitch (p), strip width (w) and thickness d through the geometrical parameter $p/(d + p * f(w/p))$ being f an approximate universal function. Fig. 4.14 shows the measured interstrip, total and backplane capacitance at fixed $w/p = 0.15$ and different thickness as a function of $p/(d+p*f(w/p))$. The backplane capacitance decreases with the thickness while interstrip capacitance increases with it. The total capacitance is approximately independent from the thickness (if $p \ll d$), and depends on the w/p ratio through the relationship[57]:

$$C_{tot}(pF/cm) = 0.8 + 1.7\frac{w}{p}. \tag{4.5}$$

The signal to noise ratio decreases with w/p and is above 12 for $w/p < 0.2$. On the other hand, the high voltage performance is spoiled for a w/p below 0.2 because the

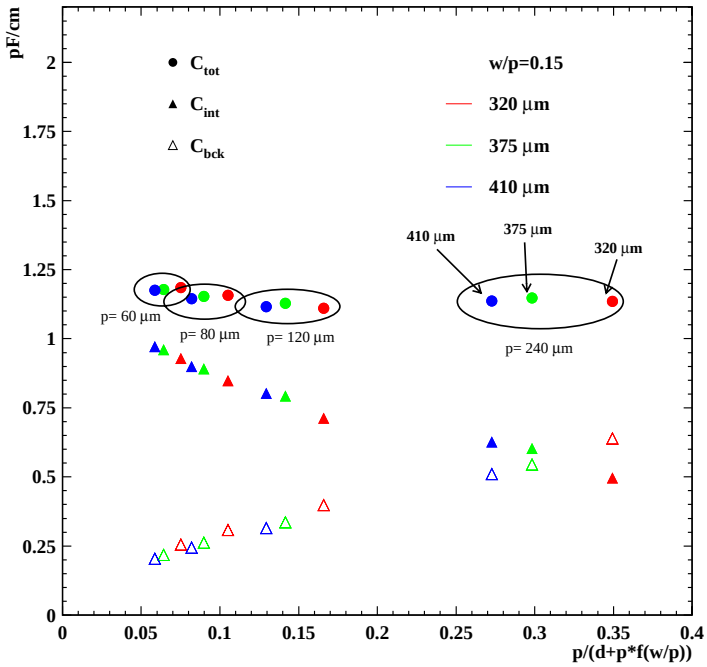

Figure 4.14: Backplane (C_{bck}), interstrip (C_{int}) and total capacitance (C_{tot}) per unit of length for 6″ not irradiated devices for different thickness (d) and the same w/p ratio as a function of $p/(d + p * f(w/p))$[57].

field lines would become denser near the strips[78]. Therefore, an optimised $w/p \sim 0.25$, corresponding to a total strip capacitance of $C_{tot} = 1.2$ pF/cm, was chosen for both thin and thick sensors.

The spatial resolution depends on the electrical and geometrical parameters through the relationship:

$$\sigma = p\sqrt{\left(\frac{1}{\sqrt{12}}\right)^2 + \left(\frac{\sigma_n}{\langle Q \rangle}\right)^2} \tag{4.6}$$

where σ_n the rms of the total noise and $\langle Q \rangle$ the average collected signal charge and p the detector pitch. The first contribution is geometrical and corresponds to the rms of the particle impact point position and the second one depends on the noise[96]. The expected resolutions are in the range of 20-30 μm for the inner detectors and 30-50 μm for the outer ones.

Radiation Hardening

Several strategies have been adopted to define a detector design and a processing technology which would allow good performance after 500 fb^{-1} integrated luminosity.

The increase in dark current can be controlled by lowering the operating temperature during data taking. It is worth noticing that a low temperature operation of the Tracker is compulsory to avoid any thermal runaway of the detector modules and to freeze all

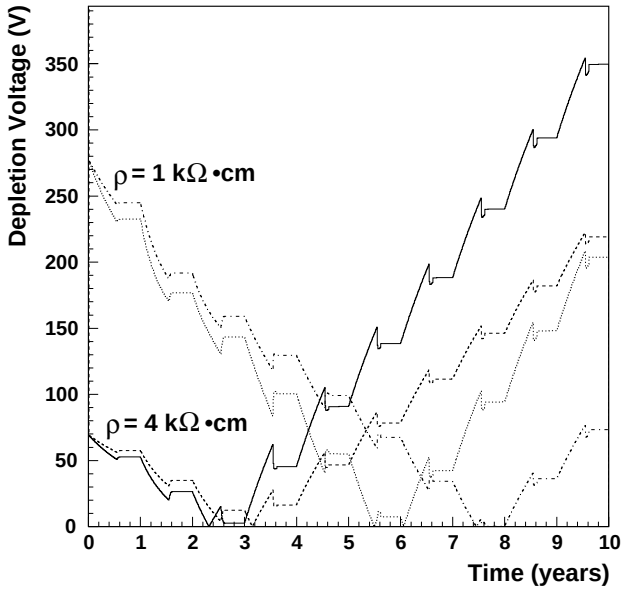

Figure 4.15: Predicted evolution of the depletion voltage with time for barrel layer 1 and two different initial resistivities. The pessimistic scenario is also shown for each initial bulk resistivity.

mechanisms of reverse annealing in damaged silicon. For these reasons, the whole Tracker will be cooled down and operated at -10^0C, corresponding to an α value $\sim (1.4 \pm 0.2) \times 10^{-18}$.

The variation in the effective dopant concentration is compensated by a change of the operating voltage during different periods of data taking which would be made possible by the use of high breakdown devices ($V_{bd} > 500$ V). Additional safety margins can be achieved with the choice of a lower bulk resistivity. The expected temporal evolution of the depletion voltage is shown in Fig. 4.15 for detectors with a standard resistivity (4 kΩcm) and low resistivity (1 kΩ cm). For each resistivity, the lower curves correspond to the expected fluence while the upper ones to a more pessimistic scenario with $\Phi \sim 2.4 \cdot 10^{14}$ (1.5 safety factor). A low resistivity implies an higher bias voltage at the beginning of operation ($V \sim 300$ V). On the other hand, the substrate inversion would occur later and the required operating voltage after 10 years of running would be lower.

The surface effects are reduced by the choice of $\langle 100 \rangle$ crystal lattice orientation, instead of the commonly used $\langle 111 \rangle$, and by overdepleting the junction during operation. It was found [78] that, depending on the strip geometry, the measurement frequency and the bias voltage, the interstrip capacitance increases up to 40% for $\langle 111 \rangle$ sensors while it remains unchanged in $\langle 100 \rangle$ ones.

Finally, by operating the sensors at a very high bias voltage some increase in charge collection efficiency is also achievable[97].

4.3 Detector Performance

An extended R&D activity has been performed by the CMS Collaboration to investigate the performance of the detectors designed for the Tracker and to study the impact of design modifications to performance. In the following, only the results of the tests which

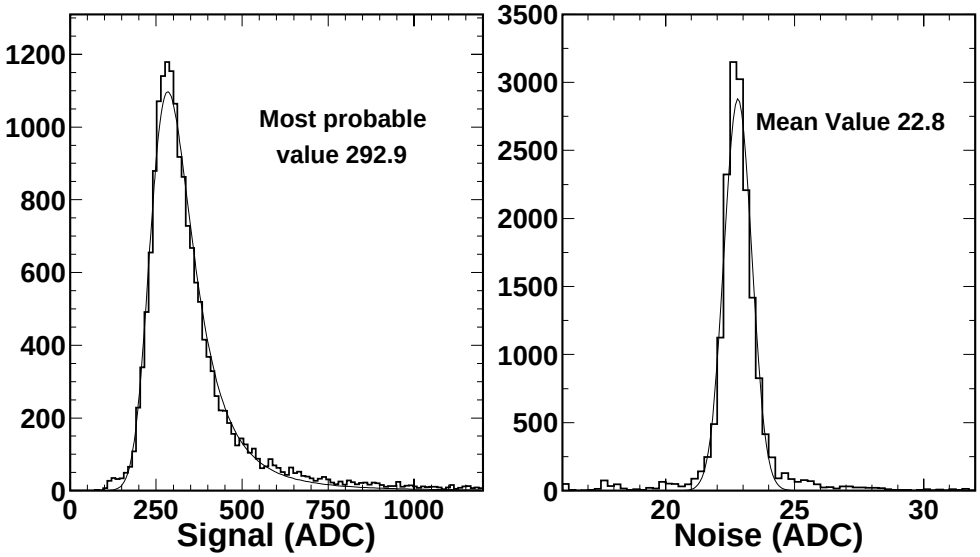

Figure 4.16: Signal and Noise distributions in ADC units at bias voltage 450 V for an irradiated ($\Phi = 3.2 \times 10^{14}$ p/cm^2) module [98].

I contributed directly to either organise, run or analyse are reported.

The performance has been studied with laboratory measurements and tests under minimum-ionising particles beams to optimise detector design and setup.

4.3.1 Performance of Inner Barrel Detectors

The performance of irradiated inner barrel detectors were evaluated with beam of particles at CERN (X5 and T9 test beam facilities) in June 1999 with 120 GeV/c muons and 8 GeV/c pions[98]. Detectors were produced by CSEM (Neuchatel, Switzerland) with $\langle 111 \rangle$ lattice orientation and 4-10 kΩcm bulk resistivity.

32 sensors were uniformly irradiated at CERN with 24 GeV/c protons to a fluence of 3.2×10^{14} p/cm^2, which is equivalent to 10 years of LHC running. They were biased at 150 V during irradiation and kept at a temperature of -10^0C. No annealing was performed and sensors were kept at -25^0C after irradiation.

16 modules were assembled with these sensors and read out with an ancestor of the APV chip (PREMUX[99] with a shaping time of 45 ns). A module was prepared with non irradiated sensors for comparison. Modules were placed in a climatic chamber able to accomodate up to 6 detectors; the temperature during data taking ranged from 0^0C to -40^0C. The chamber was placed in the middle of a telescope system made of standard silicon detectors for tracking purposes and two fast scintillators for triggering in coincidence.

The signal and noise distributions are shown in Fig. 4.16 for an irradiated module at 450 V bias voltage. The average noise as well as the signal to noise ratio are shown in Fig. 4.17 as a function of $V_{bias}/V_{depletion}$ for irradiated and non irradiated detectors.

For the non irradiated module, the noise is approximately constant. In the irradiated one, the noise is 10% higher due to radiation damage: the noise decreases with $V_{bias}/V_{depletion}$ down to a minimum corresponding to a bias voltage 1.6 times higher than the depletion voltage. After this minimum the noise increases due to dark current. The sig-

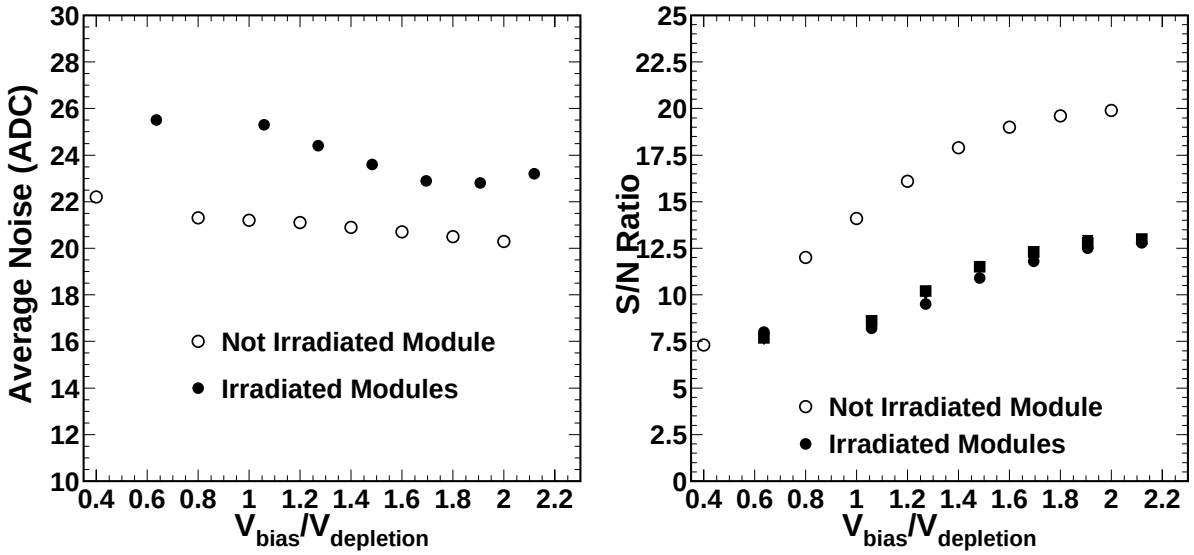

Figure 4.17: Noise (left side) and Signal to Noise ratio (right side) for an irradiated and a not irradiated module for different bias voltage[98].

nal to noise ratio tends to an asymptotic value of 20 for the non irradiated module and 12.5 for the irradiated one. The plateau is reached when the junction is already overdepleted.

The tracking performance was evaluated in terms of position resolution and hit finding efficiency. Track reconstruction was performed through the telescope using the Newton algorithm[100]. Track segments were interpolated to the detector layers and the residual distributions were fitted with gaussian function to extract the resolution. For the non irradiated and irradiated modules the measured resolution was 13.6 μm and 16.8 μm respectively. Therefore, the spatial resolution is not dramatically spoiled by radiation damage.

Hit finding efficiency is shown in Fig. 4.18 as a function of $V_{bias}/V_{depletion}$: it is 99% for the reference module while it is 80% at $V_{bias} = V_{depletion}$ and increases up to 95% for $V_{bias} > 1.5V_{depletion}$ which is considered the standard operating condition in the experiment.

Recent results obtained with final inner barrel detector modules read-out by APV25 chips are consistent with these preliminary measurements. Some of these results are shown in the last section.

4.3.2 Performance of Outer Barrel Detectors

Detectors with thick sensors were tested for the first time in June 2000 at the CERN X5 beam facility [101][102]. Sensors with 122 μm pitch were used for this test.

Irradiation was performed with neutron beam of 20 MeV at Louvain-la-Neuve (Belgium). The received dose corresponds to $\sim 1.6 \times 10^{13}$ 1 MeV equivalent neutrons. The sensors were biased at 150 V and kept at -10^0C during irradiation and at -25^0C after irradiation to prevent annealing effects. Depletion voltage after irradiation is lower than 50 V.

Two modules with thick sensors were constructed: one with non-irradiated and one with and irradiated sensor. APV6 chips (a precedent approach to the final APV25 chip) were used for readout in peak as well as in deconvolution mode. A 120 GeV/c pion beam

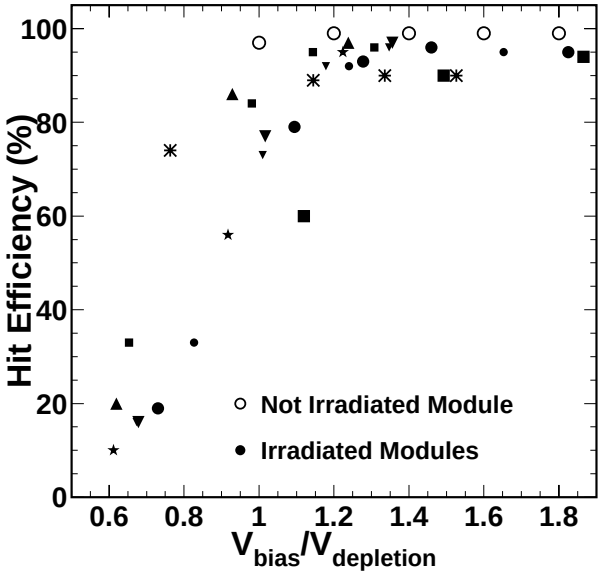

Figure 4.18: Hit finding efficiency for the not irradiated module and the irradiated ones for different bias voltage[98].

with a bunch spacing of 25 ns (LHC like environment) was used for the tests with a DAQ system very close to the final one.

Asymptotic values of signal and S/N are reported in tab.4.6.

Table 4.6: Measured values of signal and S/N ratio in peak and deconvolution mode for 300 μm reference, 500 μm non-irradiated and irradiated modules.

Module	Peak Mode		Deconvolution	
	Signal (ADC)	S/N	Signal (ADC)	S/N
300 μm	36	20	29	11
500 μm	58	45	49	23
500 μm (irradiated)	55	39	45	20

The scaling of S/N with thickness was confirmed for the first time in this test:

$$\frac{(S/N)_{thick}}{(S/N)_{thin}} \sim \frac{500\mu\text{m}}{300\mu\text{m}} \sim 1.6. \tag{4.7}$$

This relationship holds even after irradiation. The asymptotic S/N value in deconvolution mode (23) is consistent with the expected value of 14 foreseen for the outer barrel modules (19 cm long).

Recent tests on full-size sensors coupled to the final read-out electronics (APV25) are shown in the last section and confirm these preliminary expectations.

4.4 Status of Tracker Construction

The production of module components (electronics, sensors, hybrids and frames) is currently under way.

The components are produced by industries and qualified in dedicated test centers. Components fulfilling some basic selection requirements are then assembled together in dedicated laboratories and test centers. Careful tests are performed at each step of assembly and integration. The main procedures are: sensor quality assurance, module assembly, bonding and testing, sub-detector assembly and final Tracker assembly. Due to the large number of components, most of the testing and assembly procedures are performed automatically using dedicated devices.

4.4.1 Sensors Qualification

Sensors are qualified according to their electrical and mechanical properties. The main specifications for the sensors are summarised below[91]:

- depletion voltage: $V_{depl} < 300$ V
- breakdown voltage: $V_{bd} > 500$ V
- thickness: $d = 320 \pm 20$ μm and $d = 500 \pm 20$ μm for thin and thick sensors respectively
- bulk resisitivity: $\varrho = 1.5 - 3$ $k\Omega$ and $\varrho = 3.5 - 7.5$ $k\Omega$ for thin and thick sensors respectively.
- total leakage current: $I_{leak} < 10\mu$A@300 V, 20μA@450 V

The requirements on the single strips are:

- resistance with bias ring: $R_{poly} = 1.5 \pm 0.5$ MΩ
- total capacitance: $C_{tot} \leq 1.3$ pF/cm at depletion
- coupling capacitance: $C_{AC} \geq 1.2$ pF/cm per μm of implanted strip width
- $\Delta I_{leak}/\Delta V < 100$ nA/V in the range 450-550
- current through the dielectric: $I_{diel} < 1$ nA @ 10 V
- strip failure below 3%: fraction of strips with high current lower than 2% and fraction of defective strips lower than 1%.

Strip failure can be due to high noise or defective strips. Strips are defective if R_{poly} is out of range or the leakage current $I_{strip} > 100$ nA @ $V_{bias} = 400$ V or there are implant and metal shorts or pinholes in the dielectric layer between metal and implant.

Strips are noisy if their Gaussian noise at V_{depl} is 30% larger than the median Gaussian noise of the other strips of the sensor. Strips are also considered noisy if their Gaussian noise increases of more than 30% when the bias voltage is increased from V_{depl} to 1.5 V_{depl} for a maximum of 400 V.

Tests are performed with automatic test stations: a pneumatic arm permits the automatic loading and unloading of the sensor from the storage cassette to a chuck. The automatic alignment of the sensors with the probe card is performed through a pattern recognition system using microscope and video-camera. Electrical parameters are then measured and recorded for further analysis.

4.4.2 Modules Qualification

The main tests foreseen on modules are summarised below [81]:

- leakage current as a function of the bias voltage
- pedestal and noise before and after common mode subtraction
- APV gain, linearity, shaping and multiplexing with internal calibration signal
- detection of unbonded strips through pulses on the backplane via an AC coupling on the HV line
- response of the silicon to a LED and laser signal to detect defective channels
- performance of the APV pipelines
- check if the PLL chip fails in sending the proper trigger and clock signals.

Each test center has a setup to perform tests on modules with a readout system very close to the final one[103]. The main difference is that the optical link connecting the front-end hybrid with the FED is replaced by a copper connection. A special card is introduced to drive the output of the hybrid to the FED through a short cable. The card also provides the power supply to the hybrid and the interconnectivity which is necessary to bring the control signals.

4.4.3 Milestone 200 and Start-up of the Final Production

A preliminary production of 200 modules has been organised to verify the production procedures, to train the assembly centers and optimise the final hybrid technology.

The total number of 200 modules is composed of 80 outer barrel, 80 end-cap and 40 inner barrel modules. Sensors are produced by STMicroelectronics, Hamamatsu and CSEM respectively. For this pre-production, the inner barrel modules are made of two daisy-chained half-size sensors obtained from 4″ wafers. Three kinds of hybrid substrates have been used for this production: standard ceramic, FR4 and a new kapton-carbon fibre laminate which incorporates also the cable connecting the hybrid to the ancillary electronics. The latest seems to be the most promising choice although a complete evaluation of the different solutions is still going on.

All sensors of the Milestone have been tested following the qualification procedure described above. Apart from minor defects, all the basic requirements are fulfilled.

The official date for the start-up of the final module production is November 2002. Most of the needed components are already in production, in particular STMicroelectronics and Hamamatsu are producing large series of thick and thin sensors respectively. CF frames

and pitch adapters are in delivery. APV and ancillary chips have already been produced and tested. The formal procedure for ordering read-out hybrids is under way.

Fig. 4.19 illustrates the CV and IV curves for a set of OB2 sensors of the final production delivered by STMicroelectronics: the depletion voltage is always within the range and the IV profile is very similar for all sensors of the batch.

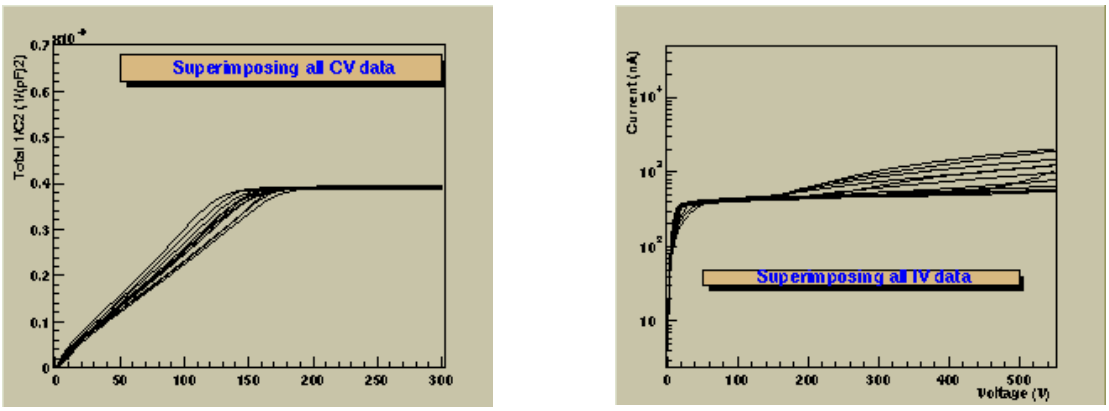

Figure 4.19: CV (left) and IV curves (right) for a set of OB2 sensors of the final production.

The left plot of Fig. 4.20 shows the leakage current at 450 V: the average current is about $I(450\ V) \sim 1 - 2\ \mu$A which is a good value for large area sensors.

The right distribution of Fig. 4.20 shows the total sensor coupling capacitance: this distribution is concentrated around 1550-1600 pF and both the central value and the spread are within specifications.

The depletion voltage of the sensors of the batch is shown in Fig. 4.21 and is again within specifications and is compatible with the required bulk resistivity.

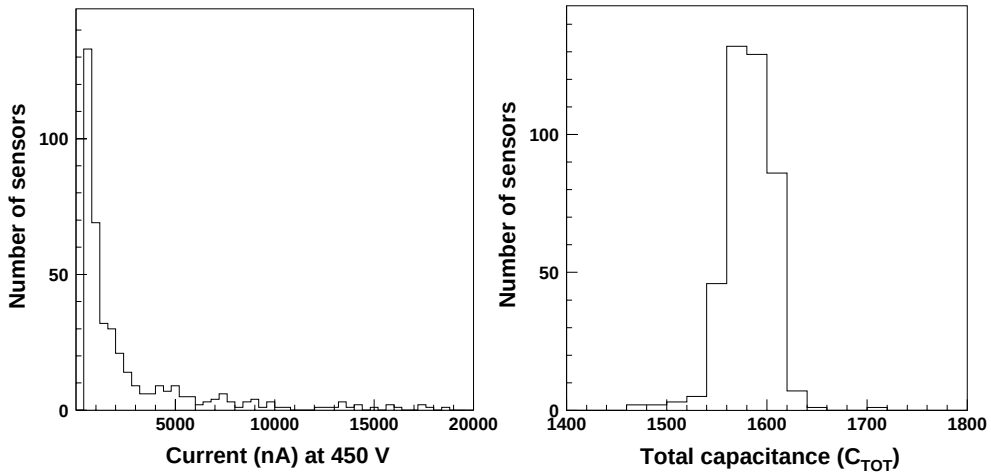

Figure 4.20: Leakage current at 450 V (left) and total sensor capacitance (right) for a set of OB2 sensors of the final production.

The total number of leaky strips, bad polysilicon resistors, bad AC capacitors and strips with a too high current through the dielectric are shown in Fig. 4.22 and Fig. 4.23 respectively: all distributions are peaked at 0 and have small tails in the region of rejection. The fraction of rejected sensors is very small: this good yield qualifies the sensor design

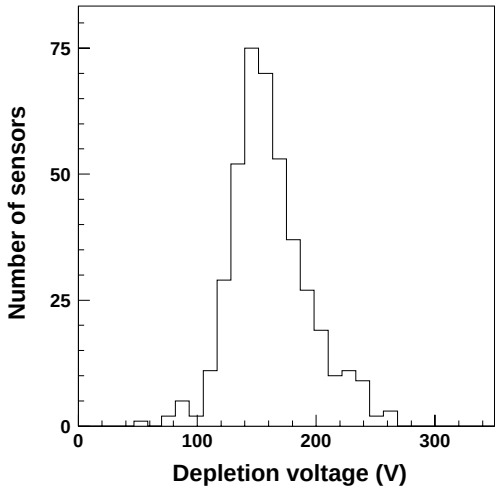

Figure 4.21: Depletion Voltage for a set of OB2 sensors of the final production.

and the production process. The thin sensors yield produced by Hamamatsu is even higher than the thick detectors one.

The assembly procedures for the different modules geometry have been successfully tested. Figures 4.24, 4.25 and 4.26 show photos of TIB, TOB and TEC modules.

Some results of the standard testing procedures used for the TIB modules qualification are shown in figures 4.27, 4.28, 4.29 and 4.30. Figures 4.27 and 4.28 show the calibration signal as a function of the latency as it is read-out for all channels of the four APV chips of the module superimposed in peak and deconvolution mode.

Figures 4.29 and 4.30 show the strip noise as a function of the strip number at a bias voltage of 300 V in peak and deconvolution mode respectively. Unbonded stribs appear as noisy strips due to a feature of the readout system.

Very recently 12 modules of TIB, TOB and TEC types, assembled for the Milestone 200, were exposed in a 350 MeV/c pion beam at PSI.

Fig. 4.31 shows the noise for a TIB, a TOB and a TEC module: the noise is in agreement with expectations and weakly depends on geometry. Signals are shown in Fig. 4.32 for all the modules under test. As already shown for the first prototypes, the signal scales with the sensor thickness.

Fig. 4.33 shows a typical event as it is seen by the whole array of detectors: the strip signal after pedestal and common mode subtraction is shown as a function of the strip number. The signals corresponding to the passage of two particles are clearly visible.

Since the performance of these pre-production modules are already within the acceptance criteria fixed for the final production, the results of this test beam are considered very encouraging.

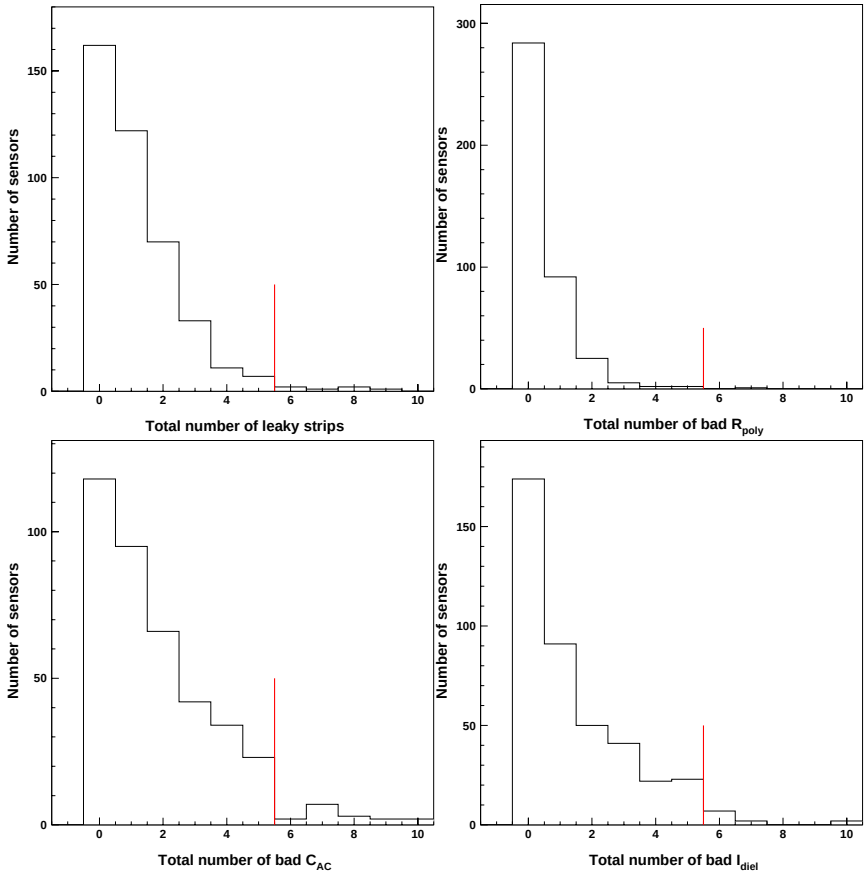

Figure 4.22: Total number of leaky strips (upper left), bad polysilicon resistors (upper right), bad coupling capacitances (lower left) and strips with a too high I_{diel} (lower right) for OB2 sensors of the final production.

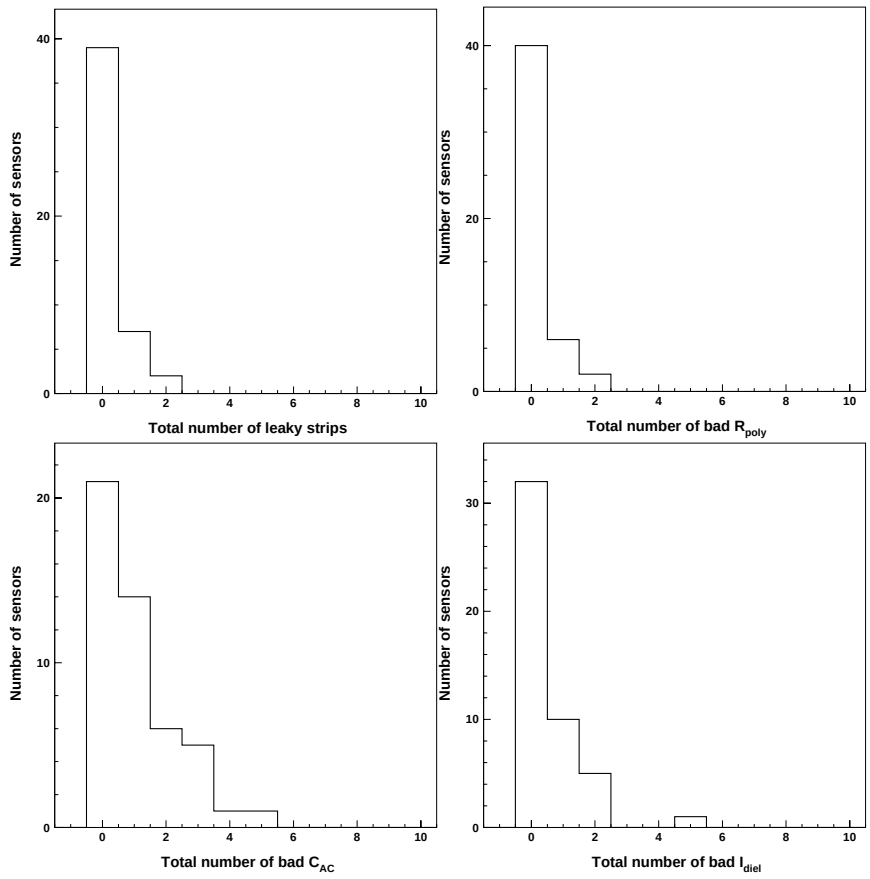

Figure 4.23: Total number leaky strips (upper left), bad polysilicon resistors (upper right), bad coupling capacitances (lower left) and strips with a too high I_{diel} (lower right) for IB1 sensors of the final production.

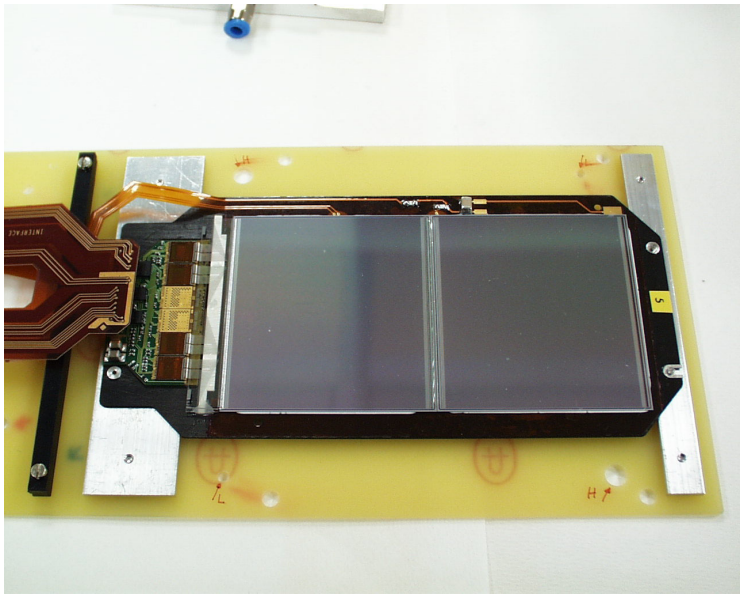

Figure 4.24: Inner barrel module.

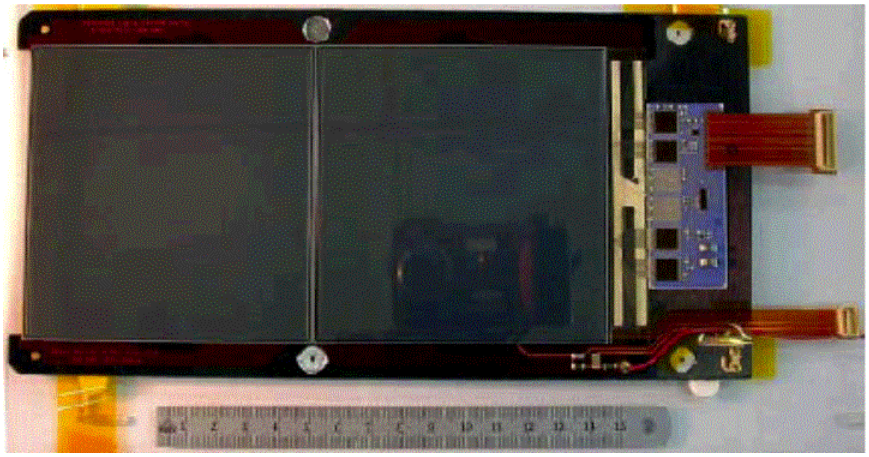

Figure 4.25: Outer barrel module.

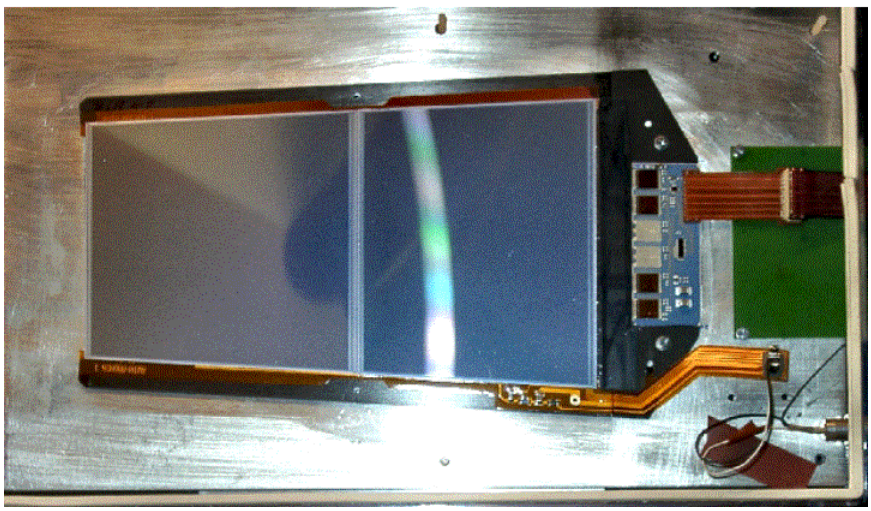

Figure 4.26: End-cap barrel module.

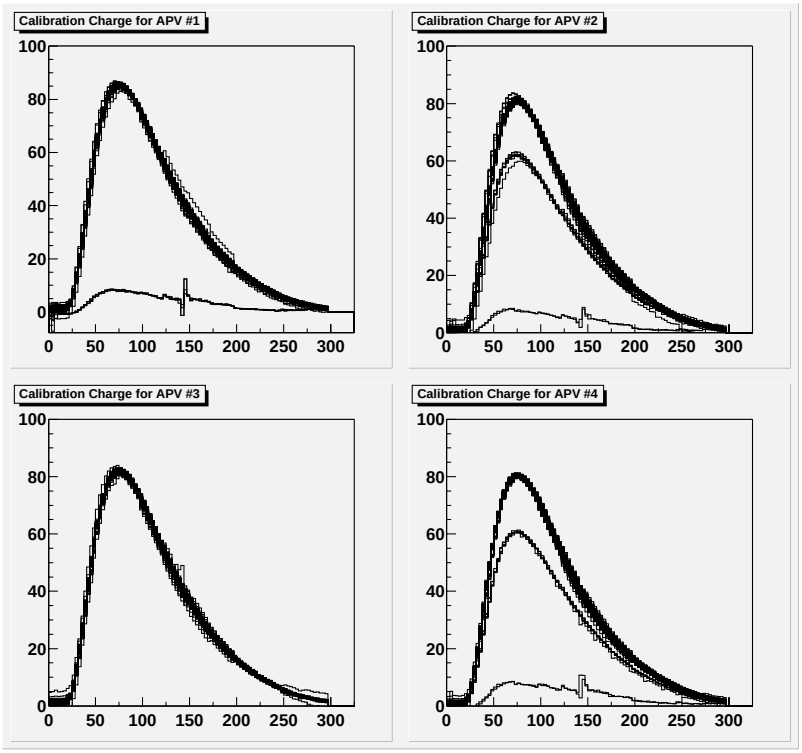

Figure 4.27: Calibration curves for the electronics channels of the APV chips of a TIB module in peak mode.

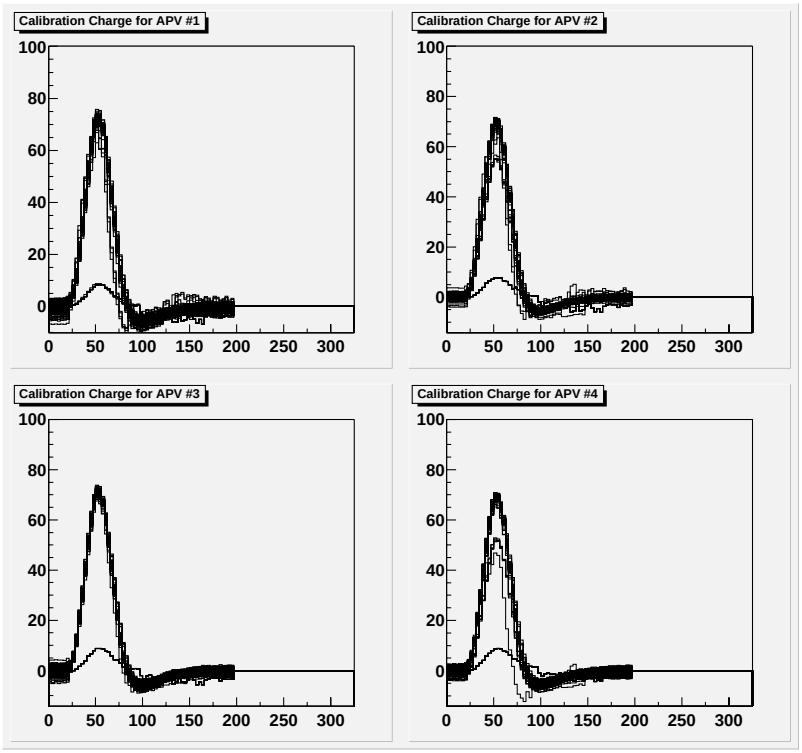

Figure 4.28: Calibration curves for the electronics of the APV chips of a TIB module in deconvolution mode.

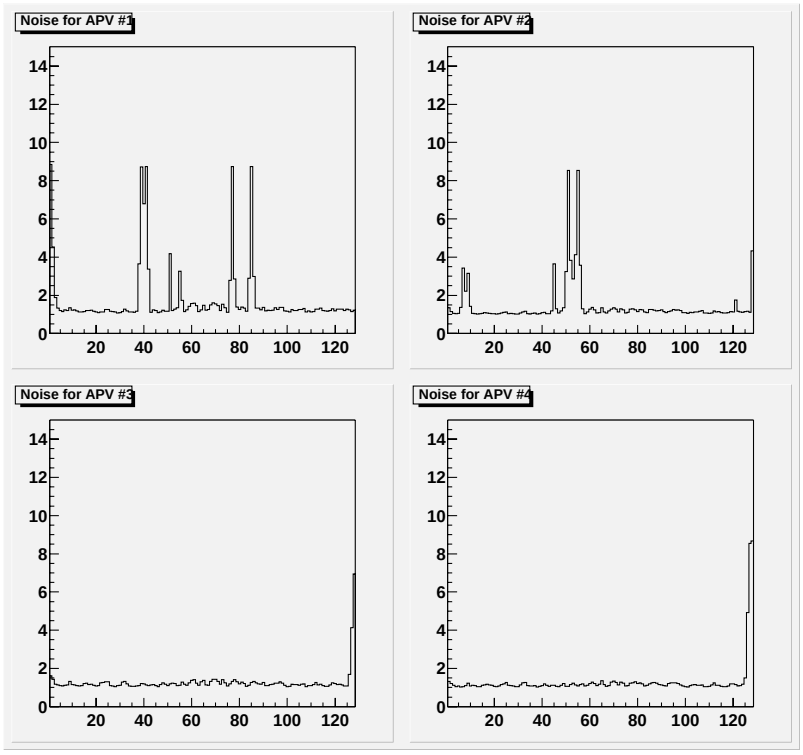

Figure 4.29: Noise (common mode subtracted) as a function of the strip position the APV chips of a TIB module in peak mode.

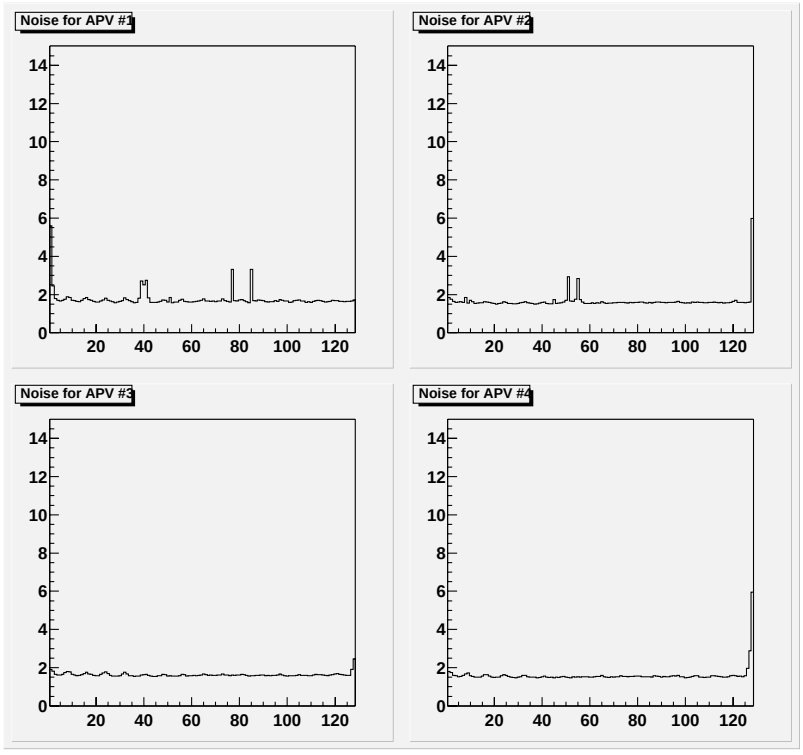

Figure 4.30: Noise (common mode subtracted) as a function of the strip position of the APV chips of a TIB module in deconvolution mode.

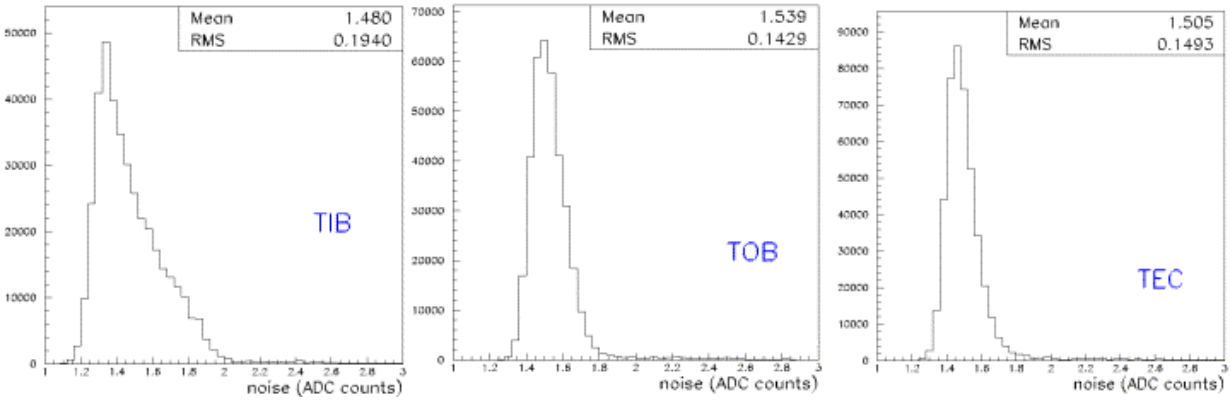

Figure 4.31: Noise of a TIB (left), TOB (center) and TEC module (right).

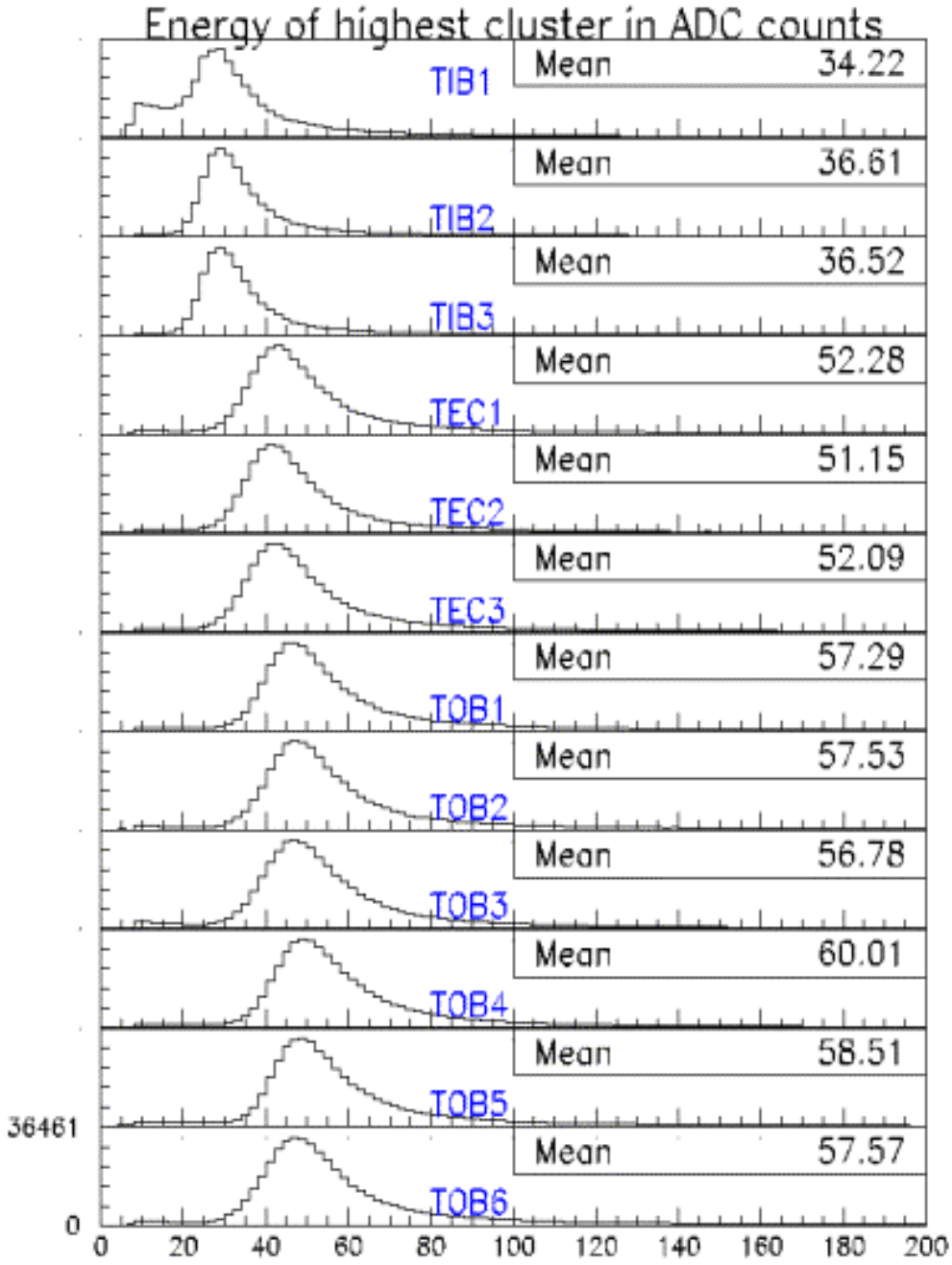

Figure 4.32: Signal of TIB, TOB and TEC modules at the PSI test-beam.

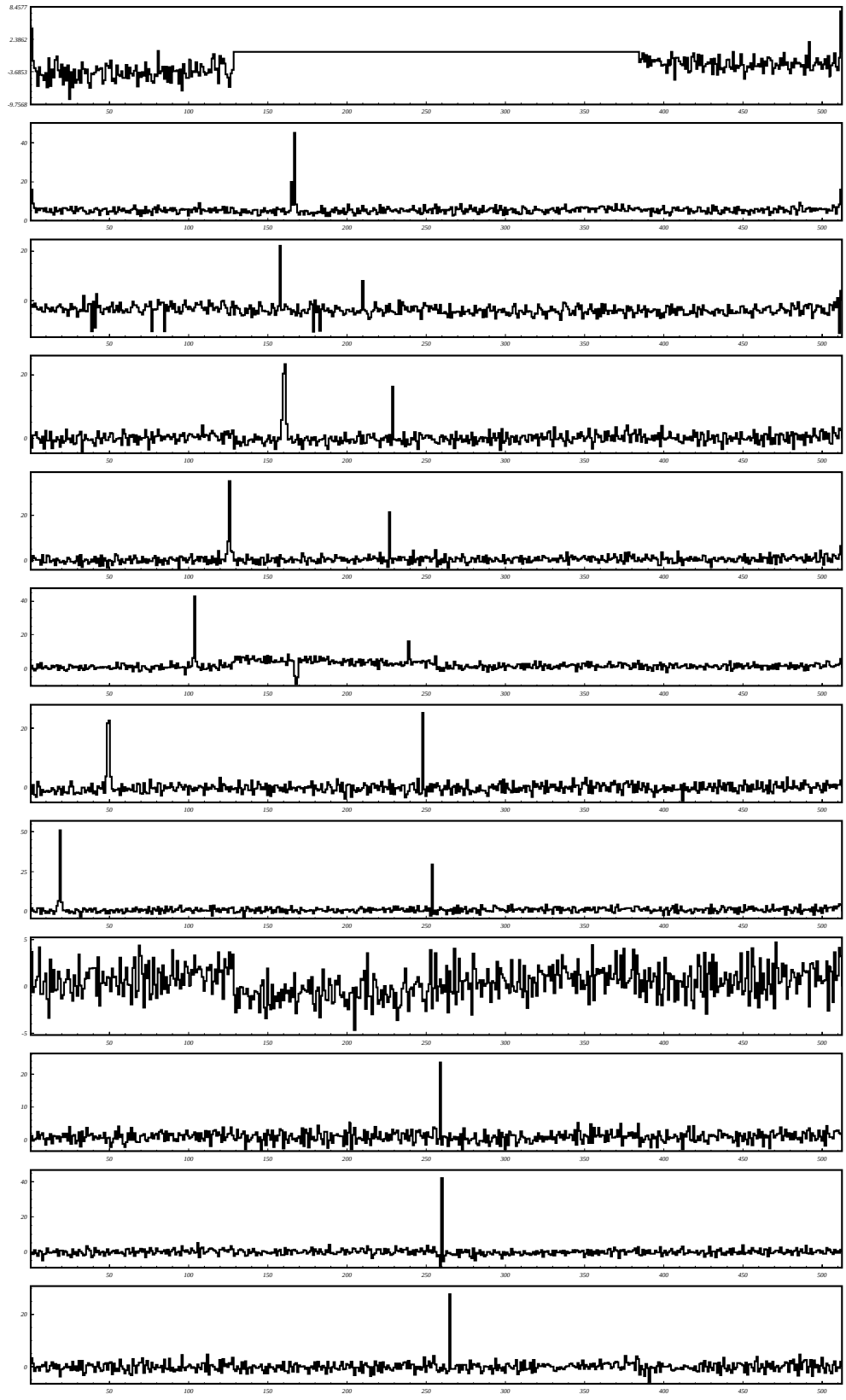

Figure 4.33: Passage of two low momentum particles through an array of 12 detectors at PSI.

Chapter 5

Track and Vertex Finding Performance

This chapter is dedicated to track and vertices reconstruction with the CMS Tracker. The track finding algorithms are described in detail with a discussion of their performance. The Vertex finding algorithms are also outlined with a particular emphasis on the Secondary Vertex Seeding which is the starting phase of vertex finding. The performance are shown in view of an optimised application to inclusive $b-$jet tagging.

5.1 The Reconstruction Framework

Track and vertices reconstruction will be very challenging issues in CMS because of the large number of particles per event.

From the mathematical point of view, tracks and vertices reconstruction have many aspects in common. In both cases the starting point is a sample of objects: the reconstructed hits in a portion of the Tracker for track reconstruction and a sample of reconstructed tracks for vertices reconstruction. A *pattern recognition* or *seed generation* is the first step, in both cases, to find out groups of hits (or tracks) that can be associated to tracks (or vertices). A *fitting* procedure is then applied to the tracks and vertices candidates to extract the values of the associated parameters. The parameters computed in this way are not necessarily the optimal ones: the inclusion of a wrong hit or track may spoil the fit and provide bad parameters. A *smoothing* phase is therefore invoked to adjust the values of the parameters: hits or tracks can be removed from the track or vertex candidate to improve the fit.

In the track reconstruction phase the main difficulty comes from the large number of hits per event ($\sim$40000 at high luminosity and a factor $\sim$ 25 times lower at low luminosity). Special efforts are needed to limit the combinatorics. The design of the algorithms depends on many aspects of the detector: shape of particles trajectories in magnetic field, type of hit information, geometry and performance of the detector. The algorithms are optimised depending on the level of reconstruction: trigger level or offline analysis. A very high reconstruction speed is required for tracking at High Level Trigger (HLT), so algorithms should be very simple and use only a fraction of the Tracker information. The offline reconstruction exploits the complete Tracker information and more sophisticated algorithms are required to achieve a very good tracking performance.

Different track finders are also foreseen for different types of particles: muon tracks

should match with track segments in the muon system, electron tracks match the ECAL clusters and tracks in jets need special track finders for particle dense environments.

Vertices reconstruction is also very challenging: from the timing point of view, it is faster than track finding because of the lower combinatorics, but the variety of vertex topologies is wider. Primary vertices have many tracks and very high precision can be achieved in the measurement of their coordinates. However, it can be difficult to separate them in the high luminosity environment, since many of them have low p_T tracks. Secondary vertices from B, D and τ decays are usually very close to the primary one and a very high precision in track parameters is required to find them. In vertices far away from the primary interaction, the associated tracks may be badly or not reconstructed at all because of the small number of hits. So specific algorithms are required for each vertex topology.

An Object Oriented framework, ORCA[104] was introduced to cope with this huge range of needs: object oriented software allows modularity in the architecture and the use of the same components and interfaces in different environments. Some examples are be provided in the following sections.

5.2 Track Reconstruction

Several track reconstruction algorithms are being developed by the CMS Collaboration. In particular, a modular track finder[105], based on the *Kalman Filter*[106][107] has been proven to be optimal for track reconstruction in jets.

The track reconstruction is divided into 4 basic steps: *Trajectory Seeding*, *Trajectory Building*, *Trajectory Cleaning* and *Trajectory Smoothing*.

The *trajectory seeds* are raw trajectories whose parameters are estimated from a limited set of informations. They can be either external or internal to the Tracker. External seeds can be track segments measured with the muon system or seeds coming from the calorimetry, while internal seeds are produced from the Tracker alone. In this latter case the seeding starts from the hits in two innermost detector layers: each pair of hits on the two layers are selected if they are compatible with the hypothesis to be generated by a track from the beam spot and with a minimum p_T (as it is sketched in Fig. 5.1). In this case the trajectory parameters would be estimated and the track parameters and the associated hits would constitute a *trajectory seed*. The pixel layers are optimal for seeding tracks in hadron jets.

The next step is the *Trajectory Building*. The Trajectory Building is an iterative procedure: at the beginning of each step a trajectory is made from a number of associated hits (two at the starting step if the Trajectory Building starts from the trajectory seeds) and with an estimate of the track parameters. The parameters are then extrapolated to a layer not yet included. If a reconstructed hit, compatible with the trajectory, is found in the layer this is added to the trajectory itself and track parameters are updated. Trajectories which have at least two consecutive layers with no compatible hits are discarded. Iterations stop as soon as all layers are included. This procedure is known as Kalman Filtering. It does not involve iterative minimisations as methods based on Least Squares fitting and allows to incorporate multiple scattering and energy loss during propagation.

The *Trajectory Cleaning* is performed after each step of Trajectory Building to reduce combinatorics: if at least two trajectories share half of the associated hits, only the best one in terms of $\chi^2/n.d.o.f.$ is retained. This step allows to save CPU time and memory.

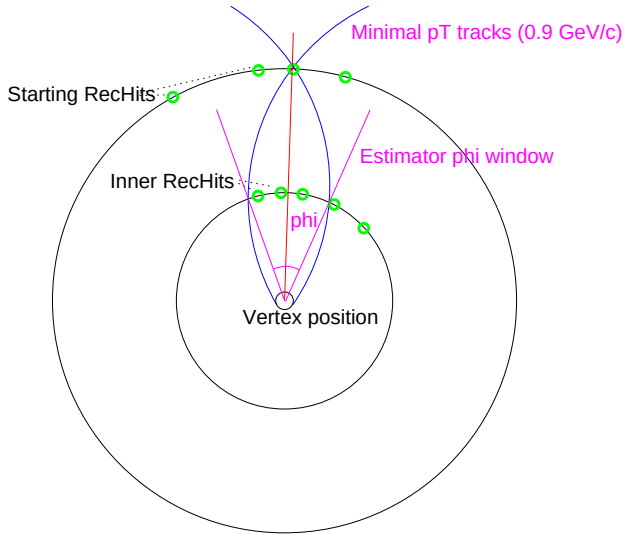

Figure 5.1: Definition of trajectory seeds in the track seeding phase.

After each step of Trajectory Building and Cleaning the track parameter precision increases. To obtain track parameters at the origin, the so-called *Smoothing* phase is lastly invoked: in this phase the tracks are fitted back and the parameters are recomputed at each previous point along the trajectory.

5.2.1 Track Reconstruction at High Level Trigger

The modular track finder designed for offline track reconstrution is also adapted to HLT reconstruction: some modifications are performed in order to achieve a reasonable timing performance while keeping the tracking reconstruction quality as high as possible[63][108].

The two additional requirements to the track finder, in order to use it at HLT are: the *regional seeding* and the *partial track reconstruction*. The regional seeding is the same of the Combinatorial one with the difference that only pixel hits within a *region of interest* are considered. This solution allows to reduce the time spent in combinatorics. In case of track reconstruction inside jets, the region of interest is defined by an interval in ϕ and η around the calorimeter jet axis, a minimum P_T and a primary vertex constraint. The geometry of the region of interest is sketched in Fig. 5.2.

Partial Reconstruction means that only a limited number of layers are used in the Trajectory Building phase to improve the timing performance. The number of hits to be used in track reconstruction depends on the specific trigger. For online inclusive $b-$tagging, the track reconstruction is stopped at 7 hits. This condition allows a tracking performance at HLT comparable with the offline performance for aspects related with $b-$tagging. The total time spent with this reconstruction algorithm is compatible with the allowed bandwidth.

5.3 Vertices Reconstruction

This section describes the vertices reconstruction algorithms with a particular attention to the algorithms which are required for $b-$jet tagging studies. In these studies, both the

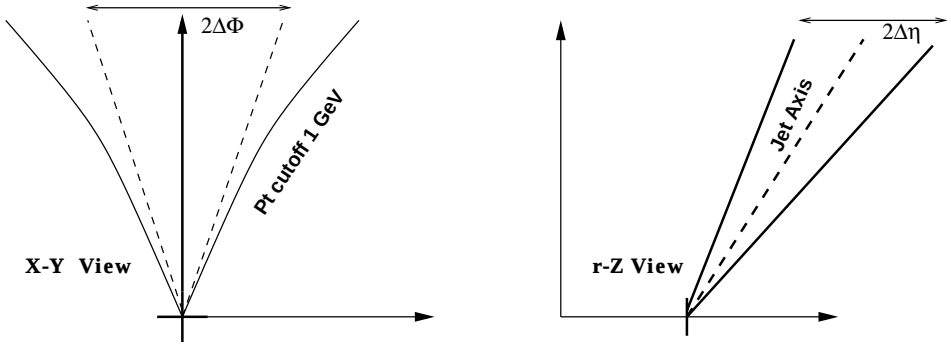

Figure 5.2: Definition of the region of interest for the regional seeding in the x-y and r-z projections [109].

primary and secondary vertices reconstruction is required since the lifetime information is related to the distance between the two.

The reconstruction of the secondary vertices is modular and is divided into a seeding and a fitting step. A seeding algorithm was developed for inclusive B decay searches and is discussed in this section as well as the fitting algorithm. The primary vertex finding algorithm is also described.

5.3.1 Primary Vertices Reconstruction

Primary vertices are placed along the beamline: since the proton bunches have a spread $\sigma_x \sim \sigma_y \sim 15$ μm, their position in the transverse plane is approximately $0\pm15\mu$m in both coordinates while, in the beam direction, the spread is larger ($\sigma_z \sim 5$ cm). The primary vertices reconstruction can be very precise in multi-jet events because of the large number of charged tracks associated with them.

The algorithm used in these studies is based on an iterative method applied to a sample of reconstructed tracks[110]. A vertex fit is performed on an initial sample of tracks. For each track, a vertex compatibility hypothesis is tested and tracks are removed from the sample if the compatibility condition is not fulfilled. After each step the vertex fit is repeated again and the entire procedure is repeated with the new sample of tracks and the new vertex position. The vertex fitting procedure is described below. Iterations continue as long as the result is not stable and the vertex obtained at the end of the last step is returned.

Here the compatibility condition is that the χ^2 probability should be higher than 5%, being χ^2 the ratio between the minimum distance of the track from the vertex and its error.

Vertex Fitting

The simplest algorithm for vertex fitting is the so called *Linear Vertex Fitter* (LVF)[111]. It has the advantage of being very fast since it does not involve any iterative minimisation.

In the LVF algorithm, the vertex position to be returned is the vector ($\mathbf{r}_v$) which minimises the sum of the squares of the minimum distance of the tracks from the vertex:

$$\chi^2 = \sum_i (\mathbf{r}_i - \mathbf{r}_v)\mathbf{Q}_i^T \mathbf{U}_i^{-1} \mathbf{Q}_i (\mathbf{r}_i - \mathbf{r}_v)^T, \tag{5.1}$$

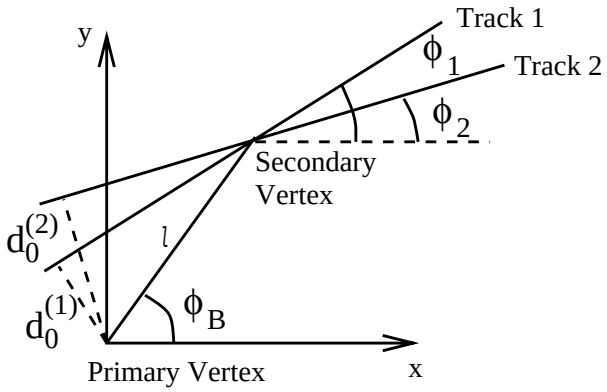

Figure 5.3: The principle of secondary vertices seeding based on correlations of tracks d_0 and ϕ.

$\mathbf{r}_i$ are the i^{th} track's point of closest approach to $\mathbf{r}_v$, $\mathbf{U}_i$ the track's covariance matrix and $\mathbf{Q}_i$ a Jacobian matrix defined as:

$$Q_i^{mn} = \frac{\partial r_i^m}{\partial \xi_i^n} \tag{5.2}$$

being ξ_n the track parameters. $\mathbf{U}_i$ are expressed with respect ξ_n.

If the tracks are approximated as straight lines in the vicinity of the vertex and the covariance matrix is assumed to be independent on $\mathbf{r}_v$ the χ^2 is quadratic in $\mathbf{r}_v$ and minimisation leads to a linear relationship in $\mathbf{r}_i$:

$$\mathbf{r}_v = (\sum_i \mathbf{W}_i)^{-1}(\sum_i \mathbf{W}_i \mathbf{r}_i) \tag{5.3}$$

being

$$\mathbf{W}_i = \mathbf{Q}_i^T \mathbf{U}_i^{-1} \mathbf{Q}_i. \tag{5.4}$$

Under these assumptions the estimation of the vertex position is reduced to a matrix product.

5.3.2 Secondary Vertices Reconstruction

The secondary vertices finding algorithm developed for this work is the adaptation of an algorithm already used by the CDF Collaboration [112][113] for the top quark discovery to the CMS experiment[114]. It is a modular algorithm divided into a *seeder*, to select the tracks associated to the secondary vertices, and a *fitter*, which extracts the vertices coordinates. The *seeder* is described in this section, while the *fitter* is the same of the Primary Vertex algorithm described above.

The *seeder* is based on correlations between the track impact parameter (d_0) and the azimutal angle (ϕ) in the transverse ($r - \phi$) plane. The transverse impact parameter is defined as the minimum distance of the track from the primary vertex in the view perpendicular to the beam direction. The principle is illustrated in Fig. 5.3. Tracks are linearised at the point of closest approach to the primary vertex. The transverse impact

parameter is signed according to the track angular momentum. Under this condition, the following relationship holds:

$$d_0^{(i)} \sim l \sin(\phi_i - \phi_B) \sim l(\phi_i - \phi_B), \tag{5.5}$$

where l is the vertex distance from the primary vertex in the transverse view and ϕ_B its azimuth as shown in Fig. 5.3.

For each track $d_0^{(i)}$ and ϕ_i are provided by the track reconstructor while l and ϕ_B are unknown. It is important to note that, according to Eq. 5.5, $d_0^{(i)}$ depends linearly on ϕ_i and the slope (l) and the constant term ($-l\phi_B$) are the same for tracks belonging to the same vertex.

Therefore, when each track is associated to a point in the $d_0 - \phi$ plane, tracks associated to the same secondary vertex are aligned with a positive slope, while primary tracks would be uncorrelated. An example is provided in Fig. 5.4: black dots are associated to tracks from a B decay while open squares are primary vertex tracks.

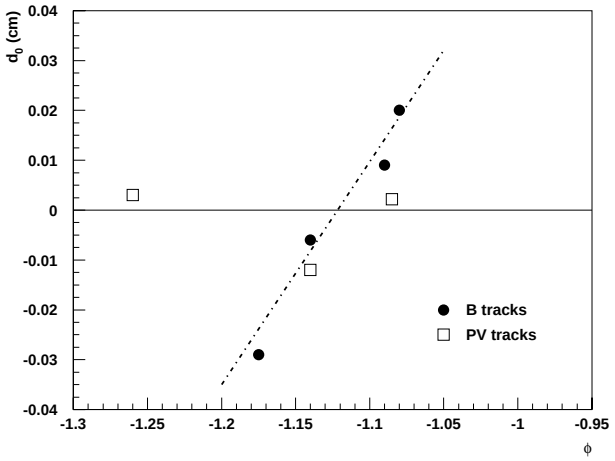

Figure 5.4: The $d_0 - \phi$ plane with points corresponding to tracks in a $b-$jet. Black dots correspond to tracks from a B decay, while open squares correspond to primary vertex tracks.

Similar correlations can be found in planes different from the transverse one with a different impact parameter and angle definition. The discussion is concentrated on the transverse view but any consideration is still be valid for any longitudinal one.

A secondary vertex seed is associated to a set of tracks aligned in the $d_0 - \phi$ plane. Several pattern recognition algorithms can be applied to find out aligned points. The algorithm here examined is divided in two steps: *Link Finding* and *Cluster Finding*.

Track Selection

The basic requirement on tracks to be entered in the algorithm is a transverse impact parameter significance larger than 2. The transverse impact parameter significance is the ratio between the transverse impact parameter calculated with respect the primary vertex and its error. This cut allows to reject tracks coming from the primary interaction, i.e. tracks whose minimum distance from the primary vertex is compatible with its error within fluctuations.

Additional requirements can be placed on the track quality according to the specific analyses.

Link Finding

The first step to find aligned points in the $d_0 - \phi$ plane is the *Link Finding*. The *Link* is a segment in the $d_0 - \phi$ plane and it is the simplest element in the clustering procedure. An example of Link is shown in in Fig. 5.5.

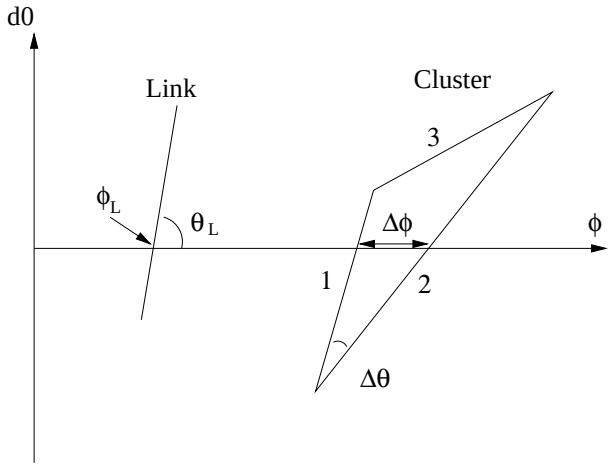

Figure 5.5: Definition of Links and Clusters. The θ_L, ϕ_L, $\Delta\theta$ and $\Delta\phi$ are also displayed.

For each pair of tracks, the θ_L and ϕ_L quantities are computed from the $d_0^{(i)}$ and ϕ_i values according to the formulas:

$$\theta_L = \arctan \frac{d_0^{(1)} - d_0^{(2)}}{\phi_1 - \phi_2}, \quad \phi_L = \frac{d_0^{(1)}\phi_2 - d_0^{(2)}\phi_1}{\phi_2 - \phi_1}. \tag{5.6}$$

θ_L and ϕ_L are also illustrated in Fig. 5.5. The pseudorapidity corresponding to the sum of the track momenta, η_L, is also computed.

The following conditions are required to tracks to form a Link:

$$\tan\theta_L > 0, \quad |\phi_L - \phi_i| < \frac{\pi}{2}, \quad |\eta_1 - \eta_2| < 0.3, \tag{5.7}$$

η_i $(i = 1, 2)$ being the tracks pseudorapidities. These thresholds can be tuned according to the physics process under study.

Cluster Finding

Clusters are sets of tracks aligned in the $d_0 - \phi$ plane. A Link is a two-tracks Cluster. Clusters with a higher number of tracks are found iteratively. Three-track Clusters are made out of two Links which have a track in common and are *aligned*. The alignment condition is defined by the following relationships:

$$\Delta\eta_L < 0.15, \quad \Delta\phi_L < 0.15, \quad \Delta\theta_L < 0.4. \tag{5.8}$$

$\Delta\phi_L$ and $\Delta\theta_L$ are illustrated in Fig. 5.5. These thresholds are tunable.

The upper cut on $\Delta\theta_L$ is crucial since the quality of the fit increases with the track multiplicity. A very small upper threshold (~ 0.3) provides vertices with a very low track multiplicity (2-3) and a very high purity, while a large upper threshold (above 0.5) allows a larger track multiplicity with an higher contamination from primary vertex tracks. A cut at 0.4 is an optimal compromise between the two situations. It can be increased in presence of a vertex smoother.

Clusters with at least three tracks can be merged if they have a Link in common. No alignment conditions are required in this case.

5.4 Performance

The track and vertex finding performance is discussed in this section. The event samples used for the performance evaluation are described and the detector simulation is discussed. The performance are then shown for tracks and vertices reconstruction separately.

5.4.1 Data Samples

Several samples of events are produced to perform track and vertex finding performance studies. The samples are divided in single track events, di-jet events and exclusive B-samples.

In all samples the primary interaction is generated with PYTHIA 6.152[115]. The pile-up event was not considered in these studies. The events were stored in the HEPEVT[115] format and passed to the Detector Simulation Package CMSIM[116] which is described in the next subsection. Only the single tracks samples were directly generated by CMSIM.

Single Tracks

Single muon and pion tracks are generated for many η bins and three p_T values ($p_T = 1$, 10 and 100 GeV) to study the track finding efficiency and the accuracy on track parameters. The very clean environment of this events allowed to improve the algorithms themselves and optimise the detector design.

Di-jet events

Di-jets events were generated to study the tracking performance in a dense environment. Jets were produced in three different η bins, $|\eta| < 0.7$, $1.2 < |\eta| < 1.6$ and $2.0 < |\eta| < 2.4$ corresponding to the barrel region, the region of overlap between barrel and end-caps and the very forward region. Different E_T bins corresponding to $E_T = 50$, 100 and 200 GeV were taken into account: in the $E_T = 50$ GeV the track p_T spectrum is softer, so the performance is limited by the multiple scattering while in $E_T = 200$ GeV jets the performance is affected by the very high particle density. The p_T spectrum for reconstructed tracks within a cone of width $\Delta R < 0.4$ from these jets is shown in Fig. 5.6 and the mean p_T values are also

reported. The average number of particles with $\Delta R < 0.4$ is 4.5, 6.3 and 8.5 in $|\eta| < 0.7$ jets with E_T=50, 100 and 200 GeV. $b-$jets as well as $u-$jets and $c-$jets were generated to

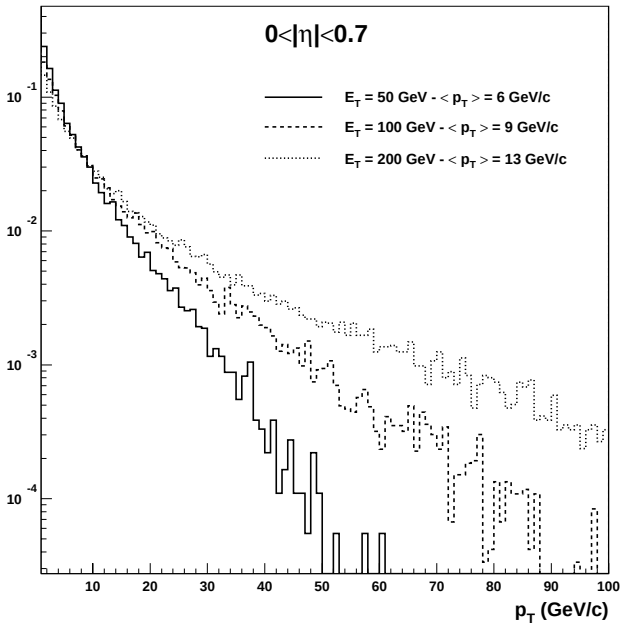

Figure 5.6: p_T spectrum for tracks in $u-$jets in the barrel region with E_T=50, 100 and 200 GeV.

study the $b-$tagging performance.

In the generation of these events, all $pp \to qq$ processes were included but only events with the jets within the correct η and E_T range were selected. Jets momenta are provided by the PYTHIA's PYCELL routine. This routine performs a coarse simulation of the calorimeter response starting from the the stable particles informations. The same resolution and segmentation of the CMS calorimeter are applied. A simple clustering algorithm is applied to calculate the jet momenta.

Exclusive $b\bar{b}$ samples

Exclusive samples of $b\bar{b}$ events were produced for B physics studies. A PYTHIA based package [117] allows to generate $b\bar{b}$ events where one of the two $b-$quarks produces a muon in the final state to provide a muon trigger and the other b is forced to decay through a selected decay mode. These samples allow to test the precision in secondary and tertiary vertices reconstruction in a wide number of decay topologies.

A sample of 500 events with a B_s decaying in the $B_s \to D_s\pi$, $D_s \to \phi\pi$ and $\phi \to KK$ was used to study the secondary vertex finding performance.

5.4.2 Detector Simulation

Events generated with PYTHIA are passed to the CMSIM program to perform the detector simulation. CMSIM is a Fortran based package based on the general purpose detector simulation GEANT3[118]. A detailed model of the CMS detector is included in the simulation: the sensitive regions as well as the passive regions (electronics, mechanical supports, cables, cooling and alignment system) are reproduced with the correct material properties.

The energies deposited in the sensitive regions are simulated according to the model of interaction of particles with matter. The electronics noise is added to the released energy and a detector output is returned in a raw data format. The parameters of the simulation are tuned in order to reproduce the test beam data.

In the Tracker case, the signal-to-noise is set according to the width over pitch of the detectors and dead strips are present at the level of 1%. Clusters are reconstructed with the clustering algorithms outlined in the previous chapter and the hit position is defined by the charge barycentre of the cluster. Reconstructed hits are then passed to the Reconstruction program to perform track and vertices finding.

5.4.3 Track Finding Performance

The track reconstruction performance are evaluated in terms of reconstruction efficiency, fake rate and resolution on track parameters.

Two kinds of efficiency were introduced to decouple the effect of the algorithms from the one of the overall tracking system: the *algorithmic efficiency* and the *global efficiency*. Both efficiencies are defined as:

$$\epsilon = \frac{N(associated\ reconstructed\ tracks)}{N(simulated\ tracks)} \tag{5.9}$$

the denominator being the number of tracks which were simulated and the numerator the number of reconstructed tracks associated to the simulated ones. Reconstructed and simulated tracks are associated if they share at least 50% of hits.

Reconstructed Tracks are required to have at least 8 reconstructed hits, $p_T > 0.7$ GeV and $|\eta| < 2.5$ to allow a reasonable reconstruction quality.

The requirements on Simulated tracks depend on the type of efficiency under study. In the algorithmic efficiency case, only simulated tracks whose associated reconstructed tracks would pass the selection above are considered. The requirements of having at least 8 reconstructable hits, $p_T > 0.9$ GeV and $|\eta| < 2.4$ were thus applied. With this definition any inefficiency would be due exclusively to the track reconstruction algorithms.

Looser cuts on simulated tracks ($p_T > 0.9$ GeV and $|\eta| < 2.4$) are used to study the global efficiency, which includes effects not depending only on the track finding algorithm (hit inefficiency or dead regions).

Algorithmic and global efficiencies are shown in Fig. 5.7 for muons and pions tracks with $p_T = 1, 10$ and 100 GeV in the entire η range. The algorithmic efficiency for muons is always above 98%. The global one has a drop at very high η values because of the lower number of detector layers close to the edge of the Tracker. For pions of 1 GeV, a drop in efficiency is observed around $|\eta| \sim 1$ because of the nuclear interactions induced by the higher amount of material.

Tracking performance is particularly important for tracks in hadron jets since it can be spoiled by the very dense particle environment. Algorithmic and global efficiencies are shown in Fig. 5.8 for tracks in $b-$jets of jet $E_T = 50$ and 200 GeV in different jet η regions. They are independent from E_T, within statistical fluctuations, in the barrel region, while they decrease with E_T at higher η due to higher material budget.

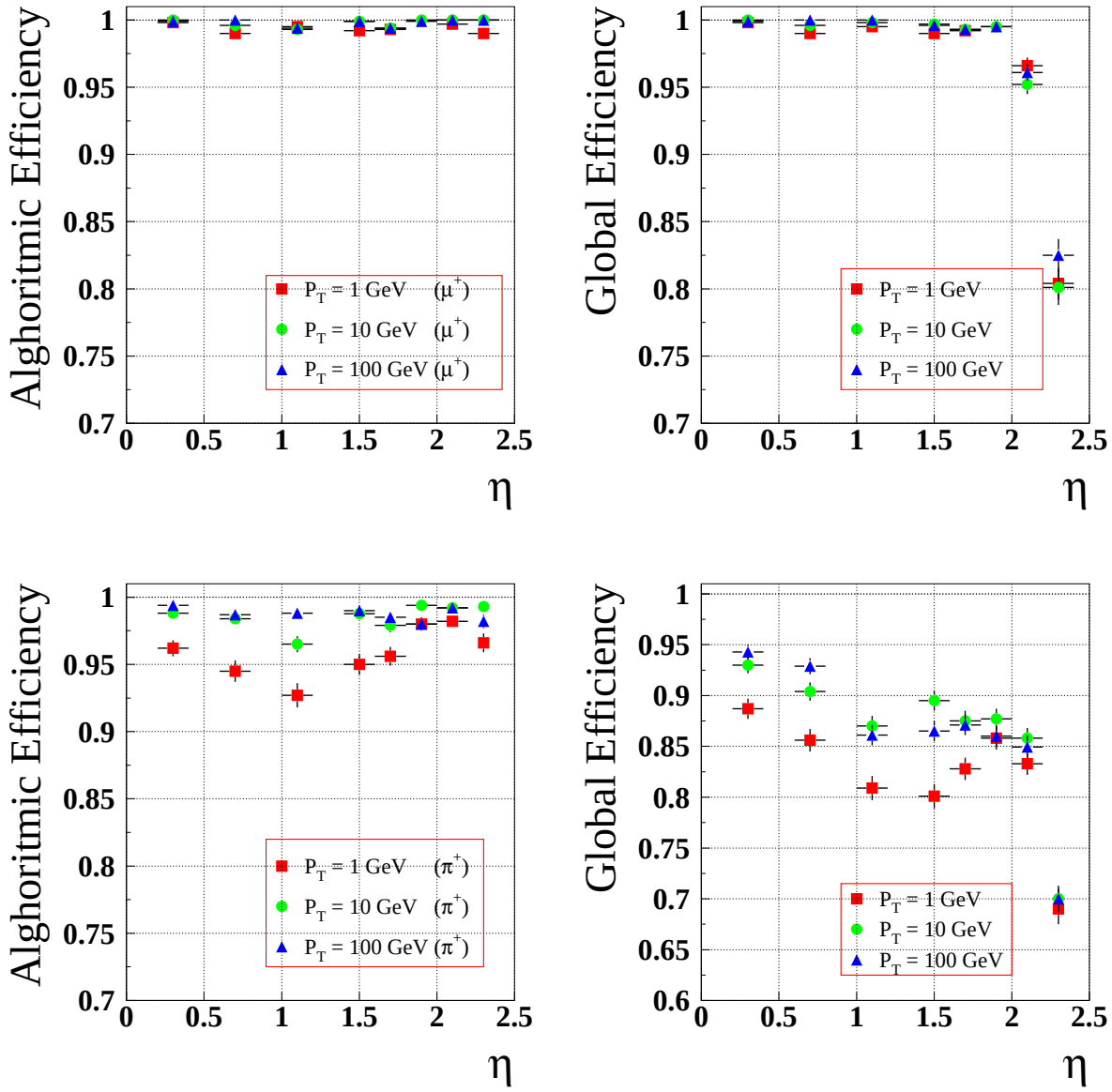

Figure 5.7: Algorithmic (left) and global (right) efficiencies for muon (up) and pion tracks (down).

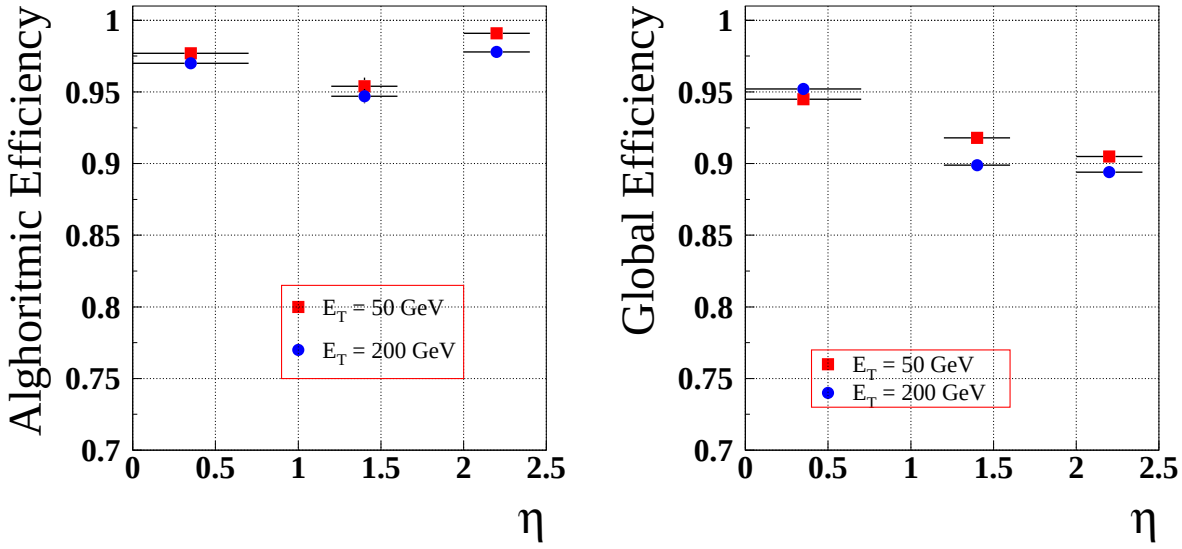

Figure 5.8: Algorithmic (left) and global (right) efficiency for tracks in $b-$jets for $E_T = 50$ and 200 GeV.

The fake rate is defined by

$$\epsilon_{fake} = \frac{N(not\ associated\ reconstructed\ tracks)}{N(reconstructed\ tracks)} \tag{5.10}$$

where the denominator is the overall number of reconstructed tracks and the numerator the number of reconstructed tracks which are not associated to any simulated one. The fake rate is required to be as low as possible in environments with a high track density where the pattern recognition would be less efficient. It was observed that it is lower than 10^{-4} for $E_T = 50$ GeV and lower than 8×10^{-3} for $E_T = 200$ GeV.

Other important variables for the evaluation of the tracking performance are the resolution on track parameters. For the i^{th} track parameter ξ_i, the difference between the reconstructed and simulated value is defined as the residual R_i:

$$R_i = \xi_i^{(rec)} - \xi_i^{(sim)}. \tag{5.11}$$

The resolution on the ξ_i parameter ($\sigma(\xi_i)$) is the relative width of a Gaussian fit of the residual distribution.

The resolution in p_T is shown in Fig. 5.9: it is around $1-2\%$ in the barrel and has a small dependence on η due to the lower lever arm at high η.

The resolution in the transverse impact parameter, which is crucial for $b-$tagging, is shown in Fig. 5.10. It is dominated by the accuracy of the innermost pixel hit. It also depends on η as the extrapolation to the Primary Vertex depends on the track momenta which is less precise at high η. The resolution in the longitudinal impact parameter z_{imp} is also shown in Fig. 5.10. The longitudinal impact parameter is the minimum distance of the track from the primary vertex in a plane containing the beamline. The resolution on z_{imp} depends mainly on the innermost pixel hits. However, the dependence on η is more

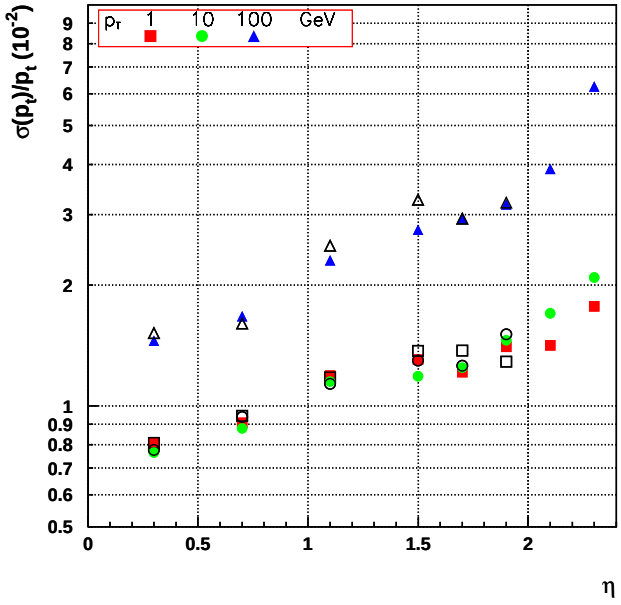

Figure 5.9: Transverse Momentum resolution for single muon tracks for several p_T and η values.

remarkable since it is related to the cluster size in z according to the relationship:

$$\sigma(z_{imp}) \sim \frac{\sqrt{r_1^2 + r_2^2}}{|r_2 - r_1|}\sigma_z \tag{5.12}$$

being r_1 and r_2 the radii of the innermost pixel layers and σ_z the pixel hit resolution in z.

Resolutions in the azimutal angle (ϕ) and $\cot\theta$ (being θ the polar angle) are shown in the same figure. The former is almost independent on η while the latter degrades significantly in the forward/backward region.

5.4.4 HLT Track Finding Performance

The main consequence of a limited number of hits on the tracking performance is the increase of the fraction of ghost tracks in jets. For tracks with less than 5 hits, the fraction of ghost tracks, i.e. reconstructed tracks not associated to simulated ones, ranges between 10% and 30%, while for tracks with more than 5 hits, it is below 1%. The efficiency slightly decreases with increasing the number of hits, mainly due to nuclear interactions with the detector: a loss in of 4% in efficiency is found passing from 7 to 10 hits.

The transverse impact parameter error, which is crucial for $b-$tagging, is very weakly affected by the partial reconstruction since it mainly relies on the innermost pixel hits. The left-hand plot of Fig.5.11 shows the error on the track transverse impact parameter as a function of the number of the total number of hits in the 2.5 GeV $< p_T <$ 5 GeV range: with more than 6 hits the transverse impact parameter error is approximately independent on the total number of hits and it is equal to the one obtained with full reconstruction.

The right-hand plot of Fig.5.11 shows the error on p_T for tracks in the same p_T and η range. With more than four hits, the error improves almost linearly with the total number of hits. The error obtained with 7 hits is a factor 3 worst than the one obtained with the full Tracker information. This effect is more remarkable for lower p_T tracks.

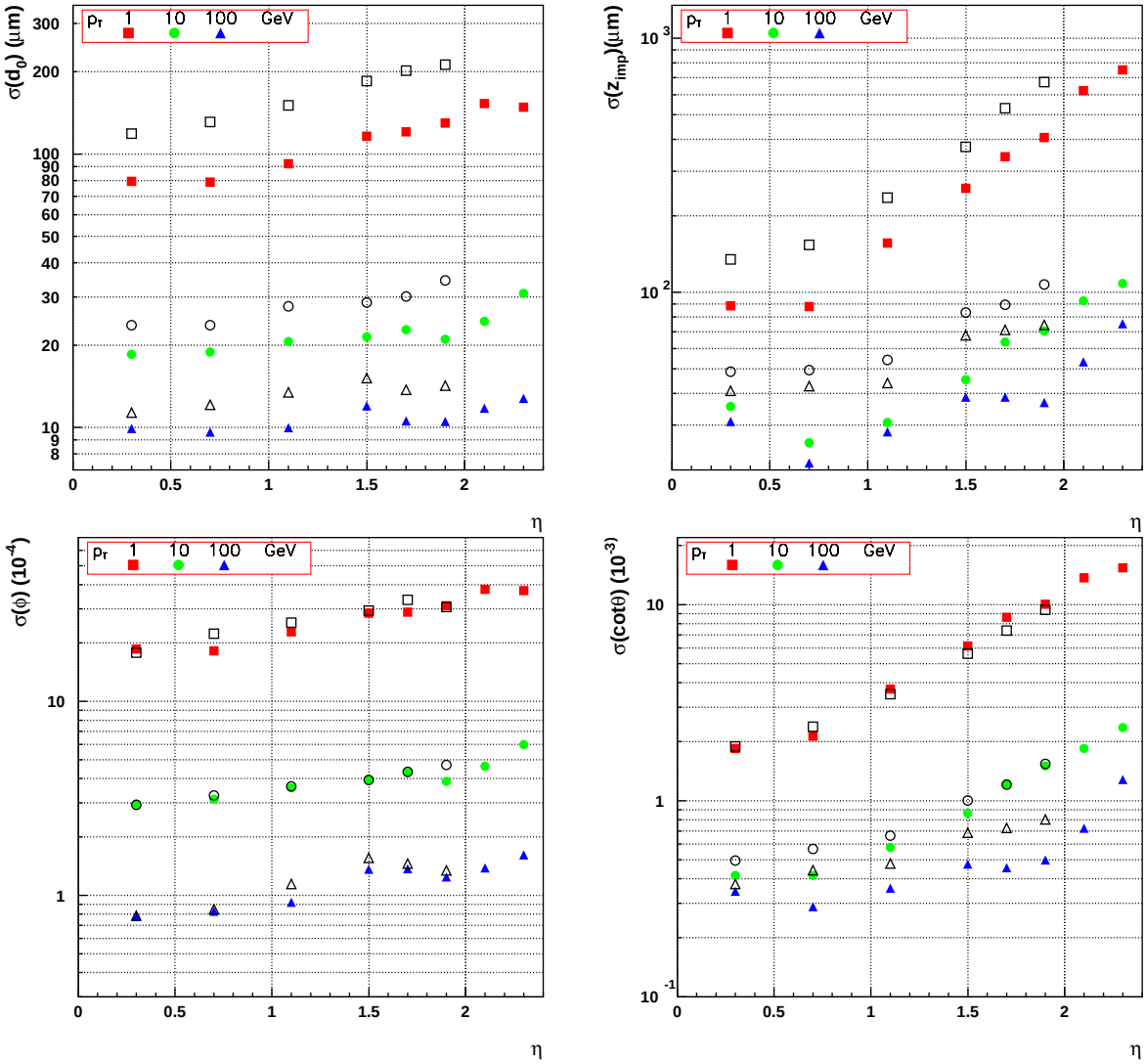

Figure 5.10: Resolutions in transverse impact parameter d_0 (upper left), longitudinal impact parameter z_{imp} (upper left), azimutal angle ϕ (lower left) and $\cot\theta$ (lower right) for muon tracks with p_t ranging between 1 and 100 GeV and $|\eta| < 2.5$.

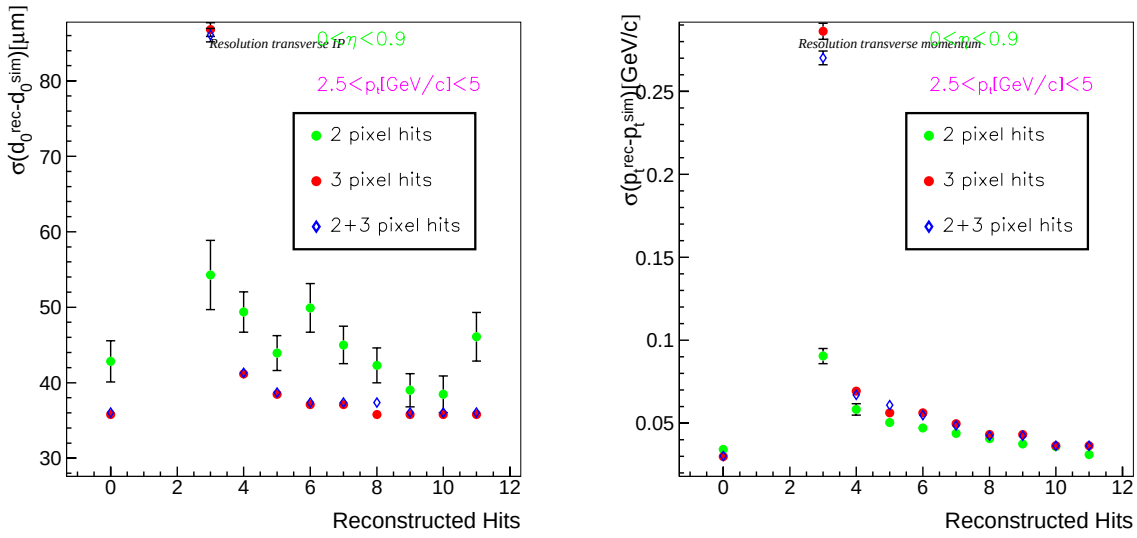

Figure 5.11: Distributions of the transverse impact parameter (left) and p_T resolution for partial track reconstruction as a function of the number of hits for tracks with $|\eta| < 0.9$ and 2.5 GeV $< p_T <$ 5 GeV. The bin with 0 reconstructed hits corresponds to full track reconstruction.

The total time spent to reconstruct a multijet QCD event and perform $b-$tagging is of the order of 200 ms, according to an estimate obtained with a Pentium III-1GHz processor. This timing performance is compatible with the allowed bandwidth.

5.4.5 Vertex Finding Performance

The vertex finding performance depends on the type of vertices and events which are being examined. The performance is studied for primary and secondary vertices separately.

Some definitions need to be introduced before describing the primary and secondary vertices performance. A reconstructed vertex is associated to a simulated vertex if at least 55% of its tracks are associated with the simulated tracks coming from the simulated one. With this definition, efficiency and fake rate definitions used for the track finding performance can be adapted to the vertex case.

Other variables, which are crucial for the vertex reconstruction performance, are the resolutions and pulls on the vertices coordinates: both inclusive $b-$tagging and exclusive B decays reconstruction rely on a precise measurement of the decay point. The resolutions and pulls are defined in the same way as it is done for tracks.

Primary Vertex Finding Performance

The primary vertex finding performance was evaluated using different di-jet event samples since the events for which the $b-$tagging is applied have hadron jets. A similar performance is expected for multijet events. The performance is very good in these events since a large number of reconstructed tracks (between 10 and 20) are associated with the primary vertex, and therefore the vertex finding efficiency is very close to 100% and resolution on vertex position is also very good.

In the LHC experiments the most crucial variable related to the primary vertex reconstruction is the z resolution. The primary interaction can occur in a 15 cm interval and its

position should be known with a good precision to separate secondary vertices from the primary one and calculate the track impact parameter in three dimensions.

The z position residual is shown in Fig. 5.12 for $b\bar{b}$ and $u\bar{u}$ events with $E_T = 100$ GeV and $|\eta|$ <0.7 and it has an almost gaussian shape in both cases. In $u\bar{u}$ events the resolution

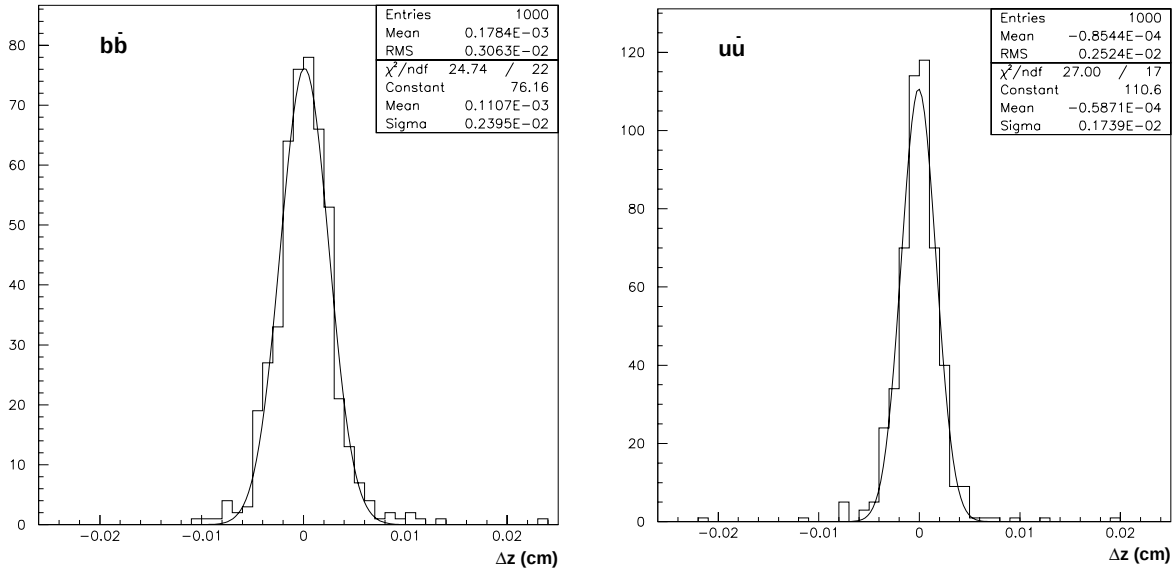

Figure 5.12: Resolution on the primary vertex z position in $b\bar{b}$ (left) and $u\bar{u}$ (right) events (E_T=100 GeV).

on z is 17μm while it is higher in $b\bar{b}$ events (24μm). The degradation in z resolution is due to the presence of displaced secondary vertices from B decays whose tracks can influence the primary vertex position measurement. In both cases the obtained resolution is excellent.

Fig. 5.13 shows the resolution in z as a function of η and different E_T values for $b\bar{b}$ and $u\bar{u}$ events. It improves with the jets E_T because higher E_T jets have more energetic tracks

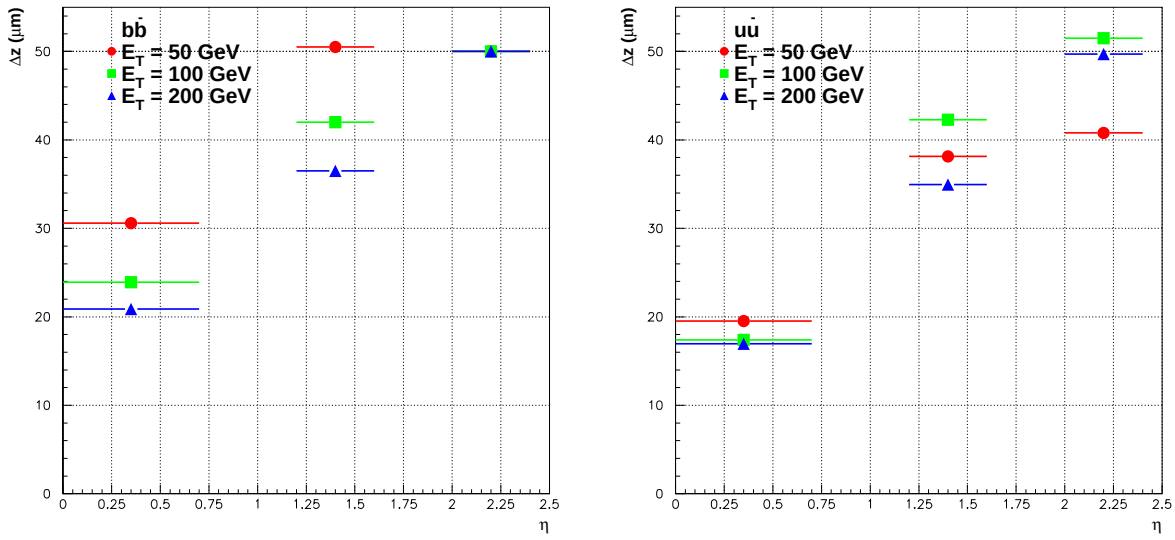

Figure 5.13: Resolution on the z component of the primary vertex in as a function of η and different E_T values for $b\bar{b}$ (left) and $u\bar{u}$ events.

and thus the effect of multiple scattering is less remarkable. The performance is spoiled at

higher η due to the higher material budget and to a larger distance of the innermost pixel layer from the collision point. The worst resolution is obtained in events with jets in the very forward region ($\sigma_z \sim 50\mu$m) but still acceptable for most of the studies.

Secondary Vertex Finding Performance

Reconstructed secondary vertices in $b\bar{b}$ events have a low number of tracks; therefore both the seeding phase and the fitting phase are more difficult. The seeding and fitting performance are treated separately.

The seeding performance is related to the $b-$tagging performance and is described in a dedicated section of the next chapter.

The fitting performance determines the resolution on the secondary vertices coordinates. It depends on the charged track multiplicity, the type of particles and the decay topology. Therefore, exclusive samples are more suitable for these studies. The $B_s^0 \to D_s^- \pi^+$, $D_s^\pm \to \phi\pi^\pm$, $\phi \to K^+K^-$ sample was used for this purpose. This process is a benchmark for B_s oscillation studies[119][120]: four charged tracks and no neutral are produced in the decay, there is a tertiary vertex and the three resonances (ϕ, D_s and B_s) allow the correct assignment of the tracks to the decay products.

In these studies the tracks are reconstructed with the Combinatorial algorithm previously described and only tracks with at least 6 hits and $p_T > 500$ MeV/c are selected. The charged tracks associated to the simulated ones coming from the D_s decay were passed to the fitting algorithm to extract the vertex position. In this way the effect of the combinatorics is decoupled from the performance of the fit. The residual distributions of the x (y is very similar) and z coordinates of the vertex are shown in Fig. 5.14: for this decay the resolution in x and z is of 118 and 127 μm respectively to be compared with the average flight path of D plus the one of the B which is of the order of 1-2 mm.

The track associated to D_s is reconstructed combining the informations of the secondary vertex and its decay products: the track starting point is provided by the vertex position and the track momentum is provided by the sum of the momenta of its decay products. Tracks associated to D_s and the track associated to the pion from the B_s decay are passed again to the vertex fitter and the B_s decay vertex is reconstructed. The residual of the x and z coordinates are shown in Fig. 5.15: for these vertices the resolution in x and z is 54 μm to be compared with the average flight path of the B which is 1-2 mm. The improvement in the vertex resolution is due to the fact that the pion from B_s has larger average momentum with respect to the D_s decay products and the D_s track has a very good momentum resolution since it is reconstructed from its decay products.

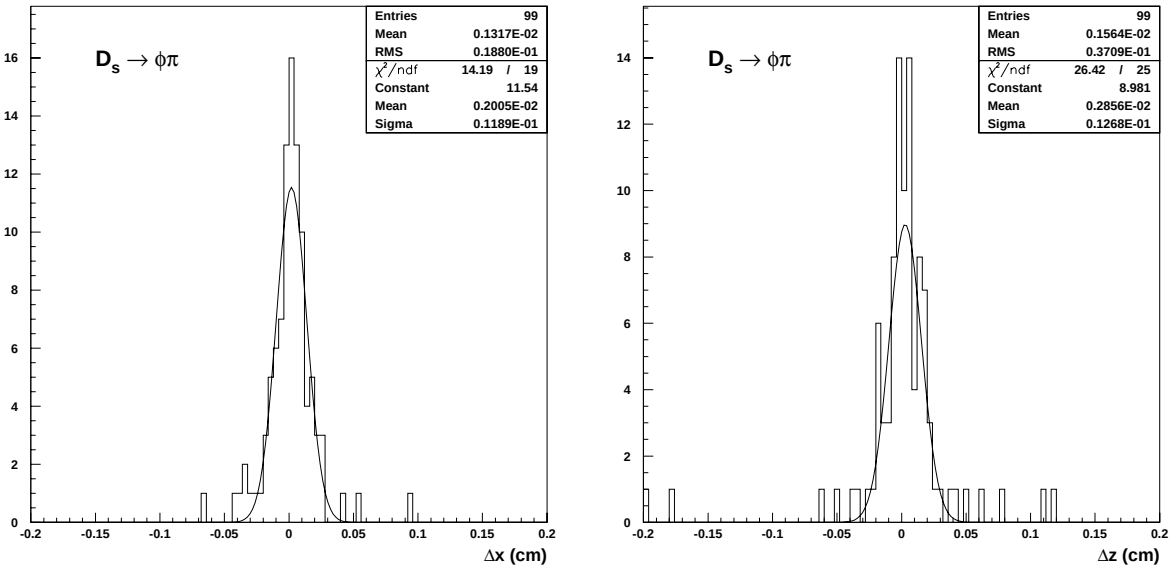

Figure 5.14: Residual distributions for the x (left) and z (right) components of the vertex associated to the $D_s^{\pm} \to \phi\pi^{\pm}$, $\phi \to K^+K^-$ decay.

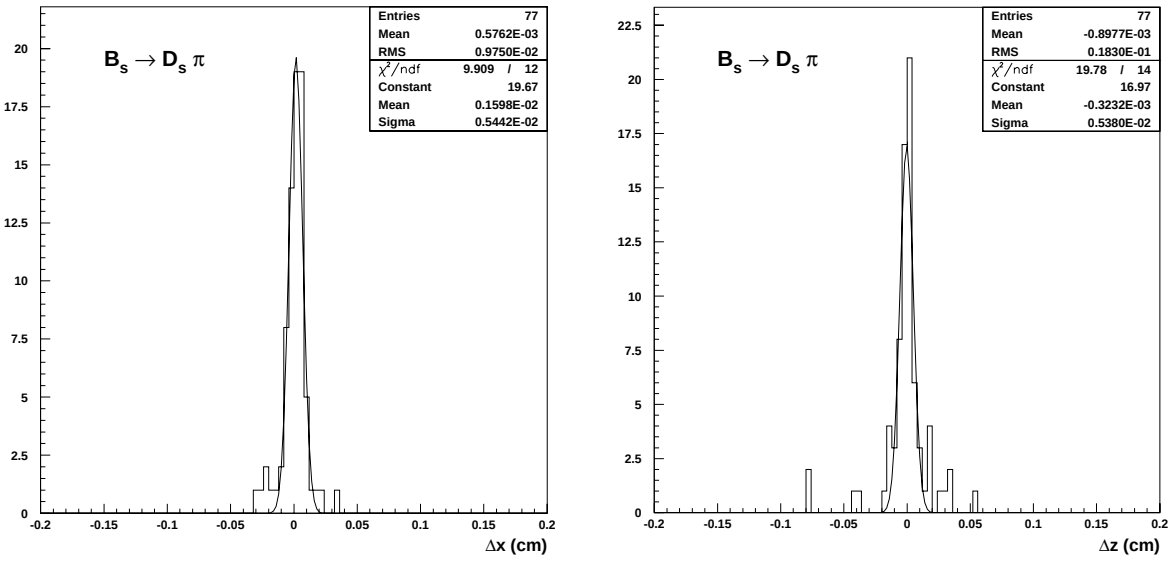

Figure 5.15: Residual distributions for the x (left) and z (right) components of the vertex associated to the $B_s^0 \to D_s^-\pi^+$ ($\bar{B}_s^0 \pm \to D_s^+\pi^-$) decay.

Chapter 6

$b-$tagging Performance

This chapter is dedicated to the identification of hadron jets produced from the $b-$quark fragmentation ($b-$tagging). Two approaches are taken into account: the first one is based on track impact parameter while the second one uses the reconstruction of a $b-$flavoured hadron decay vertex. For both approaches a detailed description of the methods are provided and the performance of the algorithms are shown for jets of different energies in various regions of the Tracker. The effect of a staged pixel detector is also studied.

6.1 Introduction

The identification of $b-$quark decays allows to select processes where b quark can be produced in heavier particles decays. Inclusive $b-$tagging played a crucial role in the past experiments: examples are the measurement of the $Z \to b\bar{b}$ branching ratio at LEP and the top quark discovery with $t \to bW$ at the Tevatron. A similar approach is proposed for the Higgs boson search ($H \to b\bar{b}$) and of the supersymmetric particles searches.

The identification of hadron jets originated from b quarks relies on the properties of B decays. B hadrons have a lifetime $\tau_B \sim$ 1.5 ps, which corresponds to a $c\tau_B \sim 480\mu$m, and produce in average 5 charged particles per decay.

The lifetime information can be exploited in different ways. The first class of methods relies on tracks with a large impact parameter. As it shown in Fig. 6.1, tracks from B decays have a large impact parameter because they originate from a displaced vertex, while the impact parameter of tracks coming from the primary vertex is compatible with the tracking resolution.

A complementary approach is based on the reconstruction of the decay vertex associated to a B hadron. The reconstruction of this vertex would be the clearest evidence of such kind of decay. This method is limited by the secondary vertex reconstruction efficiency.

Both methods rely on a powerful microvertex detector. The power of these methods is limited both by inefficiency in track and vertex reconstruction and by the experimental resolution on tracks parameters.

The mistagging rate for these algorithms is due to secondary interactions and decays of long-lived particles. Secondary interactions with the tracker material can provide secondary vertices and thus tracks with a large impact parameter. Long-lived particles as K^0_S, Λ^0 and c-hadrons can provide real decay vertices and therefore constitute a physical irreducible background, especially c-hadrons.

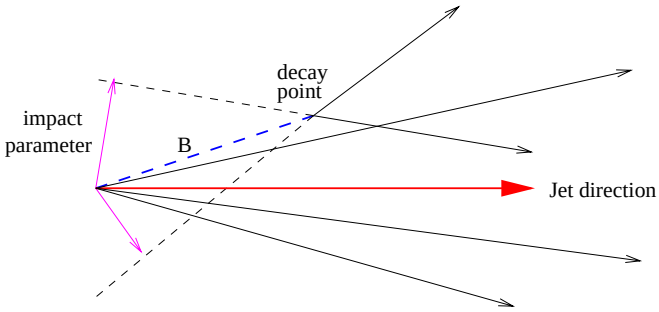

Figure 6.1: Representation (not on scale) of an hadron jet from b-quark.

A completely different approach for $b-$tagging relies on low p_T leptons produced in the decays $b \to cl\nu$ and $c \to (d,s)l\nu$. These leptons are non isolated from the jet and have a large impact parameter. This method has a lower efficiency, since it is limited only to the leptonic decays, but offers the additional jet charge information. Another information which was used in the past experiments is the reconstructed $B-$hadron mass. Taggers related with low-p_T leptons and mass reconstruction are not considered in this study.

The best performance comes from the combination of the informations from different methods since a larger number of informations about B decays would be used. An Object Oriented library[121] was created to provide the implementation of the algorithms and the tools described in this chapter under the ORCA Reconstruction Framework.

6.2 Methods Based On Track Impact Parameter

The Track Impact Parameter can be computed either in the view transverse to the beam axis (*transverse impact parameter*) or in three dimensions (*three-dimensional impact parameter*). Due to the small size of the beam in the transverse view at LHC, the transverse impact parameter is weakly affected by the uncertainty on the primary vertex position. In the case of three-dimensional impact parameter, a larger set of informations is exploited, but the error on it is spoiled by the error on the z component of the primary vertex.

In both cases, the computation is performed starting from the trajectory parameters at the innermost measurement point. In the transverse impact parameter case, the estimate can be done analytically since the trajectory is circular in the transverse view. In the three-dimensional case, the extrapolation is performed through iterations. Fig. 6.2 shows the main steps of the three-dimensional impact parameter computation: first of all, the point of closest approach of the track to the jet direction (S) is extracted (it would be approximately the decay point of the B hadron), then tracks are linearised at that point and the minimum distance of linearised tracks from the primary vertex V (i.e. the three-dimensional impact parameter) is computed. The VQ segment in Fig. 6.2 is called *decay length* and approximates the flight path of the B hadron.

In these studies, the impact parameter is signed as positive (or negative) if the decay occurs upstream (or downstream) the jet direction. Since the jet direction approximates the flight direction of the B hadron, the tracks from a B decay have positive impact parameter. Effects due to badly measured track parameters, badly reconstructed jet directions or primary vertices can flip the sign of the impact parameter.

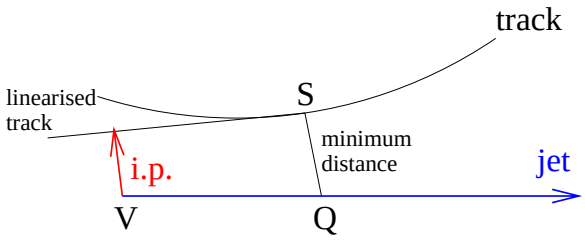

Figure 6.2: Representation (not in scale) of the three-dimensional impact parameter definition.

To take into account the experimental resolution, the track impact parameter significance is used. Fig. 6.3 shows the distribution of this variable for b and $u-$ jets with $E_T = 100$ GeV and $|\eta| < 0.7$.

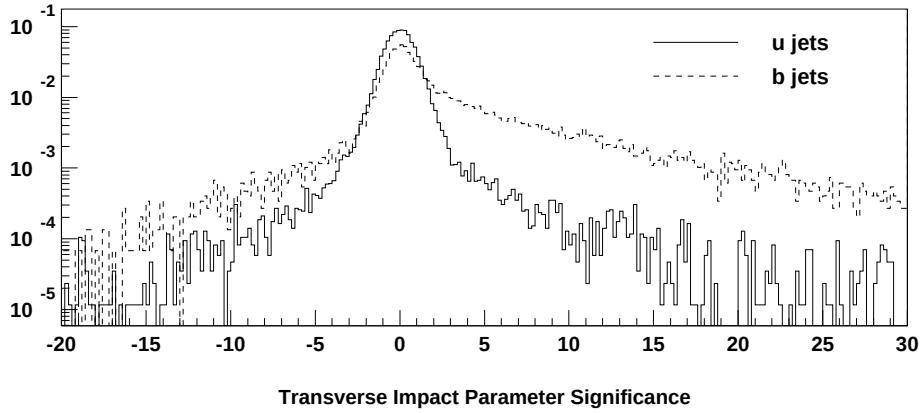

Figure 6.3: Transverse Impact parameter significance distributions for u-jets (solid line) and $b-$jets (dashed line) for jets with $E_T = 100$ GeV and $|\eta| < 0.7$.

Tracks from $u-$jets are more or less distributed according to a Gaussian function centered in 0 and width 1 because they come from the primary vertex and thus their impact parameter is compatible with zero within the experimental resolution. Tracks from b-jet show an asymmetric distribution at positive values, which is a hint of lifetime.

The distribution of the three-dimensional impact parameter significance is shown in Fig. 6.4 for tracks in b and u jets with $E_T = 100$ GeV and $|\eta| < 0.7$.

The signal still shows an asymmetric tail at positive values due to lifetime: the only difference with respect the previous case is that both signal and background show a hole around zero due to three-dimensional phase-space.

6.2.1 Track Counting Method

This method is based on the requirement of a minimum number of good quality tracks with an impact parameter significance exceeding a given threshold [56].

Different performance can be achieved by tuning the number of tracks and choosing an appropriate threshold on significance: the optimal choice of these parameters depends on the type of physics process under study. A very high efficiency on $b-$jets, with a reasonable mistagging rate for u and $c-$jets, can be achieved requiring at least two tracks with an

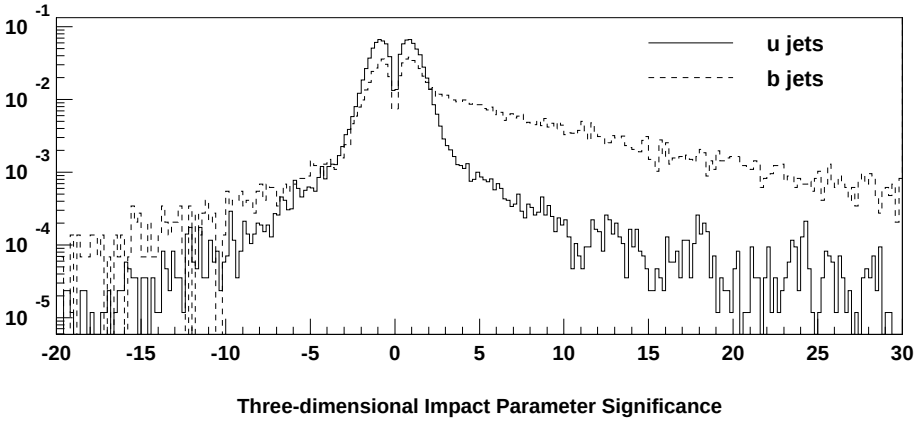

Figure 6.4: Three-dimensional impact parameter significance distributions for u-jets (solid line) and $b-$jets (dashed line) for jets with $E_T = 100$ GeV and $|\eta| < 0.7$.

impact parameter significance larger than 3: this tagger is suitable to select processes with a large number of $b-$jets. On the other hand, if the signal contains a small number of jets, a reasonable $b-$tagging efficiency with a very low mistagging rate can be achieved requiring at least 3 tracks with an impact parameter significance larger than 2.

The main advantage of this method is its simplicity: it only relies on the selection of good quality tracks and a lower cut on impact parameter significance. In addition, no further steps of reconstruction such as secondary vertex reconstruction are required.

The algorithm offers a very quick optimisation step and adaptation to the physical process due to the limited number of parameters. It also offers a quick feedback for detector optimisation and evaluation of the impact of experimental effects (like pile-up, misalignment, changes of the baseline design and detector parameters) on the $b-$tagging performance.

6.2.2 Probabilistic Method

This method is also based on track impact parameter: it consists in computing the compatibility of a set of tracks to come from the primary vertex[122][123].

The *jet probability* estimation is performed through several steps which are described in detail in this section: for each track, the *probability* to come from the primary vertex is computed and probabilities are combined together to provide the *jet probability*. The track probability is computed using as calibration the negative tails of the distribution of the impact parameter significance. Negative tails are used for this purpose since they are made mainly of primary vertex tracks.

This approach has the advantage to allow the detection of the largest range of decay topologies in an inclusive way.

Resolution Function

Tracks with negative impact parameter can be used to extract the *resolution function* $R(x)$.

The resolution function is dominated by a Gaussian distribution centered in 0 and $\sigma = 1$ for the transverse impact parameter and a Gaussian multiplied by a linear term

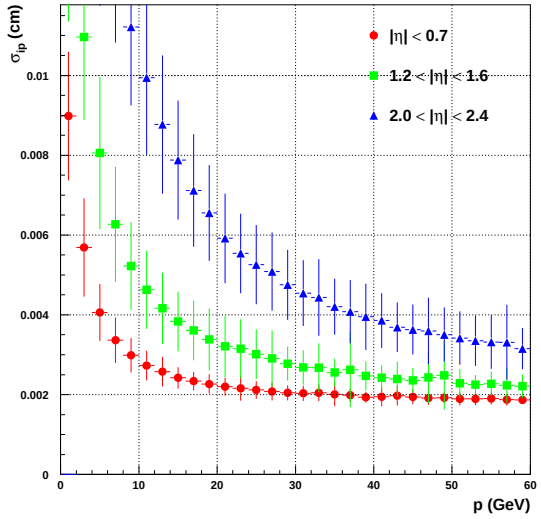

Figure 6.5: Correlations between p and $\sigma_{i.p.}$ for $u\bar{u}$ events with $E_T = 100$ GeV in different η bins.

in the three-dimensional case. The non Gaussian tails, due to effects not included in the error estimate, secondary interactions with the material and lifetime, are parametrised by exponential terms (exponential terms multiplied by linear terms in the three-dimensional case). For the transverse impact parameter, the resolution function is:

$$R^{2D}(x) = \alpha_1 \sqrt{\frac{2}{\pi}} \frac{1}{\sigma_1} \exp\left(-\frac{x^2}{2\sigma_1^2}\right) + \sum_{i>1} \alpha_i \frac{1}{\lambda_i} \exp\left(-\frac{x}{\lambda_i}\right), \tag{6.1}$$

while for the three-dimensional impact parameter it is:

$$R^{3D}(x) = \alpha_1 \frac{1}{\sigma_1^2}\, x \exp\left(-\frac{x^2}{2\sigma_1^2}\right) + \sum_{i>1} \alpha_i \frac{1}{\lambda_i^2} x \exp\left(-\frac{x}{\lambda_i}\right). \tag{6.2}$$

The track reconstruction quality is related to the momentum and the number of hits in the different types of detectors: the number of pixel hits and the position of the innermost pixel layer are crucial for impact parameter measurement.

The transverse impact parameter resolution can be approximated by the formula:

$$\sigma_{i.p.} \sim \sigma_1 \oplus \frac{\sigma_2}{p} \sqrt{\frac{1}{\sin^3 \theta}}. \tag{6.3}$$

The first contribution is due to the intrinsic position resolution of the pixel detector ($\sigma_1 \sim$ 20-25 μm for different η regions) and is independent from the particle momentum p. The the second term is due to multiple scattering and depends on p and on the polar angle θ. Fig. 6.5 shows the error on track transverse impact parameter as a function of the track momentum for u-jets with $E_T = 100$ GeV and different η intervals.

The transverse impact parameter resolution reaches its asymptotic value, σ_1, at different momenta for various η regions, while it steeply increases in the low momentum region.

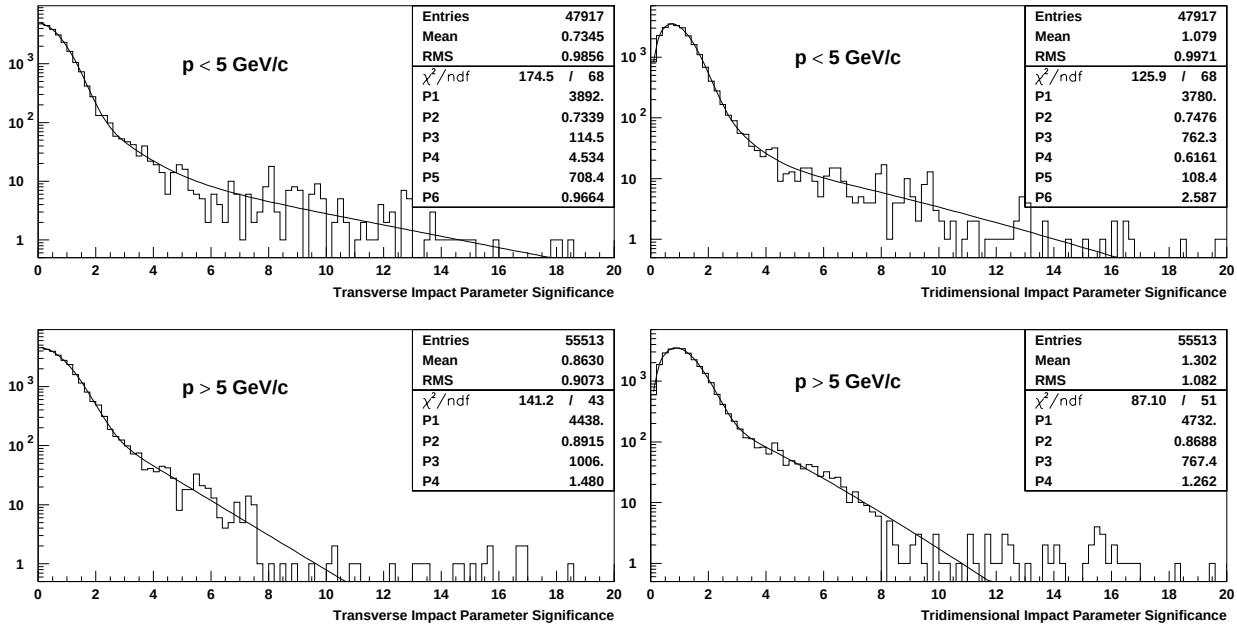

Figure 6.6: Resolution functions for transverse (left) and three-dimensional (right) impact parameter significance: the upper plots are related to $p < 5$ GeV/c while the lower plots to $p > 5$ GeV/c.

Different resolution functions are therefore introduced for different η and p bins. The fits of the transverse and three-dimensional impact parameter significance distributions are shown in Fig. 6.6 for $u\bar{u}$ events with $E_T = 100$ GeV and $|\eta| < 0.7$.

The P_1 and P_2 fit parameters are respectively the constant factor and the sigma of the Gaussian contributions, while $P_{3/5}$ and $P_{4/6}$ are the constant and λ terms of the exponential parts. The difference in the distributions for different momentum ranges are due to the multiple scattering effects which produce larger non Gaussian tails in softer tracks.

Track Probability

The probability for a track to come from the primary vertex is given by the integral of the resolution function (signed as the significance S):

$$P_{tr}^{2D,3D}(S) = sgn(S) \cdot \int_{|S|}^{\infty} R^{2D,3D}(x)dx. \tag{6.4}$$

By definition, the distribution of $P_{tr}^{2D,3D}(S)$ is flat between -1 and 1 for tracks coming from the primary vertex, because the impact parameter significance distribution is described by the resolution function (apart some relic lifetime). It is positive and concentrated around 0 for tracks with large impact parameter significance.

For the transverse view, the probability is:

$$P_{tr}^{2D}(S) = sgn(S) \cdot \left[\alpha_1 \cdot erfc\left(\frac{|S|}{\sqrt{2}\sigma_1}\right) + \sum_{i>1} \alpha_i \cdot \exp\left(-\frac{|S|}{\lambda_i}\right)\right], \tag{6.5}$$

while in three dimensions:

$$P_{tr}^{3D}(S) = sgn(S) \cdot \left[\alpha_1 \cdot \exp\left(-\frac{S^2}{2\sigma_1^2}\right) + \sum_{i>1} \alpha_i \cdot \left(1 + \frac{|S|}{\lambda_i}\right) \cdot \exp\left(-\frac{|S|}{\lambda_i}\right) \right]. \quad (6.6)$$

Fig. 6.7 shows the distribution of track probability for tracks of b and u-jets with $E_T = 100$ GeV and $|\eta| < 0.7$ in the three-dimensional case (the transverse case is similar).

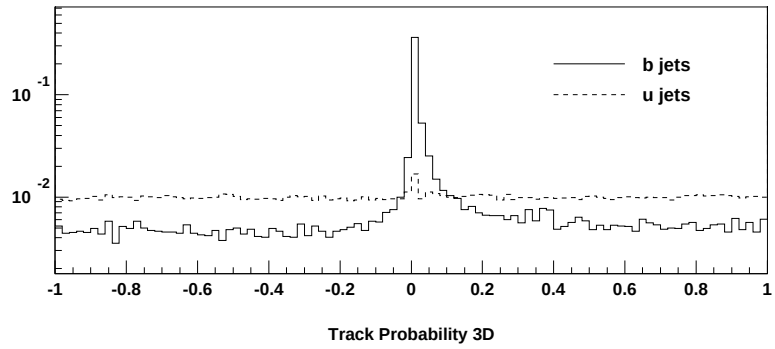

Figure 6.7: Track Probability (three-dimensional case) for $b-$jets tracks (solid line) and $u-$jet ones (dashed line) for jets with $E_T = 100$ GeV and $|\eta| < 0.7$.

The sharp spike around 0 is due to tracks coming from B decays and it is a hint of lifetime. The negative contribution of the spike is due to secondary vertex tracks whose impact parameter is signed in the wrong way. The small bump near 0 for $u-$jets tracks comes from real lifetime which is still present in those jets despite cuts: this is an irreducible background for $b-$tagging. Any other residual non-flatness is related to a non perfect fit or a wrong parametrisation of the negative tails.

Jet Probability

The jet probability for a jet containing N tracks is defined as the confidence level that any group of N tracks without lifetime would produce the observed value of track probability or any other value equally or more unlikely. The expression of this probability is the following:

$$P_{jet} = \Pi \cdot \sum_{j=0}^{N-1} \frac{(-\ln \Pi)^j}{j!} \quad (6.7)$$

being:

$$\Pi = \prod_{i=0}^{N} \tilde{P}_{tr}(i). \quad (6.8)$$

$\tilde{P}_{tr}$ is the *redefined track probability*: $\tilde{P}_{tr} = P_{tr}/2$ for $P_{tr} > 0$ and $\tilde{P}_{tr} = 1 + P_{tr}/2$ for $P_{tr} < 0$. It is introduced to allow track probability to be always positive.

Fig. 6.8 shows the distributions of $-\log P_{jet}$ for b and $u-$jets ($E_T = 100$ GeV and $|\eta| < 0.7$) in the transverse and three-dimensional impact parameter cases: this variable is concentrated near 0 for $u-$jets and has a wider distribution for $b-$jets. A cut on P_{jet} allows a $b-$flavoured jets selection and light flavours jets rejection.

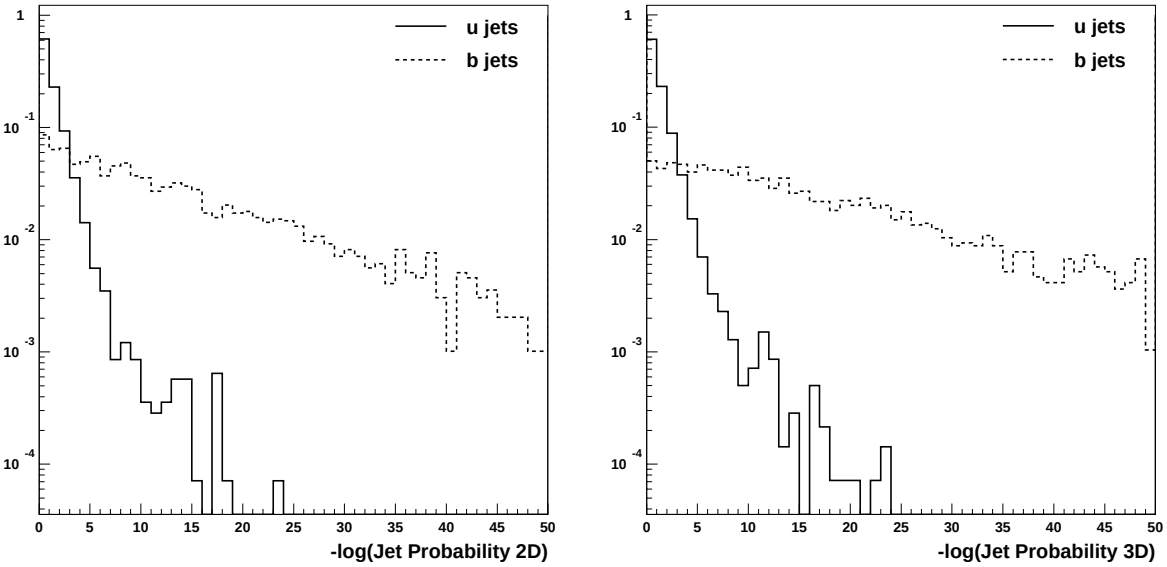

Figure 6.8: $-\log P_{jet}$ for $u-$jets (solid line) and $b-$jets (dashed line) for jets with $E_T = 100$ GeV and $|\eta| < 0.7$ in the two-dimensional (left plot) and three-dimensional (right plot) cases.

6.3 Method based on Secondary Vertices

A different approach for $b-$jet tagging relies on secondary vertex reconstruction. A relatively long lifetime ($c\tau \sim 480\mu$m) and a high multiplicity of charged tracks provide a specific vertex topology that can be exploited for $b-$jet tagging.

Since B decays are searched in an inclusive way, vertex selection should be general enough to include the largest number of topologies. The performance of the algorithm is mostly limited by the performance in secondary vertex reconstruction.

The first requirement on secondary vertex is that the flight direction with respect to the primary vertex lies within the jet cone. Additional requirements are then applied to select the $B-$like vertices.

Most of the fake vertices due to secondary interactions with Tracker and beam-pipe material can be reduced with a cut on the maximum radial distance from the beam line. This variable is shown in Fig. 6.9 for the $b\bar{b}$ sample (left plot) and $u\bar{u}$ sample (right plot) for $E_T = 100$ GeV and $|\eta| < 0.7$.

In the $u-$jets the peak at 0 is due to vertices made of primary vertex tracks while the bumps beyond 2.5 cm distance are due to interactions with the beamline (placed at 3 cm) and the Tracker.

Vertices made of primary tracks can be rejected with a lower cut of the significance on the distance from the primary vertex. This cut plays the same role played by the track impact parameter significance in the track counting method. The distributions of this variable is shown in Fig. 6.10 for vertices inside a b and an $u-$jet respectively.

The other handles which can be exploited, are related to the vertex topology and would allow a sizeable reduction of the mistagging rate. Fig. 6.11 shows the distribution of the number of tracks coming from secondary vertices in the $b\bar{b}$ and $u\bar{u}$ samples. The $u-$jets are dominated by two-tracks vertices and the fake rate can be reduced just applying tighter cuts only on two-tracks vertices. Among all studied cuts, the requirement of a positive signed impact parameter for the tracks associated to two-tracks vertices provides the best

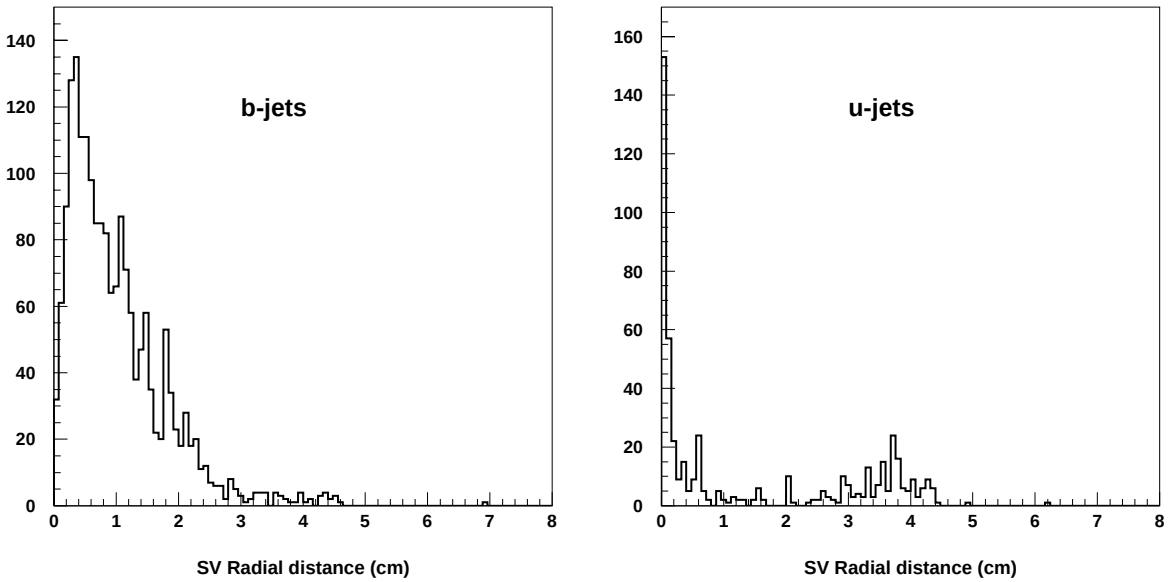

Figure 6.9: Radial distance from the beamline for secondary vertices in the $b\bar{b}$ (left plot) and $u\bar{u}$ (right plot) samples with $E_T = 100$ GeV and $|\eta| < 0.7$.

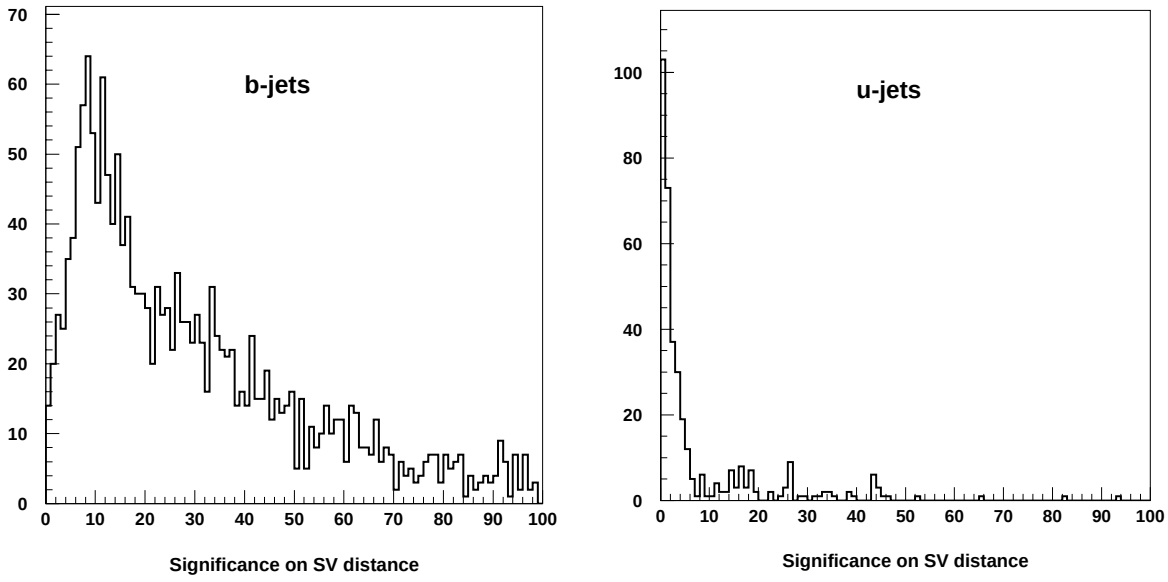

Figure 6.10: Significance of the distance from the primary vertex for secondary vertices in the $b\bar{b}$ (left plot) and $u\bar{u}$ (right plot) samples with $E_T = 100$ GeV and $|\eta| < 0.7$.

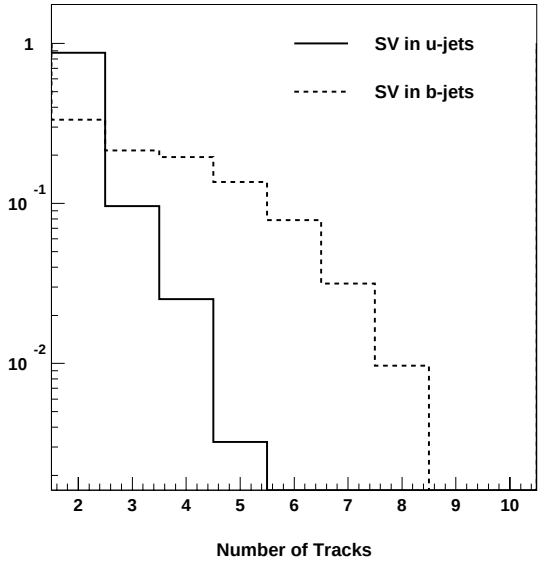

Figure 6.11: Number of tracks for vertices in E_T =100 GeV and $|\eta| < 0.7$ $b-$jets and $u-$jets.

rejection power.

6.4 Performance

The $b-$tagging performance are studied in terms of *b-tagging efficiency* (ε_b) and *mistagging rate* ($\varepsilon_{u/c}$). Both variables are related to the single jet: the $b-$tagging efficiency is the fraction of jets tagged as b in $b\bar{b}$ samples, while the mistagging rate is the fraction of non $b-$jets tagged as b in the $u\bar{u}$ or $c\bar{c}$ samples. The mistagging rate is computed for uds and $c-$jets separately.

Each point in the ε_b versus ε_u plane is defined by a set of parameter cuts of the corresponding algorithm. The optimal values of the parameters depend on the specific physics process: typical value required for the mistagging rate are around 10^{-2}. The most performant algorithm is the one which provides the highest $b-$tagging efficiency at a given mistagging rate.

In the following studies tracks and vertices are reconstructed with the algorithms described in the previous chapter. Jets momenta are provided by the PYTHIA's PYCELL routine. This is an almost ideal evaluation of the jet direction and can be achieved only with the most sophisticated off-line algorithms. On the other hand, it allows to decouple the degradation in performance due to the Tracker from those due to Calorimetry. Tracks were associated to a jet if $\Delta R < 0.4$.

The effect of the primary vertex reconstruction, jet direction reconstruction, low and high luminosity pile-up are also being investigated and will be reported in [108].

The performance of the algorithms using track counting, jet probability and secondary vertices are first analysed independently, then results are compared.

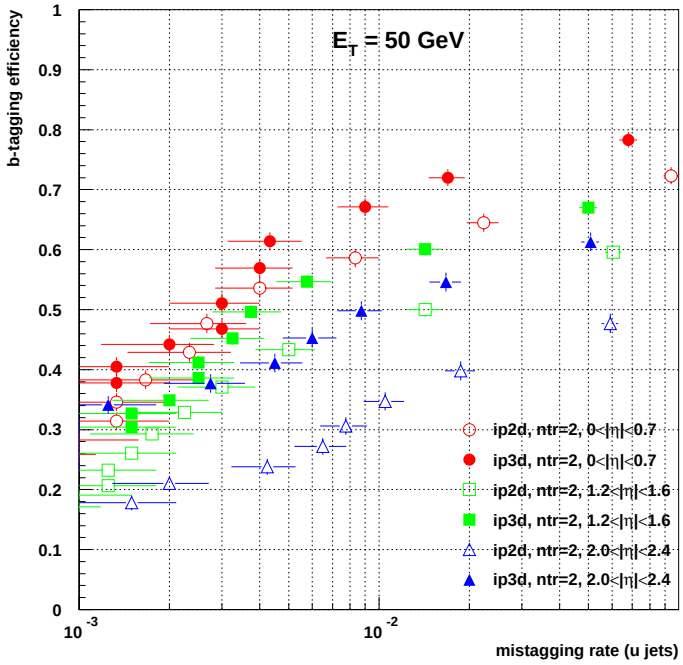

Figure 6.12: $b-$tagging efficiency vs mistagging rate from $u-$jets, obtained with the track counting algorithm based on transverse (ip2d) and three-dimensional (ip3d) impact parameter for E_T = 50 GeV jets in different pseudorapidity regions.

6.4.1 Results with the Track Counting Method

In the Track Counting method, a set of cuts are applied to select tracks with a good quality and to reject tracks from secondary interactions and Λ^0 and K_S decays. The quality cuts applied on tracks are $p_T > 1$ GeV/c, at least 3 pixel hits and at least 8 total associated hits. Secondary interactions with the material and Λ^0 and K_S decays occurring far away from the primary vertex are reduced by an upper threshold on the transverse impact parameter and the decay length. The upper threshold on the transverse impact parameter is independent on the jet transverse energy and pseudorapidity since it is a Lorentz invariant variable and is fixed at 2 mm. The upper threshold on the decay length depends on the jet momentum and varies between 1.5 and 10 cm for the events examined.

The optimisation of the cuts was performed by varying the thresholds of the cuts in order to maximise the $b-$tagging efficiency at a fixed mistagging rate between 0.1 and 1%[114].

Fig. 6.12 shows the performance of this algorithm for 50 GeV E_T jets in different pseudorapidity regions. The $b-$tagging efficiency is plotted against the mistagging rate for $u-$jets. The minimum number of tracks required above this threshold is 2. Both the transverse and three-dimensional impact parameter cases are shown: the latter has better performance since it uses a larger number of informations. At very low mistagging rates, the performance is comparable in the two cases because of the uncertainty on the primary vertex z coordinate, except for the forward region.

Very different efficiencies and mistagging rates can be achieved just tuning the threshold on significance and the number of tracks with impact parameter above threshold. The performance decreases with pseudorapidity due to the larger amount of material budget,

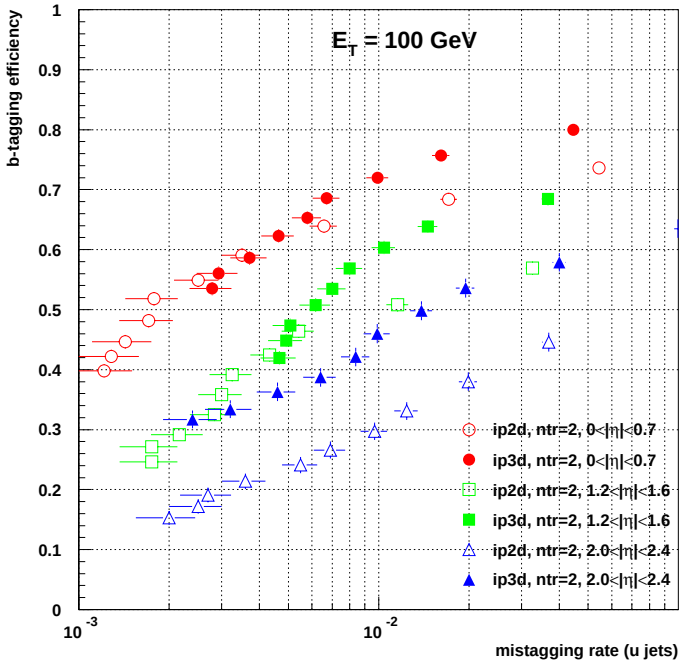

Figure 6.13: $b-$tagging efficiency vs mistagging rate from $u-$jets, obtained with the track counting algorithm based on transverse (ip2d) and three-dimensional (ip3d) impact parameter for $E_T =$ 100 GeV jets in different pseudorapidity regions.

which spoils the tracking performance, and to the larger distance of the innermost pixel hit from the primary interaction, which spoils the resolution in impact parameter.

The performance for $E_T = 100$ GeV jets is shown in Fig. 6.13. Tighter cuts are required in this case to achieve the same mistagging rate of jets with 50 GeV transverse energy due to the higher number of tracks in the jet cone coming from the underlying event. The best performance is still obtained with the three-dimensional information.

6.4.2 Results with the Probabilistic Method

A preliminary initialisation phase is required for the probabilistic method to extract the parameters of the resolution functions. Samples of approximately 10^4 $u\bar{u}$ events in the $0 < |\eta| < 0.7$, $1.2 < |\eta| < 1.6$ and $2.0 < |\eta| < 2.4$ intervals are used for this purpose. Tracks with at least 3 pixel hits, at least 8 total hits, $p_T > 1$ GeV/c and with a negative impact parameter larger than 2 mm are selected to perform the fit of the impact parameter significance distribution. For each η bin, two p intervals are considered to separate the low momentum regime, where the multiple scattering effects is more remarkable, from the high momentum regime, where the resolution on impact parameter is dominated by the intrinsic detector resolution. The thresholds on p are chosen at 5, 10 and 20 GeV for the three η bins to achieve a reasonable statistics for each bin.

The tracks inside the jets are passed to the algorithm and the following quality cuts are applied: $p_T > 1$ GeV/c, a transverse impact parameter ≤ 2 mm, and at least 3 pixel hits and 8 total hits.

The results obtained with the probabilistic algorithms are shown in figures 6.14 and 6.15 for $E_T = 50$ and 100 GeV in the same pseudorapidity regions for both transverse and

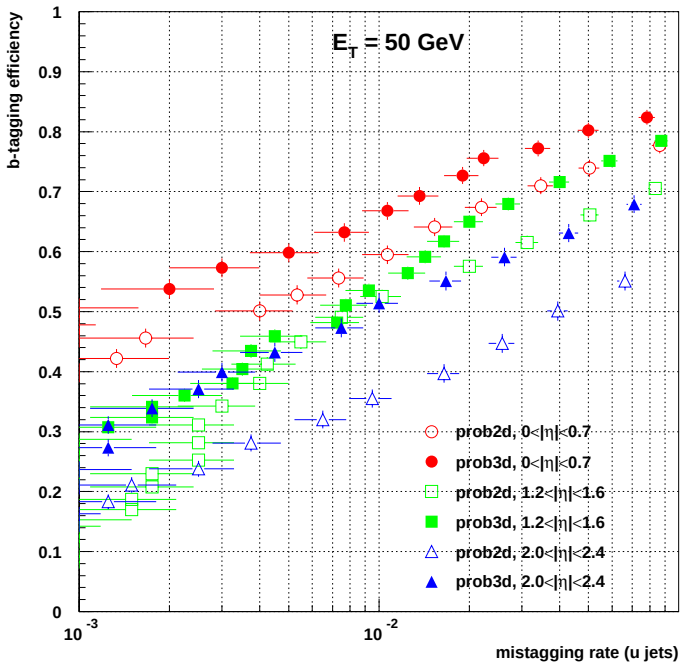

Figure 6.14: $b-$tagging efficiency vs mistagging rate from $u-$jets, obtained with the probabilistic algorithm based on transverse (prob2d) and three-dimensional (prob3d) impact parameter for $E_T = 50$ GeV jets in different pseudorapidity regions.

three-dimensional impact parameter. Points with the same markers correspond to different jet probability thresholds. Thresholds range between $10^{-0.5}$ and 10^{-10}. The performance are comparable with those of the method based on track counting: a better $b-$tagging efficiency can be achieved by the probabilistic algorithm at a mistagging rate of 0.1%.

6.4.3 Results with Secondary Vertices

Secondary Vertices were reconstructed with the method described in the previous section. Tracks with at least 3 pixel hits, at least 8 total hits, $p_T > 1$ GeV/c and a transverse impact parameter lower than 2 mm are passed to the secondary vertex finder.

Vertices are selected requiring a maximum radial distance of 3 cm from the primary vertex and a positive track impact parameter for two-tracks vertices.

The lower threshold on the significance on the three-dimensional distance from the primary vertex is varied to achieve different values of $b-$tagging efficiency and mistagging rates. The values which are used for the latter variable are 0, 2, 5, 10, 15 and 30.

Figures 6.16 and 6.17 show the performance for E_T=50 and 100 GeV respectively in different pseudorapidity regions.

The $b-$tagging efficiency of this method is limited by the secondary vertex reconstruction efficiency. On the other hand, the only requirement of a secondary vertex provides a very low mistagging rate, which can still be improved with additional kinematical requirements which are not included in these studies (invariant mass, ratio between the momentum associated to the vertex and the jet energy, etc.).

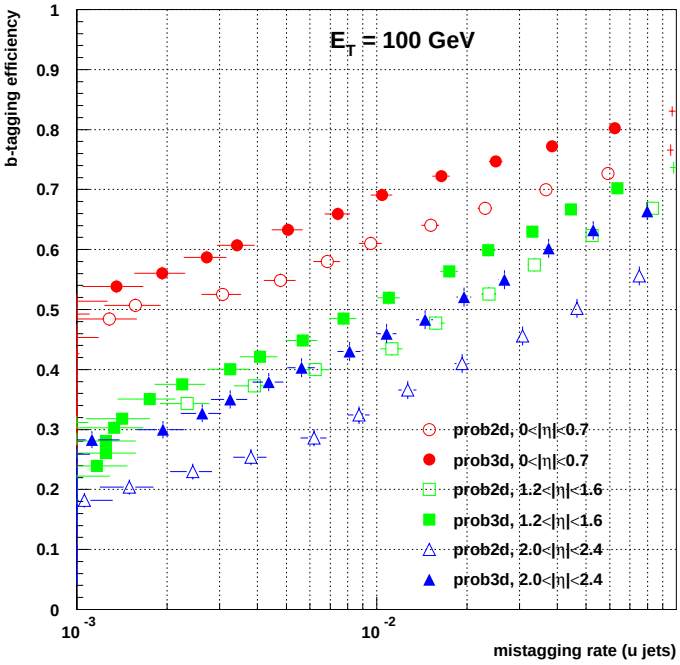

Figure 6.15: $b-$tagging efficiency vs mistagging rate from $u-$jets, obtained with the probabilistic algorithm based on transverse (prob2d) and three-dimensional (prob3d) impact parameter for $E_T = 100$ GeV jets in different pseudorapidity regions.

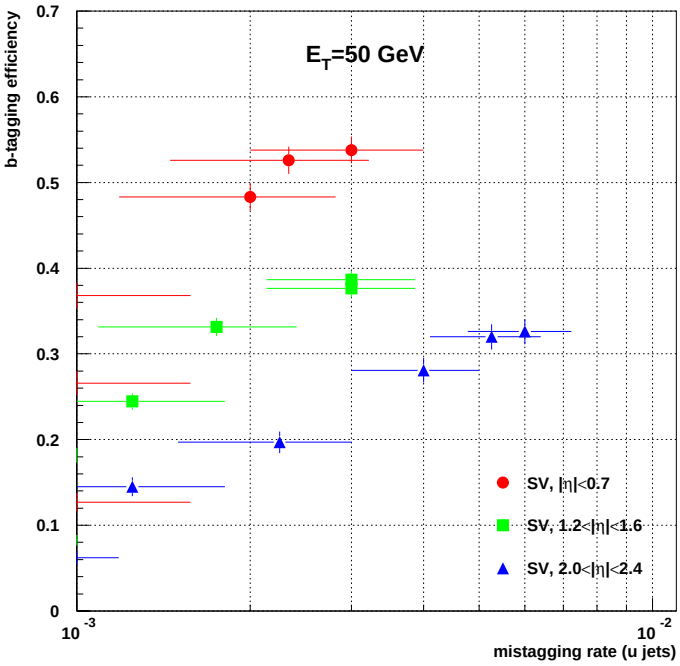

Figure 6.16: $b-$tagging efficiency vs mistagging rate from $u-$jets, obtained with the algorithm based on secondary vertices (SV) for $E_T = 50$ GeV jets in different pseudorapidity regions.

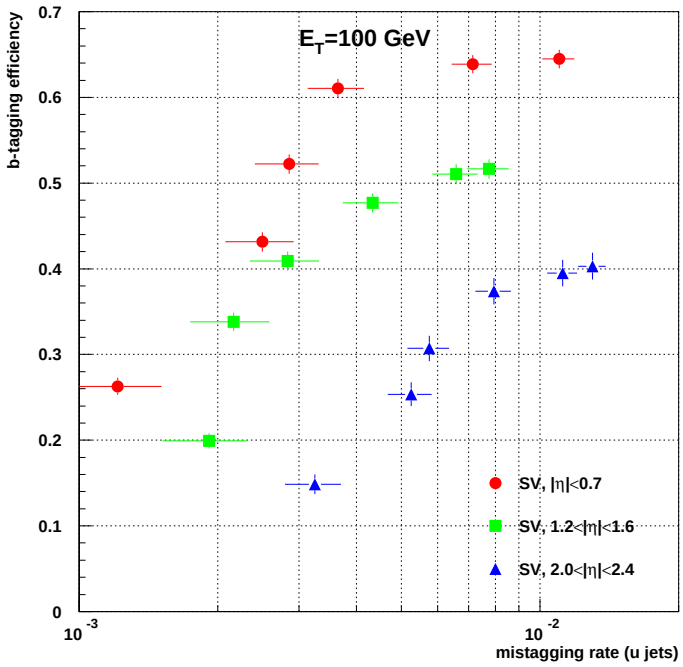

Figure 6.17: $b-$tagging efficiency vs mistagging rate from $u-$jets, obtained with the algorithm based on secondary vertices (SV) for $E_T = 100$ GeV jets in different pseudorapidity regions.

6.4.4 Comparison between Algorithms

For each algorithm described, the best $b-$tagging efficiencies which can be achieved at mistagging rates of 5×10^{-3} and 10^{-2} in different η intervals are shown in Figures 6.18 and 6.19 for $E_T = 50$ and 100 GeV respectively. In the $E_T = 50$ GeV and $\epsilon_u = 10^{-2}$ case, the performance of the algorithm based on secondary vertices is not shown since the mistagging rate is always below 10^{-2}.

For $E_T = 50$ GeV jets, the methods based on impact parameter have a comparable performance while the method based on secondary vertices has a worst $b-$tagging efficiency. This effect does not hold in 100 GeV E_T jets.

Although the methods examined exploit the informations on reconstructed tracks in different ways, they provide a similar performance in all the jet pseudorapidity intervals and at different jet transverse energies.

6.4.5 Rejection of $c-$jets

The mistagging rate due to $c-$jets is estimated by applying the same algorithms which are used for $u-$jet rejection. No dedicated cut for $c-$jets rejection is introduced. Fig. 6.20 shows the mistagging rate from $c-$jets for $E_T = 100$ GeV and $|\eta| < 0.7$ obtained with the track counting algorithm, the probabilistic algorithms (both based on three-dimensional impact parameter) and the algorithm based on secondary vertices. The mistagging rate from $c-$jets is expressed with respect to the mistagging rate for $u-$jets and is compared with the corresponding $b-$tagging efficiencies.

At mistagging rates of $u-$jets around 10^{-2}, the mistagging rates from $c-$jets is approximately 3.5 times lower than the $b-$tagging efficiency for all the algorithms.

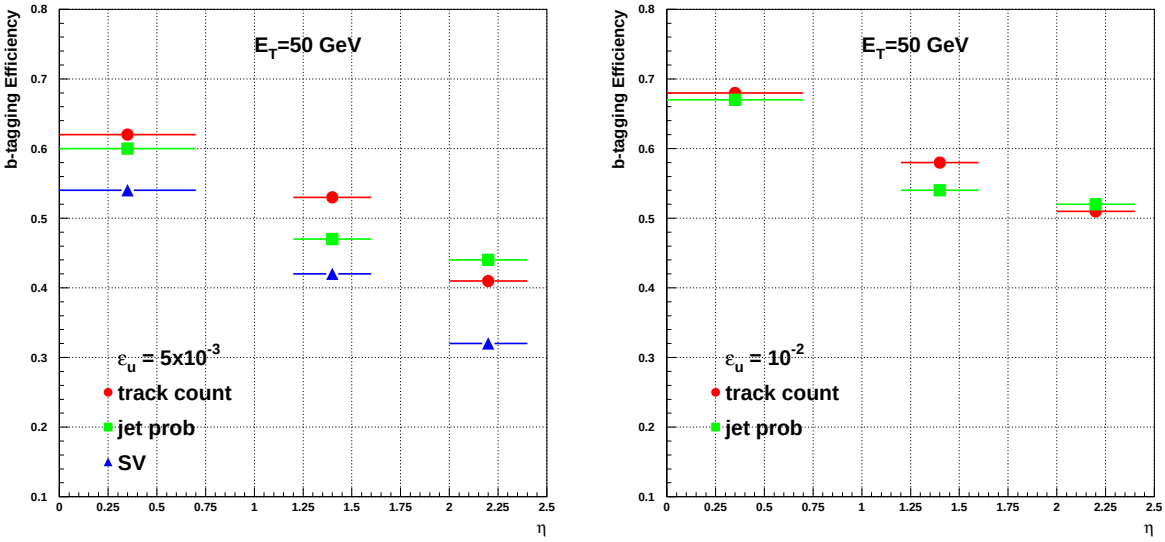

Figure 6.18: $b-$tagging efficiencies that can be achieved at 5×10^{-3} (left) and 10^{-2} (right) mistagging rate as a function of η for the algorithms based on track counting, jet probability and secondary vertices for $E_T = 50$ GeV.

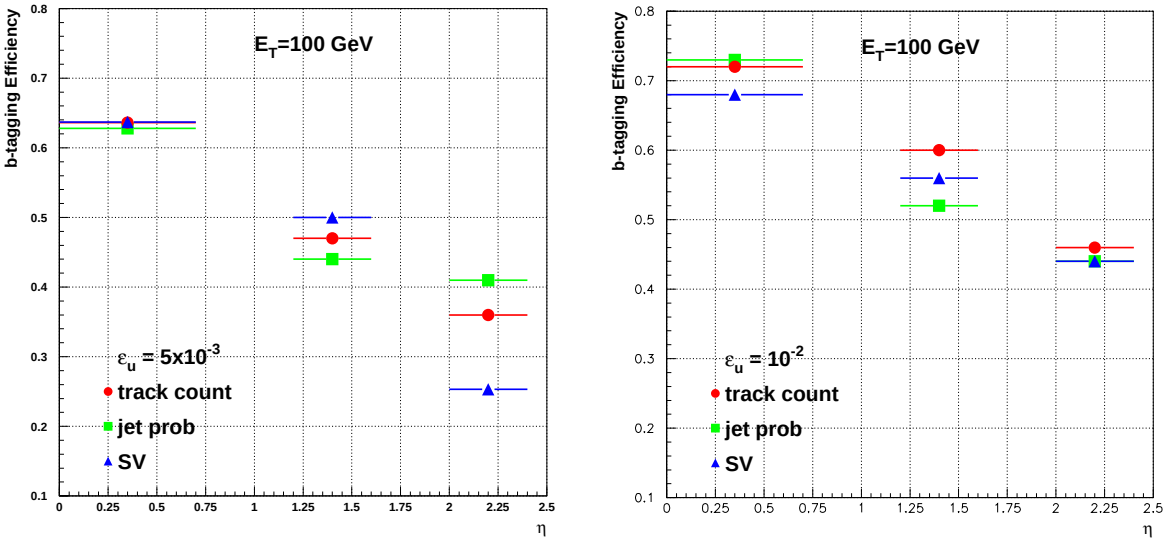

Figure 6.19: $b-$tagging efficiencies that can be achieved at 5×10^{-3} (left) and 10^{-2} (right) mistagging rate as a function of η for the algorithms based on track counting, jet probability and secondary vertices for $E_T = 100$ GeV jets.

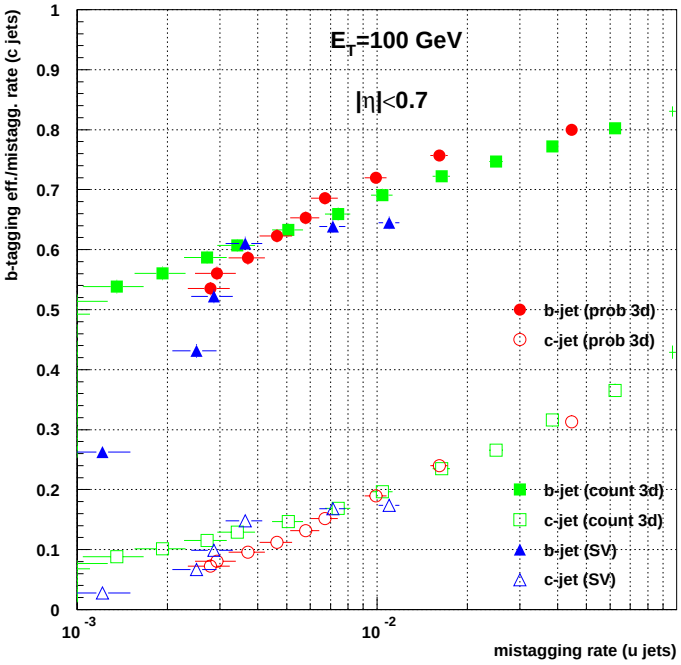

Figure 6.20: $b-$tagging efficiency and mistagging rate from $c-$jets vs mistagging rate from $u-$jets, obtained with the track counting and probabilistic algorithms and based on three-dimensional (ip3d) impact parameter and the algorithm based on secondary vertices for E_T = 100 GeV jets in different pseudorapidity regions.

Figures 6.21 and 6.22 show the mistagging rate of $c-$jets in different pseudorapidity ranges for the three algorithms for $\epsilon_u = 10^{-2}$ and 5×10^{-3} for 50 and 100 GeV E_T jets respectively.

The performance of the algorithms in $c-$hadron rejection is again comparable in each pseudorapidity interval.

6.4.6 Results with a Staged Pixel Detector Scenario

To estimate the difference in $b-$tagging performance due to the staged pixel detector layout, the hits in the outer pixel layers were ignored during the trajectory building phase.

The results obtained in these conditions are shown in Fig. 6.23 for the track counting algorithm based on transverse and three-dimensional impact parameter for $E_T = 100$ GeV di-jet events in all the pseudorapidity intervals. Tracks are required to have at least 2 and 3 pixel hits in the staged and default pixel detector scenario respectively, at least 5 hits in the Si-strip Tracker, $p_T > 1$ GeV/c and a transverse impact parameter smaller than 2 mm in module.

The effect of the staged pixel scenario is a loss of a 10% on average in $b-$tagging efficiency at the same mistagging rate.

6.4.7 HLT Performance

Inclusive $b-$tagging will be needed at HLT in order to reduce the total trigger rate below 100 Hz. In particular, a selection of events with $b-$jets will allow to control the QCD and

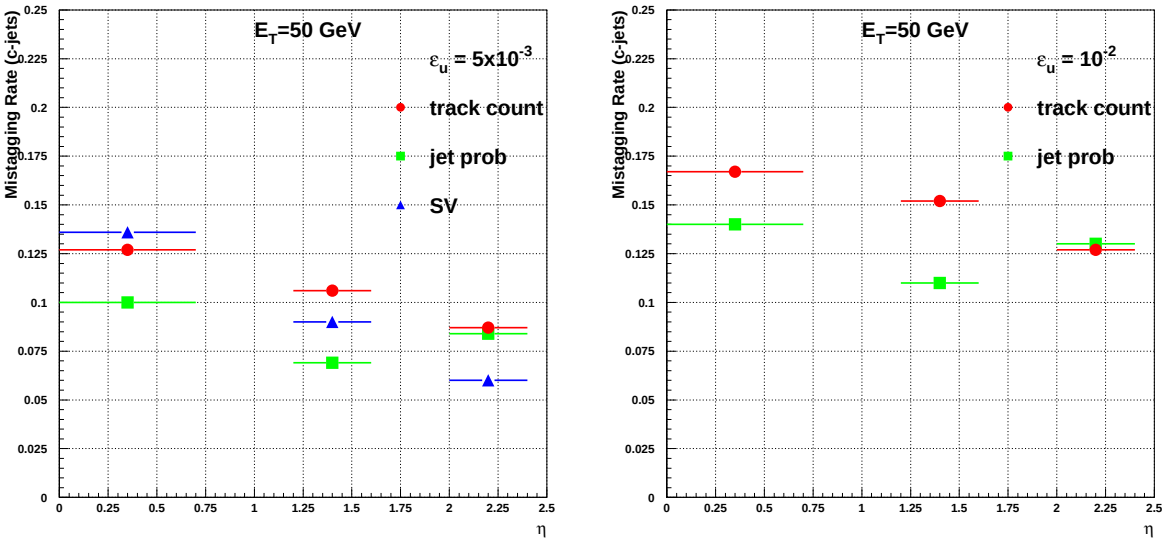

Figure 6.21: Mistagging rates of $c-$jets that can be achieved at 5×10^{-3} (left) and 10^{-2} (right) mistagging rate of $u-$jets as a function of η for the algorithms based on track counting, jet probability and secondary vertices for $E_T = 50$ GeV.

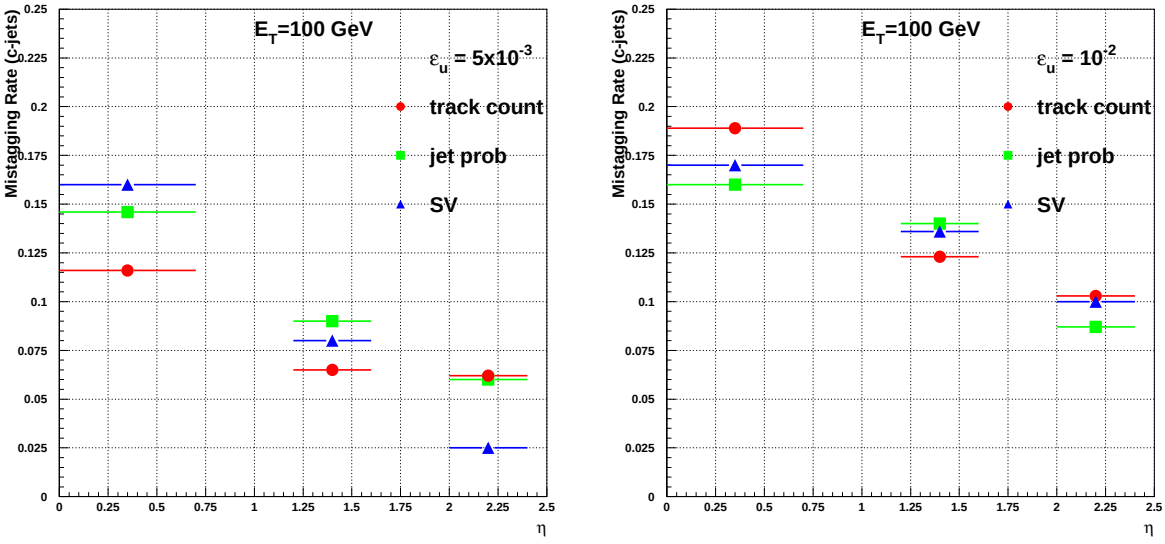

Figure 6.22: Mistagging rates of $c-$jets that can be achieved at 5×10^{-3} (left) and 10^{-2} (right) mistagging rate of $u-$jets as a function of η for the algorithms based on track counting, jet probability and secondary vertices for $E_T = 100$ GeV.

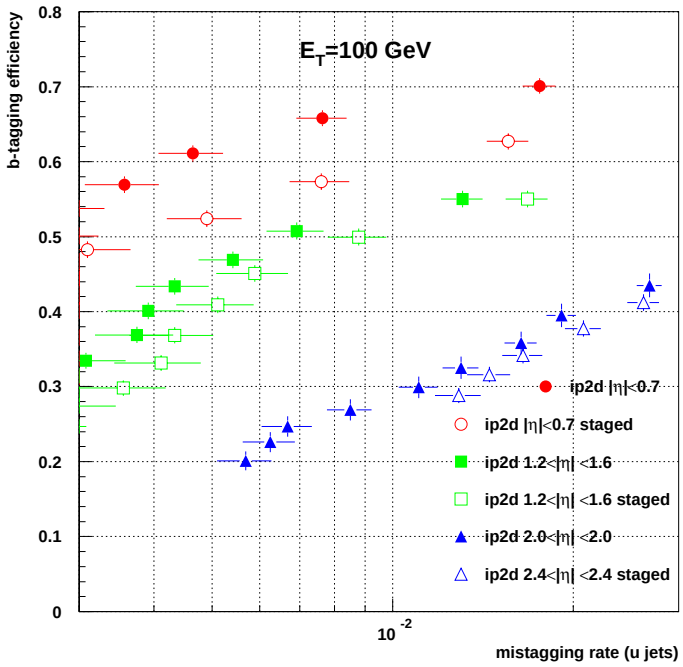

Figure 6.23: $b-$tagging efficiency vs mistagging rate from $u-$jets corresponding to different parameters of the track counting algorithm with transverse impact parameter for $E_T = 100$ GeV and different pseudorapidity intervals for the default and staged pixel detector scenario.

$W+$ jets background rates and thus keep a good trigger efficiency on the most interesting physics signals with $b-$jets in the final state.

Fig. 6.24 shows the performance which can be achieved with partial track reconstruction with 7 hits compared with the full online reconstruction in two η intervals for $E_T = 100$ GeV using the track counting algorithm based on transverse impact parameter. The performance is very similar in the two cases since it mostly depends on the resolution on the transverse impact parameter which has a weak dependence on the number of hits in the outermost layers.

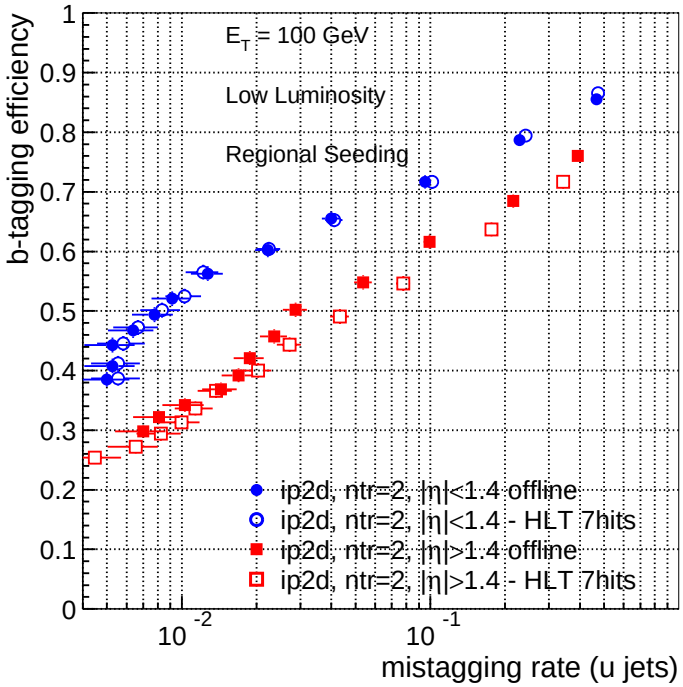

Figure 6.24: $b-$tagging efficiency vs mistagging rate from $u-$jets corresponding to different parameters of the track counting algorithm with transverse impact parameter for $E_T = 100$ GeV and different pseudorapidity intervals for complete offline reconstruction and partial track reconstruction with 7 hits.

Chapter 7

Scalar Top Quark Search

This chapter describes the scalar top quark search with the CMS detector. It contains a review of the main phenomenological aspects which motivate the search strategies together with details of the simulation, analysis and results.

7.1 Introduction

The inclusive searches, already described in section 3.1, offer the highest sensitivity to a global supersymmetry signal. However, to claim for evidence of supersymmetry, it would be very important to reconstruct each specific process foreseen by the theory.

Due to the large mixing, the scalar top quark (*stop* or $\tilde{t}$) would be the lightest among scalar quarks in a large region of supersymmetry parameter space and it would have a large production cross-section due to the fact that it would interact strongly.

For this reason this search represented one of the main discovery channels at LEP and Tevatron. Due to higher centre of mass energy and very high luminosity, LHC will allow to extend the $\tilde{t}$ search to higher masses and exploit new production and decay processes.

However, in most of the theoretical scenarios which can be envisaged, at LHC the $\tilde{t}$ would be superimposed on the overall supersymmetry processes which could have very complex final states. In this case the real challenge would be to disentangle each specific signal from the overall supersymmetry production.

7.2 Phenomenology

The mixing matrix for the $\tilde{t}$ has already been shown in eq.1.66. The eigenvalues of this matrix, $m_{\tilde{t}_{1,2}}$, are:

$$m^2_{\tilde{t}_{1,2}} = \frac{1}{2}\left[m^2_L + m^2_R \pm \sqrt{(m^2_L - m^2_R)^2 + 4a^2_t m^2_t}\right]. \tag{7.1}$$

The physical $\tilde{t}$ states associated with them, $\tilde{t}_{1,2}$ are linear superpositions of the $\tilde{t}_{L,R}$ states according to the formula:

$$\begin{pmatrix} \tilde{t}_1 \\ \tilde{t}_2 \end{pmatrix} = \begin{pmatrix} \cos\theta_t & \sin\theta_t \\ -\sin\theta_t & \cos\theta_t \end{pmatrix} \begin{pmatrix} \tilde{t}_L \\ \tilde{t}_R \end{pmatrix}. \tag{7.2}$$

Here θ_t is a mixing angle and is related to the masses and parameters of the theory through the relation[20]:

$$\tan 2\theta_t \sim \frac{2m_t(A_t + \mu \cot \beta)}{\Delta m_{\tilde{t}}^2} \sim \frac{2m_t A_t}{\Delta m_{\tilde{t}}^2}. \tag{7.3}$$

where $\Delta m_{\tilde{t}}^2$ is the difference of the diagonal terms of the $\tilde{t}$ mass matrix of eq.1.66. In absence of such mixing the eigenvalues $m_{\tilde{t}_{1,2}}$ would be exactly equal to $m_{\tilde{t}_{L,R}}$ and they would depend on the m_0 and $m_{1/2}$ parameters entering in the diagonal terms of the matrix. A large value of A_0 would increase the mixing through the A_t parameter and push the lightest eigenstate to even lower mass values[20].

Since all searches aim at the lightest $\tilde{t}$ eigenstate, the $\tilde{t}$ symbol will refer to the $\tilde{t}_1$. The dependence of the $\tilde{t}$ mass as a function of m_0, for different $m_{1/2}$ and fixed $\tan\beta = 10$, $\mu > 0$ and $A_0 = 0$, is shown in Fig. 7.1 (from PYTHIA).

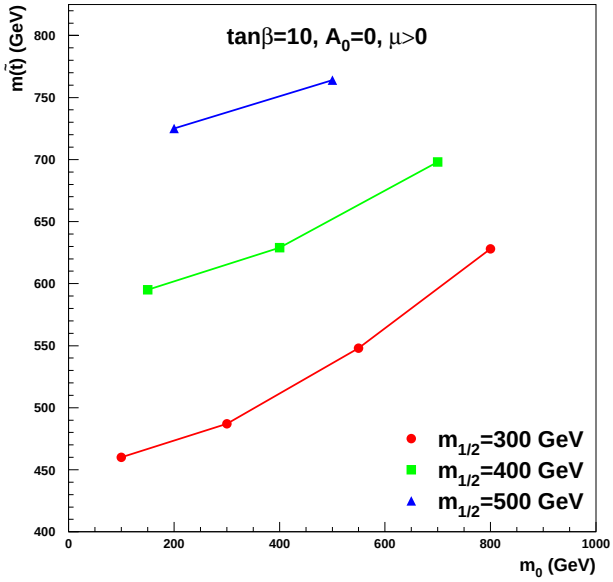

Figure 7.1: $\tilde{t}$ mass as a function of m_0 for different $m_{1/2}$ and fixed $\tan\beta = 10$, $\mu > 0$ and $A_0 = 0$ (from PYTHIA).

Fig. 7.2 shows the isomass contours for $\tilde{t}$, plotted as a function of A_0 and m_0 for $\tan\beta = 10$, $\mu > 0$ and $m_{1/2} = 300$ GeV. The shaded regions are theoretically excluded. Even at very high values of m_0, corresponding to a very high mass spectrum of supersymmetric particles, the $\tilde{t}$ can be reasonably light for suitable values of A_0.

The dependence of the $\tilde{t}$ mass on $\tan\beta$ is weak: in Fig. 7.3 the $\tilde{t}$ iso-mass contours are shown in the plane $\tan\beta - a0$ (where $a_0 = A_0/(m_0^2 + m_{1/2}^2)^{1/2}$ is a parameter related to mixing) for $m_0 = m_{1/2} = 300$ GeV and $\mu > 0$. The dark shaded regions are excluded by the LEP Higgs mass bound, while the light shaded ones are theoretically excluded.

The $\tilde{t}$ can decay into final states involving quarks and gauginos depending on its own mass and on the masses of its decay products: if $m_{\tilde{t}} > m_{\tilde{\chi}_1^0} + m_t$ and $m_{\tilde{t}} > m_{\tilde{\chi}_1^\pm} + m_b$, the decay modes $\tilde{t} \to \tilde{\chi}_i^\pm b$ or $\tilde{t} \to \tilde{\chi}_i^0 t$ would be allowed [125][126][127]. In case $m_{\tilde{t}} < m_{\tilde{\chi}_1^0} + m_t$ or $m_{\tilde{t}} < m_{\tilde{\chi}_1^\pm} + m_b$, the only decay mode allowed would be $\tilde{t} \to \tilde{\chi}_1^0 c$ occurring radiatively or through flavour changing processes.

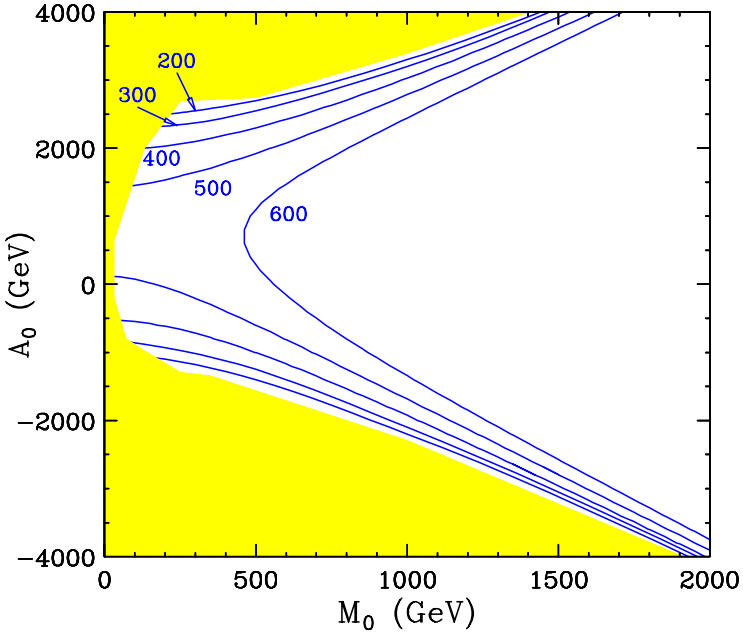

Figure 7.2: Contours of the $\tilde{t}_1$ mass (in GeV) in the $m_0 - A_0$ plane for fixed $m_{1/2} = 300$ GeV, $\tan\beta = 10$ and $\mu > 0$[32].

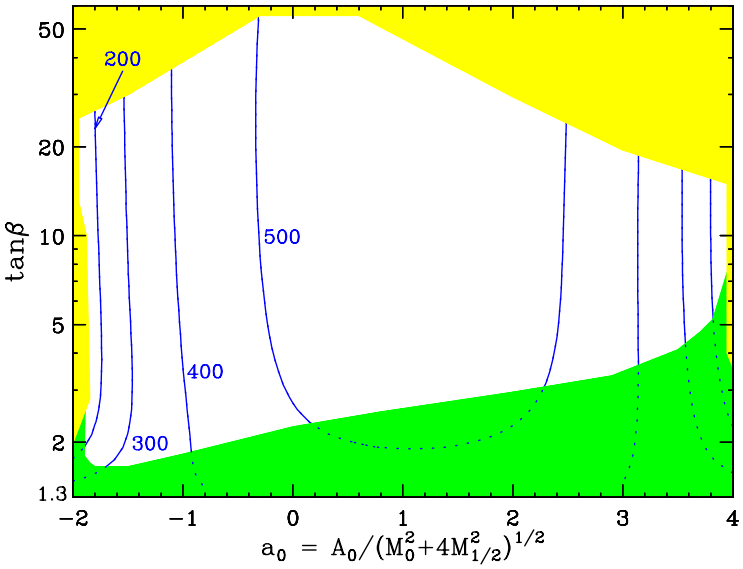

Figure 7.3: Contours of the light $\tilde{t}_1$ mass versus the parameter a_0 ($a_0 = A_0/(m_0^2 + m_{1/2}^2)^{1/2}$) related to mixing and $\tan\beta$ for $m_0 = m_{1/2} = 300$ GeV and $\mu > 0$. The light-shaded region is theoretically ruled out and the dark shaded one is ruled out by the Higgs mass constraint [32].

The branching ratios for the main decay modes are shown in Fig. 7.4 for the mSUGRA framework and $\tan\beta = 10$, $\mu > 0$ and $A_0 = 0$. The dependence on the m_0 and $m_{1/2}$ is remarkable since gaugino masses depend on $m_{1/2}$ through eq.1.65 while the $\tilde{t}_1$ mass dependence is shown in Fig. 7.1.

The decay channels to the heaviest gauginos become sizeable wherever allowed ($m_{\tilde{t}} > m_{\tilde{\chi}} + m_q$), so in the high $m_{1/2}$ region the dominant decay mode is $\tilde{t} \to \tilde{\chi}_1^0 t$ while $\tilde{t} \to \tilde{\chi}_1^\pm b$ dominates at smaller $\tilde{t}$ mass. For $m_0 > 2m_{1/2}$ the branching ratio for the mode $\tilde{t} \to \tilde{\chi}_2^\pm b$ becomes higher while the decay mode $\tilde{t} \to \tilde{\chi}_1^0 t$ decreases.

These branching ratios are approximately independent of $\tan\beta$ and sign of μ for $\tan\beta > 5$.

7.3 Production and Decay

The $\tilde{t}$ could be produced in a large number of physics processes at LHC: the dominant ones are $\tilde{t}$ production from gluino decay $\tilde{g} \to \tilde{t}\bar{t}$ ($\bar{\tilde{t}}t$) and $\tilde{t}$ pair production, $pp \to \tilde{t}\bar{\tilde{t}}$.

Inclusive gluino production has a cross section about 10 times larger than $\tilde{t}$ pair production and the decay branching ratio for $\tilde{g} \to \tilde{t}\bar{t}$ ($\bar{\tilde{t}}t$) would be larger than that of $\tilde{g} \to \tilde{q}\bar{q}$ ($\bar{\tilde{q}}q$) with $q \neq t$.

On the other hand, events with $t\tilde{t}$ plus additional jets from other $\tilde{q}$ or $\tilde{g}$ decays would be more complex to reconstruct and the higher cross section would be compensated by a lower efficiency and a larger combinatorics. However, both $\tilde{t}$ pair production and $\tilde{t}$ production from $\tilde{g}$ decays are helpful to study the $\tilde{t}$ phenomenology.

This discussion will be limited to the process $pp \to \tilde{t}\bar{\tilde{t}}$. Preliminary investigation on this process at LHC can be found in [6] and results on $pp \to \tilde{g}\bar{\tilde{g}} \to t\bar{t}\tilde{t}\bar{\tilde{t}} \to bb\bar{b}\bar{b}\mu^+\mu^+\mu^-\mu^-$ can be found in [128].

The main Feynman diagrams for $\tilde{t}$ pair production at LHC are sketched in Fig. 7.5.

The (a) diagrams correspond to the Born diagrams for $q\bar{q}$ annihilation and gluon fusion. Next-to-leading-order (NLO) diagrams through gluino and heavier squark exchange are displayed in (b) while (c) shows the diagrams for $\tilde{t}_1\tilde{t}_2$ production which is suppressed.

At fixed centre of mass energy, the cross section depends only on the $\tilde{t}$ mass and steeply decreases with it. Other parameters enter only in NLO contributions [129]. The cross-section for $pp \to \tilde{t}\bar{\tilde{t}}$ from PYTHIA is shown in Fig. 7.6 for $\tan\beta = 10$, $A_0 = 0$ and $\mu > 0$ as a function of $m_{\tilde{t}}$.

In this work only the decay modes $\tilde{t} \to \tilde{\chi}_1^0 t$ and $\tilde{t} \to \tilde{\chi}_1^\pm b$ will be taken into account since they are the simplest ones from the experimental point of view and cover a large fraction of the parameter space. The decay chains are sketched in Fig. 7.7.

In the first decay mode, the $\tilde{\chi}_1^0$ escapes from the detector, while the t decays into a $W^\pm$ and a b. In the latter case, the $\tilde{t}$ produces a b and a $\tilde{\chi}_1^\pm$ which decays through $\tilde{\chi}_1^\pm \to W^\pm\tilde{\chi}_1^0$ where the $\tilde{\chi}_1^0$ again escapes the detector. So in both decay modes a b quark, a W and a $\tilde{\chi}_1^0$ will be produced with different kinematics.

The sum of branching ratios of these decay modes is shown in Fig. 7.8 for $\tan\beta = 10$, $A_0 = 0$ and $\mu > 0$. These channels cover the whole region $m_{1/2} > m_0$. The complementary region, which is partially ruled out by the Higgs mass bound, can be covered through the process $\tilde{t} \to \tilde{\chi}_2^\pm b$ which would yield more complex signatures (mainly $\tilde{\chi}_2^\pm \to \tilde{\chi}_1^\pm Z^0$, $\tilde{\chi}_1^\pm h^0$ and $\tilde{\chi}_2^0 W^\pm$ with roughly 30% branching ratio each one).

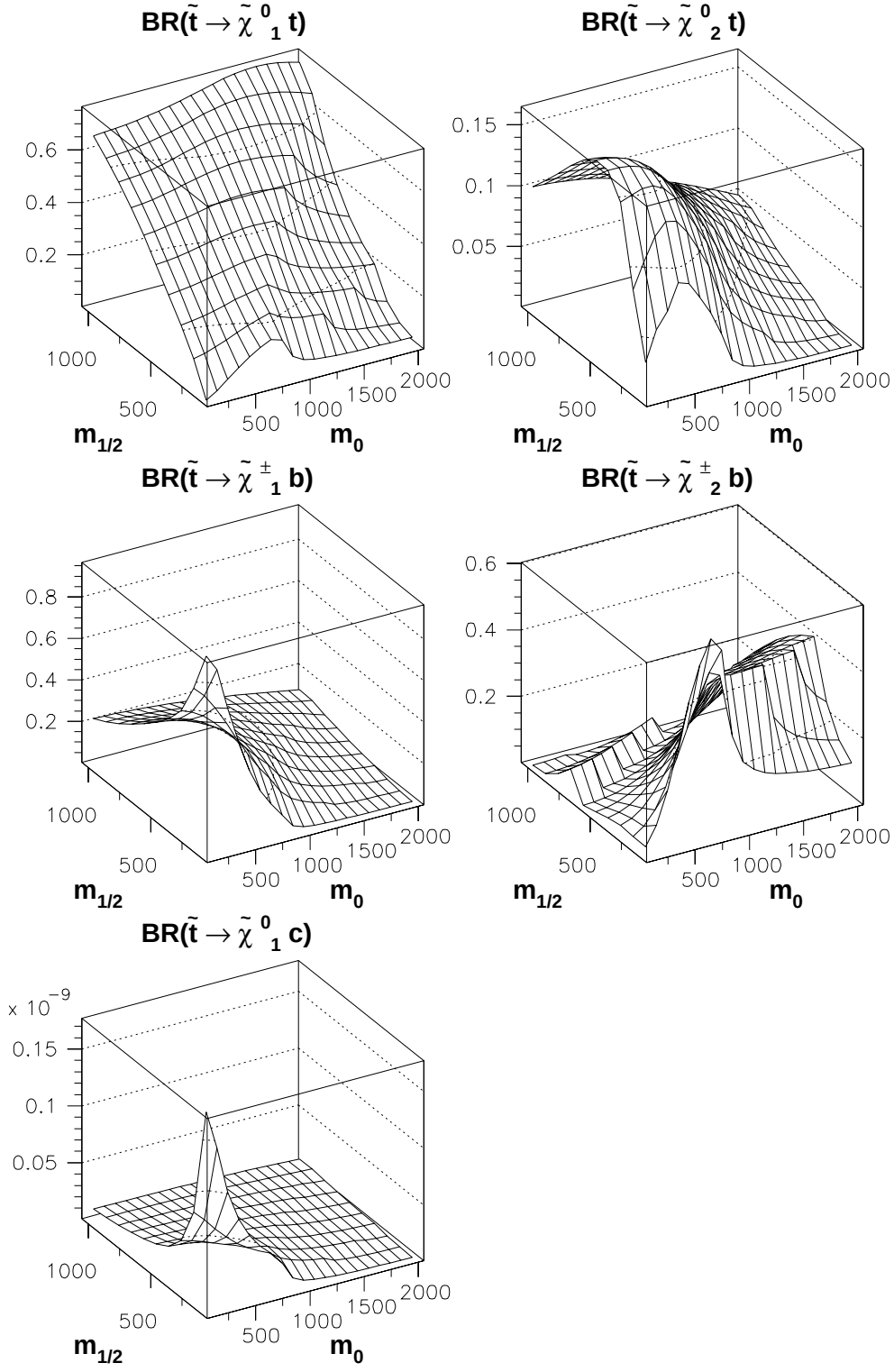

Figure 7.4: Branching ratios for the main $\tilde{t}$ decay modes at $\tan\beta = 10$, $\mu > 0$ and $A_0 = 0$ (from PYTHIA).

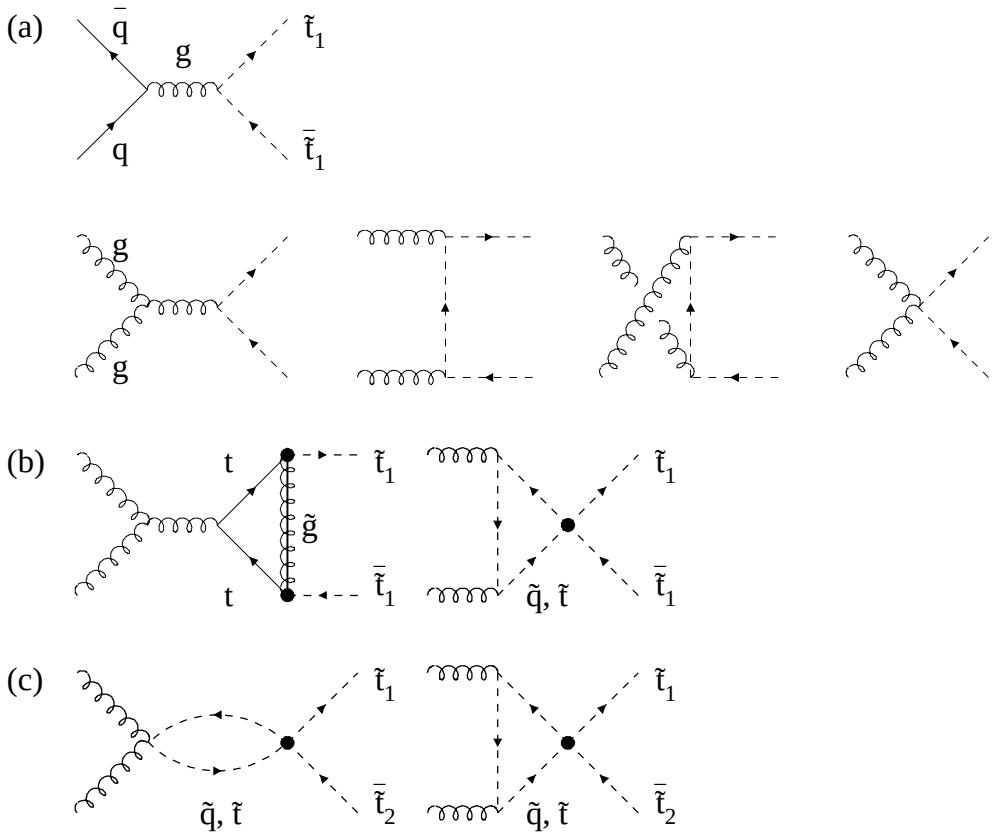

Figure 7.5: Feynman diagrams for $\tilde{t}$ pair production: (a) Born diagrams for $q\bar{q}$ annihilation and gluon fusion; (b) higher order diagrams for the diagonal production including $\tilde{t}$ mixing; (c) non-diagonal production in the limit of decoupling gluino[129].

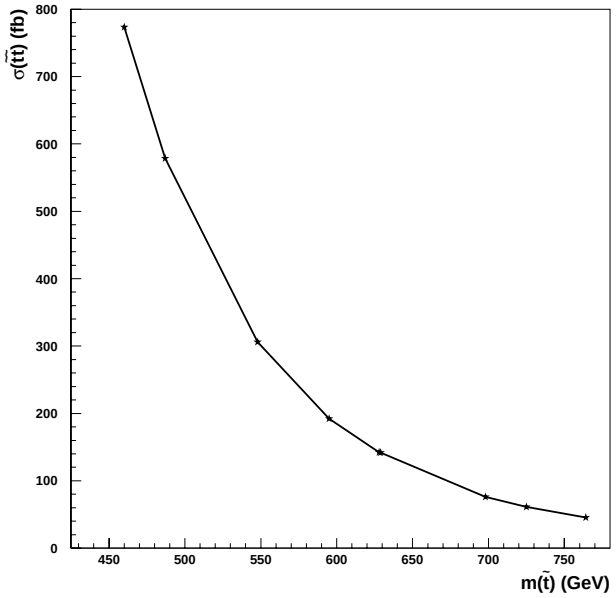

Figure 7.6: $\tilde{t}\bar{\tilde{t}}$ production cross section as a function of $m_{\tilde{t}}$ (from PYTHIA).

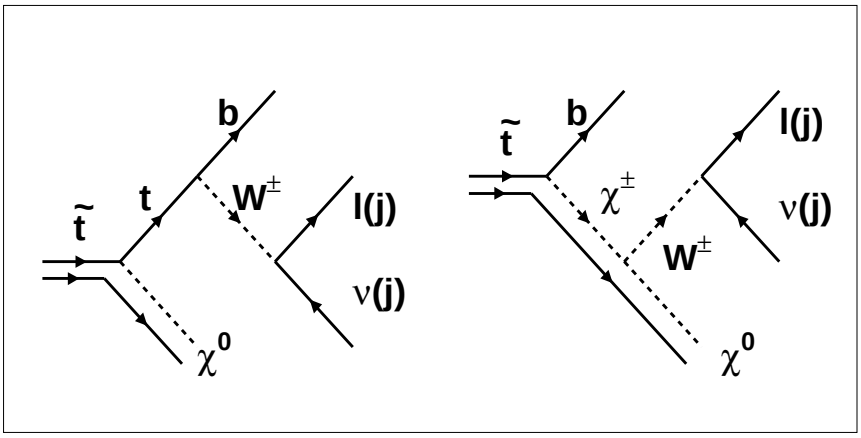

Figure 7.7: Decay chains for the processes $\tilde{t} \to \tilde{\chi}_1^0 t$ (left) and $\tilde{t} \to \tilde{\chi}_1^{\pm} b$ (right).

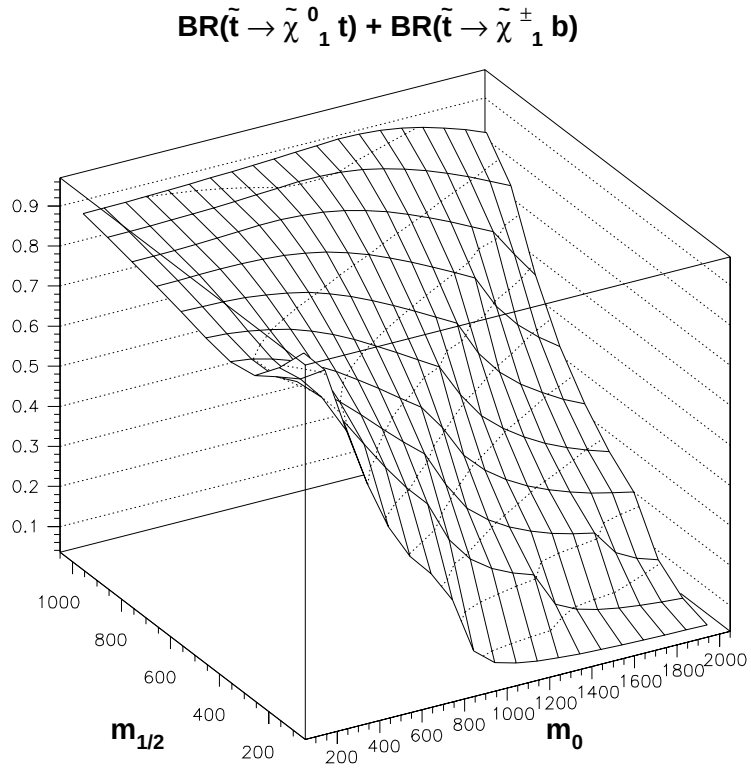

Figure 7.8: Sum of the branching ratios for the decay modes $\tilde{t} \to \tilde{\chi}_1^0 t$ and $\tilde{t} \to \tilde{\chi}_1^{\pm} b$ for different values of m_0 and $m_{1/2}$ at $\tan\beta = 10$, $\mu > 0$ and $A_0 = 0$ (from PYTHIA).

In $\tilde{t}\bar{\tilde{t}}$ events with $\tilde{t} \to \tilde{\chi}_1^0 t$ or $\tilde{t} \to \tilde{\chi}_1^{\pm} b$ there will be two b quarks, two $W^{\pm}$s and two $\tilde{\chi}_1^0$s in the final state. In this analysis one of the two Ws is required to decay leptonically into an electron or a muon in order to exploit triggers based on isolated high p_T leptons, while the other one is required to decay hadronically to increase the statistics. Therefore, signal events are required to have two $b-$jets, two non-$b-$jets from $W^{\pm}$, a lepton and a large E_T^{miss} due to a neutrino and two escaping neutralinos.

In principle, fully hadronic events could be considered, since they would have a large energy deposition in the hadron calorimeter and a large E_T^{miss} for triggering. However, in this case, reconstruction is expected to be very complex.

The main Standard Model background for this signal is the $t\bar{t}$ production: since two real top are present in these events, the particle content in the final state will be the same. The main difference will be on the kinematics, since the signal events will produce higher p_t particles and larger E_T^{miss}.

$W^{\pm}$ plus jets (Wj) would also be a dangerous background because it has a very large cross-section, a high p_T lepton and hadron jets in the final state. However, it can be reduced by the cuts for $t\bar{t}$ rejection and $b-$tagging.

Finally, there are other processes like Z^0 plus jets (Zj), $W^{\pm}W^{\pm}$ (WW), and $W^{\pm}Z^0$ (WZ) which can mimic the signal but, as it will be shown later, they will be reduced by the cuts on $t\bar{t}$ and Wj.

In Table 7.1 the cross sections for the main background processes are reported (with no cuts at generation level). The number of events expected at $\int \mathcal{L}dt = 30$ fb^{-1}, which corresponds to the overall low luminosity period of data taking is also reported. The anal-

Table 7.1: Expected cross sections and number of events at $\int \mathcal{L}dt = 30$ fb^{-1} for the main backgrounds (from PYTHIA).

	$t\bar{t}$	Wj	Zj	WW	WZ
σ (fb)	5.3×10^5	3.5×10^8	1.5×10^8	7×10^4	2.7×10^4
events	1.6×10^7	10^{10}	4.5×10^9	2.2×10^6	8×10^5

ysis is limited to the low luminosity running to study the physics potential of CMS in the first running period and to tune the analysis tools in a simpler environment. Measurements could be refined in the high luminosity period but a different detector performance is expected.

The analysis uses $\tan\beta = 10$ since it is the lowest $\tan\beta$ value with a reasonable amount of parameter space not yet excluded (see Fig. 1.8). Moreover the $\tilde{t}$ mass (Fig. 7.3) and the $\tilde{t}$ decay modes are not too sensitive to this parameter. Since this parameter is not crucial it is set at this value. The only difference is in the branching ratio of $\tilde{\chi}_1^{\pm} \to W^{\pm}\tilde{\chi}_1^0$ which decreases at higher $\tan\beta$ due to the increasing contribution of $\tilde{\chi}_1^{\pm} \to \tilde{\tau}\nu_{\tau}$ which occurs at low $m_{1/2}$. For this reason the $\tan\beta = 35$ case is also taken into account to compare the performance at different $\tan\beta$ values.

The μ sign is always kept positive since no sizeable effect related to it is observable in the $\tilde{t}$ sector and it has a larger region in the parameter space compatible with it (see Fig. 1.8). Different A_0 values were considered to explore the performance in many $\tilde{t}$ mass scenarios.

The analysis was aimed at looking for $\tilde{t}$ masses between 400 and 700 GeV. Higher masses correspond to cross-sections too small to be visible at low luminosity. In the lighter mass case, the cross section is very large but events have softer final state particles and therefore are more similar to $t\bar{t}$ events. In the latter case a different analysis based on $t\bar{t}$ counting might give a better performance.

7.4 Event and Detector Simulation

Due to the large number of background events expected (from Table 7.1) a fast detector simulation was used for this analysis to achieve a reasonable statistics in a limited time.

The Monte Carlo production was divided, as usual, into two steps: generation of the primary interaction and simulation of the detector response.

The primary interaction was generated with the PYTHIA 6.152 package [115]. The informations about stable and long-lived particles produced by PYTHIA were passed to the fast detector simulation package, CMSJET[130] which provided reconstructed object (jets, leptons, tracks, photons and E_T^{miss}).

7.4.1 Event Generation

Standard model background events were generated with a statistics compatible with the one foreseen for the low luminosity period. The numbers of events for each background process are shown in Table 7.2.

Table 7.2: Number of events generated with CMSJET to simulate the Standard Model backgrounds.

	$t\bar{t}$	Wj ($\hat{p}_T > 60$ GeV)	Zj ($\hat{p}_T > 60$ GeV)	WW	WZ
events	1.35×10^7	1.75×10^7	10^7	2×10^6	0.95×10^6

For Wj and Zj events, a cut at generation level was applied to reduce the cross-sections to values which can allow the generation of Monte Carlo samples with a statistics which is comparable with the number of expected events. A cut $\hat{p}_T > 60$ GeV was applied, $\hat{p_T}$ being the p_T of the initial parton state involved in the hard scattering process. The probability for events with $\hat{p_T} < 60$ GeV to pass the signal selection criteria is small due to the fact that E_T^{miss} would be lower than the 100 GeV value set as threshold.

The $\hat{p_T}$ cut reduces the cross-sections for Wj and Zj processes to 6.238 nb and 2.469 nb respectively, corresponding to 1.87×10^8 and 7.4×10^7 events in the low luminosity period. The number of generated events for these two processes is approximately a factor 10 lower than the expected rate.

A sample of 2×10^7 inclusive QCD events with $\hat{p_T} > 100$ GeV (corresponding to a cross-section of 1.405×10^{-3} mb) was also generated to evaluate the contribution of this background; the number of expected non-$t\bar{t}$ QCD events passing trigger and E_T cuts described later is more than ~ 250 times lower than that of W+jets events, so this background is ignored in the analysis.

Supersymmetry processes were generated with the SPYTHIA[131] Monte Carlo which is included in the PYTHIA package. Parameters at unification scale are introduced as external input parameters and the relevant quantities are calculated through the RGE equations extrapolating the input values at GUT scale down to the electroweak scale. Approximate analytical formulas[132] are used to parametrise the solutions of RGE and results are in agreement within 10% with ISAJET[65] where equations are solved analytically.

One loop corrections to chargino and neutralino masses are not yet included in the current Monte Carlo packages, so masses, cross-sections and branching ratios predictions are not yet definitive.

Events were generated in many points of the parameter space to explore different kinematical topologies. For each point, the cross-sections for stop pair production (including both $gg \rightarrow \tilde{t}_1\bar{\tilde{t}}_1$ and $qq \rightarrow \tilde{t}_1\bar{\tilde{t}}_1$ processes) vary between 100 and 500 fb, yielding a few thousands events for the first 30 fb^{-1} of integrated luminosity. 10^4 signal events were generated for each point. Two signal productions were performed: a production where $\tilde{t}$ can decay into both $\tilde{t} \rightarrow t\tilde{\chi}_1^0$ and $\tilde{t} \rightarrow b\tilde{\chi}_1^{\pm}$ decay modes according to their branching ratios (events where the two stops decay in the two different modes are therefore included) and a production where only one of the two $\tilde{t}$ decay modes is allowed. The goal of the first production is to study the physics potential of CMS in the mSUGRA parameter space, while the goal of the second one is to study the single channel performance as a function of the $\tilde{t}$ and $\tilde{\chi}_1^0$ masses.

For each point in parameter space $1 - 2 \times 10^5$ events with all supersymmetry processes (except the signal) switched on were generated to study the supersymmetry background rejection of the selection critera.

7.4.2 Detector Simulation

The CMSJET package allows a fast detector simulation based on the parametrisation of the detector response. The detector performance is investigated with the complete detector simulation based on GEANT description. The four momenta from particle-level informations are smeared according to the resolution to reproduce the experimental response.

This procedure allows a large event production in a relatively short time scale, which make it possible to study physics processes which require a very large statistics. Moreover, it is in remarkable agreement with the complete detector simulation since it draws from it the parametrisation of the detector response.

For what concerns Calorimetry, a schematic Calorimeter Model was introduced in the simulation: both the Electromagnetic and the Hadron Calorimeters are reproduced with the same granularity and resolution foreseen in the final design. Cracks and dead regions are also taken into account in the simulation.

For each particle impinging on the calorimeter a shower is generated. Its starting position and width are those foreseen by the full detector simulation. A signal is associated to each fired cell according to a gaussian smearing of the fraction of the released energy. The energy resolution is parametrised by the formula:

$$\frac{\Delta E}{E} = \frac{a}{\sqrt{E}} \oplus b \oplus \frac{c}{E}. \tag{7.4}$$

The values of a, b and c are reported in Table 7.3 for ECAL, HCAL. A gaussian noise

Table 7.3: Granularity and energy resolution parameters implemented in the CMSJET calorimetry simulation[130].

	η range	$\Delta\phi \times \Delta\eta$	a	b	c
ECAL	$\lvert\eta\rvert$ <1.479	0.0174×0.0175	0.027	0.055	0.155
barrel	1.479 < $\lvert\eta\rvert$ <1.566	dead zone			
ECAL	1.566 < $\lvert\eta\rvert$ < 2	0.022×0.022			
end-cap	2 < $\lvert\eta\rvert$ < 2.25	0.029 × 0.029	0.057	0.055	0.210
	2.35 < $\lvert\eta\rvert$ < 2.61	0.043 × 0.043			
HCAL	$\lvert\eta\rvert$ < 2.26	0.087×0.087			
	2.26 < $\lvert\eta\rvert$ < 2.61	0.174 × 0.175	0.82 ÷ 0.86	0.065÷0.093	
	2.61 < $\lvert\eta\rvert$ < 3	0.195 × 0.349			
VFCAL	2.9 < $\lvert\eta\rvert$ < 5	0.17 × 0.1745	1.82(hadr.)	0.09(hadr.)	
			1.38(electr.)	0.05(electr.)	

distribution is also added to each cell according to the type of calorimeter.

The UA1 jet finding algorithm was implemented to provide a coarse jet reconstruction. It works as follows: a cell pre-selection is performed requiring an energy threshold of 500 MeV for ECAL and VFCAL and 750 MeV for HCAL; then cells with the highest energy are taken as jet initiators and the energy of the cells within $\Delta R < 0.5$ is added. Energy and direction of the jets are then updated and the procedure is iterated until the result is stable. If two jet initiators are found within the same cone and they share more than 75% of their energy they are merged. Jets with $E_T < 20$ GeV are discarded.

The $b-$tagging is performed through a parametrisation of the $b-$tagging efficiencies and mistagging rates obtained with full-simulation as a function of η and E_T. The $b-$tagging algorithm based on track counting was used for this parametrisation: at least two tracks with a transverse impact parameter significance larger than 3 (corresponding to a $b-$tagging efficiency of 50% and a mistagging rate of $u-$ jets of 0.5% for 100 GeV E_T jets with $|\eta|$ <0.7). The parametrisation used is related to the backup Tracker layout with two pixel layers in the barrel. The effect of a third pixel layer in the barrel and a second pixel layer in the end-caps is also investigated for the analysis. The effect of the improvement of $b-$tagging performance using more sophisticated algorithms and three-dimensional impact parameter is also studied.

The association between reconstructed jets and partons is also performed. The real flavour assigned to each jet is that one of the highest p_T parton, before final state radiation, within a cone defined by $\Delta R < 0.1$.

Electron and muon reconstruction is also performed through smearing. Electron 4-momenta are smeared according to their p_T and η values and are accepted if the total deposited energy does not exceed the smeared momentum of the Tracker. Muon 4-momenta are smeared with a Landau distribution. A 90% efficiency is assumed for electron and muon reconstruction. The lowest p_T thresholds for electron and muon are 20 and 10 GeV respectively.

Muons are defined to be isolated if the energy in the calorimeters around a $\Delta R < 0.3$ cone is less than 10% of the lepton energy.

The missing transverse momentum is calculated by reversing the sign of the transverse components of the vector sum of all momenta (leptons and calorimetry cells).

7.5 Signal Selection and Background Rejection

In this paragraph a description of the strategies for signal selection and Standard Model background rejection is provided. The main distributions used for this purpose are shown for the point of parameter space $m_0 = 400$ GeV, $m_{1/2} = 400$ GeV, $A_0 = 0$, $\mu > 0$, $\tan\beta = 10$ corresponding to a $m_{\tilde{t}} = 629$ GeV, $m_{\tilde{\chi}_1^0} = 163$ GeV and $m_{\tilde{\chi}_1^\pm} = 315$ GeV.

The threshold values used in the selection were optimised for each point of parameter space under consideration.

7.5.1 Triggering

Single electron and muon triggers are exploited in these studies. These triggers are based on the requirements of an isolated electron or muon at Level 1. Lepton reconstruction is improved at higher trigger levels and $b-$tagging is performed, as it was anticipated in the previous chapter, in order to reduce the trigger rate to a level that can allow data storage.

Since the $b-$tagging performance at HLT is very close to the offline one, the effect of $b-$tagging at HLT on signal efficiency is very small. On the other hand, this solution prevents the QCD and W plus jets background rates to saturate the allowed bandwidth. Fig. 7.9 shows the total L1 muon trigger rate as a function of the muon p_T cut for a peak luminosity of $2 \times 10^{33}\ cm^{-2}\ s^{-1}$.

In the whole p_T range the rate is above 1 kHz: a muon p_T cut at 15 GeV corresponds to a L1 trigger rate of about 3 kHz. This rate can be reduced to nearly 30 Hz, which is compatible with the allowed bandwidth, requiring that at least one of the two highest E_T jets is $b - tagged$ by the track counting algorithm with at least 2 tracks with a transverse impact parameter significance larger than 2. The $b-$tagging cuts can be loosened at luminosities lower than the peak one, corresponding to a lower L1 rate. An improvement of the $b-$tagging performance allows to lower the cut on muon p_T and thus to include in the data rate a larger number of signals with softer muons in the final state.

A definitive list of trigger cuts is not yet available. However, a realistic set of tight cuts can be chosen for this analysis in order to guarantee an efficient signal trigger selection and an affordable data-rate. The threshold on the lepton p_T is set to 20 GeV/c and the isolation requirement is performed: for muon triggers the trigger efficiency is 90% and independent on p_T and η[133]. A comparable performance is assumed for the electron trigger for a higher p_T cut.

Since this analysis is focused to heavy $\tilde{t}$ far to be degenerate in mass with its decay products, this lepton p_T cut has no sizeable effect on the signal efficiency. Fig. 7.10 shows the p_T of the highest p_T lepton in signal events in one of the point in the mSUGRA parameter space studied. The fraction of leptons with p_T below the 20 GeV/c threshold is negligible.

Since the trigger simulation is not yet completely final, both signal and background estimates are multiplied by a factor 0.9 to include the inefficiency due to lepton selection at trigger level.

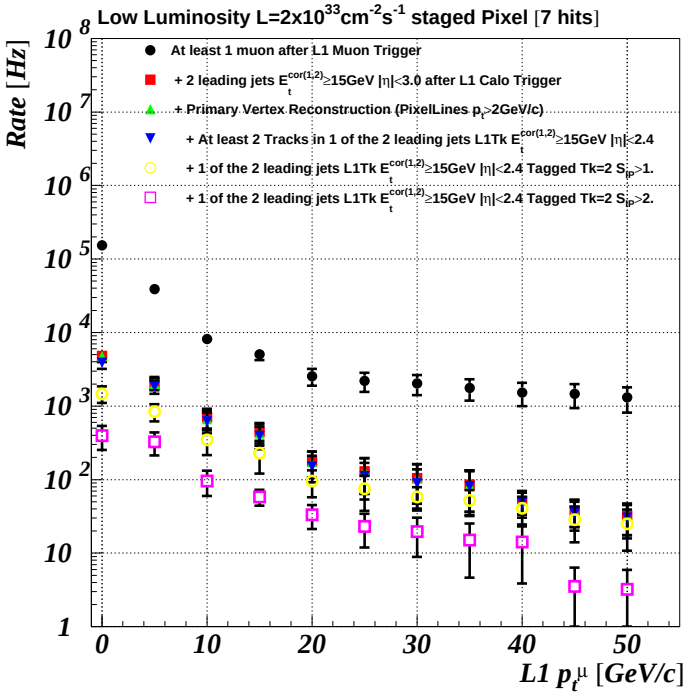

Figure 7.9: Rate at low luminosity as a function of the single muon threshold as measured by the L1 at after different requirements on jets, including $b-$tagging.

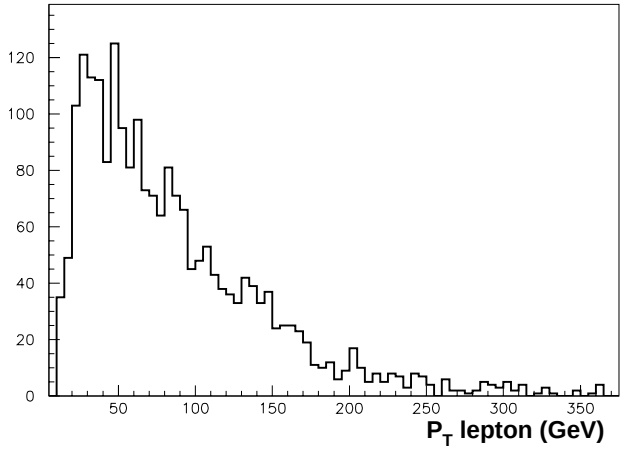

Figure 7.10: p_T of the highest p_T isolated lepton in $\tilde{t}\tilde{t}$ events ($m_0 = 400$ GeV, $m_{1/2} = 400$ GeV, $A_0 = 0$, $\mu > 0$, $\tan\beta = 10$).

For what concerns the $b-$tagging, the parametrisation described in the previous section is used: these cuts allow a good compromise between a large $b-$tagging efficiency and the required reduction of the QCD and W plus jets rates.

7.5.2 Signal Selection

In the signal events four hadron jets are foreseen. Two of the four jets are $b-$flavoured and come directly from the $\tilde{t}$ decay in case of the $\tilde{t} \to \tilde{\chi}_1^{\pm} b$ process or from $t \to bW^{\pm}$ for $\tilde{t} \to \tilde{\chi}_1^0 t$. The other two jets come from $W^{\pm}$ decays and are not $b-$flavoured. Jets from $\tilde{t}$ decay have always an E_T higher than jets coming from the underlying event since they come from a massive particle decay. The left side of Fig. 7.11 shows the E_T distribution for $b-$jets coming from the $\tilde{t}$ decay, non$-b$ jets from the $W^{\pm}$ decay and jets belonging to the underlying event for $\tilde{t} \to \tilde{\chi}_1^0 t$ (upper figure) and $\tilde{t} \to \tilde{\chi}_1^{\pm} b$ (lower figure). A jet from

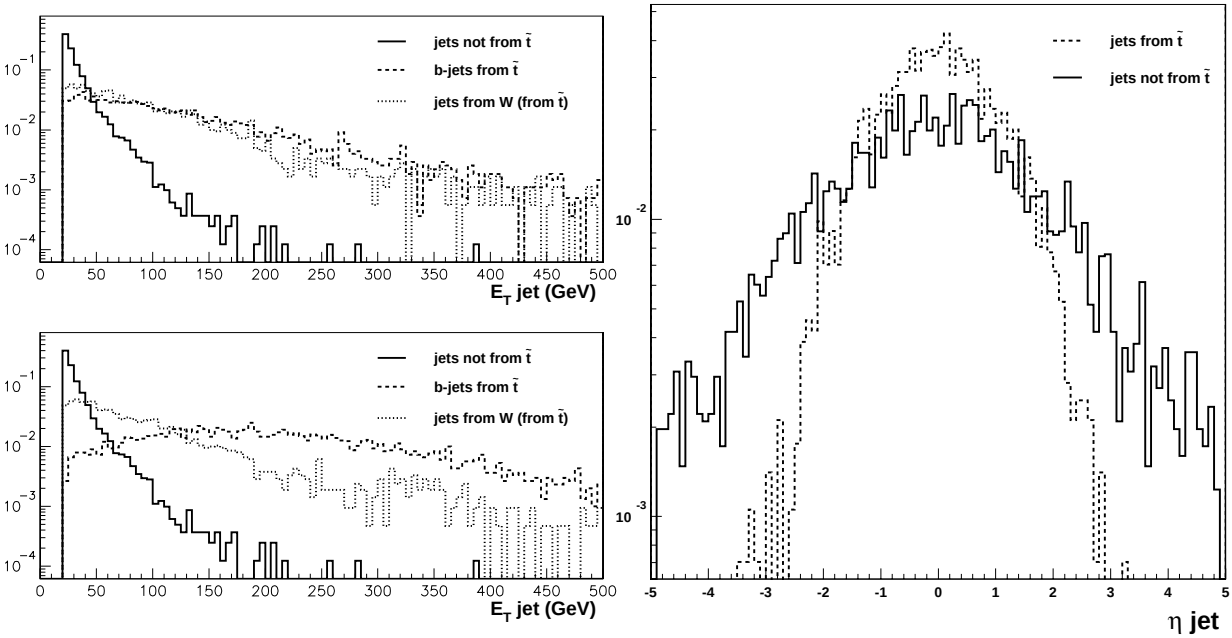

Figure 7.11: Left: Jet E_T for $b-$jets from $\tilde{t}$, jets coming from $W^{\pm}$ decays from $\tilde{t}$ and jets of the underlying event in the $\tilde{t} \to \tilde{\chi}_1^0 t$ and $\tilde{t} \to \tilde{\chi}_1^{\pm} b$ decays. Right: η distribution for jets from $\tilde{t}$ decays and from the underlying event ($m_0 = 400$ GeV, $m_{1/2} = 400$ GeV, $A_0 = 0$, $\mu > 0$, $\tan\beta = 10$).

a $\tilde{t}$ have an E_T value larger than those of the underlying event jets because of the high $\tilde{t}$ mass. Moreover the E_T values for $b-$jets are larger for the $\tilde{t} \to \tilde{\chi}_1^{\pm} b$ mode since the b comes directly from $\tilde{t}$ decay and thus gets a larger boost.

The right side of Fig. 7.11 shows the η distribution for jets from $\tilde{t}$ and the underlying event. The first ones are more central, because they are produced in a hard interaction, while the second ones have a broader distribution.

The first requirement for signal selection is the presence of at least three or four jets (depending on the values of SUSY parameters) with $|\eta| < 2.4$. No additional requirement on E_T was added to the $E_T > 20$ GeV of the jet finder because it would degrade the efficiency.

Another important requirement is a large E_T^{miss} in the event due to a neutrino from $W^{\pm}$ decay and two $\tilde{\chi}_1^0$ which escape the detector. Fig. 7.12 shows the E_T^{miss} distribution

for signal and $t\bar{t}$ background. A base cut $E_T^{miss} > 100$ GeV is required in this case. The E_T^{miss} threshold strongly depends on the masses of the supersymmetric particle involved in the process and ranges between 200 and 350 GeV for the considered points.

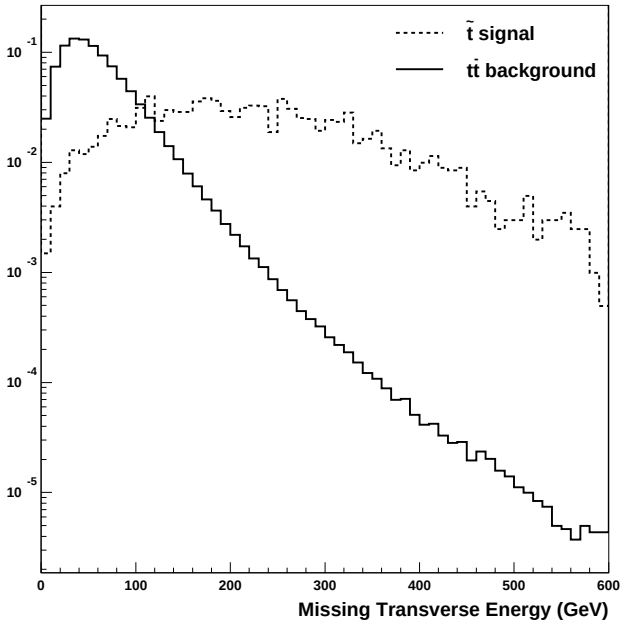

Figure 7.12: E_T^{miss} distribution for the $\tilde{t}\bar{\tilde{t}}$ signal ($m_0 = 400$ GeV, $m_{1/2} = 400$ GeV, $A_0 = 0$, $\mu > 0$, $\tan\beta = 10$) and the $t\bar{t}$ background.

7.5.3 Rejection of $W^{\pm}$+jets and Z^0+jets events

Part of the reduction of Wj and Zj backgrounds is performed at trigger level with $b-$tagging: in Wj events the only source of $b-$jets is the mistagging of c and u, d, s and $b-$jets from gluon radiation which are softer. In Zj events an additional source of real $b-$jets would be the $Z^0 \to b\bar{b}$ and mistagged $Z^0 \to c\bar{c}$ events.

Given an event with N jets , the probability to find a number of $b-$tagged jets n_b larger than s is provided by the binomial distribution:

$$P(n_b \geq s) \sim \sum_{j=s}^{N} \binom{N}{j} \varepsilon_f(E_T,\eta)\Big[1-\varepsilon_f(E_T,\eta)\Big]^{N-j} \tag{7.5}$$

$\varepsilon_f(E_T,\eta)$ being the probability to tag a jet as b and depends on E_T, η and the flavour f of the jet ($f = u,b,c$). The order of magnitude of ε_b, ε_c and ε_u are approximately $50-60\%$, 10% and $1-0.5\%$ respectively, according to the studies of the previous chapter.

Setting $s = 1$, the formula approximates to:

$$P(t\bar{t}|n_b \geq 1) \sim 2\bar{\varepsilon}_b - \bar{\varepsilon}_b^2, \qquad P(Wj|n_b \geq 1) \sim \bar{n}_J \bar{\varepsilon}_u \tag{7.6}$$

for $t\bar{t} - \tilde{t}\bar{\tilde{t}}$ and Wj events respectively after the requirement of at least one tagged jet. $\bar{n}_J$ is the average number of jets in a Wj event ($\bar{n}_J \sim 3$) and efficiencies are mediated over E_T and η. According to this estimate, the probability to find at least one $b-$jet is

larger than 70% in $t\bar{t}$ events while it is of the order of magnitude of the mistagging rate for W plus jets events. A more quantitative estimate of the effect of $b-$tagging is shown in paragraph 7.6.3.

In the Zj case the contributions of $t\bar{t}$ and WJ are summed linearly with the branching fractions of $Z^0 \to b\bar{b}$ ($BR(Z^0 \to b\bar{b})$) and $Z^0 \to q\bar{q}$ ($BR(Z^0 \to q\bar{q})$) ($q = u, d, s$) as weights plus a term corresponding to the $Z^0 \to c\bar{c}$ contribution:

$$P(Zj|n_b \geq 1) \sim \sum_{\alpha=b,c} BR(Z^0 \to \alpha\bar{\alpha})(2\bar{\varepsilon}_\alpha - \bar{\varepsilon}_\alpha^2) + BR(Z^0 \to q\bar{q})\bar{n}_J\bar{\varepsilon}_u. \qquad (7.7)$$

The number of true $b-$jets (i.e. from Monte Carlo truth) among the reconstructed ones and the identified $b-$jets is shown in Fig. 7.13 for signal and $t\bar{t}$, Wj and Zj backgrounds. This effect is compatible with the predictions of the above formulas.

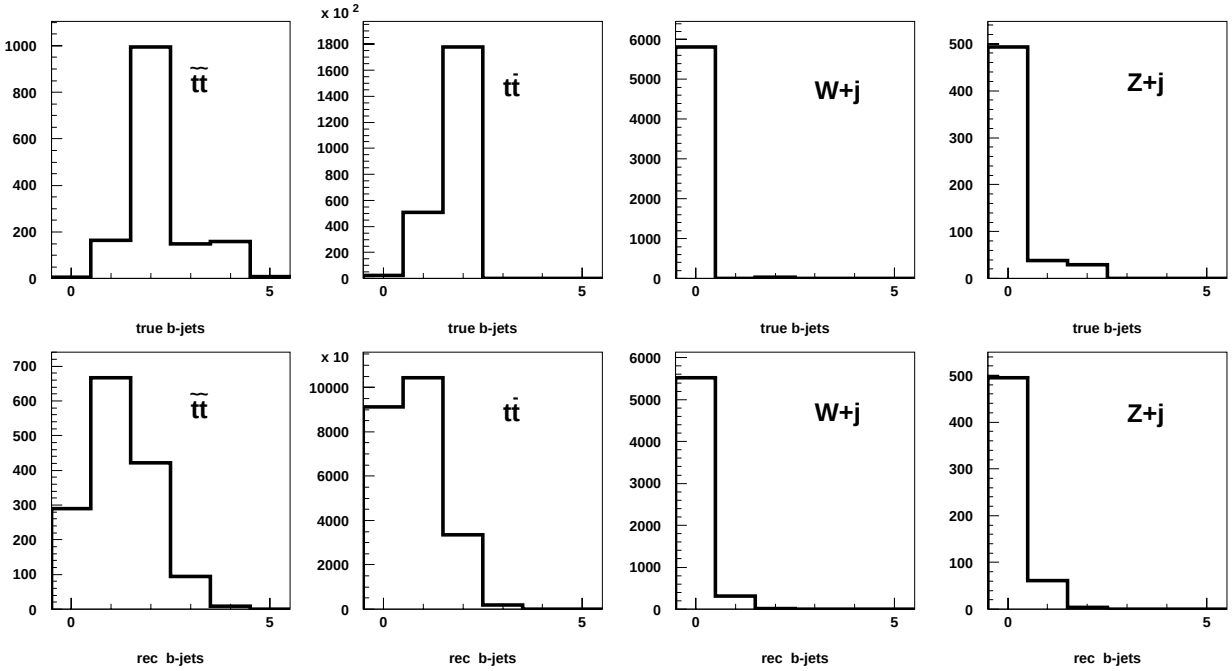

Figure 7.13: Number of true $b-$jets among all reconstructed ones and tagged $b-$jets for the $\tilde{t}\bar{\tilde{t}}$ ($m_0 = 400$ GeV, $m_{1/2} = 400$ GeV, $A_0 = 0$, $\mu > 0$, $\tan\beta = 10$), $t\bar{t}$, Wj and Zj samples.

Section 7.6 shows that the contribution of these backgrounds to the overall background is below 20%. No dedicated cuts would therefore be needed to reject the WW and WZ backgrounds.

7.5.4 Rejection of $t\bar{t}$ events

The cut on E_T^{miss} is the most powerful handle to reduce the $t\bar{t}$ background. However, the level of background events is still too large after this cut and other selection criteria must be added.

The transverse mass of the highest p_T lepton-E_T^{miss} system ($m_T^{l\nu}$) is another good variable. Since in $t\bar{t}$ events, with only one isolated lepton, the E_T^{miss} is due to the neutrino coming from the same $W^\pm$ of the lepton, the $m_T^{l\nu}$ is peaked at the $W^\pm$ mass. On the

other hand, in signal events, the lepton and E_T^{miss} should be more uncorrelated due to the presence of neutralinos and the distribution should cover higher values due to the harder signal spectrum. The distribution of $m_T^{l\nu}$ is shown in the left side of Fig. 7.14 for signal and $t\bar{t}$ events. The same considerations are valid for all other background events with a single

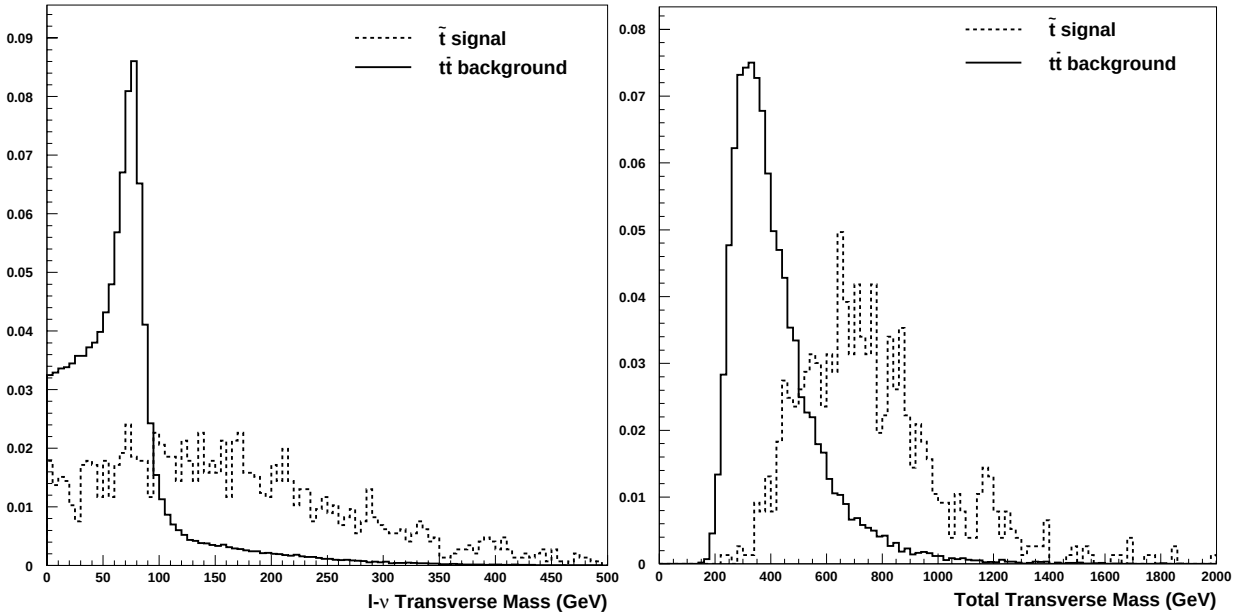

Figure 7.14: Transverse mass of the system lepton-E_T^{miss} (left) and total transverse mass (right) for the $\tilde{t}\bar{\tilde{t}}$ signal ($m_0 = 400$ GeV, $m_{1/2} = 400$ GeV, $A_0 = 0$, $\mu > 0$, $\tan\beta = 10$) and the $t\bar{t}$ background.

leptonic $W^{\pm}$ decay. A cut $m_T^{l\nu} > 100$ GeV removes a large fraction of these backgrounds.

The last variable useful to reject $t\bar{t}$ events is the total transverse mass, defined as the invariant mass between the E_T^{miss}, the p_T of all leptons and the E_T of all jets in the event (m_T^{tot}). The distribution of m_T^{tot} is shown in the right side of Fig. 7.14 for the benchmark point signal and $t\bar{t}$ background after the $m_{l\nu}$ cut. The signal has a m_T^{tot} higher than that one of the $t\bar{t}$ background and a lower bound on it is very powerful for background rejection. This threshold was tuned for each point in parameter space since its distribution strongly depends on the masses of particles involved in the process. Typical values for the lower m_T^{tot} threshold are 400-600 GeV.

7.6 Results

To fix the optimal set of cuts, the *signal significance*, s, or simply *significance*, is maximised. This quantity is defined as the ratio between the expected signal (S) and the expected background fluctuation ($\sqrt{B}$) which is assumed to be Poissonian:

$$s = \frac{S}{\sqrt{B}}. \tag{7.8}$$

Signal events were pre-selected from the Monte Carlo truth by requiring only one W decaying through $W^{\pm} \to l\nu_l$, $l = e, \mu$ and the other one decaying hadronically. With the available statistics the significance can be estimated with a 10% precision.

The cuts on E_T^{miss}, m_T^{tot}, the number of jets above threshold and $b-$jets were tuned in order to achieve the largest signal significance for each parameter space point.

Two different approaches were carried on to evaluate the performance: a *Model Independent* approach, to investigate the region in the $m_{\tilde{t}} - m_{\tilde{\chi}_1^0}$ plane where a significance larger than 5 can be achieved, and a model dependent search to investigate the sensitivity to a $\tilde{t}$ signal for a set of points in the mSUGRA parameter space.

Typical signal estimates range between 40 and 500 events in the points examined with the optimal cuts according to the mass and the cross-section. About 90% background is composed of $t\bar{t}$ events. The contribution of the Wj background is around 10% and the Zj, WW and WZ ones contribute for the 1-2%. Table 7.4 shows the signal, background and sensitivity estimates in four different points and the contribution of each background (using the samples which include both decay modes in the signal case).

Table 7.4: Expected signal and background events at $\mu < 0$, $\tan\beta = 10$ and $A_0 = 0$ and different m_0 and $m_{1/2}$ values.

m_0 (GeV)	400	200	800
$m_{1/2}$ (GeV)	400	500	300
$\tilde{t}\bar{\tilde{t}}$ signal	98 ± 6	46 ± 4	80 ± 5
$t\bar{t}$	235 ± 17	147 ± 13	238 ± 17
W+jets	11 ± 11	11 ± 11	11 ± 11
Z+jets	7 ± 7	0	7 ± 7
WW	1 ± 1	1 ± 1	1 ± 1
WZ	0	0	0
total bg	255 ± 21	159 ± 17	257 ± 22
$S/\sqrt{B}$	6.12 ± 0.5	3.6 ± 0.4	5 ± 0.5

7.6.1 *Model Independent* Results

The *Model Independent* search aims at providing separately, for each decay mode, a region in the $m_{\tilde{t}} - m_{\tilde{\chi}_1^0}$ plane where the $\tilde{t}$ would be visible with a significance larger than 5.

These results are *Model Independent* in the sense that they can be generalised to any MSSM scenario which foresees a relatively heavy $\tilde{t}$ quark decaying to the considered modes without any hypothesis on the mechanism of symmetry breaking. Moreover the $\tilde{t} \to \tilde{\chi}_1^0 t$ results can be extended to any scenario where the $\tilde{t}$ decays into a t and an LSP which would not necessarily be the lightest neutralino (e.g. it could be a gravitino in some gauge-mediated scenario with non-universal scalar masses). This is, of course, only a first approximation, since a specific model, the mSUGRA, was used to generate events and there can be additional model-dependent effects which are not included in the simulation.

Events used for this study were generated enabling only the decay mode under study: only one of the $\tilde{t} \to t\tilde{\chi}_1^0$ and $\tilde{t} \to b\tilde{\chi}_1^{\pm}$ decays is enabled in these samples. The mSUGRA parameters are tuned to achieve a wide set of $m_{\tilde{t}}$ and $m_{\tilde{\chi}_1^0}$ (and $m_{\tilde{\chi}_1^{\pm}}$). Since $m_{\tilde{\chi}_1^0}$ and $m_{\tilde{\chi}_1^{\pm}}$ depend only on $m_{1/2}$, for each value of $m_{1/2}$ different $m_{\tilde{t}}$ were obtained tuning m_0 and A_0.

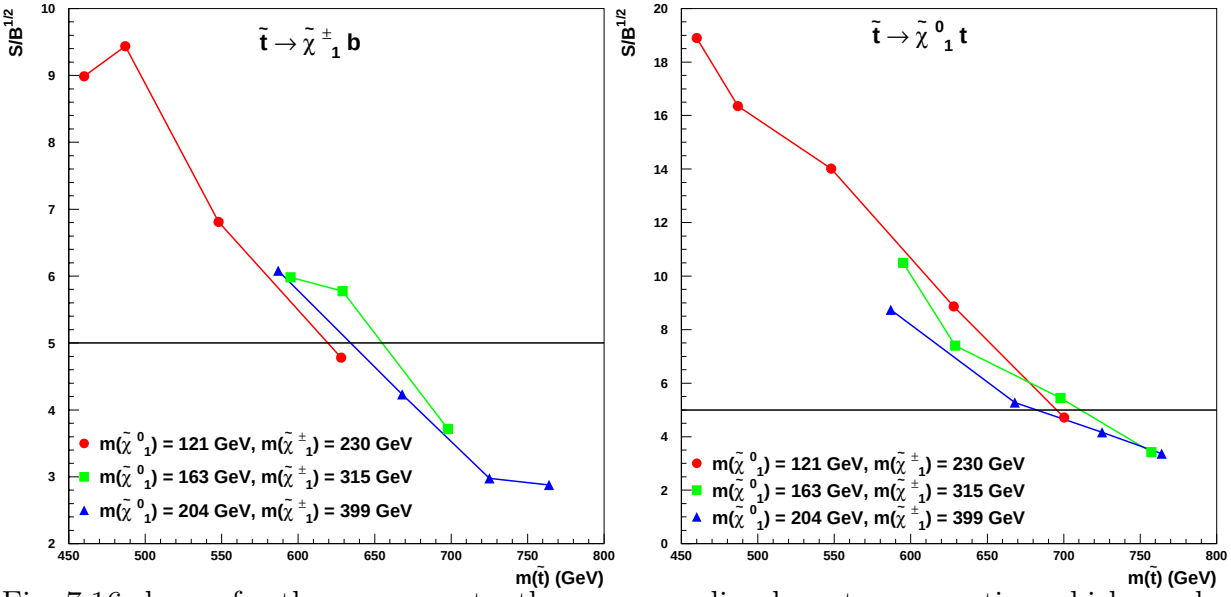

Fig. 7.16 shows, for the same events, the corresponding lowest cross-section which can be explored with a 5 sigma significance as a function of the $m_{\tilde{t}}$.

Figure 7.15: $S/B^{1/2}$ for three values of $m_{\tilde{\chi}_1^0}$ (and $m_{\tilde{\chi}_1^\pm}$) for different $m_{\tilde{t}}$ values for the processes $\tilde{t} \to \tilde{\chi}_1^\pm b$ (left) and $\tilde{t} \to \tilde{\chi}_1^0 t$ (right).

The signal significance is displayed in figure 7.15 with respect to the $\tilde{t}$ mass for different value of $m_{\tilde{\chi}_1^0}$ (and thus $m_{\tilde{\chi}_1^\pm}$) for the channels $\tilde{t} \to \tilde{\chi}_1^\pm b$ (left) and $\tilde{t} \to \tilde{\chi}_1^0 t$ (right) respectively. This quantity is defined as:

$$\sigma_{min} = \frac{5\sqrt{B}}{\mathcal{L}\varepsilon_S}, \tag{7.9}$$

B being the expected background, $\mathcal{L}$ the integrated Luminosity (30 fb^{-1} in this case) and ε_S the efficiency on signal. This formula can be easily derived from eq.7.8. The predicted $\tilde{t}\bar{\tilde{t}}$ cross section is also displayed for comparison: the $m_{\tilde{t}}$ value for which $\sigma_{min} = \sigma(\tilde{t}\bar{\tilde{t}})$ corresponds to the value for which $S/B^{1/2} = 5$ by definition of σ_{min}.

For a fixed $m_{\tilde{\chi}_1^0}$ the σ_{min} quantity would decrease with increasing $m_{\tilde{t}}$ because the efficiency on the signal would improve: the final state particles would be more energetic than those of background events and thus the signal could be better distinguished from the Standard Model background.

This effect would be compensated by the steeply decreasing $\tilde{t}\bar{\tilde{t}}$ cross section which would favor lower masses (still far from the degenerate scenario) with lower signal efficiencies. For this reason the signal significance shown in Fig. 7.15 decreases with $m_{\tilde{t}}$.

The $\tilde{t} \to \tilde{\chi}_1^0 t$ decay mode has a better performance than $\tilde{t} \to \tilde{\chi}_1^\pm b$ since it has broader E_T^{miss} and $m_T^{l\nu}$ distributions which improve the $t\bar{t}$ background rejection.

The values of $m_{\tilde{t}}$, and their corresponding $m_{\tilde{\chi}_1^0}$, for which the significance would be 5, define a contour in the $m_{\tilde{t}} - m_{\tilde{\chi}_1^0}$ plane which limits the parameter region where the signal could be detected with a significance $S/B^{1/2} > 5$ and constitutes the LHC discovery region (called *5 sigmas discovery contour*).

The contour is sketched in Fig. 7.17 for the decay modes $\tilde{t} \to \tilde{\chi}_1^\pm b$ and $\tilde{t} \to \tilde{\chi}_1^0 t$. An upper mass $m_{\tilde{t}} \sim 700$ GeV for the $\tilde{t} \to \tilde{\chi}_1^0 t$ decay mode and $m_{\tilde{t}} \sim 650$ GeV could be

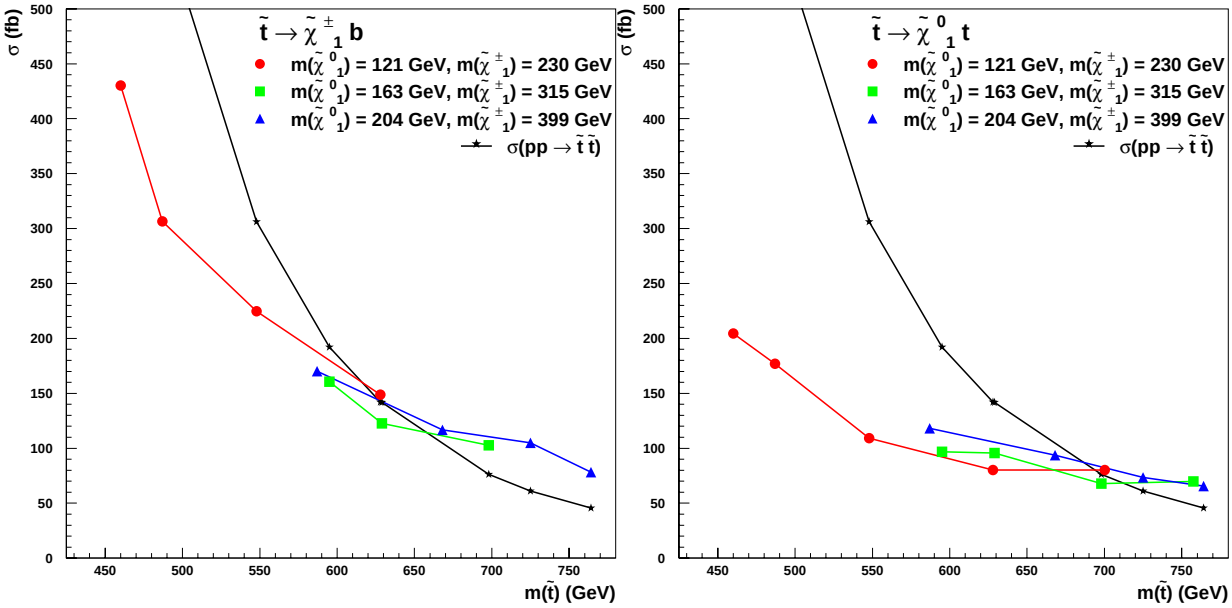

Figure 7.16: Minimum cross section which can be explored with 5 sigmas significance for three values of $m_{\tilde{\chi}^0_1}$ (and $m_{\tilde{\chi}^{\pm}_1}$) for different $m_{\tilde{t}}$ values for the processes $\tilde{t} \to \tilde{\chi}^{\pm}_1 b$ (left) and $\tilde{t} \to \tilde{\chi}^0_1 t$ (right). The $\tilde{t}$ pair production cross section is superimposed.

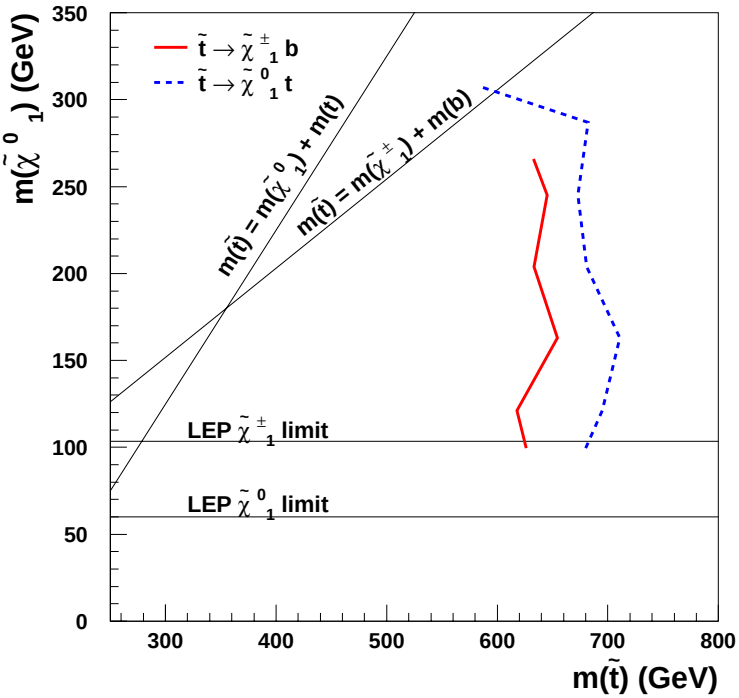

Figure 7.17: Five sigma discovery contours for the processes $\tilde{t} \to \tilde{\chi}^{\pm}_1 b$ and $\tilde{t} \to \tilde{\chi}^0_1 t$. The LEP exclusion limits on $m_{\tilde{\chi}^0_1}$ and $m_{\tilde{\chi}^{\pm}_1}$ as well as the lines corresponding to the kinematic limits for the decay channels are also displayed.

explored with this analysis. A lower bound for $m_{\tilde{t}}$ at fixed $m_{\tilde{\chi}_1^0}$ with these channels cannot be set since, for $m_{\tilde{t}}$ nearly degenerate with $\tilde{\chi}_1^0$ or $\tilde{\chi}_1^{\pm}$, a different analysis, based on low p_T decay products, would be required.

7.6.2 Results in the mSUGRA Framework

The same search strategy was also applied to the mSUGRA scenario. In this case events were generated in parameters space not yet ruled out by direct searches or by the indirect limits described in the second chapter.

A first set of events were generated for the case $\tan\beta = 10$ and $A_0 = 0$ case and then the effect of $\tan\beta$ and A_0 were analysed separately. Events were generated with the predicted branching ratios (Fig. 7.4) and only events with the decay modes $\tilde{t} \to \tilde{\chi}_1^0 t$ and $\tilde{t} \to \tilde{\chi}_1^{\pm} b$ and one $W \to l\nu_l$ ($l = e, \nu$) decay were pre-selected from the Monte Carlo truth.

The $A_0 = 0$ and $\tan\beta = 10$ case

A first set of points were chosen for signal generation at $\tan\beta = 10$, $\mu > 0$ and $A_0 = 0$ for different values of m_0 and $m_{1/2}$. Points are shown in Fig. 7.18 in the $m_0 - m_{1/2}$ plane.

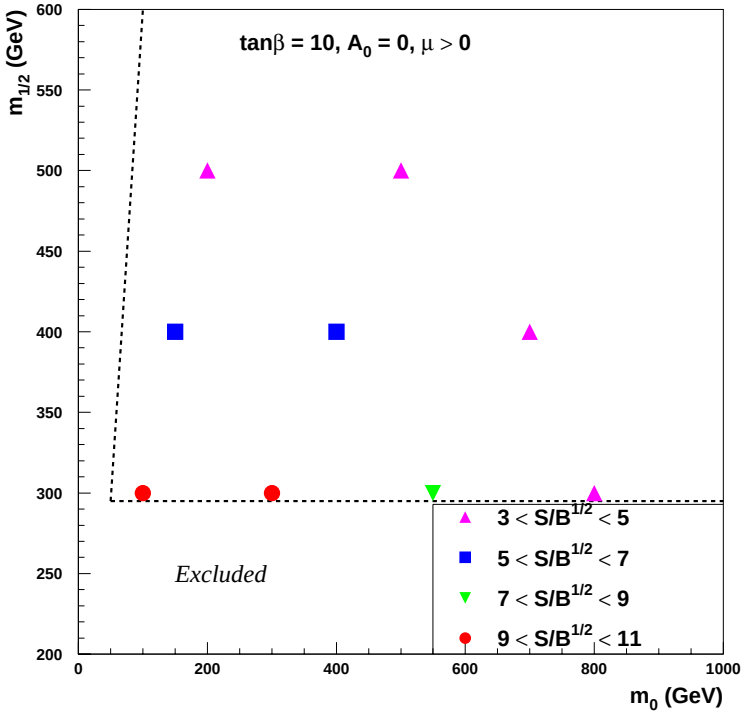

Figure 7.18: Points in the $m_0 - m_{1/2}$ plane marked with different symbols according to $S/B^{1/2}$ for $\tan\beta = 10$, $\mu > 0$ and $A_0 = 0$. A dashed line also limits the region excluded by the Higgs boson mass bound and the region theoretically excluded.

The same figure also shows the excluded region from the m_h bound and the theoretically excluded region (dashed line): all the points lie within the allowed region. Points are marked according to the highest $S/B^{1/2}$ ratio which can be achieved.

The performance is very good near the excluded region at $m_{1/2} \sim 300$ GeV for $m_0 < 550$ GeV since the $\tilde{t}$ is light enough to have a huge cross-section ($m_{\tilde{t}} < 650$) and the $\tilde{\chi}_1^0$ and

$\tilde{\chi}_1^{\pm}$ are also light ($\sim$ 120 GeV and 230 GeV) and provide high p_T final state particles. The performance decreases at $m_0 > 600$ GeV because the decay mode $\tilde{t} \to \tilde{\chi}_2^{\pm} b$ becomes dominant and at higher $m_{1/2}$ because of the smaller cross section due to the larger $\tilde{t}$. The $\tilde{t}$ can be discovered with $S/B^{1/2} > 5$ up to $m_{1/2} < 450$ GeV at $m_0 < 600$ GeV and up to $m_0 < 700$ GeV at $m_0 < 400$ GeV with this channels.

Results with $A_0 < 0$

The effect of the A_0 parameter was also investigated since a huge $|A_0|$ value can push down the $\tilde{t}$ mass and thus increase the production cross section up to values which would allow the $\tilde{t}$ discovery. The case of negative A_0 was taken into account since a positive A_0 could be associated with a Higgs boson mass below the lower bound on it. However, for what concerns the $\tilde{t}$ sector, the same mass values for positive A_0 values can also be obtained with a suitable negative A_0 value (see Fig. 7.2).

Events samples were generated at $A_0 = -500$ GeV and $A_0 = -1000$ GeV for the points $m_0 = 800$ GeV $m_{1/2} = 300$ GeV and $m_0 = 200$ GeV $m_{1/2} = 500$. In both points the signal significance is low: in the first case the reason is that the decay modes taken into account are not dominant, while, in the second case, the $\tilde{t}$ has a large mass ($m_{\tilde{t}} \sim 725$ GeV) and thus a small cross section at $A_0 = 0$.

The $m_{\tilde{t}}$ (from PYTHIA) is shown for different negative values of A_0 in the left plot of Fig. 7.19 for the two points: in both cases it falls below 600 GeV at $A_0 = -1000$ GeV. The cross section with respect to A_0 is shown in the central plot and the signal significance

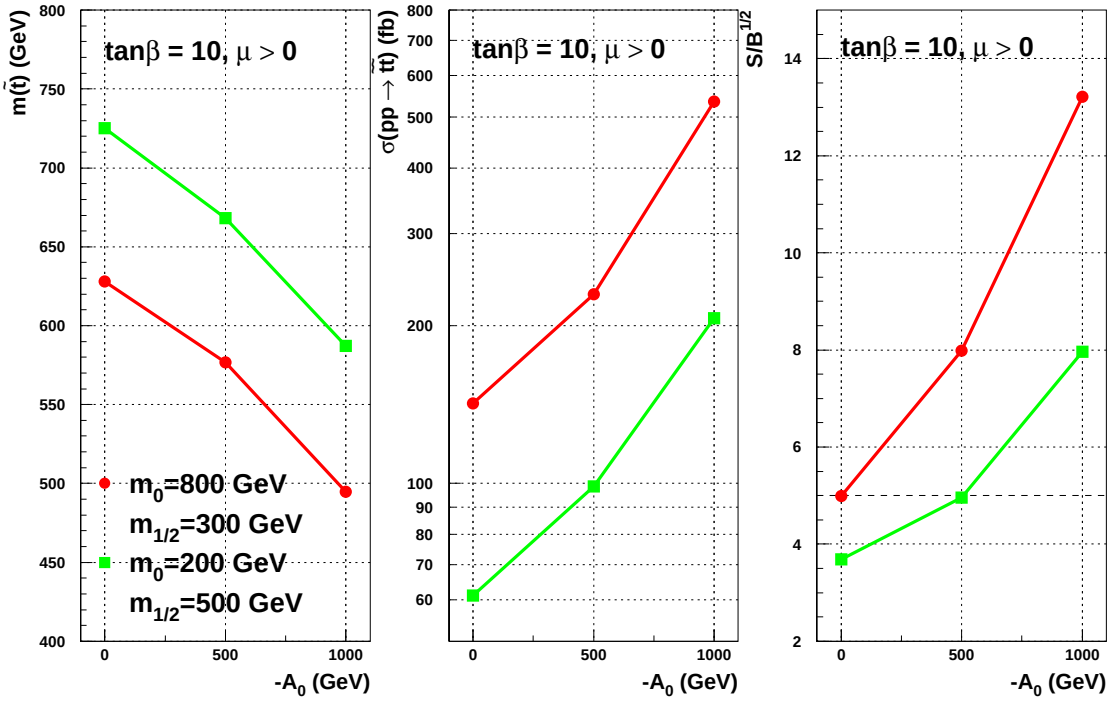

Figure 7.19: Left: $m_{\tilde{t}}$ for different A_0 values, two different points in the $m_0 - m_{1/2}$ plane, $\tan\beta = 10$ and $\mu > 0$. Center: $pp \to \tilde{t}\bar{\tilde{t}}$ cross-section for the same points and the same A_0 values. Right: $S/B^{1/2}$ ratio that can be reached by the analysis for the same points and the same A_0 values.

in the right one. In both cases the $S/B^{1/2}$ increases and passes the threshold at 5: in particular for $m_0 = 200$ GeV $m_{1/2} = 500$ a lower A_0 value would inhibit the decay modes because of the high $\tilde{\chi}_1^0$ mass and the mode $\tilde{t} \to \tilde{\chi}_1^0 c$ would have 100% branching ratio. A different analysis would be required in this case.

Results with $\tan\beta = 35$

The performance at higher value of $\tan\beta$ were also investigated. In this analysis the change of $\tan\beta$ affects the $\tilde{\chi}_1^\pm$ decay modes: at high $\tan\beta$ the mixing in the $\tilde{\tau}$ sector would be enhanced and at low m_0 the lightest $\tilde{\tau}$ eigenstate, the $\tilde{\tau}_1$, would be light enough to allow the $\tilde{\chi}_1^\pm \to \tilde{\tau}_1\nu_\tau \to \tau^\pm\nu_\tau\tilde{\chi}_1^0$ decay.

For each examined point at $\tan\beta = 10$, a sample of events was generated for $\tan\beta = 35$ to compare the discovery potential at different $\tan\beta$ values.

The effect is remarkable for the low m_0 points, $(m_0(\text{GeV}), m_{1/2}(\text{GeV})) = (100, 300)$, $(150, 400)$ and $(200, 500)$. According to the implementation of PYTHIA, the branching ratios of this decay mode are respectively $\sim 63\%$, $\sim 54\%$ and $\sim 48\%$ and the $S/B^{1/2}$ that can be achieved in these points with the $\tilde{t} \to \tilde{\chi}_1^\pm b$ ($\tilde{\chi}_1^\pm \to W^\pm\tilde{\chi}_1^0$)and $\tilde{t} \to \tilde{\chi}_1^0 t$ decay modes reduces to 6.4, 4.4 and 2.8 (to be compared with 10, 6.6 and 3.7 at $\tan\beta = 10$). No degradation was observed in the other points.

7.6.3 Effects of $b-$tagging

The role of $b-$tagging in the background reduction at trigger level has already been explained in detail: the identification of $b-$jets at trigger level is crucial to allow a background rate allowed by the band-width requirement.

The effect of the requirement of a $b-$tagged jet at offline level is shown in Table 7.5: the signal and background rates are reported for the point $m_0 = m_{1/2} = 400$ GeV, $\mu > 0$, $\tan\beta = 10$ and $A_0 = 0$ and are compared with the offline performance which would be achieved without this requirement.

Table 7.5: Expected rate for signal and background events with and without the $b-$tagging requirement at $m_0 = m_{1/2} = 400$ GeV, $\mu > 0$, $\tan\beta = 10$ and $A_0 = 0$.

	without $b-$tagging	with $b-$tagging
$\tilde{t}\tilde{t}$	118 ± 7	98 ± 6
$t\bar{t}$	304 ± 19	235 ± 17
W+jets	99 ± 33	11 ± 11
total	419 ± 39	255 ± 21
$S/\sqrt{B}$	5.7 ± 0.4	6.13 ± 0.5

According to the available statistics, the contribution of the non $t\bar{t}$ to the overall background drops from 27% to 8% with small effects on the signal and $t\bar{t}$ background. In addition, this requirement improves the sensitivity of the analysis.

The combination of the $b-$tagging performance provides a larger systematic control on the background rates since the algorithm correlations on non $b-$jets are weaker than those

of $b-$jets. On the other hand, the effect on the analysis due to a change in the $b-$tagging performance has minor effects on the sensitivity. In this sense this analysis is quite robust.

A quantitative proof of the latter statement can be provided if one assumes a $\sim 10\%$ improvement by passing from an algorithm based on transverse impact parameter to that based on three-dimensional impact parameter and three pixel layers. The signal sensitivity dependence on the $b-$tagging efficiency (ε_b) and mistagging rate (ε_u) can be approximated by the formula:

$$\frac{S}{\sqrt{B}} \sim \frac{2\varepsilon_b - \varepsilon_b^2}{\sqrt{x_t(2\varepsilon_b - \varepsilon_b^2) + (1-x_t)\bar{n}_J \varepsilon_u}} \cdot \left(\frac{S}{\sqrt{B}}\right)^{no\ btagging} \tag{7.10}$$

$x_t \sim 0.92$ being the fraction of top events in the background and $\bar{n}_J$ the average number of jets in the $W+$ jets background after all selection cuts. If the improved tagger has a better $b-$tagging efficiency $\varepsilon'_b \sim \varepsilon_b(1+\delta)$ ($\delta \sim 0.1$) for same mistagging rate, the ratio between the improved sensitivity (with $'$) and the one obtained with the default $b-$tagging algorithm is approximately:

$$\left(\frac{S}{\sqrt{B}}\right)' \Big/ \left(\frac{S}{\sqrt{B}}\right) \sim \sqrt{\frac{2\varepsilon'_b - \varepsilon'^2_b}{2\varepsilon_b - \varepsilon_b^2}} \sim 1 + \frac{1-\varepsilon_b}{2-\varepsilon_b}\delta \sim 1 + 3\%. \tag{7.11}$$

The overall 3% increase can be considered a small effect.

7.7 Analysis with Supersymmetry Background Rejection

In the mSUGRA framework, the cross sections for supersymmetric particle production are very large and the most important contribution to the signal degradation comes from supersymmetry processes which can be similar to the signal.

Most of the supersymmetric particle production at hadron colliders comes from strong interacting particles, in particular the processes $pp \to \tilde{q}\tilde{g}$ and $pp \to \tilde{g}\tilde{g}$.

Gluino and squark isomass contours were already shown in Fig. 3.1: gluino mass scales with $m_{1/2}$ while squark masses also depend on m_0, so production and decay modes crucially depends on the parameters values.

Cross sections for the overall supersymmetric particles production, $\tilde{q}\tilde{g}$, $\tilde{q}\tilde{g}$ and $\tilde{t}\bar{\tilde{t}}$ are shown in Fig. 7.20 for $\tan\beta = 10$, $A_0 = 0$, $\mu > 0$, $m_0 = 300$ GeV (left), 400 GeV (center) and 500 GeV (right) as a function of m_0.

The $\tilde{g}\tilde{g}$ cross section is between 1.5 and 10 times higher than the $\tilde{t}\bar{\tilde{t}}$ one, while the $\tilde{q}\tilde{g}$ production can be up to 10-20 times higher, especially at $m_0 \sim 300$ GeV. These backgrounds constitute approximately half of the overall supersymmetric particle production. The remaining processes have direct production of charginos and neutralinos but do not require dedicated cuts to be removed.

Events with squarks and gluinos have many jets and leptons and a large E_T^{miss} in the final state and thus they can be similar to the $\tilde{t}\bar{\tilde{t}}$ signal.

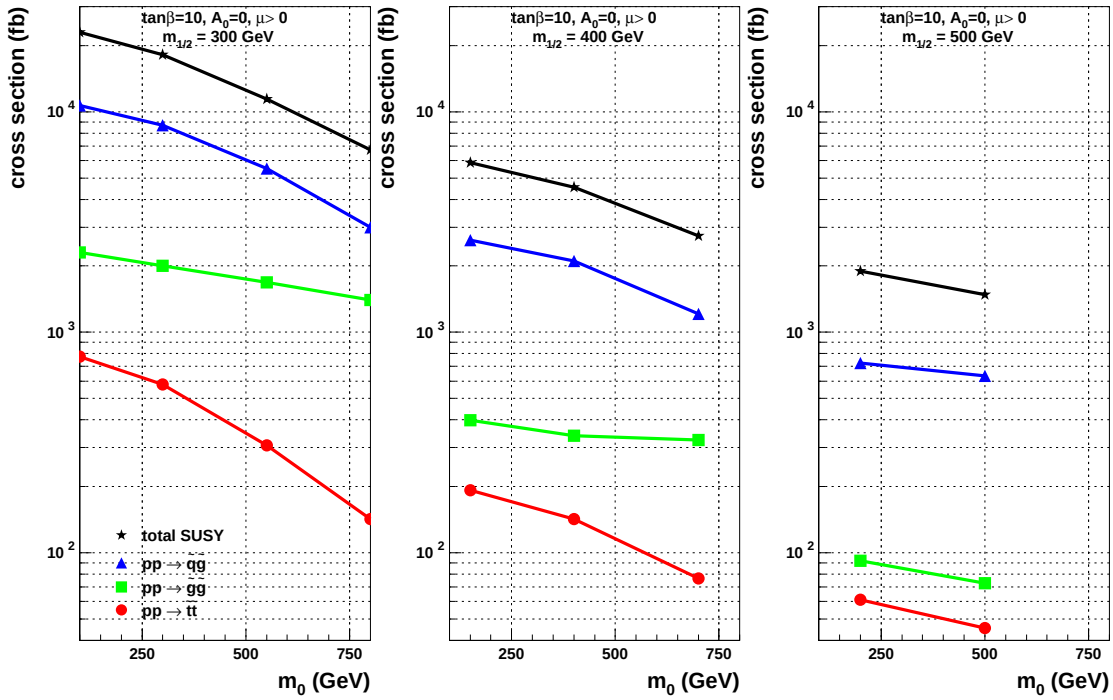

Figure 7.20: Cross sections for the overall supersymmetry particles production at $\tan\beta = 10$, $A_0 = 0$, $\mu > 0$, $m_{1/2} = 300$ GeV (left), 400 GeV (center) and 500 GeV (right) with respect m_0 (from PYTHIA).

7.7.1 Analysis

Squark and Gluino decays have very rich topologies since there can be a very large number of decay modes yielding high E_T jets, leptons and E_T^{miss} in the final state: a large number of these decay modes can pass the $\tilde{t}\bar{\tilde{t}}$ selection requirements. Since the signal occurrence relies on an excess of events than a mass peak reconstruction, such kind of excess would not allow to identify the process.

The only handles to reject supersymmetry backgrounds rely on general features of the events: supersymmetry events contain particles heavier than $\tilde{t}$ in the final state. Squarks and gluino masses are ~ 1 TeV, at least a factor 2 higher than the $\tilde{t}$ in out framework. The decay products are thus expected to be more energetic than those of the $\tilde{t}$. Therefore the only way to claim evidence of a $\tilde{t}$-like particle would be to find out an excess of events in an intermediate region of the kinematical variables used for Standard Model background rejection.

In Fig. 7.21 the E_T^{miss} and the total transverse mass are shown for the signal and the supersymmetric backgrounds for the $m_0 = 400$ GeV, $m_{1/2} = 400$ GeV, $A_0 = 0$, $\tan\beta = 10$ and $\mu > 0$ case. The values of these variables are higher in supersymmetric backgrounds rather than in signal events.

Another variable which is helpful in the supersymmetry background rejection is the p_T of the highest p_T jet since in $\tilde{q}\tilde{g}$ a very high p_T quark of the same flavour of $\tilde{q}$ is produced from the decay $\tilde{q} \to q\tilde{\chi}_i^0$ or $\tilde{q} \to q'\tilde{\chi}_i^{\pm}$. Its distribution is shown in Fig. 7.22 for the $\tilde{t}\bar{\tilde{t}}$ signal and the supersymmetric background.

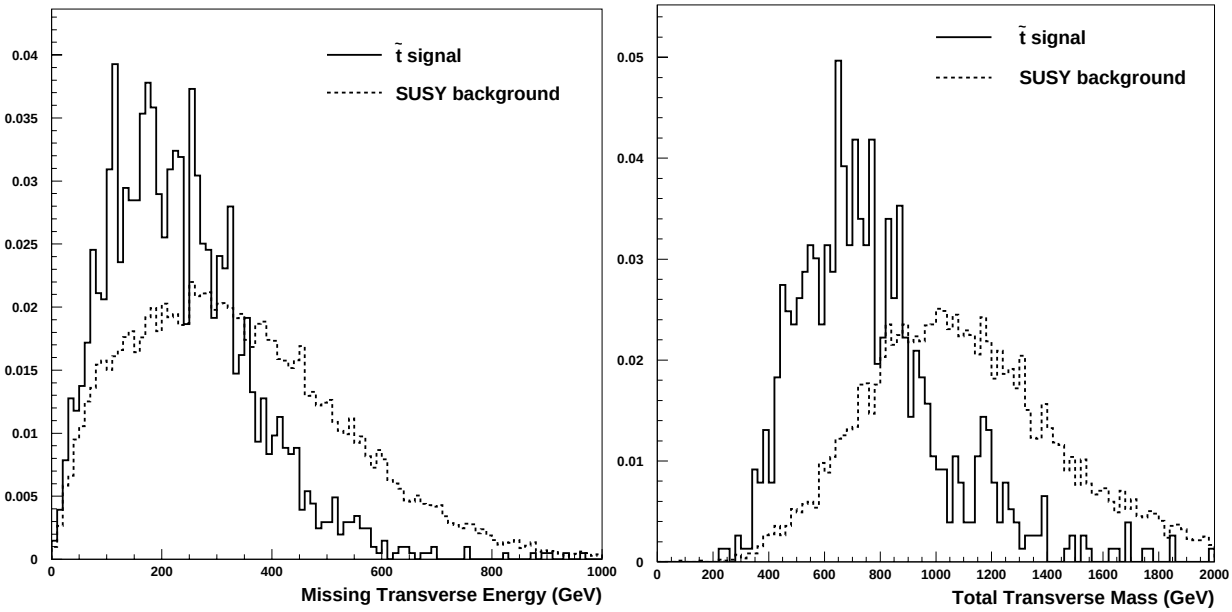

Figure 7.21: E_T^{miss} (left) and m_T^{tot} (right) distributions for the signal (solid line) and the overall supersymmetry background (right).

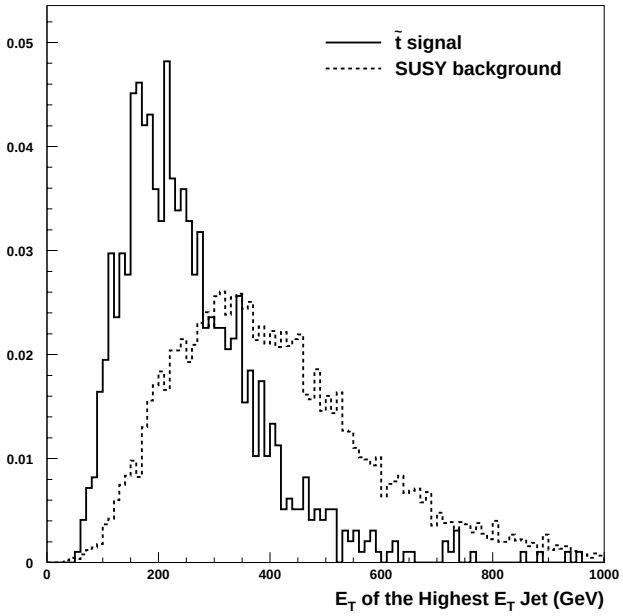

Figure 7.22: p_T of the highest p_T jet for the $\tilde{t}\bar{\tilde{t}}$ signal and the supersymmetry backgrounds.

7.7.2 Performance

To evaluate the results of the analysis, 2×10^5 events with all supersymmetry processes were generated for each point of the parameter space of Fig. 7.18.

As for the Standard Model background, selection criteria were optimised for each point requiring a maximum $S/B^{1/2}$ where B stands for the Standard Model and Supersymmetry background contributions. An upper threshold on m_T^{tot} and on the p_T of the highest p_T jet were also added.

In Fig. 7.23 the points are reported in the $m_0 - m_{1/2}$ plane at $\tan\beta = 10$, $A_0 = 0$ and $\mu > 0$ with different markers according to the value of $S/B^{1/2}$ in analogy with Fig. 7.18 for the Standard Model background rejection case. The performance is remarkably spoiled

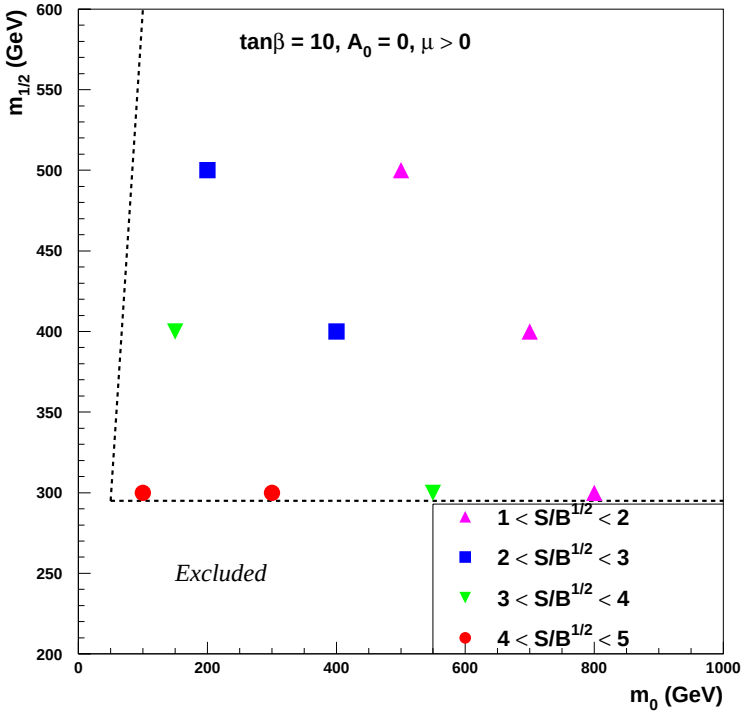

Figure 7.23: Points in the $m_0 - m_{1/2}$ plane marked with different symbols according to the predicted $S/B^{1/2}$ in the analysis with supersymmetry backgrounds for $\tan\beta = 10$, $\mu > 0$ and $A_0 = 0$. A dashed line also limits the region excluded by the Higgs boson mass bound and the region theoretically excluded.

with respect to the analysis without supersymmetry backgrounds and the 5 sigma discovery is guaranteed only at $m_{1/2} < 400$ GeV and $m_0 < 600$ GeV. The signal observability can however be recovered with the high luminosity run where a factor ~ 4 in signal significance would be expected assuming a comparable detector performance.

The performance is still improved at high $|A_0|$ values where the production cross-section for this process would be enhanced with respect to the overall SUSY production due to the lower $\tilde{t}$ mass. Fig. 7.24 shows the signal significance for the points $(m_0(\text{GeV}), m_{1/2}(\text{GeV}))$ $= (300, 800)$ and $(200, 500)$ for $A_0 = 0$, $A_0 = -500$ GeV and $A_0 = -1000$ GeV. The significance for the analysis with only Standard Model background is also superimposed to show the performance degradation. With this analysis a significance higher than 5 can

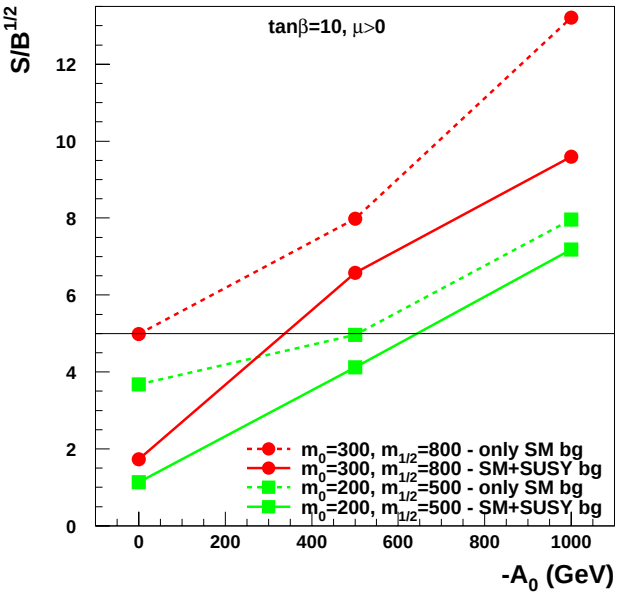

Figure 7.24: Signal significance at different values of A_0 for $(m_0(\text{GeV}), m_{1/2}(\text{GeV})) = (300, 800)$ and $(200, 500)$ at $\tan\beta = 10$ and $\mu > 0$ for the analysis with and without supersymmetry background.

be achieved at low luminosity for $A_0 < -350$ GeV at $(m_0(\text{GeV}), m_{1/2}(\text{GeV})) = (200, 500)$ and for $A_0 < -700$ GeV at $(m_0(\text{GeV}), m_{1/2}(\text{GeV})) = (300, 800)$.

7.8 Results with a Staged ECAL Scenario

The effects of a reduced ECAL coverage was investigated for this analysis: the staging of the CMS detector affects the signal sensitivity by modifying the rate of expected signal and background events. The effects on reconstruction efficiencies on signal and backgrounds can be approximately factorised through the formula:

$$\varepsilon' = K_{trig} K_{kin} \varepsilon \tag{7.12}$$

ε' being the efficiency with the staged detector layout, ε the one with the default layout, factors K_{trig} and K_{kin} parametrise the effect of ECAL on the trigger and reconstruction of the event kinematics. K_{trig} is related to a decrease in efficiency due to the loss of events in triggers produced by an electron impinging on the electron end-caps. K_{kin} is related to the effect of the kinematical cuts due to a variation of the main kinematic variables used to select signal, E_T^{miss}, $m_T^{l\nu}$ and m_T^{tot}: the variation is due to the degradation in energy and position measurement of the electromagnetic showers.

A sample of 5×10^5 $t\bar{t}$ event, one of 5×10^5 W plus jets events and one of 10^4 signal events at $m_0 = 400$ GeV, $m_{1/2} = 400$ GeV, $\tan\beta = 10$, $\mu > 0$ and $A_0 = 0$ were produced removing the ECAL end-caps from the fast simulation. An estimate of the K_{trig} and K_{kin} factors were provided for these events and the effect on sensitivity for the parameter space point above was investigated.

Fig. 7.25 shows η distribution for electrons which provide the trigger in the default and the staged ECAL scenario for $t\bar{t}$ events. The latter distribution is truncated at the $|\eta|$

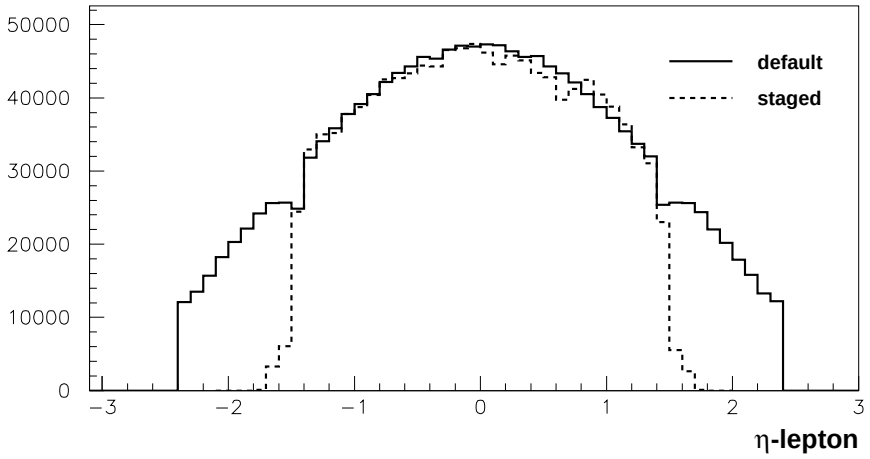

Figure 7.25: η distribution of the highest p_T electrons in the default and in the staged ECAL layout (arbitrary scale).

values corresponding to the ECAL barrel coverage.

The distributions of the main kinematical variables used in the analysis, E_T^{miss}, $m_T^{l\nu}$ and m_T^{tot} are shown in Fig. 7.26 for the default detector layout and the staged one for $t\bar{t}$ events. No remarkable effects are found for the E_T^{miss} and m_T^{tot} variables. A broadening of the $m_T^{l\nu}$ distribution is found due to the degradation of the resolution on the $E_T^{miss}-$lepton angle. This effect spoils the rejection power of the $m_T^{l\nu}$ cut. The estimates of the K_{trig} and K_{kin} factors from the distributions above are shown in Table 7.6 for the $t\bar{t}$, Wj and $\tilde{t}\bar{\tilde{t}}$ events. The errors are due to statistical fluctuation.

Table 7.6: K_{trig} and K_{kin} for the $t\bar{t}$ and Wj backgrounds and the $\tilde{t}\bar{\tilde{t}}$ signal in the point $m_0 = 400$ GeV, $m_{1/2} = 400$ GeV, $\tan\beta = 10$, $\mu > 0$ and $A_0 = 0$.

	$t\bar{t}$	Wj	$\tilde{t}\bar{\tilde{t}}$
K_{trig}	$0.89 \pm 2 \times 10^{-4}$	$0.83 \pm 5.5 \times 10^{-4}$	$0.93 \pm 5 \times 10^{-3}$
K_{kin}	1.50 ± 0.04	1.4 ± 0.3	0.95 ± 0.03

The effect on the signal sensitivity with respect to the Standard Model backgrounds can be factorised through the formula:

$$(S/\sqrt{B})' = K_{S/\sqrt{B}} \cdot (S/\sqrt{B}). \tag{7.13}$$

The $K_{S/\sqrt{B}}$ parameter is provided by the relationship:

$$K_{S/\sqrt{B}} \sim \frac{K_{trig}(\tilde{t}\bar{\tilde{t}})K_{kin}(\tilde{t}\bar{\tilde{t}})}{\sqrt{K_{trig}(t\bar{t})K_{kin}(t\bar{t})}} \cdot \frac{1}{\sqrt{x_t + (1-x_t)y_W}} \tag{7.14}$$

x_t being the fraction of top background in the overall Standard Model background and y_W defined by:

$$y_W = \frac{K_{trig}(Wj)K_{kin}(Wj)}{K_{trig}(t\bar{t})K_{kin}(t\bar{t})} \tag{7.15}$$

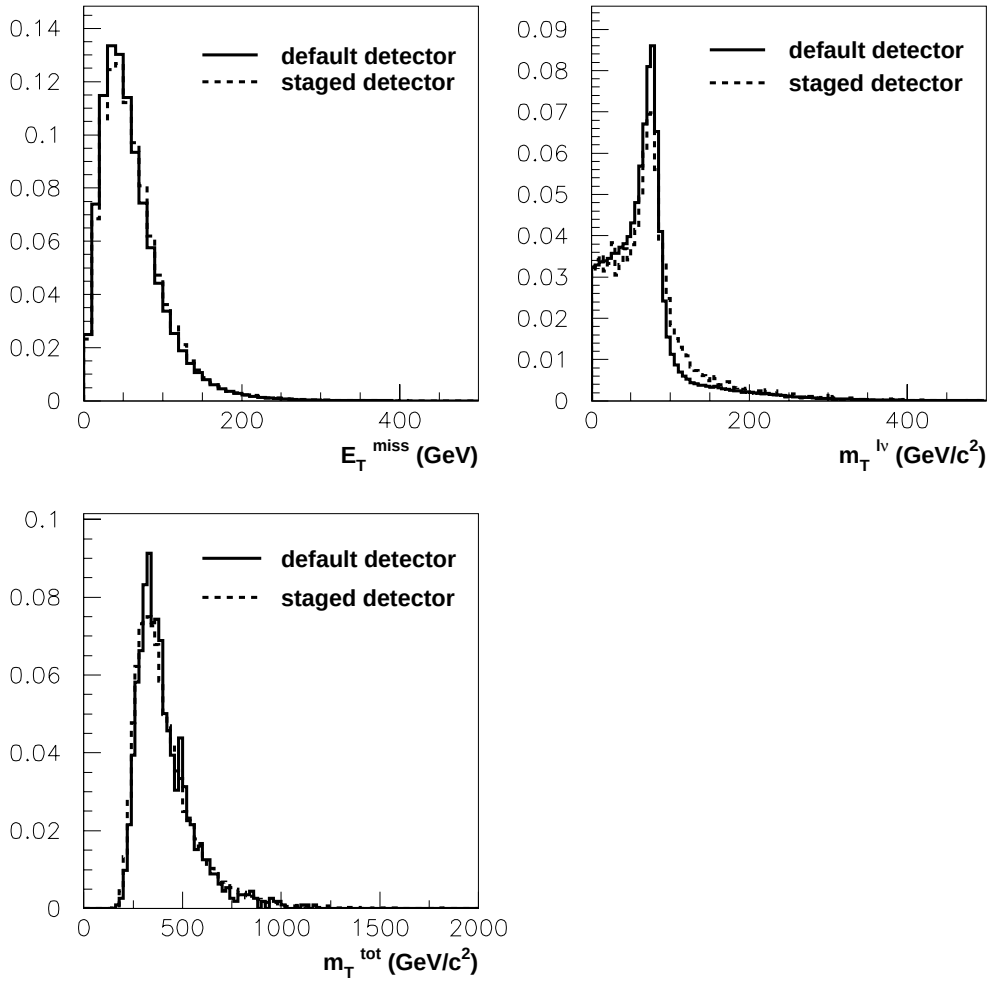

Figure 7.26: Distributions of E_T^{miss} (upper left), $m_T^{l\nu}$ (upper right) and m_T^{tot} (lower left) for the $t\bar{t}$ events sample in the default and staged detector scenario.

According to the estimates provided above the correction factor on the signal sensitivity is of the order of 77%.

7.9 Conclusions

The scalar top quark search has been analysed in a large set of theoretical and experimental conditions.

Different parameter space points were analysed in the mSUGRA framework and the discovery potential was investigated as a function of the $\tilde{t}$ and $\tilde{\chi}_1^0$ masses and as a function of the mSUGRA parameters. The effect of the expected Standard Model background and the model-dependent SUSY background were treated separately. In most of these conditions results are encouraging and demonstrate that the CMS experiment can extend this search up to mass ranges which cannot be explored by the current experiments.

Different experimental scenarios were also analysed: the effect of an improved $b-$tagging with sophisticated algorithms and the possibility of using three pixel layers and 2+2 forward disks are investigated as well as the the effects of a reduced coverage of the electromagnetic calorimeter. In all these conditions the physics results are quite stable with respect to changes in the baseline detector design.

Conclusions

A tracking system completely based on silicon detectors was designed for CMS in order to operate in experimental conditions which were never experienced by the past experiments. An extensive R&D activity on silicon microstrip detectors demonstrated the feasibility of this device, allowed to define the Tracker detector design and processing technologies, and to start a massive production and test of all components.

The offline reconstruction performance of this system, and in particular the $b-$tagging performance were analised in detail. The $b-$tagging performance of various algorithms were studied in different Tracker regions. The tools which were developed for this study, also allowed to evaluate the impact of different tracker design on the $b-$tagging performance. These studies demonstrate that, although the difficult experimental conditions, this kind of tracking system has a $b-$tagging performance as excellent as that one that led previous experiments to important discoveries. Moreover, the possibility to perform $b-$tagging at High Level Trigger provides a background trigger rate reduction which allows data storage with a good efficiency on the relevant physics signals.

Finally, the CMS discovery potential of a specific process, the scalar top quark production, was analysed using the current knowledge of the detector response. Different theoretical and experimental scenarios were considered and in most cases the CMS experiment allows to observe an excess of events over the predicted background.

The development of the online and offline reconstruction algorithms and the improvement of the knowledge of the detector response are providing encouraging and reliable results on the CMS physics potential.

Bibliography

[1] S.Weinberg, Phys. Rev. Lett. **19** (1967) 1264

S.L Glashow, Nucl. Phys. B **22**, 579 (1961)

[2] The ALEPH, DELPHI, L3 and OPAL Collaborations and LEP Electroweak Working Group and SLD Heavy Flavor and Electroweak Groups, hep-ex/0112021

[3] P.Nilles, Phys. Rep. **110** (1984), 1

J.Wess and J.A.Bagger, *'Supersymmetry and Supergravity'*, Princeton University Press, Princeton NJ, 1992

S.P.Martin, hep-ph/9709356

M.Drees, hep-ph/9611409

R.Barbieri, Riv. Nuovo Cimento **11** (1998)

[4] Joint LEP 2 Supersymmetry Working Group,

`http://lepsusy.web.cern.ch/lepsusy/Welcome.html`

[5] J.Ellis, K.A.Olive and Y.Santoso, New J. Phys. **4** (2002), 32

[6] U.Dydak, CMS TN/96-022

[7] P.W.Higgs, Phys. Lett. **12**, 132 (1964)

[8] J.F.Gunion, H.E.Haber, G.Kane and S.Dawson, *'The Higgs Hunter Guide'*, Perseus Publishing, Cambridge, Massachussets, 2000

[9] T.Hambye and K.Riesselmann, Phys. Rev. D **55** (1997), 7255

[10] A.D.Martin, J.Outhwaite and M.G.Ryskin, Phys. Lett. **B492** (2000), 69

[11] R.Barate *et* al, the ALEPH Collaboration, Phys. Lett. **B495** (2000), 1

M.Acciarri *et* al, the L3 Collaboration, Phys. Lett. **B495** (2000), 18

P.Abreu *et* al, the DELPHI Collaboration, Phys. Lett. **B499** (2001), 23

G.Abbiendi *et* al, the OPAL Collaboration, Phys. Lett. **B499** (2001), 38

[12] The ALEPH, DELPHI, L3 and OPAL Collaborations and the LEP Working Group for Higgs boson Search, hep-ex/0107029

[13] S.Coleman and J.Mandula, Phys. Rev. **159** (1967), 1251

[14] R.Haag, J.Lopuszanski and M.Sohnius, Nucl. Phys. **B88** (1975), 257

[15] P.Fayet and J.Iliopoulos, Phys. Lett. **B51** (1964), 461
P.Fayet, Nucl. Phys. **B90** (1975), 304

[16] L.O'Raifertaigh, Nucl. Phys. **B96** (1975), 331

[17] A.H.Chamseddine, R.Arnowitt and P.Nath, Phys. Rev. Lett. **49** (1982), 970

[18] M.Dine, A.Nelson and Y.Shirman, Phys. Rev. **D48** (1993), 1277

[19] L.Girardello and M.T.Grisaru, Nucl. Phys. **B194** (1982), 65

[20] J.Ellis and S.Rudaz, Phys. Lett. **B128** (1983), 248

[21] P.Langacker, Phys. Rep. **72** (1981), 185

[22] L.Ibañez and G.Ross, Phys. Lett. **B110** (1982), 215

[23] K.Inoue, A.Kakuto, H.Komatsu and S.Takeshita, Progr. Theor. Phys. **68** (1982), 927

[24] S.Abel *et* al., hep-ph/0003154

[25] T.Affolder *et al.*, the CDF Collaboration, Phys. Rev. Lett. **88** (2002), 041801

[26] B.Abbott *et al.*, the D0 Collaboration, Phys. Rev. Lett. **83** (1999), 4937

[27] T.Affolder *et al.*, the CDF Collaboration, Phys. Rev. Lett. **87** (2001), 251803

[28] A.Bartl, W.Majerotto and W.Porod, Z. Phys. **C64** (1994), 499

[29] T.Affolder *et al.*, the CDF Collaboration, Phys. Rev. Lett. **84** (2000), 5704

[30] B.Abbott *et al.*, the D0 Collaboration, Phys. Rev. **D60** (1999), 031101

[31] T.Affolder *et al.*, the CDF Collaboration, Phys. Rev. Lett. **84** (2000), 5273

[32] R.Demina, D.J.Lykken, K.T.Matchev and A.Nomerotski, Phys. Rev. **D62**, 035001

[33] V.M.Abazov *et al.*, the D0 Collaboration, Phys. Rev. Lett. **88** (2002), 171802

[34] S.Abachi *et al.*, the D0 Collaboration, Phys. Rev. Lett. **76** (1996), 2222

[35] R.Barate *et al.*, the ALEPH Collaboration, Phys. Lett. **B** 499 (2001), 67

[36] S.Heinemeyer, W.Hollik and G.Weigelein, Comp. Phys. Commun. **124** (2000), 76
S.Heinemeyer, W.Hollik and G.Weigelein, Eur. Phys. J. **C9** (1999), 343

[37] J.Ellis, G.Ganis, D.V.Nanopoulos and K.Olive, Phys. Lett. **B502** (2001), 171

[38] H.Baer, M.Drees, F.Paige, P.Quintana and X.Tata, Phys. Rev. **D61** (2000), 095007

[39] C.Boehm, A.Djouadi and M.Drees, Phys. Rev. **D62** (2000), 035012

[40] J.Ellis, K.A.Olive and Y.Santoso, hep-ph/0112113

[41] R.Barbieri and G.F. Giudice, Phys. Lett. **B309** (1993), 86

[42] M.S.Alam *et al.*, the CLEO Collaboration, Phys. Rev. Lett. **74** (1995), 2885
S.Ahmed *et al.*, the CLEO Collaboration, CLEO-CONF 99-10
The BELLE Collaboration, BELLE-CONF-0003

[43] C.Degrassi, P.Gambino and G.F.Giudice, JHEP **0012** (2000), 009

[44] H.N.Brown *et al.*, the Muon $g-2$ Collaboration, Phys. Rev. Lett. **86** (2001), 2227

[45] H.Hayakawa and T.Kinoshita, hep-ph/0112102

[46] J.Ellis, J.S.Hagelin, D.V.Nanopoulos, K.Olive and M.Srednicki, Nucl. Phys. **B238** (1984), 453
H.Goldberg, Phys. Rev. Lett. **50** (1983), 1419

[47] C.Pryke *et al.*, Astrophys. J. **568** (2002), 46
C.B.Netterfield *et al.*, the Boomerang Collaboration, Astrophys. J. **571** (2002), 604

[48] J.Ellis, T.Falk, K.Olive and M.Srednicki, Astropart. Phys. **13** (2000), 181

[49] J.Ellis, T.Falk, G.Ganis, K.Olive, M.Srednicki, Phys. Lett. **B510** (2001), 236

[50] The LHC Study Group, CERN/AC/95-05

[51] the ATLAS Collaboration, ATLAS Technical Proposal, CERN/LHCC 94-43

[52] the CMS Collaboration, CMS Technical Proposal, CERN/LHCC 94-038

[53] the ALICE Collaboration, ALICE Technical Proposal, CERN/LHCC 95-71

[54] the LHCb Collaboration, LHCb Technical Proposal, CERN/LHCC 98-4

[55] the CMS Collaboration, CMS TDR - Technical Design Report: CMS - MAGNET

[56] the CMS Collaboration, CMS TDR - Technical Design Report: CMS - TRACKER, CERN/LHCC 98-6

[57] the CMS Collaboration, Addendum to the CMS Tracker TDR, CERN/LHCC 2000-016

[58] the CMS Collaboration, CMS TDR - Technical Design Report: CMS - ECAL, CERN/LHCC 97-33

[59] D.Green, K.Maeshima, R.Vidal, W.Wu and S.Kunori, CMS NOTE 2002/004

[60] the CMS Collaboration, CMS TDR - Technical Design Report: CMS - HCAL, CERN/LHCC 97-31

[61] the CMS Collaboration, CMS TDR - Technical Design Report: CMS - MUON, CERN/LHCC 97-32

[62] the CMS Collaboration, CMS TDR - Technical Design Report: CMS - TRIGGER, Vol.1 CERN/LHCC

[63] the CMS Collaboration, CMS TDR - Technical Design Report: CMS - TRIGGER, Vol.2 in preparation

[64] D.Kotlinski, CMS-NOTE 2001/022

[65] H.Baer, F.Paige, S.Protopopescu and X.Tata, in *Proceedings of the Workshop on Physics on Current Accelerators and Supercolliders*, eds. J.Hewett, A.White, D.Zeppenfeld (Argonne National Laboratory, Argonne, Illinois, 1993)

[66] S.Abdullin and F.Charles, Nucl. Phys. **B547** (1999), 60

[67] S.Abdullin, Ž.Antunovic, F.Charles and M.Dželalija, CMS NOTE 1999/018

[68] H.Baer, C.H.Chen, F.Paige and X.Tata, Phys. Rev. **D53** (1996), 597

[69] G.Segneri, CMS CR 2002/007, INFN-PI-AE 2002-01

[70] I.Iashvili and A.Kharchilava, Nucl. Phys. **B526** (1998), 153

[71] S.Abdullin and D.Denegri, CMS NOTE 1997/070

[72] I.Hinchliffe, F.E.Paige, M.D.Shapiro, J.Söderqvist and W.Yao, Phys. Rev. **D55** (1997), 5520

[73] M.Chiorboli, CMS CR 2002/013

[74] M.French, APV User manuals, available at:

`http://www.te.rl.ac.uk/med`

[75] D.Lucchetti *et al.*, in *'Proceedings of the Fifth International Symposium on High Purity Silicon'*, Electrochemical Society Proceedings, Vol.98-13

[76] G.Segneri *et al.*, Nucl. Instr. Meth. **A476** (2002), 729

[77] L.Borrello *et al.*, to appear on IEEE Trans. Nucl. Sci.

[78] S.Braibant *et al.*, CMS NOTE 2000/011

[79] N.Demaria *et al.*, Nucl. Instr. Meth. **A447** (2000), 142

S.Albergo *et al.*, Nucl. Instr. Meth. **A466** (2001), 300

[80] A.Honma *et al.*, CMS NOTE 2002/005

[81] L.Demaria, M.Meschini, F.Hartman and G.Dirkes, 'Procedures for Module Test - Draft1', available at:

`http://hep.fi.infn.it/CMS/moduletest/wg.html`

[82] G.Lutz, *'Semiconductor Radiation Detector'*, Springer Verlag

[83] M.Moll, Ph.D. Thesis (Hamburg University), DESY-THESIS-1999-040

[84] A.Chilingarov *et al.*, Nucl. Instr. Meth. **A360** (1995), 432

[85] E.Fretwurst *et al.*, Nucl. Instr. Meth. **A342** (1994), 19

[86] F.Lemeilleur *et al.*, Nucl. Instr. Meth. **A360** (1995), 438

[87] Bates *et al.*, IEEE Trans. Nucl. Sci. **43** (1996), 199
Bates *et al.*, CERN/ECP 95-18

[88] `http://cms.web.psi.ch/cms.html`

[89] R.Baur, Nucl. Instr. Meth. **A465** (2000), 159
D. Kotlinski, R. Baur, K. Gabathuler, R. Horisberger, R. Schnyder and W. Erdmann, in *Proceedings of the 6th Workshop on Electronic for LHC Experiments* (Cracow, Poland, Sept. 11-15 2000)

[90] D.Passeri, P.Ciampolini, A.Scorzoni and G.M.Bilei, IEEE Trans. Nucl. Sci. **47** (2000), 1468

[91] *'Supply of Silicon Micro-Strip Detector for the CMS SST'*, IT-2777/EP/CMS

[92] `http://abbaneo.home.cern.ch/abbaneo/cms/layout/whole.html`

[93] A.Marchioro, *'CMS Microstrip Tracker Electronics'*, available at:
`http://www.cmstrackercontrol.web.cern.ch/CMSTrackerControl/documents/GeneralDoc.htm`

[94] S.Gadomski *et al.*, Nucl. Instr. Meth. **A320** (1992), 217

[95] E.Barberis *et al.*, Nucl. Instr. Meth. **A342** (1994), 90

[96] V.Radeka and R.A.Boie, Nucl. Instr. Meth. **A178** (1980), 543

[97] L.Borrello *et al.*, Nucl. Instr. Meth. **A461** (2000), 178

[98] S.Dutta *et al.*, IEEE Trans. Nucl. Sci. **48** (2001), 2303

[99] O.Adriani *et al.*, Nucl. Instr. Meth. **A396** (1997), 76

[100] A.Heikkinen and V.Kärimaki, CMS NOTE 1999/029

[101] S.Dutta *et al.*, Nucl. Instr. Meth. **A476** (2002), 739

[102] M.Lenzi *et al.*, IEEE Trans. Nucl. Sci. **48** (2001), 1016

[103] A.Marchioro and M.Meschini, *'Modules for test system'*, available at:
`http://cms.pi.infn.it:8088/roby/moduletest/index.html`

[104] ORCA reference guide available at:

`http://www.cmsdoc.cern.ch/orca`

[105] T.Todorov, in *Proceedings of the International Conference on Computing in High Energy and Nuclear Physics* (Padova, Italy, Feb. 7-11 2000)

[106] R.Frühwirth, M.Regler, R.K.Bock, H.Grote and D.Notz, *'Data Analysis Techniques for High Energy Physics'*, Cambridge University Press, 2000

[107] R.Frühwirth, Nucl. Instr. Meth. **A262** (1997), 444

[108] L.Fanò, F.Palla, R.Ranieri and G.Segneri, CMS NOTE in preparation

[109] G.Bagliesi, S.Dutta, S.Gennai and G.Sguazzoni, CMS IN 2001/045

[110] P.Vanlaer, CMS NOTE in preparation

[111] V.Kärimaki, CMS NOTE 1997/051

[112] F.Abe *et al.*, the CDF Collaboration, Phys. Rev. **D50** (1994), 2966

[113] S.Dell'Agnello, Ph.D. Thesis (Università di Pisa), FERMILAB-THESIS-1994-24, INFN-PI-AE-94-10

[114] G.Segneri and F.Palla, CMS NOTE already submitted

[115] T.Sjöstrand, Comp. Phys. Comm. **82** (1994), 74

[116] V.Kärimaki *et al.*, *CMS Simulation Package CMSIM, User's Guide and Reference Manual*, CMS Detector and Simulation software group, CERN, Geneva 2000

[117] M.Konecki and A.Starodumov, $b\bar{b}$ *Events simulation package user's manual*:

`http://cmsdoc.cern.ch/shulga/SIMUB/SIMUB.html`

[118] GEANT-3, Detector description and Simulation Tool, CERN Program Library entry W5013, CERN, Geneva, Ed. March 1995

R.Brun *et* al., GEANTS3, CERN DD//EE/84-1, revised 1987

[119] Z.Xie, F.Palla and A.Starodumov, CMS NOTE 2000/038

[120] G.Segneri, to appear on Nucl. Phys. Proc. Suppl.

[121] G.Segneri, CMS IN already submitted, draft documentation available at:

`http://cmsdoc.cern.ch/Physics/btau/management/activities/physics/btagging/btag.html`

[122] D.Buskulič *et al.*, the ALEPH Collaboration, Phys. Lett. **B313** (1993), 535

[123] D.Brown and M.Franck, ALEPH NOTE 1992-135

[124] N.Stepanov and V.Drollinger, CMS NOTE 2000/059

[125] K.Hikasa and M.Kobayashi, Phys. Rev. **D36** (1987), 724

[126] H.Baer, M.Drees, R.Godbole, J.F.Gunion and X.Tata, Phys. Rev. **D44** (1991), 725

[127] H.Baer, J.Sender and X.Tata, Phys. Rev. **D50** (1994), 4517

[128] U.Dydak, H.Röhringer and J.Tuominiemi, CMS TN/96-103

[129] W.Beenakker, M.Krämer, T.Plehn, M.Spira and P.M.Zerwas, Nucl. Phys. **B515** (1998), 3

[130] S.Abdullin, A.Khanov and N.Stepanov, CMS-TN 94-180

[131] M.Mrenna, Comp. Phys. Comm. **101** (1997), 232

[132] M.Drees and S.P.Martin, hep-ph/9504324

[133] D.Acosta *et al.*, CMS NOTE 2001/011